Models in search of signals:

pulsar glitches, solar flares, and continuous gravitational waves

Julian Brian Carlin

ORCID: 0000-0001-5694-0809

March, 2023

A thesis submitted in complete fulfillment of the requirements for the degree of

Doctor of Philosophy
Physics
The University of Melbourne

"A meaningful quote or special dedication"

Abstract

Lorem ipsum dolor sit amet, consectetuer adipiscing elit. Ut purus elit, vestibulum ut, placerat ac, adipiscing vitae, felis. Curabitur dictum gravida mauris. Nam arcu libero, nonummy eget, consectetuer id, vulputate a, magna. Donec vehicula augue eu neque. Pellentesque habitant morbi tristique senectus et netus et malesuada fames ac turpis egestas. Mauris ut leo. Cras viverra metus rhoncus sem. Nulla et lectus vestibulum urna fringilla ultrices. Phasellus eu tellus sit amet tortor gravida placerat. Integer sapien est, iaculis in, pretium quis, viverra ac, nunc. Praesent eget sem vel leo ultrices bibendum. Aenean faucibus. Morbi dolor nulla, malesuada eu, pulvinar at, mollis ac, nulla. Curabitur auctor semper nulla. Donec varius orci eget risus. Duis nibh mi, congue eu, accumsan eleifend, sagittis quis, diam. Duis eget orci sit amet orci dignissim rutrum.

Nam dui ligula, fringilla a, euismod sodales, sollicitudin vel, wisi. Morbi auctor lorem non justo. Nam lacus libero, pretium at, lobortis vitae, ultricies et, tellus. Donec aliquet, tortor sed accumsan bibendum, erat ligula aliquet magna, vitae ornare odio metus a mi. Morbi ac orci et nisl hendrerit mollis. Suspendisse ut massa. Cras nec ante. Pellentesque a nulla. Cum sociis natoque penatibus et magnis dis parturient montes, nascetur ridiculus mus. Aliquam tincidunt urna. Nulla ullamcorper vestibulum turpis. Pellentesque cursus luctus mauris.

Declaration

This page certifies that:

- This thesis contains only original work towards a Doctor of Philosophy, except where indicated in the preface
- Due acknowledgement has been made in the text to all other material used
- This thesis is fewer than 100 000 words in length, exclusive of tables, figures, bibliographies, and appendices

Your Signature

Your Name Here

Preface

This thesis is an original work by the author reporting research done alone or in collaboration with other authors. This section provides a chapter-by-chapter summary of the author's contributions and the publication status of all material.

Chapter 1 is a comprehensive literature review written by the author for this thesis. It is an original work of the author. This chapter has not and will not be submitted for publication.

Chapter 2 is...

Acknowledgments

A long list of acknowledgements, inside jokes, etc

Contents

List of Figures

List of Tables

CHAPTER 1

Long-term statistics of pulsar glitches triggered by a Brownian stress accumulation process

1.1. Introduction

The secular braking of rotation-powered pulsars is perturbed by two phenomena: glitches and timing noise. Timing noise, or stochastic wandering of the spin frequency, shows up in timing residuals as a red-noise process with an auto-correlation time-scale of days to weeks [5–7]. Glitches are impulsive spin-up events that recur erratically [2, 4, 8].

The microphysical mechanism that triggers glitches is an open question. Candidates include superfluid vortex avalanches [9, 10], starquakes [11, 12], hydrodynamic instabilities [13–15] and more; see Haskell and Melatos [16] for a modern review. Most of these mechanisms are predicated on the idea that the electromagnetic braking of the crust increases stress (e.g. elastic strain or differential rotation) in the system, some fraction of which is released spasmodically at each glitch. If the stress increases deterministically between glitches, the long-term glitch activity can be described by a state-dependent Poisson (SDP) process which links the instantaneous glitch rate to the stress in the system; glitches become more likely as the stress approaches a threshold [1]. The SDP process is a meta-model in the sense that it encompasses phenomenologically the stress-release idea at the core of the mechanisms listed above without specializing to the microphysics of the mechanism. It makes falsifiable statistical predictions about long-term observations of the sizes and waiting times of glitches and their correlations [1, 17–19].

Pulse-to-pulse observations of a glitch in the Vela pulsar (PSR J0835−4510) were made at the Mount Pleasant radio telescope in December 2016 [20]. Bayesian analysis finds evidence for a rotational slowdown ("precursor") immediately prior to the glitch [21]. The slowdown is of the same order as the pulse jitter, i.e. pulse-to-pulse variations in the pulse profile, possibly caused by magnetospheric fluctuations unrelated to the internal stress. Another possibility — certainly not unique — is that the slowdown represents a random internal (e.g. hydrodynamic) fluctuation, which drives the stress above a critical threshold, triggering the glitch [21]. Stochastic fluctuations in the internal stress may be caused by superfluid turbulence, for example [22–24].

In this paper we do not seek to adjudicate on the putative link between internal stochastic fluctuations and an observed rotational slowdown prior to a glitch. Nor do we seek to model such a link directly. Instead, motivated partly by the Vela data, we investigate an alternative to the SDP meta-model, wherein glitches are the result of an internal, unobservable, globally averaged stress that evolves stochastically as a Brownian process, until a glitch is triggered at a critical stress threshold. The Brownian meta-model differs from the SDP meta-model by allowing the stress to evolve stochastically between glitches (instead of increasing deterministically), and triggering a glitch only when a critical threshold is reached (instead of at any time before the threshold is reached). Together the two meta-models encompass a large set of plausible microphysical mechanisms. Both models make falsifiable predictions about long-term statistics, a valuable feature. We describe the details of the Brownian meta-model in Section 1.2. In Section 1.3 we explore its long-term statistical predictions. In Section 1.4 we compare data from the six pulsars with the highest number of recorded glitches with the predictions of the Brownian meta-model, with an eye towards falsification. An analogous study of the SDP meta-model can be found elsewhere [17–19]. In Section 1.5 we discuss how population trends may inform meta-model parameters.

1.2. Brownian stress accumulation

1.2. Equation of motion

We define X to be a stochastic variable equal to the globally averaged stress in the system. In the superfluid vortex avalanche picture X is proportional to the lag between the angular speed of the rigid crust and the superfluid interior. In the crustquake picture X is proportional to the elastic strain in the crust.

Between glitches we propose that $X(t)$ evolves according to a Wiener process, which obeys the Langevin (Itô) equation

$$\frac{\mathrm{d}X(t)}{\mathrm{d}t} = \xi + \sigma B(t) \ , \tag{1.1}$$

with drift coefficient ξ (units: stress/time) and diffusion coefficient σ [units: stress/(time)$^{1/2}$], and where $B(t)$ is a white noise process of zero mean and unit variance [25, 26]. We assume both ξ and σ are constant with time. Practically, at each time step, the stress increments by ξ and undergoes a random step (up or down) by σ multiplied by a random number drawn from a Gaussian with zero mean and variance equal to the time step. Equation (1.1) leads to the Fokker-Planck equation

$$\frac{\partial p}{\partial t} = -\xi \frac{\partial p}{\partial X} + \frac{\sigma^2}{2} \frac{\partial^2 p}{\partial X^2} \ , \tag{1.2}$$

where $p\,\mathrm{d}X = p(X, t\,|\,X_0)\,\mathrm{d}X$ is the probability of finding the stress in the region $(X, X + \mathrm{d}X)$ at time t, given that it started at $X = X_0$ after a glitch at $t = 0$, viz.

$$p(X, t = 0\,|\,X_0) = \delta(X - X_0) \ . \tag{1.3}$$

The Brownian process terminates at $X = X_c$, i.e. X_c is the stress threshold where a glitch is triggered. The glitch decrements the stress by a random amount ΔX, drawn from a stress-release distribution, discussed in Section 1.2.2. Mathematically, the termination of the Brownian process at $X = X_c$ corresponds to an absorbing boundary condition:

$$0 = p(X = X_c, t \,|\, X_0) \ . \tag{1.4}$$

We also require $X(t) \geq 0$; the stress is never negative[1]. This corresponds to a reflecting boundary condition at $X = 0$:

$$0 = \left.\frac{\partial p(X, t \,|\, X_0)}{\partial X}\right|_{X=0} - \frac{2\xi}{\sigma^2} p(X = 0, t \,|\, X_0) \ . \tag{1.5}$$

Equations (1.2)–(1.5) are solved analytically assuming that $p(X, t \,|\, X_0)$ is separable in X and t. The solution is presented in Appendix 1.A1, following the approach in Sweet and Hardin [27]. Higher values of $\xi X_c/\sigma^2$ imply drift dominates over diffusion; lower values of $\xi X_c/\sigma^2$ imply diffusion dominates over drift. Figure 1.1 shows four representative time series of the evolution of X for four different values of ξ/σ^2, with $X_c = 1$ fixed in each panel. For $\xi/\sigma^2 = 0.1$ the process appears by eye to fluctuate randomly, with large, rapid excursions both up and down in stress. On the other hand, for $\xi/\sigma^2 = 50$, the stress accumulates steadily with small random excursions and large glitches are clearly demarcated from inter-glitch fluctuations.

1.2. Waiting time and size distributions

The stress is not observable. Instead, what we observe are sequences of glitch sizes and waiting times.

The conditional waiting time distribution, $g(\Delta t \,|\, X_0)$, gives the probability density function (PDF) of waiting times Δt, when the inter-glitch evolution starts at X_0, according to (1.3). It is calculated as [25]

$$g(\Delta t \,|\, X_0) = -\frac{\mathrm{d}}{\mathrm{d}(\Delta t)} \left[\int_{-\infty}^{X_c} \mathrm{d}X \, p(X, \Delta t \,|\, X_0) \right] \ . \tag{1.6}$$

The integral inside the square brackets, often called the survivor function, equals the probability density that the process stays in the interval $-\infty < X(t) \leq X_c$ for $0 \leq t \leq \Delta t$.

The starting stress X_0 is a random variable, related to the size of the previous glitch. To find the observable waiting time distribution, $p(\Delta t)$, we marginalize over the starting stress by calculating,

$$p(\Delta t) = \int_0^{X_c} \mathrm{d}X_0 \, g(\Delta t \,|\, X_0) \, \eta(X_c - X_0) \ , \tag{1.7}$$

where $\eta(\Delta X)$ equals the probability density of releasing an amount of stress $\Delta X = X_c - X_0$ during a glitch.

[1] In the vortex unpinning picture, for example, a vortex avalanche cannot ever transfer so much angular momentum, that the crust rotates faster than the pinned superfluid; see Fulgenzi et al. [1] and the output of Gross-Pitaevskii simulations [10]

We henceforth express t in units of $2X_c^2/\sigma^2$ and X in units of X_c, unless otherwise stated. In these units, equations (1.6) and (1.26) combine to yield (see Appendix 1.A1)

$$g(\Delta t\,|\,X_0) = 2\mu \exp\left[\mu^2 \Delta t + \mu(1 - X_0)\right] \sum_{n=1}^{\infty} \exp(-\lambda_n^2 \Delta t) \frac{\lambda_n \sin[\lambda_n(1 - X_0)]}{\mu + \cos^2 \lambda_n} \ , \tag{1.8}$$

where λ_n is the n-th positive root of the transcendental equation

$$\mu \tan \lambda_n = -\lambda_n \ , \tag{1.9}$$

with

$$\mu = \xi X_c/\sigma^2 \ . \tag{1.10}$$

In this paper, we assume for simplicity that ΔX is proportional to the observed glitch size, $\Delta\nu$, i.e. the observed increment in the crust's spin frequency. Glitches represent small perturbations to an underlying equilibrium state, with $\Delta\nu/\nu \ll 1$, where ν is the spin frequency, so it is reasonable to model them in terms of a linear response, although nonlinear alternatives are certainly conceivable [28, 29]. In the vortex avalanche picture, for example, where $X(t)$ equals the crust-core angular velocity lag we have [1]

$$\Delta X = -\frac{2\pi(I_c + I_s)\Delta\nu}{I_s} \ , \tag{1.11}$$

where I_c and I_s are the moments of inertia of the crust and superfluid interior respectively. An analogous proportionality exists in the starquake picture [12, 30]. The size distributions observed from individual pulsars are approximated by power-law, Gaussian, lognormal, and exponential distributions [2–4]. Assuming $\Delta X \propto \Delta\nu$, we adjust $\eta(\Delta X)$ to match the measured size PDF $p(\Delta\nu)$ of the pulsar under consideration.

1.2. *Average waiting time*

The average waiting time, $\langle \Delta t \rangle$, is conditional on X_0. It can be calculated from $g(\Delta t\,|\,X_0)$ via

$$\langle \Delta t \rangle = \int_0^{\infty} \mathrm{d}(\Delta t)\, \Delta t\, g(\Delta t\,|\,X_0) \ . \tag{1.12}$$

With the boundary conditions (1.4) and (1.5), we obtain (see Appendix 1.A1)

$$\langle \Delta t \rangle = 2\mu \exp\left[\mu(1 - X_0)\right] \sum_{n=1}^{\infty} \left(\lambda_n^2 + \mu^2\right)^{-2} \frac{\lambda_n \sin[\lambda_n(1 - X_0)]}{\mu + \cos^2(\lambda_n)} \ . \tag{1.13}$$

The behavior of $\langle \Delta t \rangle$ as a function of μ is complicated, even after marginalizing over X_0. Numerical tests indicate that for $\mu \lesssim 1$, $\langle \Delta t \rangle$ is roughly constant with μ, while for $\mu \gtrsim 1$ it varies inversely with μ. The latter behavior can be understood with the help of the approximate non-reflecting solution at large μ (see Appendix 1.A2), which has $\langle \Delta t \rangle \propto \mu^{-1}$, via equation (1.29) and (1.12). The behavior at low values of μ makes sense physically, as σ dominates the time to reach X_c in this regime. On the other hand, at high values of μ and fixed σ, a high value of the drift coefficient ξ leads the process to quickly reach X_c while a low value of ξ takes comparatively longer.

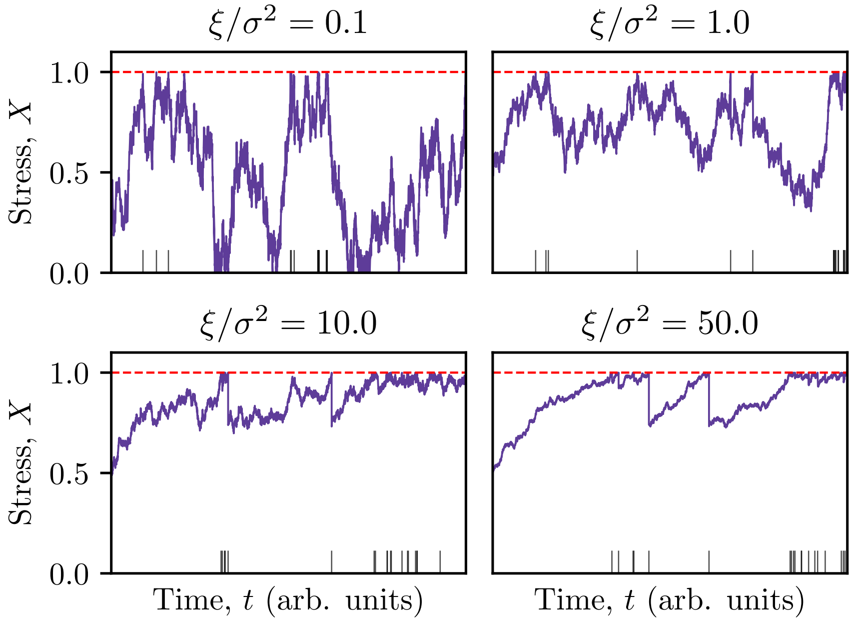

Figure 1.1: Visual comparison of the evolution of the internal, unobservable stress, $X(t)$, for four different values of ξ/σ^2. The red dashed line indicates the stress threshold, set to $X_c = 1$, where glitches are triggered. The same sequence of glitch sizes, drawn from a power-law $\eta(\Delta X)$ distribution, is used in each panel. The small black tick marks indicate the epoch of each glitch.

1.2. Comparison with the SDP meta-model

A key goal of this paper is to create a framework for falsifying one or both of the Brownian and SDP meta-models by making quantitative predictions about long-term glitch statistics. As the two meta-models encompass a range of plausible microphysics, falsifying one or both has significant scientific value in understanding which microphysical theories are consistent with the data.

The Brownian meta-model shares several similarities with the SDP meta-model [1, 17–19]. Both link the observed changes in $\nu(t)$ to a globally averaged, unobservable stress, which fluctuates around marginal stability. Both are examples of a self-organized critical system [see Aschwanden et al. [31] for a review], where an external driver pushes the system towards criticality, until a glitch releases internal stress and transfers angular momentum from the core to the crust [32]. Neither meta-model assumes a specific microphysical trigger mechanism; together the two meta-models embrace a wide variety of plausible mechanisms of stress accumulation and threshold triggering.

The meta-models also differ in important respects. The driver in the SDP meta-model is secular; it does not vary with time. In the Brownian meta-model the driving torque is a fluctuating Langevin torque with white noise statistics, as in (1.1). The SDP process never quite reaches $X = X_c$, as glitches become increasingly likely for $X \to X_c$. In contrast, the Brownian meta-model reaches $X = X_c$ at every glitch. This has important implications regarding the "memory" of previous events, as explored in Section 1.3.2. Finally, $\eta(\Delta X)$ plays a different role in the two meta-models. As mentioned in Section 1.2.2, one has $\Delta\nu \propto \Delta X$, so $\eta(\Delta X)$ and $p(\Delta\nu)$ have the same shape in the Brownian meta-model. In the SDP meta-model $\eta(\Delta X)$ is conditional on $X(t)$ just before the glitch, so $\eta(\Delta X)$ and $p(\Delta\nu)$ have the same shape only under certain conditions; see Carlin and Melatos [18] for details.

The similarities and differences between the two meta-models are illustrated in Figure 1.2. Time series $X(t)$ and $\nu(t)$ are constructed by repeatedly evolving the stress in the system until a glitch is triggered (probabilistically at $X < X_c$ for the SDP meta-model, deterministically at $X = X_c$ for the Brownian meta-model), then drawing a glitch size from the stress-release PDF $\eta(\Delta X)$. Visually, with 20 glitches, the crust angular velocity evolves similarly for the two meta-models, despite the different stress evolution between glitches (deterministic for the SDP meta-model and stochastic for the Brownian meta-model). However, as we find in Section 1.3, the long-term statistical behavior of the two meta-models is different.

1.2. Inter-glitch spin wandering

Besides its influence on glitch statistics, the Brownian process may also drive stochastic spin wandering between glitches, unlike the SDP process. In principle, therefore, observations of inter-glitch timing noise in radio pulsars [5–7, 33] should place constraints on the meta-model parameters ξ and σ^2 independent of the constraints derived from glitches. As an illustrative special case, if ξ and X_c are held fixed, $\langle \Delta t \rangle$ decreases and the inter-glitch timing noise amplitude increases simultaneously, as σ^2 increases. Hence a measured upper limit on the timing noise amplitude implies a maximum value of σ^2 and hence a minimum value of $\langle \Delta t \rangle$, which provides an additional, independent opportunity to falsify the Brownian meta-model.

In practice, falsification experiments of the above kind are complicated by the unknown coupling between various components of the stellar interior. The meta-model parameters ξ and σ^2 control the statistical behavior of the internal, i.e. unobservable, stress, $X(t)$. In Sections 1.2.1 and 1.2.2 we assume that changes in $X(t)$ couple linearly to the rotational frequency of the crust, $\nu(t)$, only when a glitch occurs, via (1.11). If we relax this restriction and couple $X(t)$ linearly to the crust between glitches, we have

$$\frac{\mathrm{d}\nu}{\mathrm{d}t} = -A\frac{\mathrm{d}X}{\mathrm{d}t} \ , \tag{1.14}$$

where A is an unknown coupling constant (units: Hz per unit stress) which depends on the physical mechanism of stress accumulation and the microphysics controlling how the star's internal angular momentum reservoir is tapped in between glitches. Equation (1.14) implies that, if the crust undergoes the same type of Brownian process with drift as described by (1.1), the observable, long-term, average spin-down rate, $\langle\dot{\nu}\rangle$, is proportional to ξ, while the observed spin-wandering amplitude is proportional to σ^2.

In the special case of $A = A_{\mathrm{max}}$ (its maximum allowed value) the coupling is the same as during a glitch, e.g. $A = I_{\mathrm{s}}/[2\pi(I_{\mathrm{c}}+I_{\mathrm{s}})]$ in the vortex avalanche picture. This is a problem for the Brownian meta-model, as we see from Figure 1.1. To distinguish glitches from stochastic wandering we need $\mu \gtrsim 50$, otherwise large Brownian fluctuations can be mistaken for glitches. For $\mu \gtrsim 50$, there should be a strong cross-correlation between glitch sizes and waiting times until the next glitch, as discussed in Section 1.3.2. We do not see this cross-correlation in most pulsars, so we can rule out the special case of $A = A_{\mathrm{max}}$ or the Brownian meta-model (or both).

On the other hand, for $A < A_{\mathrm{max}}$, where the inter-glitch coupling is weaker than during a glitch, the problem outlined above is alleviated. Another scenario is that A is not constant, i.e. it varies with time or the stress in the system. These scenarios are motivated by the observations of the "precursor" slowdown in the Vela pulsar immediately prior to the 2016 glitch [21], and by studies of non-linear coupling mechanisms [29, 34]. A detailed study of the microphysical implications of inter-glitch spin wandering for the coupling mechanism between the stress reservoir and the crust is left for future work. For simplicity, we assume henceforth that coupling only occurs at a glitch, via (1.11).

1.3. Observable long-term statistics

To prepare for comparing the Brownian meta-model to data, we study how changing the input parameters affects the long-term statistical predictions.

1.3. Waiting time distribution

The long-term waiting time PDF, $p(\Delta t)$, constructed after many glitches are observed, is calculated from (1.7) given μ and $\eta(\Delta X)$. Figure 1.3 shows $p(\Delta t)$ for four representative values of μ when $\eta(\Delta X)$ is a power law of the form

$$\eta(\Delta X) \propto \Delta X^{-\delta} H(1-\Delta X) H(\Delta X - \beta) \ , \tag{1.15}$$

where the proportionality constant is fixed by $1 = \int_0^1 \mathrm{d}(\Delta X)\, \eta(\Delta X)$, δ is the power-law index, β is the lower cut-off to ensure normalisability, and H is the Heaviside function

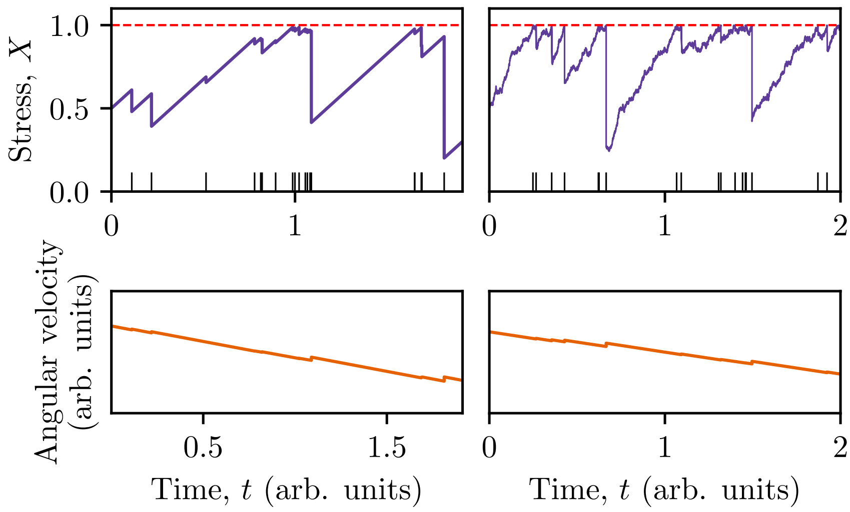

Figure 1.2: Comparison between two representative time series of stress (top panels) and crust angular velocity (bottom panels) from the SDP meta-model (left) and the Brownian meta-model (right). A deterministic, secular torque drives the stress between glitches in the SDP meta-model, whereas a stochastic Langevin torque drives the stress between glitches in the Brownian meta-model. Black tick marks in the top panels indicate the glitch epochs. Parameters for SDP meta-model: $\alpha = 1$, power law conditional jump distribution, as described in equations (17) and (19) of Fulgenzi et al. [1] respectively. Parameters for Brownian meta-model: $\mu = 50$, power law stress-release distribution, as in (1.15). Parameters shared between meta-models: $\delta = -1.5$, $\beta = 10^{-2}$ in (1.15).

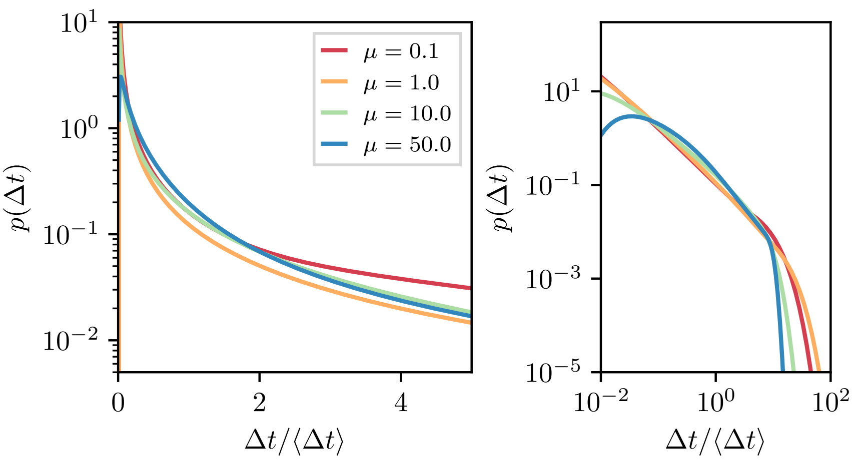

Figure 1.3: Waiting time PDF, $p(\Delta t)$, for four values of μ on log-linear (left panel) and log-log (right panel) scales. The stress release distribution, $\eta(\Delta X)$, is a power law, as in (1.15), with $\delta = -1.5$ and $\beta = 10^{-2}$.

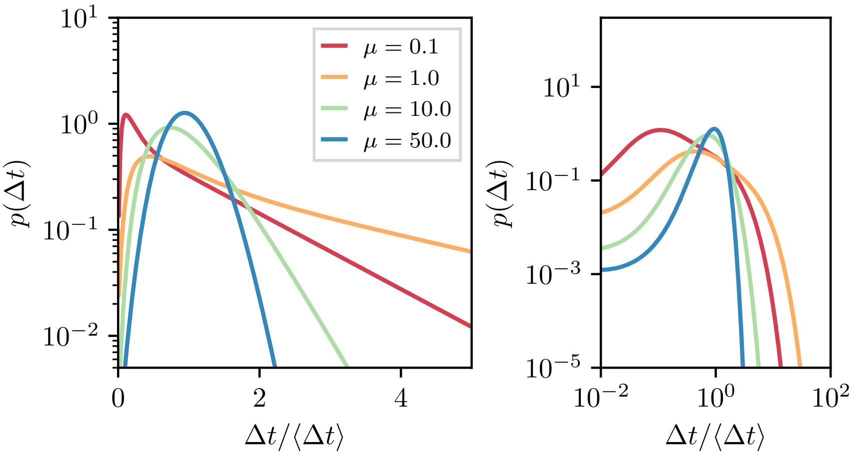

Figure 1.4: As for Figure 1.3 but with a Gaussian $\eta(\Delta X)$, as in (1.16), with $\mu_G = 0.5$ and $\sigma_G = 0.125$.

($\beta \leq \Delta X \leq 1$ implies $0 \leq X \leq 1$ at all times). The abscissae are normalized by $\langle \Delta t \rangle$ to highlight how the shape of $p(\Delta t)$ evolves with μ. On the log-log axes (right panel) $p(\Delta t)$ resembles a power law over at least 3 decades, with a cut-off at $\Delta t \approx 10\langle \Delta t \rangle$. The cut-off steepens as μ grows. The shape of $p(\Delta t)$ depends weakly on δ and β for $\mu \lesssim 10$, but depends strongly for $\mu \gtrsim 10$. For example, for $\mu \gtrsim 10$ and $\beta = 10^{-1}$, $p(\Delta t)$ becomes unimodal, as small waiting times become less likely when each glitch reduces the stress by $\Delta X \geq \beta$.

What about other functional forms of $\eta(\Delta X)$? Figure 1.4 shows $p(\Delta t)$ for four representative values of μ, with a Gaussian $\eta(\Delta X)$, viz.

$$\eta(\Delta X) \propto \exp\left[\frac{-(\Delta X - \mu_G)^2}{2\sigma_G^2}\right] H(1 - \Delta X) H(\Delta X) \ , \tag{1.16}$$

where the proportionality constant is fixed to normalize $\eta(\Delta X)$, μ_G is the mean, and σ_G is the standard deviation. For $\mu \lesssim 1$, $p(\Delta t)$ resembles an exponential distribution, if the smallest waiting times with $\Delta t \lesssim 0.25\langle \Delta t \rangle$ are ignored. For $\mu \gtrsim 1$, $p(\Delta t)$ is unimodal. Increasing the size of the average ΔX, via increasing μ_G, reduces the variance in $p(\Delta t)$ for all μ, whereas reducing μ_G makes $p(\Delta t)$ resemble the results for a power law $\eta(\Delta X)$. Reducing the variance of each stress-release event by reducing σ_G also reduces the variance of $p(\Delta t)$, as expected.

The third functional form of $\eta(\Delta X)$ that we test is a log-normal distribution,

$$\eta(\Delta X) \propto \frac{1}{\Delta X} \exp\left[\frac{-(\log \Delta X - \mu_{LN})^2}{2\sigma_{LN}^2}\right] H(1 - \Delta X) H(\Delta X) \ , \tag{1.17}$$

where μ_{LN} and σ_{LN} are the mean and standard deviation, and the proportionality constant is set by normalization. Figure 1.5 shows that the general shape of $p(\Delta t)$ with a log-normal $\eta(\Delta X)$ is similar to what is seen with a Gaussian $\eta(\Delta X)$. There are fewer small waiting times for a given μ. If the average stress release is increased, by increasing μ_{LN}, the same response is seen as with a Gaussian $\eta(\Delta X)$, i.e. the variance of $p(\Delta t)$ drops. If we increase σ_{LN}, $p(\Delta t)$ resembles what is seen with a uniform $\eta(\Delta X)$.

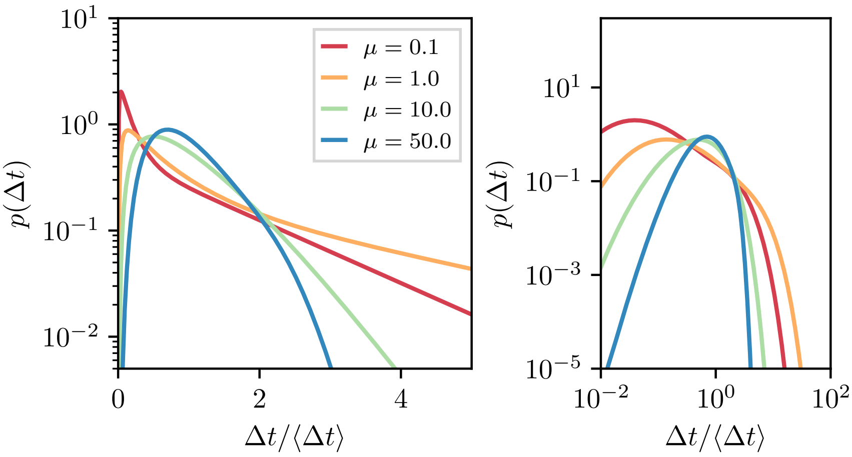

Figure 1.5: As for Figure 1.3 but with a log-normal $\eta(\Delta X)$, as in (1.17), with $\mu_{\mathrm{LN}} = -1$ and $\sigma_{\mathrm{LN}} = 0.5$.

An analogous study of $p(\Delta t)$ for the SDP meta-model, with $\eta(\Delta X)$ taken to be a power law, Gaussian, and a variety of other functional forms, is presented by Carlin and Melatos [18].

1.3. Correlations and memory

The meta-model in Section 1.2.1 predicts whether we should see a correlation between the size of a glitch and the subsequent waiting time, which we call a forward cross-correlation. As the glitch size is independent of the history of the stress evolution, there is no backward cross-correlation between the size of a glitch and the previous waiting time in the Brownian meta-model. Forward and backward cross-correlations have been investigated previously in the context of the SDP meta-model, and numerous falsifiable predictions are made [17–19].

Figure 1.6 shows the Spearman correlation coefficient for the forward cross-correlation, ρ_+, for $5 \times 10^{-2} \leq \mu \leq 5 \times 10^{3}$. The cross-correlation is always positive and increases from $\rho_+ \approx 0.25$ for $\mu \lesssim 1$ to $\rho_+ \approx 1$ for $\mu \gg 1$. Figure 1.6 is generated with $\eta(\Delta X)$ as a power law, but the result is insensitive to the form of $\eta(\Delta X)$. The trend in Figure 1.6 is intuitive. The size of the stress release in a glitch dictates how much stress must be accumulated before the next glitch occurs. For μ high, the diffusion of the Brownian process is negligible compared to the secular drift, and so the waiting time is determined almost completely by the size of the previous glitch. For μ low, the diffusion randomizes the waiting time and decouples it from the size, while still maintaining a slight forward cross-correlation; even a process with zero drift is more likely to reach the threshold faster, if X_0 is closer to X_c.

The Brownian meta-model predicts zero autocorrelations between glitch sizes, or between waiting times. The threshold at $X = 1$ is reached before every glitch in the Brownian meta-model, removing "memory" in the system of the behavior of the stress prior to reaching that threshold. In contrast, the SDP meta-model predicts sizable autocorrelations in certain regimes [19].

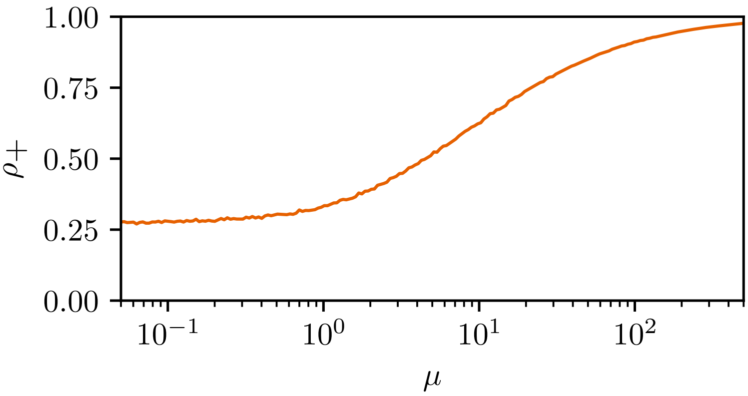

Figure 1.6: Spearman cross-correlation between the size of a glitch and the waiting time until the next glitch versus μ. At 200 logarithmically spaced values of μ, 10^5 waiting times and sizes are drawn from (1.8) and (1.15) respectively, using each generated size to determine the starting point for the next inter-glitch interval and hence waiting time.

1.4. Falsifying the Brownian meta-model

There are six pulsars with more than 15 recorded glitches[2]. Their names, the number of recorded glitches, the forward Spearman cross-correlation coefficient (along with associated p-value and 95% confidence interval), as well as the best-fitting size and waiting time distributions are listed in Table 1.1. The Spearman correlation coefficient minimizes the impact of outliers by testing for monotonic correlations, as opposed to the strictly linear correlations which the standard Pearson correlation coefficient describes. The confidence interval is calculated as described in Section 4 of Carlin and Melatos [19]. The best-fitting PDFs are copied from Fuentes et al. [4] and are selected based on the Akaike Information Criterion [36]. These shapes are broadly consistent with previous analyses using different techniques, although there are minor individual differences [2, 3]. We note that PDF shape fitting is uncertain when the sample size is small. Often the best one can do in the glitch context is to distinguish between a monotonic (e.g. exponential, power law) and unimodal (e.g. Gaussian) PDF, without tying down the functional form. Even then some functional forms (e.g. Weibull) straddle both categories [37]. Further shape-fitting studies should be carried out in the future, as the data sets grow.

Although not listed in Table 1.1, we note that the backward cross-correlation, the autocorrelation between glitch sizes, and the autocorrelation between waiting times are all consistent with zero, at a 95% confidence level for all six objects [4, 17, 19].

One virtue of the Brownian meta-model, like the SDP meta-model studied elsewhere [1, 17–19], is that it makes specific, quantitative predictions about PDFs and correlations. These predictions are open to falsification using existing and future data. With an eye to falsifying the meta-model presented in Sections 1.2 and 1.3 we now ask whether existing long-term observations of the pulsars in Table 1.1 can be adequately explained. In doing

[2]Up-to-date online catalogues of pulsar glitches are available through the Jodrell Bank Centre of Astrophysics at `http://www.jb.man.ac.uk/pulsar/glitches.html` [8], and the Australian National Telescope Facility at `https://www.atnf.csiro.au/research/pulsar/psrcat` [35]

Table 1.1: Pulsar name, number of glitches (N), Spearman correlation coefficient between glitch size and subsequent waiting time (ρ_+), associated p-value, and the 95% confidence interval (CI). The last two columns indicate the functional form of the best-fitting distribution for glitch sizes, $p(\Delta X)$, and waiting times, $p(\Delta t)$ [2–4].

Name (PSR J)	N	ρ_+	p-value	95% CI	$p(\Delta X)$	$p(\Delta t)$
0537−6910	42*	0.93	10^{-18}	(0.84, 0.97)	Gaussian	Gaussian
1740−3015	36	0.29	0.091	(−0.06, 0.58)	Power law	Exponential
0534+2200	25†	−0.060	0.78	(−0.45, 0.35)	Log-normal	Exponential
1341−6220	23	0.58	0.0048	(0.13, 0.83)	Log-normal	Exponential
0835−4510	21	0.30	0.20	(−0.19, 0.67)	Gaussian	Gaussian
0631+1036	17	0.21	0.44	(−0.33, 0.65)	Power law	Exponential

*The number and parameters of glitches in PSR J0537−6910 vary between Middleditch et al. [12], Antonopoulou et al. [37], and Ferdman et al. [38]. We include in our analysis glitches that appear in two out of three sources.
†The first four PSR J0534+2200 glitches in the Jodrell Bank catalogue occurred before daily monitoring commenced and are excluded from the analysis [39].

so, we caution that there is debate about whether the existing glitch catalogues are complete and accurate. Espinoza et al. [40] claimed that all glitches in the Crab pulsar (PSR J0534+2200) are detected. Yu and Liu [41] used a Monte Carlo study to confirm that the Yu et al. [42] analysis of 165 pulsars observed between 1990 and 2011 using the Parkes Observatory has "detected all detectable glitches in the data" (verbatim quote). However, as the cadence of observations for most pulsars is not constant [43], post-glitch recovery time-scales vary [44, 45], and glitch detections still rely on human intervention [41], it remains uncertain whether or not we are seeing the smallest glitches, or resolving glitches that happen in quick succession.

1.4. PSR J0537−6910

PSR J0537−6910 has the most recorded glitches and the highest forward cross-correlation amongst all the prolific glitching pulsars. In the context of the Brownian meta-model, these properties place PSR J0537−6910 in the $\mu \gtrsim 10^2$ regime, via Figure 1.6. The glitch size distribution for PSR J0537−6910 is approximately Gaussian [4]. Looking at Figure 1.4, where $\eta(\Delta X)$ is a Gaussian, we note that $p(\Delta t)$ should also be a Gaussian, with $\mu \gtrsim 10^2$, in accord with observations. Therefore, the main features of the long-term statistics of this pulsar conform to the Brownian meta-model, if $\eta(\Delta X)$ is a Gaussian, and one has $\mu \gtrsim 10^2$.

We note that the waiting time distribution for PSR J0537−6910 is also well described by a Weibull distribution [37], a more general functional form, which includes the exponential and a skewed Gaussian as special cases.

1.4. PSR J1740−3015

PSR J1740−3015 has a forward cross-correlation that is consistent with zero. However the 95% confidence interval is broad enough to encompass ρ_+ up to 0.58. According to Figure 1.6 this means PSR J1740−3015 has $\mu \lesssim 10$, in the context of the Brownian meta-model. As PSR J1740−3015 has a power-law size PDF [4], we look to Figure 1.3, where $\eta(\Delta X)$ is a power law. For $\mu \lesssim 10$ the Brownian meta-model predicts that $p(\Delta t)$ is a power law with a cut-off at large Δt. Therefore, as $p(\Delta t)$ is observed to be exponential in this object, the long-term statistics are not explained by the Brownian meta-model with any set of input parameters.

Power-law and log-normal distributions are often hard to distinguish for such small sample sizes. If $\eta(\Delta X)$ is actually a log-normal distribution for this object, then we look at Figure 1.5. With $\mu \lesssim 10$ we note that $p(\Delta t)$ should be an exponential, if the smallest waiting times are not observed. Therefore, as $p(\Delta t)$ is observed to be exponential in this object, it is consistent with the Brownian meta-model, if we are unable to observe glitches with $\Delta t \lesssim 0.25\langle \Delta t \rangle$. Note that $\langle \Delta t \rangle$ refers to the true underlying average waiting time, rather than the estimate from the sample of glitches we have observed.

1.4. PSR J0534+2200

PSR J0534+2200 has a forward cross-correlation that is consistent with zero, with $\rho_+ \le 0.35$ at 95% confidence. This limits PSR J0534+2200 to $\mu \lesssim 2$, according to Figure 1.6. PSR J0534+2200 has a log-normal size distribution [4]. Taking $\eta(\Delta X)$ to be log-normal, as in Figure 1.5, we see that $p(\Delta t)$ should be an exponential, if the smallest waiting times are not observed. Therefore, as $p(\Delta t)$ is observed to be exponential in this object, it is consistent with the Brownian meta-model, if we are unable to observe glitches with $\Delta t \lesssim 0.25\langle \Delta t \rangle$. If we do see all glitches in PSR J0534+2200, as claimed by Espinoza et al. [40], then the observations are inconsistent with the Brownian meta-model.

We note that the semi-autonomous glitch-finding algorithm of Espinoza et al. [40] may miss closely spaced glitches occasionally. For example, it missed one glitch, at epoch MJD 52146.8 with a size of $\Delta\nu = 0.27\,\mu$Hz, which occurred $\Delta t \approx 63\,$d after the previous glitch with Espinoza et al. [40] noting that the likely cause is "influence of the recovery from the previous glitch" (verbatim quote). If we take 63 d as the minimum resolvable waiting time, the true underlying average waiting time is $\langle \Delta t \rangle \approx 63\,\mathrm{d}/0.25 = 252\,$d, in order for the long-term statistics to be consistent with the Brownian meta-model. The observed average waiting time is 501 d, while the median waiting time is 284 d. On the other hand, the Brownian meta-model may be ruled out, and the minimum resolvable waiting time may be shorter than 63 d. More work is needed to clarify these issues, including systematic studies of the false alarm and false dismissal probabilities of glitch-finding algorithms [33, 41, 43, 46].

1.4. PSR J1341−6220

PSR J1341−6220 has a forward cross-correlation that is significantly positive. However the 95% confidence interval is broad, allowing $0.13 \le \rho_+ \le 0.83$. According to Figure 1.6 this limits μ to $\mu \lesssim 10^2$. PSR J1341−6220 has a log-normal size distribution [4], and so like PSR J0534+2200 is consistent with Brownian the meta-model, only if we do not detect glitches with $\Delta t \lesssim 0.25\langle\Delta t\rangle$. The observed waiting time distribution is an exponential.

1.4. *PSR J0835−4510*

PSR J0835−4510 has a forward cross-correlation that is consistent with zero. The 95% confidence interval encompasses ρ_+ up to 0.67, consistent with $\mu \lesssim 30$, according to Figure 1.6. The size PDF, and hence $\eta(\Delta X)$, for PSR J0835−4510 is approximately Gaussian [4]. Therefore according to Figure 1.4 the meta-model predicts $p(\Delta t)$ to be an exponential (for $\mu \lesssim 5$) or a skewed Gaussian (for $5 \lesssim \mu \lesssim 30$). The observed $p(\Delta t)$ is a Gaussian, not an exponential. Therefore, the observations are currently consistent with the Brownian meta-model for $5 \lesssim \mu \lesssim 30$, if $\eta(\Delta X)$ is a Gaussian.

The somewhat strict constraints on μ imply that, with more glitches, the measured forward cross-correlation should increase to $0.4 \lesssim \rho_+ \lesssim 0.6$. If ρ_+ stays outside this range, PSR J0835−4510 will become another counterexample to the Brownian meta-model.

1.4. *PSR J0631+1036*

PSR J0631+1036 has roughly half the recorded glitches of PSR J1740−3015 but is otherwise similar statistically. Hence the same conclusion holds: as long as the size distribution is a power law [4], the Brownian meta-model does not adequately explain the observations, as exponential waiting times cannot be generated if $\eta(\Delta X)$ is a power law.

As with PSR J1740−3015, if $\eta(\Delta X)$ is actually a log-normal distribution, instead of a power law, the conclusion is different: the observations are consistent with the predictions of the Brownian meta-model, if we do not resolve glitches with $\Delta t \lesssim 0.25\langle\Delta t\rangle$.

1.5. Population trends

The primary goal of this paper is to formulate rigorously and then falsify (if possible) the Brownian meta-model, rather than engage in a parameter estimation exercise. Nevertheless the results in Section 1.4 do carry some interesting preliminary implications concerning the parameters of the Brownian meta-model, in the event that it survives falsification in the future. In this section, we touch briefly on two population trends that are consistent with (albeit not guaranteed by) the results in Section 1.4: why do $\eta(\Delta X)$ and μ seem to vary significantly among the six pulsars in Table 1.1?

Regarding $\eta(\Delta X)$, laboratory studies of self-organized critical systems with avalanche dynamics, like sand piles, reveal that $\eta(\Delta X)$ is power-law-like when the driver is "slow", and Gaussian-like when the driver is "fast" [32]. In the former regime, avalanches occur sporadically at well-separated points within the system, so consecutive avalanches are independent and scale invariant: they can have any size, ranging from a solitary nearest-neighbor interaction to a catastrophic collapse of the whole system. In the latter regime, consecutive avalanches "trip over one another" (i.e. are correlated, not independent) and involve most of the system every time, so they all have comparable sizes, and $\eta(\Delta X)$ is unimodal. Broadly speaking the foregoing physics may suggest a correlation between the shape of $\eta(\Delta X)$ and $\langle\dot{\nu}\rangle$, and it will be interesting to test for such a correlation in the future, as more data are gathered. However, one must approach such a test with caution. The demarcation between "slow" and "fast" drivers is a subtle and unsolved question in idealized systems like sand piles, let alone in neutron stars where the microphysics is complicated and unknown (e.g. vortex avalanches, starquakes). Moreover observables like $\langle \dot{\nu} \rangle$ cannot be related easily to the behavior of the stress reservoir, e.g. due to uncertain coupling between multiple components of the star's interior, as discussed in Section 1.2.5.

To understand how $\mu = \xi X_c/\sigma^2$ could vary pulsar-to-pulsar we need to unpack the various internal parameters, and relate them to potential observables. In the standard picture, $\langle \dot{\nu} \rangle$ is set by the spin-down torque, $N_{\rm ext}$, and moment of inertia of the crust, I_c. As discussed in Section 1.2.5, one can invoke a linear coupling between the internal stress and observed behavior of the crust. Linear coupling faces many issues, as we discuss in Section 1.2.5, but taking it to be valid for the moment, we find $\xi \propto \langle \dot{\nu} \rangle \approx N_{\rm ext}/I_c$, where the proportionality constant controls the strength of the coupling. For the six objects discussed in this paper, $N_{\rm ext} \propto B^2 \nu^3$ (where B is the strength of the dipole magnetic field at the surface) varies across three orders of magnitude, using values of B and ν from the ATNF pulsar catalogue[3]. The other factor is I_c. There are two popular scenarios for this quantity, as discussed in Section 3 of Melatos et al. [47]: (a) if the crust is a thin crystalline lattice and the rest of the star is composed of a superfluid we have $I_c/I_0 \sim 10^{-2}$, where I_0 is the total moment of inertia of the star [48, 49]; (b) if the crust has most of the interior superfluid pinned and co-rotating with it (via magnetic flux tubes or charged particles), with only a bit of the inner crust superfluid decoupled, we have $I_c/I_0 \sim 1$ [8, 50, 51]. We do not explore which of these scenarios is more likely, as both have strong support in the literature. We do note that the difference between these scenarios widens the possible range of ξ by another two orders of magnitude. The other factors in μ are σ and X_c. Again, as discussed in Section 1.2.5, σ is proportional to the observed spin-wandering amplitude, if we assume a linear coupling. The spin-wandering amplitude in the six objects considered in this paper is not well quantified in the literature. However, Shannon and Cordes [52] found that for a general population of "canonical pulsars", the timing noise strength, $\sigma_{\rm TN}$, spans three orders of magnitude. Finally, the critical stress X_c may vary from object to object, as it is a complex combination of microphysical (e.g. pinning potential) and thermodynamic (e.g. equation of state) parameters [53]. Hence, even for linear coupling (which is already ruled out by looking at inter-glitch spin wandering, as discussed in Section 1.2.5), the possible range of μ inferred from external observables spans more than eight orders of magnitude, comfortably encompassing the range of μ which the meta-model considers.

1.6. Conclusions

The physical mechanism that triggers pulsar glitches is unknown. Phenomenological meta-models offer one way to link — and potentially falsify — broad classes of plausible microphysical mechanisms with measurements of long-term glitch statistics. The SDP meta-model [1] describes microphysical mechanisms in which glitches are triggered probabilistically, while the stress in the system rises secularly, becoming more likely as

[3] https://www.atnf.csiro.au/research/pulsar/psrcat/ [35]

the stress increases. It makes falsifiable, quantitative predictions for size and waiting-time cross-correlations [17], autocorrelations [19], and PDFs [18]. However, the SDP meta-model does not allow the stress to fluctuate stochastically in between glitches due to random processes in the stellar interior, e.g. superfluid vortex motion [10], superfluid turbulence [23, 54], or crust cracking [55].

Motivated partly by recent observations of PSR J0835−4510 [21], we introduce an alternative meta-model, where the stress evolves between glitches according to a Brownian process with drift and diffusion components, and where glitches are triggered deterministically once the stress surmounts a threshold. The rotational slowdown observed by Ashton et al. [21] just prior to the glitch may be a coincidently large instance of pulse jitter, but it may also indicate a large, stochastic fluctuation in the internal stress, which briefly couples the magnetosphere to the interior and triggers the glitch. While we do not model the microphysics in detail, the Brownian meta-model encompasses such a trigger mechanism. We show in Section 1.4 and Carlin and Melatos [19] that the glitch statistics of PSR J0835−4510 are consistent with the predictions of both the Brownian and SDP meta-models.

We find that the Brownian meta-model predicts various long-term statistical fingerprints. If the glitch size distribution is not a power law, and diffusion dominates drift (i.e. $\mu \lesssim 1$), the waiting time PDF is predicted to be an exponential, if glitches that occur soon after one another are not resolved. As μ increases, the observed waiting time PDF resembles more closely the glitch size PDF. The Spearman cross-correlation coefficient between glitch size and waiting time until the next glitch is predicted to be at least 0.25 for all pulsars.

Current observations of the long-term glitch statistics in all six of the pulsars with the most recorded glitches cannot be explained adequately by the Brownian meta-model. The two "quasi-periodic" glitchers (PSR J0537−6910 and PSR J0835−4510) with Gaussian size and waiting time distributions [3, 4] can be explained with the Brownian meta-model, while PSR J1740−3015 and PSR J0631+1036 cannot (regardless of input parameters), unless their glitch sizes are distributed as a log-normal instead of a power law [4]. PSR J0534+2200 and PSR J1341−6220 are consistent with the meta-model, if there are many glitches with small waiting times that we do not resolve. More data could falsify the Brownian meta-model as it applies to individual pulsars in several ways: i) if the measured forward cross-correlation is statistically inconsistent with $\rho_+ \geq 0.25$; ii) if a non-zero backward cross-correlation is measured; or iii) if the size or waiting time autocorrelations are nonzero. Additionally, measurements of the forward cross-correlation, combined with the size and waiting time PDFs, further constrain the meta-model parameters.

We note that i) the SDP meta-model is broadly consistent with the long-term statistics in the six pulsars with the most recorded glitches [18, 19], and ii) it predicts a different set of long-term statistics. Thus, over time we can distinguish between the two meta-models and falsify one, the other, or both. We remind the reader that most plausible microphysical mechanisms contemplated in the literature (e.g. superfluid vortex avalanches, starquakes, hydrodynamic instabilities and turbulence) fit broadly within one or both of the Brownian and SDP meta-models.

Acknowledgements

Parts of this research are supported by the Australian Research Council (ARC) Centre of Excellence for Gravitational Wave Discovery (OzGrav) (project number CE170100004) and ARC Discovery Project DP170103625. JBC is supported by an Australian Postgraduate Award. We thank the anonymous referee for pointing out that inter-glitch spin wandering places independent constraints on the Brownian meta-model in principle, as discussed in Section 1.2.5.

1.A1. Analytic solution of the Fokker-Planck equation for the inter-glitch stress distribution

The Fokker-Planck equation for the globally averaged stress variable, X, together with the initial and boundary conditions, (1.3)–(1.5), constitute a standard diffusion problem. Namely, equation (1.2) is a parabolic partial differential equation with constant coefficients solved on the finite interval $0 \le X \le X_c$, subject to mixed Dirichlet-Neumann (also called Robin) boundary conditions. The problem can be solved analytically by expanding the solution in eigenfunctions on the interval $0 \le X \le X_c$ [27].

We assume a separable ansatz

$$p(X,t) = Y(X)T(t) \ , \tag{1.18}$$

which converts (1.2) into two coupled ordinary differential equations,

$$\frac{2}{\sigma^2 T}\frac{\mathrm{d}T}{\mathrm{d}t} = -\alpha^2 \ , \tag{1.19}$$

$$\frac{1}{Y}\left(\frac{-2\xi}{\sigma^2}\frac{\mathrm{d}Y}{\mathrm{d}X} + \frac{\mathrm{d}^2Y}{\mathrm{d}X^2}\right) = -\alpha^2 \ , \tag{1.20}$$

for some constant α. Equation (1.20) has exponential solutions of the form

$$Y(X) \propto \exp\left[\left(\frac{\xi}{\sigma^2} \pm \sqrt{-\lambda^2}\right)X\right] \ , \tag{1.21}$$

with $\lambda^2 = \alpha^2 - \xi^2/\sigma^4$.

As (1.2) is linear, we apply the boundary conditions to the eigenfunctions defined in (1.21) independently, then sum over the eigenvalues using the principle of superposition. For $\lambda^2 \le 0$, $Y(X)$ becomes a linear combination of $\sinh(\lambda X)$ and $\cosh(\lambda X)$. The boundary conditions imply $\tanh(\lambda X) \propto -\lambda$, whose only solution $\lambda = 0$ leads to the trivial result $Y(X) = 0$. We therefore restrict our attention to $\lambda^2 > 0$ and hence

$$Y(X) = \exp\left(\frac{\xi}{\sigma^2}X\right)(A\sin\lambda X + B\cos\lambda X) \ , \tag{1.22}$$

where A and B are constants. The reflecting boundary condition (1.5) implies

$$B = \frac{\lambda\sigma^2}{\xi}A \ , \tag{1.23}$$

while the absorbing boundary condition (1.4) fixes the eigenvalues, λ, via

$$\tan(\lambda X_c) = -\frac{\lambda\sigma^2}{\xi} \ . \tag{1.24}$$

Hence we write the full solution for $P(X,t)$ as

$$P(X,t) = \exp\left(\frac{\xi}{\sigma^2}X\right)\sum_{n=1}^{\infty} A_n \exp\left[-t\left(\frac{\lambda_n^2\sigma^2}{2} + \frac{\xi^2}{2\sigma^2}\right)\right]\left[\sin(\lambda_n X) + \frac{\lambda_n\sigma^2}{\xi}\cos(\lambda_n X)\right] \tag{1.25}$$

or equivalently

$$P(X,t) = \exp\left(\frac{\xi}{\sigma^2}X\right)\sum_{n=1}^{\infty} A'_n \exp\left[-t\left(\frac{\lambda_n^2\sigma^2}{2} + \frac{\xi^2}{2\sigma^2}\right)\right]\sin[\lambda_n(X - X_c)] \ , \tag{1.26}$$

where λ_n is the n-th positive root of (1.24), and the A'_n constant coefficients are to be determined.

We find the A'_n factors by applying the initial condition (1.3) and noting that the eigenfunctions are orthogonal on $0 \leq X \leq X_c$ (not the standard Fourier domain $0 \leq X \leq 2\pi$) as a consequence of Sturm-Liouville theory [56]. Orthogonality implies

$$A'_n = \frac{\int_0^{X_c} \mathrm{d}X \, \exp\left(-\xi X/\sigma^2\right)\sin[\lambda_n(X - X_c)]\, p(X, t=0)}{\int_0^{X_c} \mathrm{d}X \, \sin^2[\lambda_n(X - X_c)]} \tag{1.27}$$

$$= 2\exp\left(-\xi X_0/\sigma^2\right)\sin[\lambda_n(X_0 - X_c)]\,\frac{\xi/\sigma^2}{\xi X_c/\sigma^2 + \cos^2(\lambda_n X_c)} \ . \tag{1.28}$$

The full solution is given by (1.24), (1.26), and (1.28).

1.A2. Conditional waiting time PDF without the reflecting boundary

If the reflecting boundary condition (1.5) is relaxed, such that the process operates on the semi-infinite domain $X < X_c$, the conditional waiting time distribution is an inverse Gaussian [25],

$$g(\Delta t\,|\,X_0) = \frac{X_c - X_0}{\sigma\sqrt{2\pi\Delta t^3}}\exp\left[\frac{-(X_c - X_0 - \xi\Delta t)^2}{2\sigma^2\Delta t}\right] \ . \tag{1.29}$$

For $\xi/\sigma^2 \gtrsim 10$, numerical tests show that (1.29) agrees with (1.8) to within 1% for $0 \leq \Delta t \leq 5\langle\Delta t\rangle$. This makes intuitive sense, as the process is driven strongly away from $X = 0$ for large $\xi/\sigma^2 > 0$. We use (1.29) instead of (1.8) for $\xi/\sigma^2 \gtrsim 10$, because (1.8) converges slowly in the latter regime.

CHAPTER 2

Long-term statistics of pulsar glitches due to history-dependent avalanches

2.1. Introduction

More than 500 rotational glitches have been detected in radio pulsars[1]. The sample is large enough that it is meaningful to disaggregate the data and study the long-term statistics of glitch activity in some individual objects with enough recorded glitches. Quantities of interest include waiting time and size cross-correlations, autocorrelations, and probability density functions (PDFs) [2–4, 8, 17–19].

Given measurements of the above quantities, one can falsify popular phenomenological meta-models describing glitch activity as a stress-relax process, wherein stress accumulates between glitches and relaxes partially at a glitch. A meta-model unifies a broad class of stochastic processes under its umbrella while remaining agnostic about the specific microphysics and the physical nature of the stress. It makes concrete, falsifiable predictions about long-term glitch statistics. The pay-offs from falsifiability are considerable and have driven work in this area recently. For example, existing data have been used to discriminate between the state-dependent Poisson (SDP) and Brownian stress accumulation (BSA) meta-models in six objects with high glitch activity [57]. In the SDP meta-model, glitches are triggered stochastically via a Poisson process with a stress-dependent rate, while the stress increases deterministically between glitches [1, 58]. In the BSA meta-model, glitches are triggered deterministically when the stress reaches a threshold, while the stress evolves stochastically via a Brownian process between glitches [57]. Both meta-models are consistent with various flavors of microphysics in the literature, e.g. superfluid vortex avalanches [9, 10], starquakes [11, 12], and hydrodynamic instabilities [13–15], but they embody important physical differences in how the stress accumulates and when the relaxation events are triggered.

[1] Up-to-date online catalogues are maintained at the Jodrell Bank Centre of Astrophysics, http://www.jb.man.ac.uk/pulsar/glitches.html [8], and the Australian National Telescope Facility, https://www.atnf.csiro.au/research/pulsar/psrcat/ [35]

The roughly scale invariant glitch size PDFs observed in some pulsars suggest that the stress relaxes via an *avalanche process*, i.e. a relaxation event triggered somewhere in the star propagates to adjacent regions via some knock-on mechanism [2, 32]. "Chain reactions" of this kind are observed in Gross-Pitaevskii simulations [10, 58–60] and mean-field or N-body simulations [61, 62] of superfluid vortex avalanches. They are typical of other systems cited as analogues of pulsar glitches in the literature, e.g. self-organized critical systems like sand piles, earthquakes, and magnetic fluxoids in type II superconductors [31, 32, 63]. In the meta-models published to date, a key input is the *conditional distribution of avalanche sizes*, $\eta[\Delta X^{(n)} | X(t_n^-)]$, specifically the PDF of the spatially averaged stress released during the n-th avalanche, $\Delta X^{(n)}$, if the stress just prior to the avalanche is $X(t_n^-)$. There is no way to infer the functional form of $\eta[\Delta X^{(n)} | X(t_n^-)]$ uniquely from neutron star data, although one can get a rough idea from the observed glitch size distribution. Quantities of interest, such as size and waiting time PDFs, cross-correlations, and autocorrelations all depend jointly on the form of $\eta[\Delta X^{(n)} | X(t_n^-)]$, however, opening the door to falsifiability [18, 19, 57].

In this paper, we generalize the successful SDP meta-model by adding a recipe to calculate $\eta[\Delta X^{(n)} | X(t_n^-)]$ endogenously instead of stipulating it exogenously by fiat. We refer to this generalization as the endogenous-η meta-model. The recipe makes concrete the following key idea, which underpins the traditional picture of superfluid vortex avalanches in the literature: i) the vortex pinning strength varies randomly from one location to the next within the star; ii) the stress $\Delta X^{(n)}$ released in a glitch is proportional to the number of locations where the stress X exceeds a threshold, when the glitch is triggered; and iii) the unpinned vortices are reassigned randomly to new pinning locations after the glitch. In other words, as time passes, the distribution of occupied pinning sites is continually revised in a history-dependent fashion, as the star spins down secularly and glitches occur stochastically. This idea is based on the "coherent noise" meta-model introduced by Sneppen and Newman [64] to describe sand piles [65], earthquakes [65], and biological extinctions [66][2]. It has been repurposed successfully as a pulsar glitch meta-model in previous work [67].

Haskell [68] investigated a meta-model that connects the "snowplow" mechanism for hydrodynamically triggered glitches [69] to simulations of vortex unpinning and re-pinning in a two-component fluid framework [70]. It differs from the meta-model considered here in two fundamental ways: i) it unpins a random fraction of vortices at each avalanche event, independent of the past avalanche history; and ii) it assumes event waiting times are exponentially distributed (i.e. the waiting times do not depend on the stress, as in the SDP meta-model). However it does explicitly consider the mutual friction between the different fluid components, and shows that these hydrodynamic considerations produce deviations from power-law size distributions and exponential waiting time distributions.

We emphasize that we do not elect to analyze the endogenous-η meta-model because we favor it over other options. True, it is reasonable from a physical standpoint, but so too are other options. The main motivation is that it formalizes the dominant (albeit idealized) idea in the literature about how vortex unpinning leads to glitches. We there-

[2]The term "coherent noise" is not perfectly apt in the context of pulsar glitches, where the stress is coherent, while the noise, namely thermal creep, acts incoherently throughout the star. We retain the original terminology for consistency with previous literature [64, 67].

fore quantify for the first time the long-term statistics predicted by the broad consensus behind what determines $\eta[\Delta X^{(n)} | X(t_n^-)]$ in the superfluid vortex avalanche picture. As we show below, the long-term statistics are somewhat inconsistent with observations to date, although the conclusion is not final; more data are needed. As a matter of fact the exogenous SDP meta-model, where $\eta[\Delta X^{(n)} | X(t_n^-)]$ is stipulated by fiat instead of being calculated self-consistently, seems to be more consistent with the data. It is unclear what this result implies more broadly, but it is intriguing and likely to inspire more investigations. It serves as a reminder of the value of falsification of physically-motivated meta-models.

The paper is structured as follows: in Section 2.2 we specify how $\Delta X^{(n)}$ is decided at each glitch. In Section 2.3 we connect this method of determining $\Delta X^{(n)}$ at a glitch to the SDP meta-model. In Section 2.4 we explore the long-term statistical observables predicted by the endogenous-η meta-model, and discuss how they compare to current glitch observations in Section 2.5. We conclude in Section 2.6.

2.2. Pinning threshold distribution

We start by formalizing an idealized version of how the coherent stress mechanism may operate, which reflects standard ideas in the literature about stress accumulation and relaxation in pulsar glitches; see Haskell and Melatos [16] for a recent review. As argued below, there are at least three reasons why the simple version may not be what is truly occurring: i) it introduces a cross-correlation between sizes and waiting times, which is largely absent from the data; ii) it struggles to generate exponentially distributed waiting times, which are seen in some pulsars; and iii) it assumes a spatially uniform stress distribution which is qualitatively different to the spatially correlated stress distribution observed in Gross-Pitaevskii [10, 60] and N-body simulations [62] of superfluid vortex avalanches. Nonetheless it is important to study the simple version first, partly to falsify it if possible, and partly because it highlights the key idea that the stress distribution is history-dependent. As in previous papers, we develop the meta-model in the context of superfluid vortex avalanches for concreteness. Adapting it to the context of other microphysics, e.g. starquakes, is possible but outside the scope of this paper [65].

2.2. Standard picture

To fix ideas, suppose that the region of the stellar interior where glitch activity occurs is divided into “sites”. In the vortex avalanche picture, for example, the sites are nucleons or interstices in the nuclear lattice, where a superfluid vortex may pin [71–73]; in the starquake picture, the sites are segments of a fault or other tectonic element of the rigid crust [12, 30, 74]. At an arbitrary site located at $\mathbf{r}$, there is a local stress $X(\mathbf{r}, t)$ at time t, which evolves in response to the global driver and local relaxation physics. In the vortex avalanche picture, $X(\mathbf{r}, t)$ is proportional to the Magnus force; in the starquake picture, $X(\mathbf{r}, t)$ is proportional to the elastic stress (or equivalently the strain in the linear regime).

Let $X_{\text{th}}(\mathbf{r})$ denote the stress threshold at $\mathbf{r}$, which is assumed to be constant on the time-scales of interest (see below). Whenever the stress satisfies $X(\mathbf{r}, t) \geq X_{\text{th}}(\mathbf{r})$, and a glitch is triggered, the stress relaxes locally and is redistributed to nearby sites. In the vortex avalanche picture, a vortex at a site unpins when it escapes the nuclear pinning potential; in the starquake picture, the crustal lattice fails locally when the breaking strain is exceeded. On the other hand, if the stress satisfies $X(\mathbf{r}, t) < X_{\text{th}}(\mathbf{r})$, it remains supported stably at $\mathbf{r}$ during a glitch. A group of contiguous sites with $X(\mathbf{r}, t) < X_{\text{th}}(\mathbf{r})$ form a stress reservoir or capacitive domain [75]. Note that $X(\mathbf{r}, t) > X_{\text{th}}(\mathbf{r})$ can be supported metastably for some time before a glitch is triggered.

The coarse-grained stress threshold is assumed to be spatially uniform, because the length-scale of vortex avalanches or starquakes (inferred from the size of observed glitches) is smaller than the length-scale over which the nuclear lattice is stratified (typically $\sim 10^2\,\text{m}$) [76]. However the fine-grained stress threshold varies randomly from one site to the next, due to defects and microscopic compositional gradients in the lattice.

2.2. *Available versus occupied sites*

When describing the pinning thresholds statistically, it is essential to distinguish between their "available" distribution (defined without reference to any vortices) and their "occupied" distribution (defined with reference only to those pinning sites where a vortex is pinned). These are not the same in general. The available distribution is governed by the physics of the nuclear lattice. The occupied distribution is governed by a combination of the available distribution and the history-dependent vortex dynamics; vortices may congregate preferentially in deeper pinning potentials, for example.

Let $\phi(X_{\text{th}})$ denote the PDF of the thresholds at all available pinning sites. We assume that $\phi(X_{\text{th}})$ is constant in time, because the nuclear properties of the star evolve slowly (e.g. on the cooling time-scale $\sim 10^5\,\text{yr}$) compared to the inter-glitch waiting time and the length of glitch monitoring campaigns to date. Let $X_{\text{th,max}} = \max_{X_{\text{th}}} X_{\text{th}}$ denote the maximum pinning threshold in the star. In the superfluid vortex picture, for example, $X_{\text{th,max}}$ corresponds to the nuclear site with the deepest pinning potential; if a uniform stress satisfying $X \geq X_{\text{th,max}}$ is applied to the system, every vortex unpins when a glitch is triggered. The functional form of $\phi(X_{\text{th}})$ is unknown from first principles, but theoretical calculations suggest that it is broad, with standard deviation comparable to the mean [71–73], and $X_{\text{th,max}}$ is certain to be finite as stipulated by quantum mechanics. In this work we assume $\phi(X_{\text{th}})$ has compact support on the interval $0 = X_{\text{th,min}} \leq X_{\text{th}} \leq X_{\text{th,max}}$ for simplicity, but the results carry over straightforwardly to the case $X_{\text{th,min}} \neq 0$ without changing qualitatively. We emphasize that $X_{\text{th,max}}$ need not equal X_{c}, the critical stress at which a glitch is certain in either the SDP or BSA meta-models. This subtle point is discussed further in Section 2.3.3.

What is the PDF $g(X_{\text{th}}, t)$ of the stress thresholds at pinning sites actually occupied by vortices at time t? In the absence of a global driver, we have $g(X_{\text{th}}, t) = \phi(X_{\text{th}})$ in the limit $t \to \infty$, after initial transients die away. In the presence of a persistent global driver, however, $g(X_{\text{th}}, t)$ depends on time and does not equal $\phi(X_{\text{th}})$ for any t in general (except perhaps $t = 0$, or in the special situation where all vortices unpin at once, resetting the system back to $g(X_{\text{th}}, t) = \phi(X_{\text{th}})$, as described in Section 2.2.3). Whenever a glitch occurs, vortices unpin from relatively shallow pinning sites and repin randomly, changing the relative occupation of sites with lower and higher X_{th}. Thus $g(X_{\text{th}}, t)$ is not only time- and history-dependent but also stochastic; it depends on the random sequence of glitch sizes and waiting times up to the instant t.

How $g(X_{\rm th}, t)$ evolves depends, among other things, on whether one treats the system as spatially uniform or nonuniform. In self-organized critical systems like sand piles, for example, long-range spatial correlations exist between the stress at different locations $\mathbf{r}$ and $\mathbf{r}'$, with $|\langle X(\mathbf{r},t)X(\mathbf{r}',t)\rangle - \langle X(\mathbf{r},t)\rangle\langle X(\mathbf{r}',t)\rangle| \propto |\mathbf{r}-\mathbf{r}'|^{-a}$ and $a > 0$ typically [31, 32]. The system self-organizes through spatial gradients to produce scale-invariant dynamics (e.g. power-law avalanche size PDFs). A strong case can be made, through Gross-Pitaevskii and N-body simulations, that superfluid vortex avalanches or starquakes in a neutron star are self-organized critical systems too [2, 16, 62]. However, the theoretical treatment of a far-from-equilibrium system with correlated spatial gradients is a notoriously challenging (and unsolved) problem in statistical mechanics [32]. In this paper, therefore, we derive an equation of motion for $g(X_{\rm th}, t)$ under the assumption that every pinning site in the star experiences the same, spatially-averaged stress, $X(\mathbf{r}, t) = X(t)$. This mean-field approximation [1, 61] has been employed successfully in the analysis of pulsar glitch observational data on size and waiting time PDFs, cross-correlations, and autocorrelations in the context of the SDP and BSA meta-models [1, 17–19, 57, 77] as well as in previous work on "coherent noise" models of pulsar glitches [see footnote 2 and Melatos and Warszawski [67]].

2.2. *Unpinning and repinning*

Consider two consecutive glitches that occur at times t_n and t_{n+1}. Let $t_n^{\pm}$ denote the instants infinitesimally after (+) and before (−) the event at $t = t_n$[3]. During the interval $t_n^+ \leq t \leq t_{n+1}^-$, the vortices are pinned, so the occupied sites do not change, and neither does $g(X_{\rm th}, t)$. That is, we have $g(X_{\rm th}, t) = g(X_{\rm th}, t_n^+)$ for $t_n^+ \leq t \leq t_{n+1}^-$. We also have $g(X_{\rm th}, t) = 0$ for $X_{\rm th} \leq X(t_n^+)$, because vortices repin exclusively at sites with $X_{\rm th} > X(t_n^+)$, when the avalanche at $t = t_n$ occurs; they cannot get stuck at sites where the stress exceeds the local threshold, while they are moving freely. Simultaneously, $X(t)$ evolves during the interval $t_n^+ \leq t \leq t_{n+1}^-$ (deterministically in the SDP process, stochastically in the BSA process). By the time the instant $t = t_{n+1}$ is reached, we have $X(t_{n+1}^-) \geq X_{\rm th}$ at many sites; the corresponding vortices are pinned metastably and are ready to unpin when provoked by some minuscule statistical (e.g. thermal) fluctuation. When they do unpin, they are assumed to do so instantaneously at $t = t_{n+1}$. The instantaneous approximation is justified amply by Gross-Pitaevskii simulations, where vortex avalanches are observed to occur on a time-scale shorter than one rotation period, and by high-time-resolution radio timing observations, which reveal that the spin up during a glitch takes less than $\sim 30\,$s [20, 21, 78, 79]. Both these time-scales are much shorter than the typical inter-glitch waiting time of weeks to months.

How many vortices unpin at $t = t_{n+1}$? In the mean-field approximation, the answer is all of them pinned in sites that satisfy $X_{\rm th} \leq X(t_{n+1}^-)$, which represent a fraction, F, of

[3] It is important to distinguish t_n from $t_n^{\pm}$, because the glitch is assumed to occur instantaneously, as in previous work.

the total, with

$$F = \int_0^{X(t_{n+1}^-)} \mathrm{d}X'_{\mathrm{th}} g(X'_{\mathrm{th}}, t_{n+1}^-) \tag{2.1}$$

$$= \int_{X(t_n^+)}^{X(t_{n+1}^-)} \mathrm{d}X'_{\mathrm{th}} g(X'_{\mathrm{th}}, t_n^+) \, . \tag{2.2}$$

The unpinned vortices move radially outward by a distance Δr comparable to one inter-vortex (Feynman) separation λ_F before repinning (as seen in Gross-Pitaevskii and N-body simulations), reducing the angular momentum of the superfluid in proportion to Δr and their number. By angular momentum conservation, the crust spins up, and the crust-superfluid angular velocity lag (i.e. the spatially averaged stress) decreases. That is, we have

$$X(t_{n+1}^+) - X(t_{n+1}^-) = -KF \, , \tag{2.3}$$

where $K > 0$ is a constant measured in units of stress. To ensure $X(t) \geq 0$ we require $K \leq X_{\mathrm{th,\,max}}$.

In the vortex avalanche picture, where X is the crust-core differential angular velocity, angular momentum conservation implies [1, 47]

$$KF = \frac{2\pi(I_{\mathrm{C}} + I_{\mathrm{S}})\Delta\nu}{I_{\mathrm{S}}} \tag{2.4}$$

or equivalently

$$K = \frac{2\pi(I_{\mathrm{C}} + I_{\mathrm{S}})}{I_{\mathrm{C}}} \frac{\nu \Delta r}{R} \, , \tag{2.5}$$

where ν is the rotational frequency of the rigid crust (with $X \ll \nu$), $\Delta\nu$ is the increase in ν at the glitch, I_{S} and I_{C} are moments of inertia of the superfluid and crust respectively, and R is the neutron star radius. For $\Delta r \sim \lambda_F = 4.1 \times 10^{-2} (\nu / 10\,\mathrm{Hz})^{-1/2}$ cm, we estimate

$$K \sim 10^{-7} \left(\frac{I_{\mathrm{C}} + I_{\mathrm{S}}}{I_{\mathrm{C}}} \right) \left(\frac{\nu}{10\,\mathrm{Hz}} \right)^{1/2} \left(\frac{R}{10\,\mathrm{km}} \right)^{-1} \mathrm{Hz}. \tag{2.6}$$

The factor $(I_{\mathrm{C}} + I_{\mathrm{S}})/I_{\mathrm{C}}$ amounts to $\sim 10^2$ if the crust is a thin crystalline lattice while the rest of the star is composed of a superfluid [48, 49] or ~ 1 if the crust is coupled tightly to most of the neutrons and protons throughout the star, e.g. by pinning between neutron vortices and magnetic fluxoids of the superfluid [8, 50, 51, 80]. As discussed in Section 2.5 of Carlin and Melatos [57] the coupling between the rotation of the superfluid and the crust may be imperfect [81]. In light of the uncertainty, we allow K to remain a free parameter in the meta-model.

The unpinned vortices repin instantaneously. The number of pinning sites per unit area is $\sim 10^{20}$ times the number of vortices per unit area, so there is no reason for a vortex to pin preferentially to a shallower or deeper pinning site, as it circulates freely during an avalanche. Hence the probability that a vortex repins at a site with stress threshold X_{th} is simply proportional to the number of such sites present in the crustal

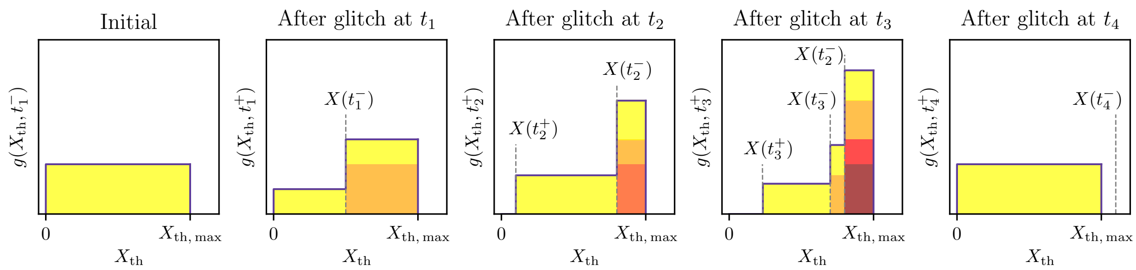

Figure 2.1: A toy example illustrating schematically the evolution of $g(X_{\rm th}, t)$ during a sequence of four glitches, with $X(t_1^+) < X(t_3^+) < X(t_2^+) < X_{\rm th,max} < X(t_4^-)$, where $g(X_{\rm th}, t_1^-) = \phi(X_{\rm th})$ is the uniform distribution between $0 \le X_{\rm th} \le X_{\rm th,max}$. The colors correspond to how many glitches occur in the time elapsed since vortices unpin from pinning sites with a certain threshold. Darker colors indicate that the vortices have stayed pinned during more events.

lattice, i.e. the fraction of the total sites with threshold $X_{\rm th}$. Therefore the distribution of thresholds at which the vortices repin satisfies $g_{\rm repin}(X_{\rm th}, t_{n+1}^+) \propto \phi(X_{\rm th})$[4]. Of course, freely moving vortices cannot repin at a site whose threshold is lower than the global stress, as discussed above, so we have

$$g_{\rm repin}(X_{\rm th}, t_{n+1}^+) = A\,\phi(X_{\rm th})\,H[X_{\rm th} - X(t_{n+1}^+)]\,, \tag{2.7}$$

where $H(\dots)$ denotes the Heaviside function. The constant A is determined by normalization with respect to the unpinned fraction and is given by

$$A = \left[\int_{X(t_{n+1}^+)}^{X_{\rm th,max}} {\rm d}X'_{\rm th}\,\phi(X'_{\rm th})\right]^{-1} F\,. \tag{2.8}$$

2.2. *Equation of motion for the distribution of occupied pinning sites*

We are now in a position to combine the results on unpinning and repinning in Section 2.2.3 to write down the equation of motion for $g(X_{\rm th}, t)$. We remind the reader that $g(X_{\rm th}, t)$ does not evolve at all during the inter-glitch interval $t_n^+ \le t \le t_{n+1}^-$, while vortices are pinned. Its evolution is described completely, in the above approximation, by discontinuous adjustments at each glitch. That is, at $t = t_{n+1}$, the following things happen to the stress threshold PDF:

i) we start with $g(X_{\rm th}, t_{n+1}^-) = g(X_{\rm th}, t_n^+)$, which is nonzero for $X_{\rm th} > X(t_n^+)$;

ii) we calculate the change in stress $-KF$ in equation (2.3) by integrating $g(X_{\rm th}, t_n^+)$ according to equation (2.2);

[4]In other words, as there many more pinning sites than vortices, the distribution of thresholds of pinning sites at which a free vortex may repin is equal to the distribution of thresholds of pinning sites in general. A free vortex is not biased towards pinning sites with higher or lower thresholds. It pins indiscriminately to any site, whose threshold exceeds the global stress [82].

iii) we set $g(X_{\rm th}, t^-_{n+1})$ to zero in the range $X(t^+_n) \le X_{\rm th} \le X(t^-_{n+1})$, because the vortices therein unpin;

iv) we reassign the unpinned vortices to sites with thresholds in the range $X(t^+_{n+1}) < X_{\rm th} \le X_{\rm th,\,max}$ according to equations (2.7) and (2.8).

Putting steps i)–iv) together yields

$$\begin{aligned} g(X_{\rm th}, t^+_{n+1}) &= g(X_{\rm th}, t^-_{n+1}) H[X_{\rm th} - X(t^-_{n+1})] \\ &\quad + \left[\int_{X(t^+_{n+1})}^{X_{\rm th,\,max}} dX'_{\rm th} \phi(X'_{\rm th}) \right]^{-1} F\, \phi(X_{\rm th}) H[X_{\rm th} - X(t^+_{n+1})] \end{aligned} \tag{2.9}$$

It is easy to check that this normalizes correctly with $1 = \int_0^{X_{\rm th,\,max}} dX'_{\rm th} g(X'_{\rm th}, t^+_{n+1})$. Note that $g(X_{\rm th}, t^+_{n+1})$ depends on $g(X_{\rm th}, t^+_n)$ implicitly through F. It also depends on $X(t^-_{n+1})$ and $X(t^+_n)$ independently, because the evolution of $X(t)$ during the interval $t^+_n \le t \le t^-_{n+1}$ is controlled by the stress accumulation process, which does not depend on the unpinning and repinning physics.

Equation (2.9) resembles, but is not the same as, the equations of motion in Sneppen and Newman [64] and Melatos and Warszawski [67]. The foregoing papers treat unpinning and repinning similarly, i.e. by nullifying the unpinned portion of $g(X_{\rm th}, t)$ and reassigning it elsewhere $\propto \phi(X_{\rm th})$[5]. However neither paper evolves $g(X_{\rm th}, t)$. It is assumed that $g(X_{\rm th}, t)$ converges rapidly to its steady-state form, $g(X_{\rm th}, t) = g(X_{\rm th})$, i.e. the system establishes detailed balance between unpinning and repinning at each individual value of $X_{\rm th}$ [see equations (3) and (4) in Melatos and Warszawski [67]]. This approach is perfectly defensible, when the goal is to calculate the statistically stationary size and waiting time PDFs, but it does not contain enough information to study the cross- and autocorrelations we are interested in here [17–19].

To build intuition, Figure 2.1 illustrates schematically the evolution of $g(X_{\rm th}, t)$ over the course of four hypothetical glitches at t_1, t_2, t_3, and t_4. For simplicity we choose $\phi(X_{\rm th})$ to be uniform in the range $0 \le X_{\rm th} \le X_{\rm th,\,max}$, with $K = X_{\rm th,\,max}$. The system starts with $g(X_{\rm th}, t^-_1) = \phi(X_{\rm th})$. In this particular realization we choose $X(t^+_1) < X(t^+_3) < X(t^+_2) < X_{\rm th,\,max} < X(t^-_4)$ for illustrative purposes. The first glitch, at t_1, unpins half of the vortices, and they are reassigned according to equation (2.7). The second glitch, at t_2, unpins more than half of the vortices, but due to the previous glitch we have $X(t^+_2) \neq 0$, as $g(X_{\rm th}, t)$ is no longer uniform. The third glitch, at t_3, occurs with $X(t^-_3) < X(t^-_2)$, demonstrating that the memory of the previous stress in the system is imprinted on $g(X_{\rm th}, t)$, i.e. $g(X_{\rm th}, t^+_3)$ depends on $X(t^-_2)$, not just $X(t^\pm_3)$. The fourth glitch, at t_4, resets the system back to $\phi(X_{\rm th})$ because we have $X(t^-_4) > X_{\rm th,\,max}$, and so all vortices unpin.

Note that there is a complex feedback loop at play which relates the glitch sizes and waiting times to $g(X_{\rm th}, t)$. If chance produces a long sequence of frequent glitches, i.e. the stress does not increase much before another glitch is triggered, vortices pile up at larger values of $X_{\rm th}$ near $X_{\rm th,\,max}$. Then, when there is a long delay, which gives the stress time to reach $X \approx X_{\rm th,\,max}$, the vortex pile pinned at sites with $X_{\rm th} \approx X_{\rm th,\,max}$ unpins all at once to produce a relatively large glitch resetting the system. By contrast,

[5] They also include an optional thermal unpinning process independent of $X_{\rm th}$, which is not essential and is omitted in this paper.

a similarly long delay produces a smaller glitch, if it is preceded by a glitch sequence which does not pile up vortices at $X_{\rm th} \approx X_{\rm th,\,max}$.

2.3. State-dependent Poisson process

The above recipe for updating $g(X_{\rm th}, t)$ must be combined with a compatible recipe for choosing the waiting times between glitches. Two approaches have been explored previously, in the SDP [1, 18] and BSA meta-models [57]. In the BSA meta-model the stress accumulates stochastically to a fixed threshold, whereupon a glitch is triggered deterministically. In the SDP meta-model glitches are triggered probabilistically, at an instantaneous rate which depends on the stress in the system. If $X(t_n^-) = X_{\rm c}$ is identical for each glitch as in the BSA meta-model, the system does not produce glitches of different sizes, as the same fraction of vortices would unpin every time, and repopulate the same distribution of pinning sites. To avoid this trivial behavior, which is inconsistent with pulsar data, we henceforth adopt the SDP meta-model to pick waiting times, and therefore determine $X(t_{n+1}^-)$, given $X(t_n^+)$.

We position the SDP and related meta-models in the broader context of point processes and time series modeling in Appendix 2.A3.

2.3. Equation of motion for the stress

The stress, $X(t)$, in the star evolves according to

$$X(t) = X(0) + t + \sum_{n=1}^{N(t)} \Delta X^{(n)} \,, \tag{2.10}$$

where X and t are here and henceforth expressed in dimensionless units of $X_{\rm c}$ (the critical stress at which a glitch becomes certain) and $X_{\rm c} I_{\rm C}/N_{\rm em}$ respectively, where $N_{\rm em}$ is the electromagnetic torque acting on the crust, and $X(0)$ is an arbitrary initial condition. The number of glitches up to time t, $N(t)$, is a random variable, implicitly determined by the waiting times between each glitch. The size $\Delta X^{(n)}$ of the n-th relaxation event is a deterministic function of the fluctuating PDF $g(X_{\rm th}, t)$. The recipe for determining $\Delta X^{(n)} = -KF$ is outlined in Section 2.2.3, specifically equations (2.2) and (2.3).

One key assumption of the SDP meta-model is that the instantaneous glitch rate, $\lambda(t)$, is a function of the spatially-averaged stress, $X(t)$. We assume $\lambda[X(t)]$ grows monotonically between glitches according to

$$\lambda[X(t)] = \frac{\alpha}{1 - X(t)} \,, \tag{2.11}$$

where

$$\alpha = \frac{I_{\rm C} X_{\rm c} \lambda_0}{N_{\rm em}} \tag{2.12}$$

is a dimensionless control parameter, and λ_0 is a reference rate defined as $\lambda_0 = \lambda(1/2)/2$. The exact functional form of $\lambda[X(t)]$ does not significantly change the long-term dynamics, as long as the rate diverges as $X \to X_{\rm c}$ [1, 18].

The PDF of waiting times after the n-th glitch is [1, 83]

$$p[\Delta t | X(t_n^+)] = \lambda[X(t_n^+) + \Delta t] \exp\left\{ - \int_{t_n^+}^{t_n^+ + \Delta t} \mathrm{d}t' \lambda[X(t_n^+) + t'] \right\}. \tag{2.13}$$

2.3. Monte Carlo simulations

The evolution of $X(t)$ and $g(X_{\mathrm{th}}, t)$ is jointly modeled with a simple Monte Carlo automaton.

1. Initialize the system at $t = 0$ with $g(X_{\mathrm{th}}, 0) = \phi(X_{\mathrm{th}})$, and $X = X(0)$.
2. Pick a random Δt from equation (2.13), given the current stress X.
3. Update the stress to $X + \Delta t$ to account for the deterministic evolution up to the glitch.
4. Evaluate $\Delta X = -KF$ deterministically via equations (2.2) and (2.3), given $g(X_{\mathrm{th}}, t)$ and X.
5. Update $g(X_{\mathrm{th}}, t)$ according to equation (2.9).
6. Update X by adding ΔX according to equation (2.10).
7. Repeat from step 2.

Random numbers for step 2 are picked using the standard inverse cumulative algorithm [84]. As $\phi(X_{\mathrm{th}})$ is chosen to be a uniform distribution between $0 \leq X_{\mathrm{th}} \leq X_{\mathrm{th,max}}$, $g(X_{\mathrm{th}}, t)$ is a piecewise-constant function. Hence, we efficiently update it by storing the heights at change-points X_{th} in memory, as opposed to sampling $g(X_{\mathrm{th}}, t)$ on a grid of X_{th} values.

2.3. Qualitative results

There are three control parameters in the dimensionless meta-model: α, $X_{\mathrm{th,max}}$, and K. We fix $\phi(X_{\mathrm{th}})$ to be a uniform distribution between 0 and $X_{\mathrm{th,max}}$. For simplicity, we assume $K = X_{\mathrm{th,max}}$ (its maximal value) for the rest of this work. Appendix 2.A1 contains a brief exploration of the impact $K < X_{\mathrm{th,max}}$ has on long-term observables. Figures 2.2–2.4 illustrate the qualitative impact of α on the evolution of X and $g(X_{\mathrm{th}}, t)$, given $X_{\mathrm{th,max}} = 0.95 X_{\mathrm{c}}$. Figure 2.2 shows that at low values $\alpha \lesssim 0.5$, longer waiting times are more likely, and the stress often exceeds $X_{\mathrm{th,max}}$ before each glitch, resetting the system. Therefore one finds $g(X_{\mathrm{th}}, t) \approx \phi(X_{\mathrm{th}})$, i.e. there is little long-term memory in the system. In Figure 2.4 high values $\alpha \gtrsim 5$ produce shorter waiting times. Thus long sequences of small glitches unfold before rare, large events reset the system once the stress finally accumulates to $X \gtrsim X_{\mathrm{th,max}}$. Figure 2.3 shows that for intermediate values of α between the above two extremes the behavior of both the stress $X(t)$ and the evolution of $g(X_{\mathrm{th}}, t)$ is complex.

The qualitative long-term behavior of X is shown in Figure 2.5. In the top panel with $\alpha = 0.2$, the stress often exceeds $X_{\mathrm{th,max}}$ due to the long waiting times between glitches,

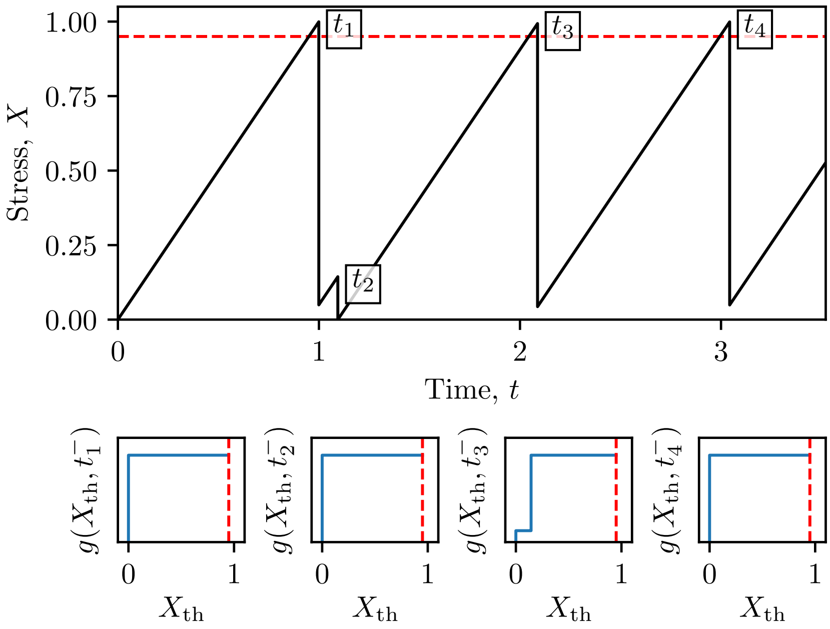

Figure 2.2: Evolution of X (main panel) and $g(X_{\rm th}, t)$ (sub-panels) across four glitches at $t_1, \dots, t_4$, generated via the automaton outlined in Section 2.3.2. Parameters: $\alpha = 0.2$, $X_{\rm th,\,max} = 0.95$ (indicated in both the main panel and sub-panels with a red dashed line), $K = X_{\rm th,\,max}$. X and $X_{\rm th}$ are in units of $X_{\rm c}$ and t is in units of $X_{\rm c} I_{\rm C}/N_{\rm em}$.

resetting the system and keeping the average stress around $X \sim 0.5$. In the middle panel with $\alpha = 1$, the average stress climbs stochastically until finally a longer than average waiting time allows $X > X_{\rm th,\,max}$, resetting the system. In the bottom panel with $\alpha = 10$, waiting times are short and the stress builds asymptotically towards $X = X_{\rm th,\,max}$. For $\alpha \gtrsim 1$ the automaton takes some time to stabilize such that the memory of the arbitrary initial conditions $X(t = 0) = 0$ and $g(X_{\rm th}, t = 0) = \phi(X_{\rm th})$ is lost. When calculating long-term statistics predicted by the meta-model in Section 2.4 we throw away the first $\lfloor 100\alpha \rfloor$ glitches generated.

Figures 2.2–2.4 demonstrate that how often the system completely resets is closely linked to the dynamics of how X and $g(X_{\rm th}, t)$ evolve, and therefore observables such as waiting times and glitch sizes. The fraction of glitches that fully reset the system, i.e. result in $g(X_{\rm th}, t_n^+) = \phi(X_{\rm th})$ after a glitch at time t_n, is plotted as a function of α and $X_{\rm th,\,max}$ in Figure 2.6. The smallest value of α where over half the glitches reset the system shifts from 0.5 to 0.3 to 0.15 as $X_{\rm th,\,max}$ decreases from 0.99 to 0.95 to 0.8 respectively. This is intuitive, as lower α results in longer waiting times, all else being equal, and the stress is more likely to exceed $X_{\rm th,\,max}$ by the time a glitch is triggered.

For $X_{\rm th,\,max} \geq 1$, X never exceeds $X_{\rm th,\,max}$, and the system never completely resets. That is, the repinning step in equation (2.7) assigns vortices to pinning potentials with $X_{\rm th} \geq 1$, which never unpin. The system stagnates eventually, with all vortices pinned at sites whose stress thresholds cannot be reached. Melatos and Warszawski [67] ameliorated this stagnation by allowing a “thermal creep” term, whereby a small fraction of vortices at sites with $X_{\rm th} > X$ unpin randomly at a glitch [64].

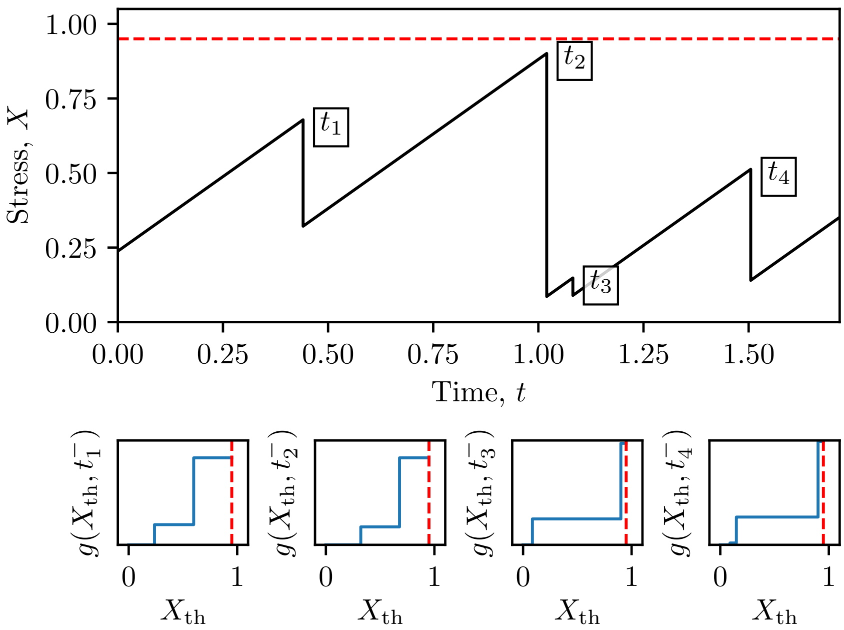

Figure 2.3: As in Figure 2.2 but with $\alpha = 1$.

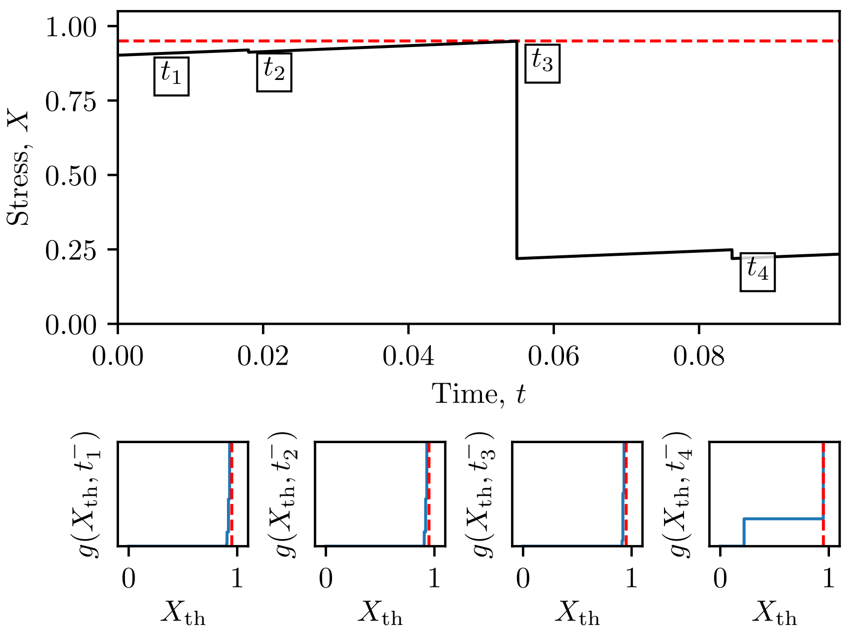

Figure 2.4: As in Figure 2.2 but with $\alpha = 10$.

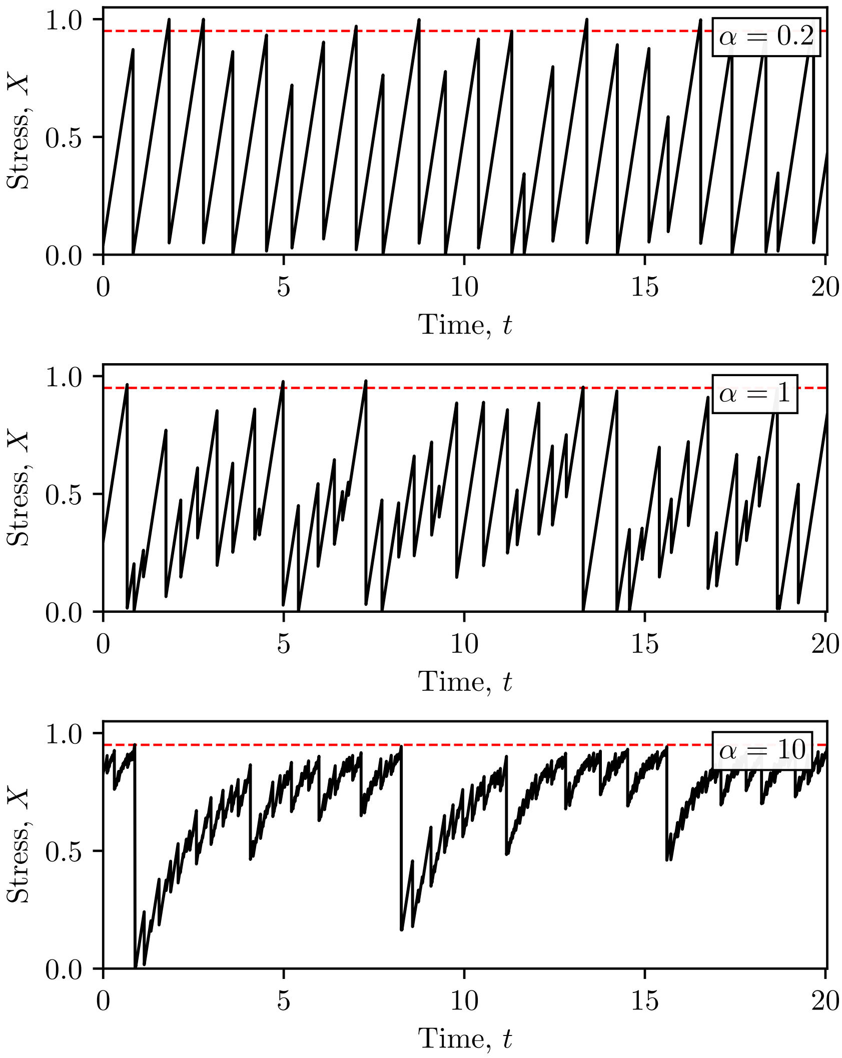

Figure 2.5: Long-term qualitative behavior of X for three different values of $\alpha = 0.2$, 1, and 10 in the top, middle and bottom panel respectively. Parameters: $X_{\text{th, max}} = 0.95$ (indicated with a red dashed line in each panel), $K = X_{\text{th, max}}$.

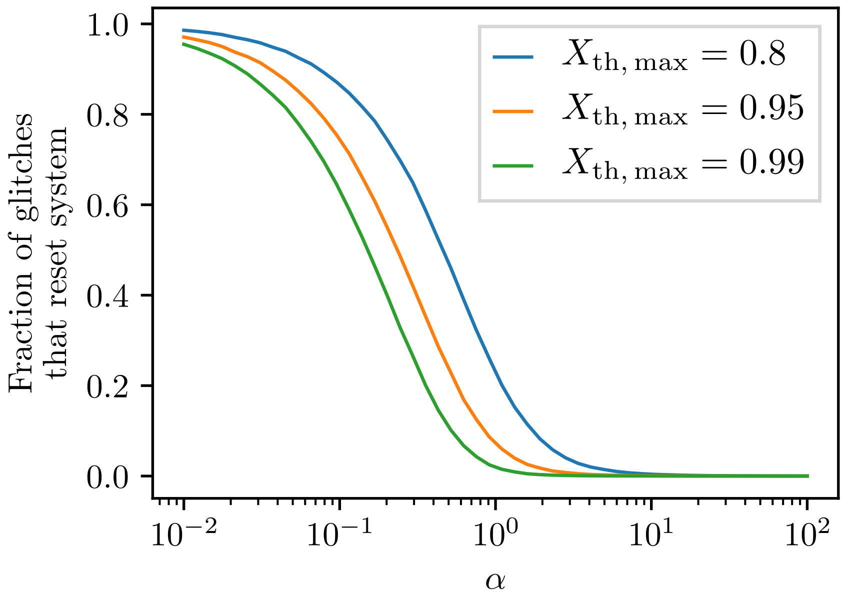

Figure 2.6: Fraction of glitches that reset the system as a function of α for three different values of $X_{\mathrm{th,max}}$. Parameters: $N = 10^5$ glitches generated at 50 logarithmically spaced values of α for each value of $X_{\mathrm{th,max}}$, with $K = X_{\mathrm{th,max}}$.

2.3. Differences from previous meta-models

The recipe for updating $g(X_{\mathrm{th}}, t)$ and hence generating $\Delta X^{(n)}$ differs fundamentally from the recipe in previous meta-models [1, 18, 57]. Firstly $\Delta X^{(n)}$ is generated from $g(X_{\mathrm{th}}, t)$, which is a new step. In the SDP and BSA meta-models, $\Delta X^{(n)}$ is drawn from an exogenously defined conditional jump distribution, $\eta[\Delta X^{(n)} | X(t_n^-)]$, which makes no reference to which pinning sites are occupied. Secondly, $\Delta X^{(n)}$ is generated deterministically; once $g(X_{\mathrm{th}}, t_n^+)$ and $X(t_{n+1}^-)$ are known, so is $\Delta X^{(n)}$ without rolling dice. This fundamentally alters the meta-model from a doubly stochastic process, where the waiting time Δt and avalanche size $\Delta X^{(n)}$ are drawn randomly from independent PDFs (inhomogeneous Poisson and $\eta[\Delta X^{(n)} | X(t_n^-)]$ respectively), to a singly stochastic process, where only Δt is drawn randomly, according to the stress accumulation process of choice.

With that said, the sequence of avalanche sizes is still unpredictable in a long-term sense in the endogenous-η meta-model, because it is driven by stochastic draws of Δt. Furthermore, the ensemble average $g_s(X_{\mathrm{th}}) = \langle g(X_{\mathrm{th}}, t_n^+) \rangle$, is analogous to the statistically stationary global stress PDF $p(X)$ discussed in Section 6 of Fulgenzi et al. [1]. From $g_s(X_{\mathrm{th}})$, it is possible to calculate an effective $\eta[\Delta X^{(n)} | X(t_n^-)]$, which is also statistically stationary. We do so in Appendix 2.A2. If the goal of the theory is to predict the stationary glitch size and waiting time PDFs, then running the SDP meta-model as developed in previous papers and drawing randomly from $\eta[\Delta X^{(n)} | X(t_n^-)]$ derived from $g_s(X_{\mathrm{th}})$ as in Appendix 2.A2 is adequate. However, if the exact temporal sequence of sizes and waiting times is of interest, e.g. to investigate cross- and autocorrelations, then the evolution of $g(X_{\mathrm{th}}, t)$ must be tracked according to equation (2.9) or some variant thereof.

2.3. Mutual friction

In hydrodynamical multi-component models, the coupling between the inviscid and viscous components is called the mutual friction [85–87]. The strength and functional form of the mutual friction is fundamentally linked to how the vortices transfer angular momentum from the unobservable stress reservoir and the observable crust [34, 87, 88]. The SDP meta-model, and endogenous-η extension considered in this paper, tacitly assume that mutual friction is weak between glitches as the stress grows linearly, irrespective of its absolute magnitude, until a glitch is triggered. These meta-models align qualitatively with phenomenological models that abruptly change the form (and usually weaken the strength) of the mutual friction when a glitch occurs, due to a phase transition between turbulent and laminar flow states [89–91]. We note that the meta-model treats glitches as impulsive events and has nothing to say in its present form about post-glitch recoveries, where hydrodynamic effects are likely to play a role.

2.4. Observable long-term statistics

Following the steps outlined in Section 2.3.2 one can generate sequences of waiting times and sizes of arbitrary length, given α, K, and $X_{\mathrm{th,max}}$. From these sequences, observable long-term statistics are predictable. They offer a baseline for falsification studies involving astronomical observations [17–19]. As stated in equation (2.4), we have $\Delta X = -KF \propto \Delta\nu$, implying the shape of the event size PDF $p(\Delta X)$ is the same as the observed glitch size PDF $p(\Delta\nu)$.

2.4. Waiting time and size PDFs

Figure 2.7 shows the waiting time PDF, $p(\Delta t)$, and size PDF, $p(\Delta X)$, for three values of α on a log-linear scale. For $\alpha \lesssim 0.5$, $p(\Delta t)$ has two peaks, one at $\Delta t = X_{\mathrm{th,max}}$ and one at $\Delta t = 1$, and increases monotonically for $\Delta t < X_{\mathrm{th,max}}$. In the low-$\alpha$ regime X regularly exceeds $X_{\mathrm{th,max}}$, triggering a glitch of size $\Delta X = X_{\mathrm{th,max}}$. With $X \approx 1$ before the glitch, and $X \approx 1 - X_{\mathrm{th,max}}$ after, the maximum Δt until the next glitch is $X_{\mathrm{th,max}}$. As equation (2.13) increases monotonically with Δt for $\alpha < 1$, the maximum Δt allowed by equation (2.13) is the most likely waiting time. When plotted on a log-log scale, we see that for $\alpha \gtrsim 3$, $p(\Delta t)$ is well approximated by a power-law distribution, with a turn-off at $\Delta t \lesssim 10^{-2}$ (in units of $X_c I_C / N_{\mathrm{em}}$). Where this turn-off occurs depends on both α and $X_{\mathrm{th,max}}$. The slope of the power-law component of $p(\Delta t)$ is approximately -3 for $\alpha = 10$ and decreases to -4 for $\alpha = 50$. In the intermediate regime $0.5 \lesssim \alpha \lesssim 3$, $p(\Delta t)$ is approximately uniform.

The size PDFs also display distinctive features in the low- and high-α regimes. For $\alpha \lesssim 0.5$, $p(\Delta X)$ increases monotonically, with a significant fraction of the probability mass close to $\Delta X = X_{\mathrm{th,max}}$. The latter events correspond to the glitches that completely reset the system, if one has $X \geq X_{\mathrm{th,max}}$ prior to the glitch. On a log-log scale, we see that for $\alpha \gtrsim 3$, $p(\Delta X)$ can be approximated as a broken power law distribution, with a smooth turn-over at $\Delta X \approx 10^{-2}$ (in units of X_c). The location of this turn-over depends on α and $X_{\mathrm{th,max}}$. The slope of $p(\Delta X)$ for $\Delta X \gtrsim 10^{-2}$ is approximately -2 for $\alpha = 10$, and decreases to -2.5 for $\alpha = 50$. For $0.5 \lesssim \alpha \lesssim 3$, $p(\Delta X)$ is approximately uniform,

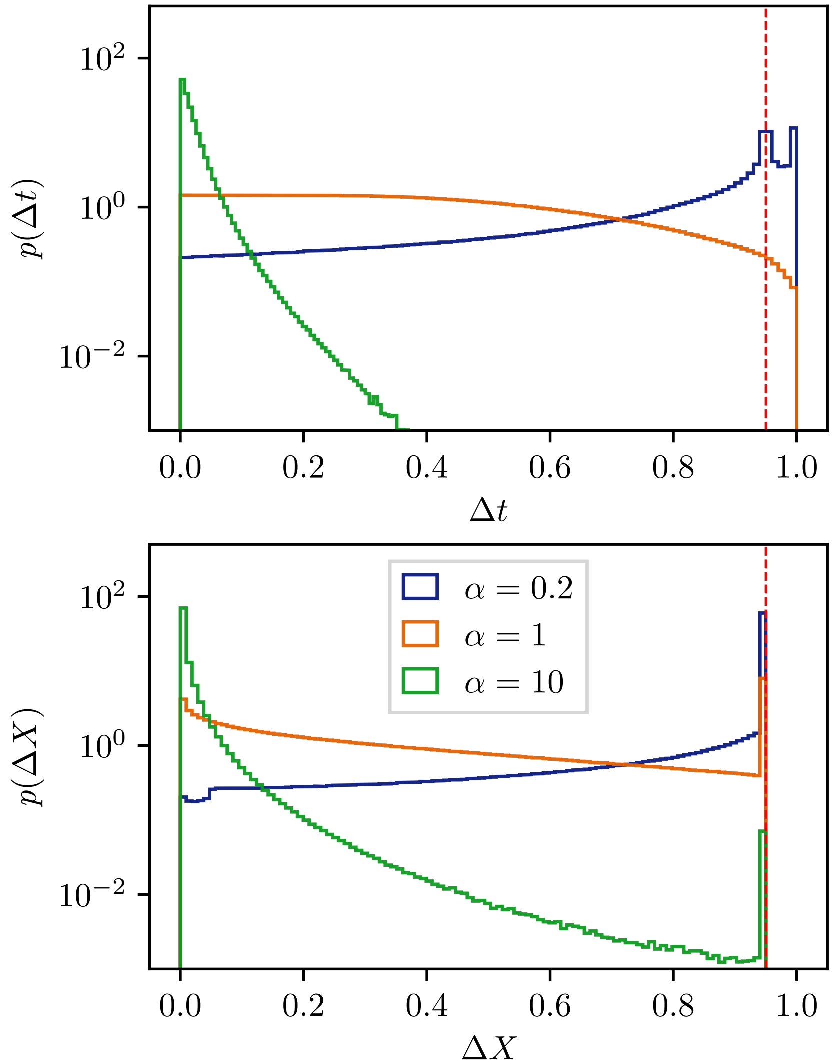

Figure 2.7: Waiting time, Δt, and size, ΔX, PDFs on the top and bottom panel respectively. Parameters: $N = 10^7$ simulated glitches for each value of α, $X_{\text{th, max}} = 0.95$ (indicated with a red dashed line in each panel), $K = X_{\text{th, max}}$.

with a spike at $\Delta X = X_{\mathrm{th,\,max}}$, again corresponding to glitches that completely reset the system.

In summary, in the low-α regime $p(\Delta t)$ is bimodal with peaks at $\Delta t = X_{\mathrm{th,\,max}}$ and $\Delta t = 1$, while $p(\Delta X)$ is monotonically increasing until $\Delta X = X_{\mathrm{th,\,max}}$ where there is a spike in the PDF then a sharp cut-off. In the high-α regime both $p(\Delta t)$ and $p(\Delta X)$ are approximately power-law distributed, with low-end turn-offs at $\Delta t \approx 10^{-2}$ and $\Delta X \approx 10^{-2}$.

2.4. Cross- and autocorrelations

The time-ordered nature of waiting times and relaxation events invites investigation into what relationships exist between events that happen consecutively. For example, in the SDP meta-model certain combinations of observables, such as the rate of spin-down and average waiting time, predict the cross-correlation between waiting times and the next glitch size [17]. In the SDP and BSA meta-models combinations of cross-correlations and autocorrelations restrict possible values of meta-model control parameters in individual glitching pulsars [19, 57].

Figure 2.8 shows the Spearman correlation coefficients for the forward cross-correlation, ρ_+, i.e. the correlation between the size of the previous glitch and the next waiting time; the backward cross-correlation, ρ_-, i.e. the correlation between the size of the glitch and the preceding waiting time; as well as the autocorrelations between consecutive waiting times, $\rho_{\Delta t}$, and sizes, $\rho_{\Delta X}$. It is clear that ρ_+ is high for all but the smallest values of α. The longer the waiting time, the larger the upper terminal in equation (2.2), and thus a greater fraction of the vortices unpin. At small values $\alpha \lesssim 10^{-2}$ most glitches completely reset the system, and the forward cross-correlation is lower. The backward cross-correlation, ρ_-, is small and negative for $\alpha \lesssim 0.2$, but small and positive for $\alpha \gtrsim 0.2$. Size autocorrelations, $\rho_{\Delta X}$, are negligible for all α. Waiting time autocorrelations satisfy $\rho_{\Delta t} \sim -0.5$ for $\alpha \lesssim 0.1$, but are negligible for $\alpha \gtrsim 0.2$.

The impact of decreasing $X_{\mathrm{th,\,max}}$ on Figure 2.8 is minimal; the magnitudes of the Spearman correlation coefficients decrease marginally, and the Spearman correlation coefficients as functions of α shift towards the right a small amount. As $X_{\mathrm{th,\,max}}$ decreases, Figure 2.6 shows that more glitches reset the system, at a fixed value of α.

2.4. Aftershocks and precursors

Aftershocks occur after a large event, when subsequent events are larger and more frequent than usual. They are common in spatially correlated knock-on processes such as avalanches and earthquakes [32, 92, 93]. Naively, one might expect that the endogenous-η meta-model should not exhibit aftershocks, as it does not include spatial correlations, due to the assumption that each pinning site experiences the same spatially-averaged stress. Aftershocks are not discussed in the context of the SDP or BSA meta-models, as large events in those meta-models do not correspond to a rearrangement of occupied pinning sites. A large event does not impact the next waiting time or size, beyond reducing the stress in the system.

We investigate whether the above naive expectation holds for the endogenous-η meta-model by calculating the conditional waiting time and size PDFs for glitches im-

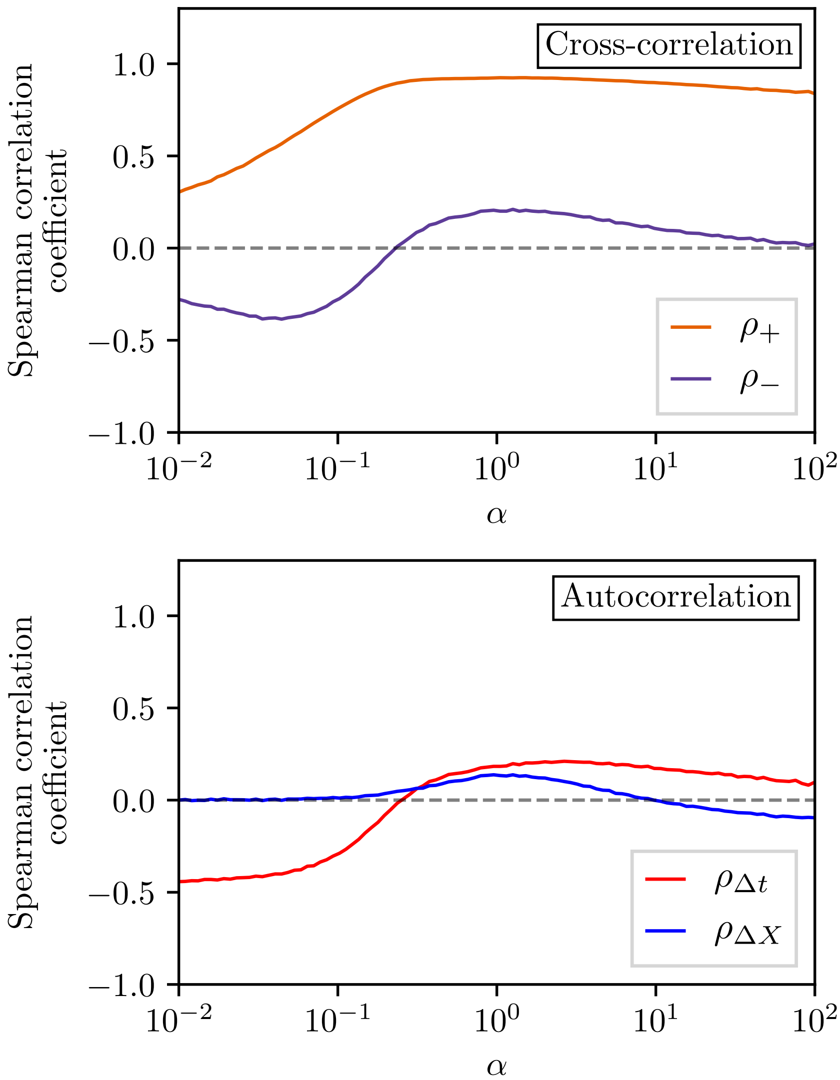

Figure 2.8: Top panel: Forward cross-correlation, ρ_+, and backward cross-correlation, ρ_-, as a function of α (orange and purple curves respectively). Bottom panel: Autocorrelation between waiting times, $\rho_{\Delta t}$, and sizes, $\rho_{\Delta X}$, as a function of α (red and blue curves respectively). Parameters: $N = 10^5$ glitches generated at 100 logarithmically spaced values of α, $X_{\mathrm{th,\,max}} = 0.95$, $K = X_{\mathrm{th,\,max}}$.

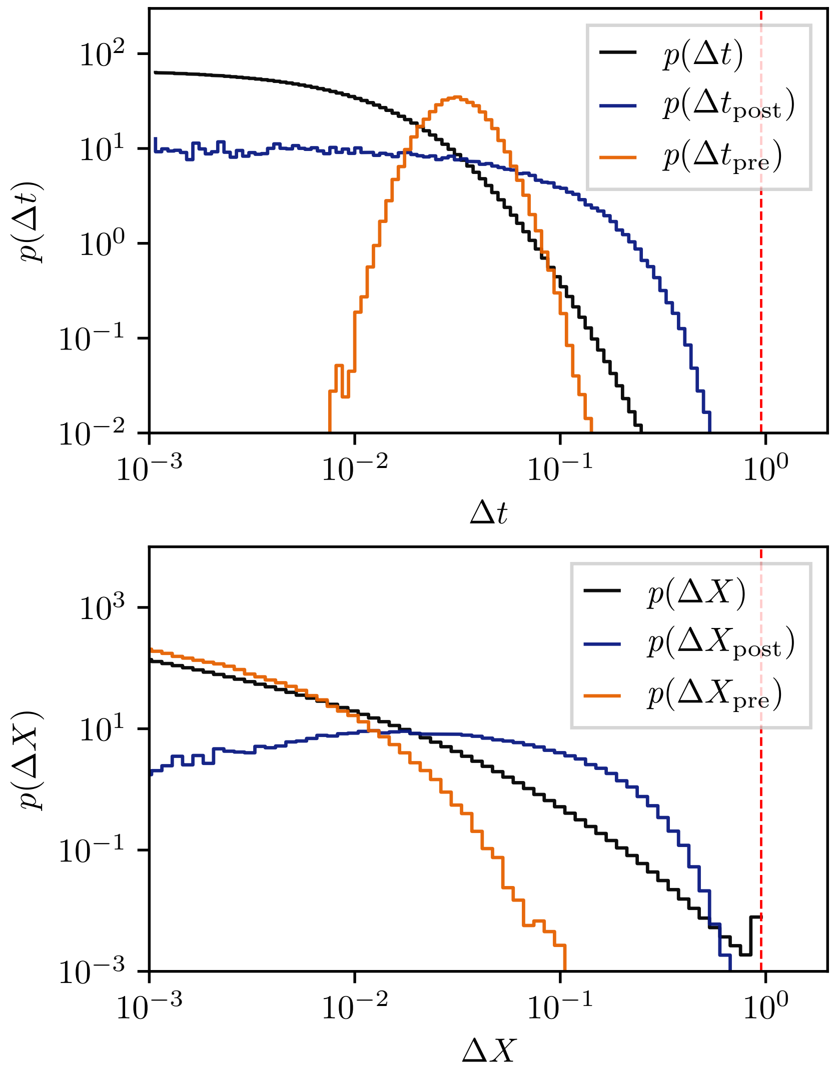

Figure 2.9: Top panel: PDFs of all waiting times, Δt, waiting times just prior to a system-resetting glitch, $\Delta t_{\rm pre}$, and waiting times just after a system-resetting glitch, $\Delta t_{\rm post}$. Bottom panel: Corresponding PDFs for sizes. Parameters: $\alpha = 10$, $N = 10^8$ total glitches, $\sim 10^5$ of which reset the system completely, $X_{\rm th,\,max} = 0.95$, $K = X_{\rm th,\,max}$.

mediately following a glitch that completely resets the system, $p(\Delta t_{\text{post}})$ and $p(\Delta X_{\text{post}})$ respectively. Figure 2.9 shows these PDFs, and the waiting time and size PDFs of events just prior to a glitch that completely resets the system, $p(\Delta t_{\text{pre}})$ and $p(\Delta X_{\text{pre}})$ respectively. There is an excess of longer waiting times in $p(\Delta t_{\text{post}})$ compared to $p(\Delta t)$, as the system takes some time to build up stress before another glitch is likely, after such a system-resetting glitch. There is a corresponding excess of larger sizes in $p(\Delta X_{\text{post}})$ compared to $p(\Delta X)$. The precursor waiting times, Δt_{pre}, are distributed as a log-normal distribution, with $\langle \Delta t_{\text{pre}} \rangle > \langle \Delta t \rangle$. There are relatively few small Δt_{pre} events, because the system-resetting condition $\Delta X \geq X_{\text{th,max}}$ occurs only if enough stress accumulates before the glitch. There are few large glitches in $p(\Delta X_{\text{pre}})$ compared to $p(\Delta X)$, as large glitches place the system in a configuration which is unlikely to fully reset at the next glitch, as X is low.

The behavior of aftershocks and precursors in Figure 2.9 is replicated qualitatively for other values of $\alpha \neq 10$ and $X_{\text{th,max}} \neq 0.95$. That is, there is always an excess of longer waiting times, and larger glitches, following a system-resetting glitch, while the precursor waiting times are longer than average. For $\alpha \lesssim 0.2$ these features in the PDFs are less prominent, as the system resets after almost every event.

2.5. Astronomical observations

How do the long-term statistical predictions in Section 2.4 compare to what we currently see in glitching pulsars? This question has been answered previously in the context of the SDP [17–19], and BSA [57] meta-models. For the five pulsars with the most recorded glitches, there are regimes of parameter space in the SDP meta-model which adequately explain observations. For example, PSR J0537−6910 is consistent with the SDP meta-model if $\alpha \lesssim 0.1$ [19]. However this is not the case for the BSA meta-model, for which two pulsars, namely PSR J0534+2200 and PSR J1341−6220, are consistent with the meta-model only if there exists an undetected population of frequent small glitches.

The endogenous-η meta-model presented here is falsifiable using the same approach: the meta-model must predict simultaneously, with one set of input parameters, the long-term $p(\Delta t)$, $p(\Delta X)$, cross-correlations, and autocorrelations, otherwise it is rejected. In principle we have one additional potential observable in this meta-model, the aftershocks and precursors discussed in Section 2.4.3. However, due to the small number of glitches recorded in individual pulsars ($N < 50$), it is not yet clear whether we have witnessed any large, system-resetting glitches in astronomical data, and so we cannot compare to the aftershock or precursor predictions of Section 2.4.3.

Current observations of glitch waiting time and size distributions [3, 4] do not show clear signs of a sharp cut-off at the upper end, as the meta-model predicts in Figure 2.7 for $\alpha \lesssim 5$. For $\alpha \gtrsim 5$, where the distributions are steeper, the sharp cut-off may have escaped detection until now due to the paucity of recorded glitches. Even so, if most glitching pulsars fall in the $\alpha \gtrsim 5$ regime we should expect to see significant forward cross-correlations, $\rho_+ \gtrsim 0.8$, in more pulsars, as seen in Figure 2.8. Yet only two pulsars, PSR J0537−6910 and PSR J1341−6220 have ρ_+ significantly different from zero, at 95% confidence. Neither of these objects favor a power-law glitch size distribution, as the model predicts for $\alpha \gtrsim 5$. We therefore conclude provisionally that the endogenous-η meta-model is incompatible with existing pulsar observations, although more data are needed to be confident of course. This is an important result, because the endogenous-η meta-model codifies the traditional, popular understanding in the literature regarding how vortex pinning and unpinning occurs stochastically, as explained in Sections 2.1–2.3.

Model parameters such as α, the dimensionless control parameter that determines the speed at which stress accumulates, and K, the coupling constant between changes in stress and the observable change in frequency, may be partially informed by independent (i.e. non-glitch) observations of pulsars. As discussed in Section 3 of Melatos et al. [17], and Section 5 of Carlin and Melatos [57], we have

$$\alpha \approx \frac{X_{\mathrm{c}}}{\langle \Delta t \rangle \dot{\nu}}\,, \tag{2.14}$$

up to a factor of order unity, where $\langle \Delta t \rangle$ is the mean waiting time between glitches, and $\dot{\nu}$ is the long-term spin-down rate of the pulsar, after correcting for glitches and timing noise. The critical stress at which a glitch becomes certain, X_{c}, depends on the equation of state and is unknown in general [53, 72]. Nevertheless, the denominator in Equation (2.14) varies between pulsars by many orders of magnitude; see Table 2 of Melatos et al. [17], for example. The coupling constant K has even more uncertainties surrounding it, as described in Section 2.2.3. If a linear coupling between the crust and the stress is assumed at a glitch, we recover Equation (2.5), however non-linear couplings are also plausible, and may easily change the dependence of K on observables [34, 81, 94]. A preliminary exploration of how K impacts the endogenous-η meta-model is presented in Appendix 2.A1.

Direct comparisons of the meta-model predictions to long-term statistics derived from glitch catalogues are predicated on the assumption that all glitches are detected, i.e. that the datasets are complete. Espinoza et al. [40] and Espinoza et al. [95] claimed that this assumption is true for PSR J0534+2200 and PSR0835−4510 respectively. Monte Carlo injection studies have been published which seek to quantify completeness, but they are hampered by human intervention in traditional glitch finding algorithms [41, 43]. Autonomous glitch finding algorithms, such as those based on hidden Markov models [96] and nested sampling [33, 46, 97], will probe this question quantitatively for more pulsars, especially as more pulsars are regularly timed.

2.6. Conclusion

The long-term predictions from meta-models of stress-relax processes are avenues to falsify otherwise plausible microphysical mechanisms that the meta-model encompasses. The SDP meta-model [1] encompasses mechanisms wherein glitches are triggered probabilistically, and are more likely to occur when the system-wide stress is higher. The falsifiable predictions such as size and waiting-time cross-correlations [17], and autocorrelations [19], depend on the functional form of the conditional avalanche size PDF, $\eta[\Delta X^{(n)} | X(t_n^-)]$ [18]. Previously, this PDF was fixed exogenously to be a power law [1, 17, 77], motivated by Gross-Pitaevskii simulations of vortex avalanches [10], and the sizes of stress-release avalanches in other self-organized critical systems [32]. However, when $\eta[\Delta X^{(n)} | X(t_n^-)]$ is a power law, the SDP meta-model does not explain the quasiperiodic waiting times and unimodal size PDF seen in some pulsars [3]. This is ameliorated by adjusting "by hand" $\eta[\Delta X^{(n)} | X(t_n^-)]$ to a unimodal distribution, whereupon the SDP meta-model remains consistent with the data [18].

In this paper, we generalize the SDP meta-model so that $\eta[\Delta X^{(n)} | X(t_n^-)]$ is generated endogenously via the coherent stress mechanism [64, 67]. The coherent stress mechanism encapsulates the traditional understanding of how superfluid vortex pinning and unpinning proceeds stochastically in a neutron star. The memory of previous glitches is imprinted on the PDF of occupied pinning sites, $g(X_{\mathrm{th}}, t)$, which we emphasize does not equal the distribution of available sites $\phi(X_{\mathrm{th}})$ in general. Vortices pinned at sites with thresholds below the stress at a glitch unpin when a glitch is triggered, repinning at sites with thresholds above the stress after the glitch. The size of the glitch is proportional to the fraction of vortices unpinned in this manner.

The endogenous-η meta-model produces a broad phenomenology of observable waiting time and size PDFs, conditional on the choice of control parameters. In all circumstance, though, it produces high forward cross-correlations between glitch sizes and subsequent waiting times ($\rho_+ \gtrsim 0.8$), which are largely absent from observational data. It also predicts that either i) the system stagnates, for $X_{\mathrm{th,\,max}} \geq X_{\mathrm{c}}$, or ii) there is an excess of the largest waiting times and sizes, corresponding to events which completely reset the system by unpinning all vortices. Associated with these system-resetting events are aftershocks, which are larger and occur later than an average glitch, and precursors, which are smaller than an average glitch. There is no evidence for such large, system-resetting events in the size or waiting time PDFs of any glitching pulsar. We therefore conclude provisionally that the endogenous-η version of the SDP meta-model is falsified by existing data, although more data are needed to be sure.

The provisional falsification of the endogenous-η version of the SDP meta-model is important. The coherent stress process is not just any process; it embodies the traditional understanding of how vortex pinning and unpinning works throughout the literature [16]. Moreover it is intriguing that the version of the SDP meta-model in which $\eta[\Delta X^{(n)} | X(t_n^-)]$ is specified exogenously is not falsified by existing pulsar data. What are we to make of this situation? Is it a hint that some microphysics other than superfluid vortex avalanches is at work? Is the success (at escaping falsification) of the SDP meta-model with exogenous $\eta[\Delta X^{(n)} | X(t_n^-)]$ thanks simply to the flexibility it affords, when choosing $\eta[\Delta X^{(n)} | X(t_n^-)]$ selectively to suit every individual pulsar? It is too early to say. The endogenous-η meta-model is still an idealized, phenomenological representation of what happens inside a pulsar during a superfluid vortex avalanche. For example, recent N-body point-vortex simulations of collective, glitch-like vortex motion indicates that the stress is spatially correlated [62]. Spatial correlations are notoriously hard to treat theoretically, but it is known that they can alter the observable statistics of a far-from-equilibrium system comprehensively, e.g. in self-organized critical systems [31, 32]. Larger and more complete glitch catalogs generated by the latest generation of glitch monitoring campaigns at radio wavelengths are likely to play a central role in resolving some of the physical puzzles above [97, 98].

Acknowledgements

Parts of this research are supported by the Australian Research Council (ARC) Centre of Excellence for Gravitational Wave Discovery (OzGrav) (project number CE170100004)

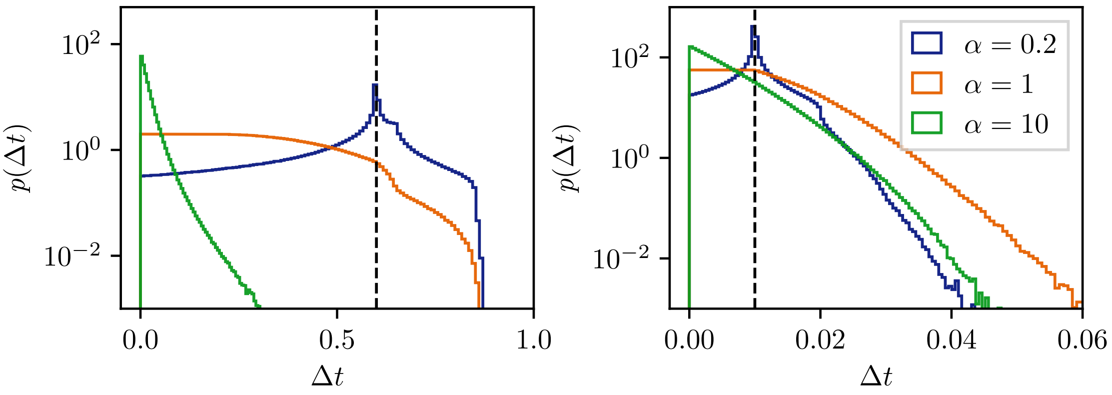

Figure 2.10: Waiting time PDFs for $K = 0.6$ (left panel) and $K = 0.01$ (right panel). Parameters: $N = 10^7$ simulated glitches for each value of α, with $X_{\mathrm{th,max}} = 0.95$. The black dashed vertical line indicates $\Delta t = K$ in each panel.

and ARC Discovery Project DP170103625. JBC is supported by an Australian Postgraduate Award.

2.A1. Non-maximal stress-crust coupling

The coupling factor K defined in equation (2.3) and appearing in equations (2.4) and (2.5) relates changes in the stress variable X to the angular velocity $2\pi\nu$ of the crust. The long-term observables in Section 4 are predicted assuming K takes its maximum value, $X_{\mathrm{th,max}}$. Somewhat counter-intuitively, the long-term statistics do change — modestly, but meaningfully — when non-maximal coupling is considered.

One always has $K \leq X_{\mathrm{th,max}}$ to ensure $X(t) \geq 0$. In Section 2.2.3, we specialize to $K = X_{\mathrm{th,max}}$ for the sake of definiteness. In this appendix we briefly check the case $K < X_{\mathrm{th,max}}$. Figure 2.10 shows the PDF of waiting times, $p(\Delta t)$, for two representative values of $K < X_{\mathrm{th,max}} = 0.95$. For $K = 0.6$, $p(\Delta t)$ looks broadly similar to the top panel of Figure 2.7 ($K = X_{\mathrm{th,max}}$), except for $\alpha = 0.2$, which no longer has a peak at $\Delta t = 1$. Long waiting times are suppressed as K sets the maximum event size in equation (2.4). Smaller K increases the minimum stress in the system, as less stress is released at the largest glitches (i.e. when $F = 1$). For $K = 0.01$ and $\alpha \gtrsim 1$, $p(\Delta t)$ is exponentially distributed. For $\alpha \lesssim 1$, $p(\Delta t)$ is peaked around $\Delta t = K$, but has an exponential tail. The size PDFs, $p(\Delta X)$, are broadly the same shape as in the bottom panel of Figure 2.7 ($K = X_{\mathrm{th,max}}$), but for $K < X_{\mathrm{th,max}}$ and $\alpha \lesssim 1$ they are more strongly peaked around $\Delta X = K$, and for $\alpha \gtrsim 1$ they are power-law distributed over many decades, with a small peak at $\Delta X = K$. In summary, if $K < X_{\mathrm{th,max}}$, in the high-α regime $p(\Delta t)$ is exponentially distributed and $p(\Delta X)$ is power-law distributed, while in the low-α regime $p(\Delta t)$ is unimodal around a peak at $\Delta t = K$ and $p(\Delta X)$ is sharply peaked at $\Delta X = K$.

The behavior of the cross-correlations and autocorrelations as a function of α does not change for $K < X_{\mathrm{th,max}}$ compared to $K = X_{\mathrm{th,max}}$, beyond shifting the features seen in Figure 2.8 to the right, e.g. for $K = 0.1$ the peak in ρ_+ occurs at $\alpha \approx 10$ instead of $\alpha \approx 0.5$. Reducing K has a similar impact as reducing $X_{\mathrm{th,max}}$ on the fraction of events that completely reset the system, as shown in Figure 2.6. At a fixed α, reducing K reduces the amount of stress released. Hence we reach $X \geq X_{\mathrm{th,max}}$ more often by the time the next glitch is triggered.

2.A2. Ensemble-averaged stress threshold distribution at occupied pinning sites

The PDF $g(X_{\mathrm{th}}, t)$ is a stochastically fluctuating function, dependent on the random sequence of waiting times drawn up to time t, as described in Section 2.2.4. A stationary analogue, $g_s(X_{\mathrm{th}})$, would allow for a priori prediction of long-term statistics that do not depend on the exact time-ordered nature of events, such as $p(\Delta t)$ and $p(\Delta X)$ [64, 67].

Following the notation in Daly and Porporato [99] and Fulgenzi et al. [1], $p(\Delta t)$ and $p(\Delta X)$ are related to the PDFs $p_e(Y)\mathrm{d}Y$ and $p_s(X)\mathrm{d}X$, the probabilities that the stress is in $(Y, Y + \mathrm{d}Y)$ just before a glitch and in $(X, X + \mathrm{d}X)$ just after a glitch respectively. With these definitions we obtain

$$p(\Delta t) = \int_0^{1-\Delta t} \mathrm{d}Y p_s(Y)\lambda(Y + \Delta t)\exp[-\Lambda(Y + \Delta t)\Lambda(Y)]\,, \tag{2.15}$$

and

$$p(\Delta X) = \int_{\Delta X}^{1} \mathrm{d}Y p_e(Y)\eta(\Delta X\,|\,Y)\,, \tag{2.16}$$

with $\Lambda(x) = \int_0^x \mathrm{d}x'\lambda(x')$, and $\Delta X = Y - X$. In the endogenous-η meta-model $\eta(\Delta X\,|\,Y)$, is a deterministic function of the occupied pinning site PDF, $g(X_{\mathrm{th}})$, as discussed in Section 2.2.3. The relationship becomes probabilistic again, as in the SDP meta-model, if we consider the statistically stationary PDF, $g_s(X_{\mathrm{th}}) = \langle g(X_{\mathrm{th}}, t)\rangle$, where the brackets indicate an ensemble average. The PDF $g_s(X_{\mathrm{th}})$ is related to $\eta(\Delta X\,|\,Y)$ via

$$\eta(\Delta X\,|\,Y) = K \int_0^{p_e(Y)} \mathrm{d}X_{\mathrm{th}}\, g_s(X_{\mathrm{th}})\,. \tag{2.17}$$

Solving equations (2.15)–(2.17) analytically for $g_s(X_{\mathrm{th}})$ is outside the scope of this paper. Instead, we show an estimate of $g_s(X_{\mathrm{th}})$ at three values of α in Figure 2.11, calculated by running the automaton outlined in Section 2.3.2 and sampling $g(X_{\mathrm{th}}, t)$ after every glitch. As expected, $g_s(X_{\mathrm{th}})$ is a strictly increasing function of X_{th}, i.e. sites with a higher threshold are occupied more often than those with a lower threshold. For $\alpha \lesssim 1$, $g_s(X_{\mathrm{th}})$ is well approximated by a power law with upper and lower cut-offs, i.e. $g_s(X_{\mathrm{th}}) \propto X_{\mathrm{th}}^{\gamma} H(X_{\mathrm{th}})H(X_{\mathrm{th,max}} - X_{\mathrm{th}})$, with $0 < \gamma \lesssim 3$, and γ growing with α.

2.A3. Relation to point processes and time series modeling

The endogenous-η meta-model in this paper and its exogenous-η alternatives, such as the SDP [1] and BSA [57] meta-models, are examples of stochastic time series with

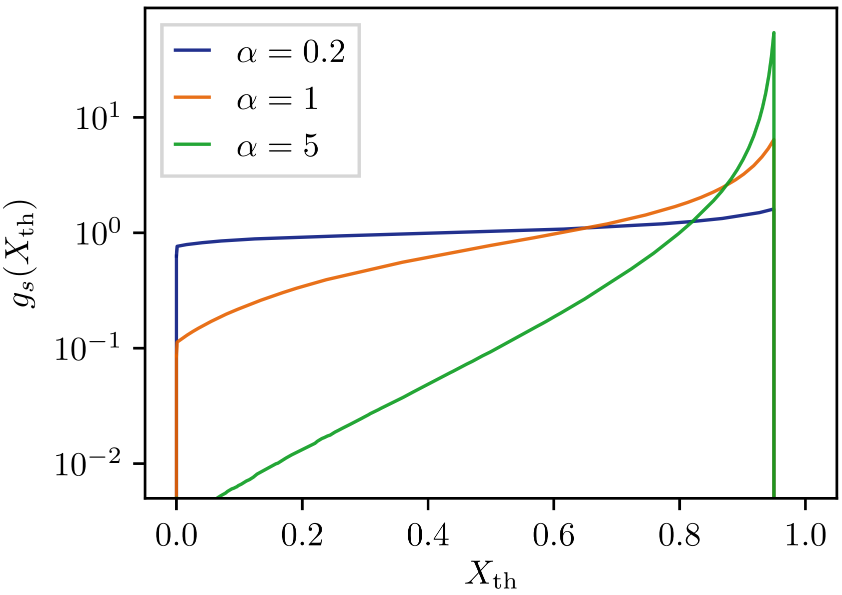

Figure 2.11: Ensemble averaged PDF of occupied pinning sites $g_s(X_{\rm th}) = \langle g(X_{\rm th}, t)\rangle$ calculated empirically for three values of α. Parameters: 10^7 samples of $g(X_{\rm th})$ for each value of α, $X_{\rm th,\,max} = 0.95$, with $K = X_{\rm th,\,max}$.

jumps. We observe the jumps as a point process. In this appendix, we situate the endogenous-η meta-model within canonical classification schemes for such processes. The classification schemes are not unique.

The SDP meta-model is an example of a doubly stochastic, marked point process [1, 100, 101]. It is a one-dimensional point process because it is a sequence of instantaneous events ordered in time. Marked refers to additional information (i.e. the event size) that is associated with the epoch of each event. It is doubly stochastic as both the event sizes and the waiting times between events are random processes. The endogenous-η meta-model is not doubly stochastic, as the event sizes are deterministic, after the waiting time is chosen (given a certain history of past avalanches), as described in Section 2.2. For both the SDP and endogenous-η meta-models, the state of the system jumps discontinuously at each event making them examples of a jump process. The SDP meta-model is Markovian, the current state only depends on the immediately previous state. However the endogenous-η meta-model is not, as the threshold distribution of occupied pinning sites contains a long-lasting memory of states before the one immediately previous.

The analysis of point processes from a statistical perspective is often presented alongside time series modeling [102, 103]. Autoregressive models, such as the autoregressive integrated moving average (ARIMA) model, can be used to model a wide variety of astronomical time series data [104]. Adopting the formalism of autoregressive models unlocks a large, well-tested literature for common tasks such as maximum likelihood parameter estimation, model comparison, and model validation [103]. Recent advances in filters for hidden semi-Markov models are another intriguing avenue, as these models are explicitly designed to track a process that jumps between states at irregularly spaced intervals [105].

In this paper and others investigating glitch meta-models, we elect not to analyze the problem in terms of autoregressive models for three reasons. i) Glitch sample sizes are small ($N \lesssim 50$), so there is no practical imperative to exploit the computational efficiency offered by autoregressive models. ii) We are motivated by the astrophysical goal of exploring the long-term statistical behavior of an automaton which formalizes directly the popular intuitive picture of glitches as a stick-slip, stress-relax phenomenon. It is possible in principle to formulate the stress-relax dynamics less directly in the language of an autoregressive model, and we leave that for future work. iii) Some work has been done on parameter estimation by Markov chain Monte Carlo methods for the SDP meta-model [77]. Extending this work to other meta-models or larger data sets may benefit from the computational efficiency of autoregressive modeling, but is outside the scope of this work.

Chapter 3

A statistical search for a uniform trigger threshold in solar flares from individual active regions

3.1. Introduction

Broad consensus exists that the micro-physical process triggering individual solar flares is magnetic reconnection in the corona. A reconnection event becomes more likely to occur, the more magnetic energy accumulates in the time between flares [106, 107]. This phenomenological class of stress-relax model, was popularized by Rosner and Vaiana [108], and expounded by Wheatland and Glukhov [109], Wheatland [110, 111], Kanazir and Wheatland [112], and Hudson [113], among others. A complementary phenomenological description is the avalanche or self-organized criticality model [114–116], inspired by the canonical sandpiles of Bak et al. [117, 118]. These two classes of model are broadly compatible, but make different predictions about some long-term statistical observables [110, 119–123].

Upon aggregating historical datasets, the probability density function (PDF) of the energy released in solar flares is found to be a power law or log-normal over multiple decades [108, 114, 124]. The PDF of time intervals between successive flares in the same active region, henceforth termed waiting times, is less clear-cut. Wheatland [125] found evidence that the power-law-like shape of the tail of the waiting time PDF found by Boffetta et al. [120] is explained by a sum of exponentials, with individual rates themselves drawn from an exponential PDF. This interpretation is further developed by Aschwanden et al. [126]. Non-stationary flaring rates are also noted by Lepreti et al. [127] and Gorobets and Messerotti [128]. Cross-correlations between the size of a flare and the subsequent (preceding) waiting time, henceforth termed forward (backward) cross-correlations, are a key differentiator between the stress-relax and avalanche descriptions — the latter predicts no size–waiting-time cross-correlations [32]. Forward and backward correlations are broadly absent from solar flares datasets [110, 129–131], with the exception of strong forward cross-correlations found in two active regions [113].

Rotational glitches in rotation-powered pulsars [16, 132] are an analogous astrophysical phenomenon to solar flares, in the limited sense that they are consistent with a stress-relax process even though they do not involve magnetic reconnection as far as one knows [31]. While the exact process that triggers a glitch is unknown, most models are encompassed by the fundamental idea that "stress" (possibly differential rotation or elastic deformation) builds up secularly between glitches, and is released sporadically and partially at a glitch. The instantaneous glitch rate is assumed to grow with the stress in the system. This idea is formalized phenomenologically in the state-dependent Poisson (SDP) process popularized by Fulgenzi et al. [1]. Precise, falsifiable predictions about size and waiting time PDFs, auto-, and cross-correlations, as well as comparisons to current datasets, show the power and flexibility of the SDP model in the neutron star context [17–19, 77]. The same falsifiable predictions also deliver new physical insights when applied to solar flare data, as we show in this paper.

Our goal in this paper is to search the *Geostationary Operational Environmental Satellite* (*GOES*) soft X-ray flare database for signatures of a threshold-driven stress-relax process. We do this by de-aggregating the data from different active regions, and studying summary statistics of flare waiting times and sizes. In Section 3.2 we outline the SDP framework, and how it maps to solar flares. In Section 3.3 we explore various regimes of the SDP process. We also specify precise, falsifiable tests for the question of whether solar flares are triggered once the energy reaches a static threshold, if it obeys a stress-relax process. The *GOES* soft X-ray dataset to which we apply these tests is described in Section 3.4. In Section 3.5 we look for associations between matching waiting time and size PDFs and high size–waiting-time cross-correlations, as predicted for the SDP process. We conclude with a discussion of the microphysical implications of the data analysis in Section 3.6.

3.2. State-dependent Poisson process

3.2. *Equation of motion*

The SDP process is a doubly stochastic renewal process which models the "stress" in the system as a function of time, $X(t)$, as

$$X(t) = X(0) + t - \sum_{i=0}^{N(t)} \Delta X_i\,, \tag{3.1}$$

where X and t are expressed respectively in dimensionless units of X_c (the critical stress in the system at which a stress-release event becomes certain), and τ (the time taken for the system to accumulate the critical stress X_c, in the absence of any stress-release events). We attach a physical interpretation to $X(t)$ in the solar flare context in Section 3.2.3 and Appendix 3.A1. The amount of stress released at the i-th event, ΔX_i, is a random variable, drawn from a user-specified PDF, $\eta\left[\Delta X_i \,|\, X(t_i^-)\right]$, where $X(t_i^-)$ is the stress in the system immediately prior to the i-th event. In the standard configuration, $\eta\left[\Delta X_i \,|\, X(t_i^-)\right]$ is fixed as a power law, but other options exist [18, 133]. Conditioning η on $X(t_i^-)$ is necessary to ensure that the stress remains positive-definite and is plausible physically. The second random variable in Equation (3.1) is $N(t)$, a Poisson counting function of the number of events up to time t. It is determined iteratively via the waiting time between each event.

We assume the instantaneous event rate is a monotonically increasing function of the stress in the system, viz.

$$\lambda[X(t)] = \frac{\alpha}{1 - X(t)}, \tag{3.2}$$

where $\alpha = \lambda_0 \tau$ is a dimensionless control parameter, and $\lambda_0 = \lambda(X = 1/2)/2$ is a reference rate. The long-term statistical output of the SDP process does not depend strongly on the functional form of $\lambda[X(t)]$, so long as it diverges in the limit $X \to 1$ as in Equation (3.2) [1, 18]. As the stress increases deterministically between events, the PDF of waiting times Δt following the i-th event is that of a variable-rate Poisson process [1, 83]

$$p[\Delta t \,|\, X(t_i^+)] = \lambda[X(t_i^+) + \Delta t] \exp\left\{ - \int_{t_i^+}^{t_i^+ + \Delta t} \mathrm{d}t' \lambda\left[X(t')\right] \right\}, \tag{3.3}$$

where $X(t_i^+)$ is the stress immediately following the event at time t_i.

3.2. *Monte Carlo automaton*

Analytically solving the coupled equations (3.1)–(3.3) to calculate the PDFs of event waiting times or sizes is usually not feasible, except for particular choices of $\eta\left[\Delta X_i \,|\, X(t_i^-)\right]$; see section 6 of Fulgenzi et al. [1] for an example. Instead, it is simple to run the following automaton to generate numerical solutions:

1. Pick Δt from Equation (3.3), given the current stress X.
2. Update the stress to $X + \Delta t$ to account for the deterministic evolution.
3. Pick ΔX from $\eta\left[\Delta X \,|\, X + \Delta t\right]$, and subtract it from the stress.
4. Repeat from step 1.

Given α and $\eta\left[\Delta X_i \,|\, X(t_i^-)\right]$ the automaton generates a time-ordered sequence of waiting times and sizes. From the sequence we can calculate the long-term PDFs for waiting times and sizes [1, 18], as well as the cross-correlation [17, 18], autocorrelations [19], and other observables.

3.2. *Mapping to solar flares*

We identify the stress that accumulates between flares and relaxes at a flare with the spatially-averaged magnetic energy density in a given active region. One could equally choose a different physical quantity, such as the magnetic shear, depending on the particular microphysics of the flare trigger. We assume that active regions have independent stress reservoirs, i.e. the coronal magnetic fields of different active regions do not interact strongly, and all flares from the same active region extract energy from one reservoir. An idealized toy model relating the foregoing definition of stress to magnetic energy

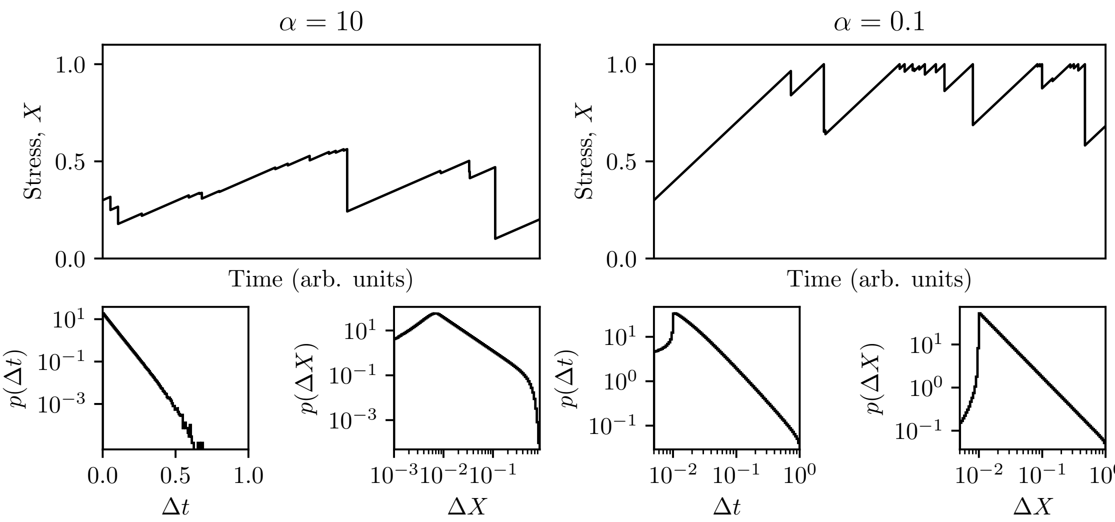

Figure 3.1: Top panels: qualitative behavior of the evolution of the stress, $X(t)$, in the SDP process in the two main regimes, slowly driven (left panel, $\alpha = 10$), and rapidly driven (right panel, $\alpha = 0.1$). Bottom panels: predicted waiting time and size PDFs $p(\Delta t)$ and $p(\Delta X)$ respectively in the above regimes. For all panels we fix $\eta\left[\Delta X_i \,|\, X(t_i^-)\right] \propto (\Delta X_i)^{-3/2} H\left[\Delta X_i - 10^{-2} X(t_i^-)\right]$, where the Heaviside function $H(...)$ enforces a minimum stress-release size of 1% of the stress in the system, ensuring integrability. The histograms in the bottom panels each include $N = 10^7$ events.

input from the photosphere is outlined in Appendix 3.A1, as a simplified but concrete illustration of the physical picture under consideration.

Two major simplifying assumptions are that the rate at which energy is fed into the reservoir, τ^{-1}, is constant in time, and so is the critical, spatially-averaged magnetic energy density, X_c, for a given active region. These assumptions are motivated in Appendix 3.A1, but a key goal of the paper is to test their veracity. We also assume that flares reduce $X(t)$ instantaneously. This assumption is defensible as the typical time between flares (typically hours) is much larger than the typical duration of flaring events (typically minutes) [134]. In what follows we do not prescribe a particular functional form for $\eta\left[\Delta X_i \,|\, X(t_i^-)\right]$, to keep the SDP process as flexible as possible.

The SDP process generates sequences of dimensionless waiting times, $\left\{\Delta t_i^{\rm SDP}\right\}$ and sizes, $\left\{\Delta X_i^{\rm SDP}\right\}$. It is natural to ask how they correspond to directly observable sequences of waiting times, $\left\{\Delta t_i^{\rm obs}\right\}$ and sizes, $\{\Delta s_i\}$. The waiting times satisfy

$$\Delta t_i^{\rm obs} = \Delta t_i^{\rm SDP} \tau \,, \tag{3.4}$$

where τ is unknown a priori but can be estimated, as discussed in Appendix 3.A2. The sizes are related in a more complicated way, because some energy is released through channels that are not directly observed. We make the simplifying assumption that the peak soft X-ray flux multiplied by the duration of the flare (henceforth Δs_i for the i-th flare in a given active region) is proportional to the stress released from the reservoir. This implies

$$\Delta s_i \propto \Delta X_i^{\rm SDP} X_c \,. \tag{3.5}$$

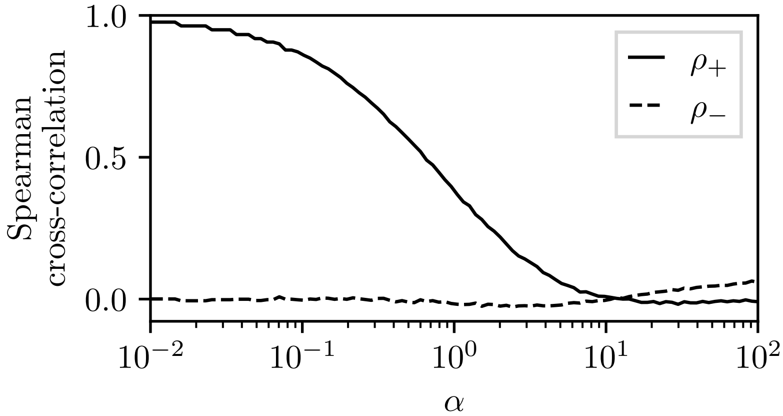

Figure 3.2: Forward, ρ_+ (solid curve), and backward, ρ_- (dashed curve), cross-correlations between event sizes and waiting times for 10^2 values of $10^{-2} \leq \alpha \leq 10^2$, with $N = 10^5$ events generated per value of α. We fix $\eta\left[\Delta X_i \,|\, X(t_i^-)\right]$ to the same functional form as in Figure 3.1. A version of this figure first appeared as figure 13 in Fulgenzi et al. [1].

The unknown constant of proportionality in Equation (3.5) hampers direct parameter estimation of X_c from an observed size PDF.

Full parameter estimation for the SDP process given a set of observed waiting times and sizes is discussed in Melatos and Drummond [77]. It lies outside the scope of this paper. In Appendix 3.A2 we also describe for completeness an alternative parameter estimation procedure using a hierarchical Bayesian scheme. The advantage of the hierarchical scheme is that it clarifies as a matter of principle the information content and flow in the estimation problem, i.e. the parameter combinations that can be estimated uniquely, and the data components that inform each parameter estimate. The disadvantage is that it can be implemented in practice only if $\eta\left[\Delta X_i \,|\, X(t_i^-)\right]$ is drawn from a certain class of mathematical functions. The favored class produces waiting time and size PDFs which do not match solar flare observations (see Section 3.5), so the hierarchical scheme is not applied to real data in this paper. Nonetheless, it is included for the benefit of the reader, who may wish to develop it further for solar flare analysis in the future.

3.3. Observable signatures of a rapidly-driven process

Broadly speaking, an SDP process operates in one of two regimes: slowly-driven, with $\alpha \gg 1$, and rapidly-driven, with $\alpha \ll 1$. In this section we identify the key dynamics in both regimes, in Sections 3.3.1 and 3.3.2 respectively. We then infer, in Section 3.3.3, a set of observable signatures, which if absent rule out the operation of a rapidly-driven process of the form described in Section 3.3.2.

3.3. Slow driver

When the system is slowly driven, we have $X(t) \ll 1$, as events are usually triggered before the stress accumulates to near the threshold. When $\eta\left[\Delta X_i \,|\, X(t_i^-)\right]$ is a power law, the predicted waiting time PDF $p(\Delta t)$ is an exponential, and the predicted size PDF $p(\Delta X)$ is a power law over multiple decades. We show the qualitative behavior of the stress in the slowly driven regime in the top-left panel of Figure 3.1, where for the sequence of 20 stress-release events shown we have $0.1 < X(t) < 0.6$. In the bottom-left panels of the same figure we show the predicted waiting time and size PDFs. The size PDF $p(\Delta X)$ has a turn-over in logarithmic slope at $\Delta X \approx 10^{-2}$ due to the particular choice of $\eta\left[\Delta X_i \,|\, X(t_i^-)\right]$ (see caption for the functional form).

Depending on the choice of $\eta\left[\Delta X_i \,|\, X(t_i^-)\right]$, there may be detectable backward cross-correlations (i.e. a correlation between the size of an event and the waiting time since the preceding event). This is because the size of an event cannot exceed the amount of stress in the system, so longer periods of stress-accumulation allow for the possibility of larger events. This backward cross-correlation is especially pronounced with the choice $\eta\left[\Delta X_i \,|\, X(t_i^-)\right] \propto \delta\left[\Delta X - X(t_i^-)\right]$, where $\delta(\dots)$ is the Dirac-delta function. This choice forces the stress reservoir to empty at each event, and collapses the SDP process to other stochastic processes in the literature, e.g. forest fire models [135]. In the solar flare context, a backward cross-correlation is a long-standing prediction of the Rosner and Vaiana [108] stress build-up model; and the "reset" model of Hudson [113] and Hudson et al. [130]. If instead $\eta\left[\Delta X_i \,|\, X(t_i^-)\right]$ prefers small stress-release events, e.g. if it is a power law [1], the backward cross-correlation is small.

3.3. Fast driver

When the system is rapidly driven, we have $X(t_i^-) \lesssim 1$, i.e. the stress is driven close to the threshold before each event. As the dynamics of the system are strongly influenced by the presence of the threshold, we sometimes call this regime "threshold-driven". A prediction of the SDP process in this regime is that the size and waiting time PDFs should "match", i.e. they should be the same distribution, up to a linear scaling [1]. For example, if $\eta\left[\Delta X_i \,|\, X(t_i^-)\right]$ is a power law, both the waiting time and size PDFs are power laws. We show this in the bottom-right panels of Figure 3.1. We also show the qualitative behavior of the stress versus time in this regime in the top-right panel of the same figure, where we see $X(t) \to 1$ (i.e. unit critical stress) before every stress-release event.

A strong forward cross-correlation (i.e. a correlation between the size of an event and the waiting time to the next event) is observed in this regime. This is because a large stress-release event results in a longer delay before the system accumulates enough stress to approach the threshold. In the solar flares context, this cross-correlation is predicted by the "saturation" model of Hudson et al. [130] and Hudson [113]. The smooth transition between the fast-driven regime ($\alpha \ll 1$), with high forward cross-correlations, and the slow-driven regime ($\alpha \gg 1$), is shown in Figure 3.2.

3.3. *Heuristic test for a threshold-driven process*

Ideally, we fit the parameters of the SDP process (τ, X_c, λ_0, and $\eta\left[\Delta X_i \,|\, X(t_i^-)\right]$) to a paired sequence of solar flare sizes and waiting times, and infer what regime applies. In practice, however, at least some of these parameters vary between active regions, which limits us to sequences of length $N \lesssim 50$ (typical active regions have at most dozens of events; see Section 3.4), which are insufficient to infer four or more parameters. Instead, we combine the results in Sections 3.3.1 and 3.3.2 to deduce qualitative features, which must be present in multiple observables simultaneously (e.g. PDFs, cross-correlations), if the SDP process operates in a particular α regime or indeed operates at all. Specifically, we summarize the behavior in Sections 3.3.1 and 3.3.2 into the following observationally testable prediction. If solar flares are well-modeled with a rapidly-driven process (e.g. the SDP process with $\alpha \ll 1$), then we should see large forward cross-correlations, accompanied by waiting time and size PDFs with the same shape in individual active regions. This coincident signature should become more prominent as α (or a proxy thereof) decreases. We quantify this prediction in Section 3.5.2.

With the test above we also ameliorate the impact of a potentially mis-specified model. Although it is agnostic about the microphysics, the SDP process is not the only possible prescription of stress accumulation and release. If some of the assumptions outlined in Section 3.2.3 do not hold, a different underlying model may underpin solar flares. For example, one may build a model in which stress accumulates according to a Brownian random walk with some underlying drift, until a threshold is breached, at which point a stress-release event is triggered [57]. In the Brownian stress accumulation model, $X(t)$ is always driven to the threshold before each event. If drift occurs faster than diffusion, we predict the same coincident signature as for the SDP process: large forward cross-correlations are accompanied by matching waiting time and size PDFs.

3.4. *GOES* soft X-ray observations

The X-ray Sensor (XRS) on the *Geostationary Operational Environmental Satellites* (*GOES*) has continuously monitored the Sun in soft X-rays (0.5 to 8 Å) since 1975. In Section 3.4.1 we introduce the flare summary data analyzed in this paper. In Section 3.4.2 we remind the reader of the obscuration effect described in Wheatland [136], and explain how it affects our analysis. In Section 3.4.3 we analyze aggregated waiting time and size PDFs across all active regions.

3.4. *Flare data*

We use the publicly available flare summary data hosted by the National Geophysical Data Center (NGDC)[1] for flares before June 29 2015, and by the Space Weather Prediction Center (SWPC)[2] for flares after June 28 2015. We combine these two data sources into a homogeneous, cleaned database (henceforth "catalog"), with some anomalies corrected as described in Appendix 3.A3. These data are collated with the flare start epochs, t^s,

[1] ftp://ftp.ngdc.noaa.gov/STP/space-weather/solar-data/solar-features/solar-flares/x-rays/GOES/xrs/

[2] ftp://ftp.swpc.noaa.gov/pub/indices/events/

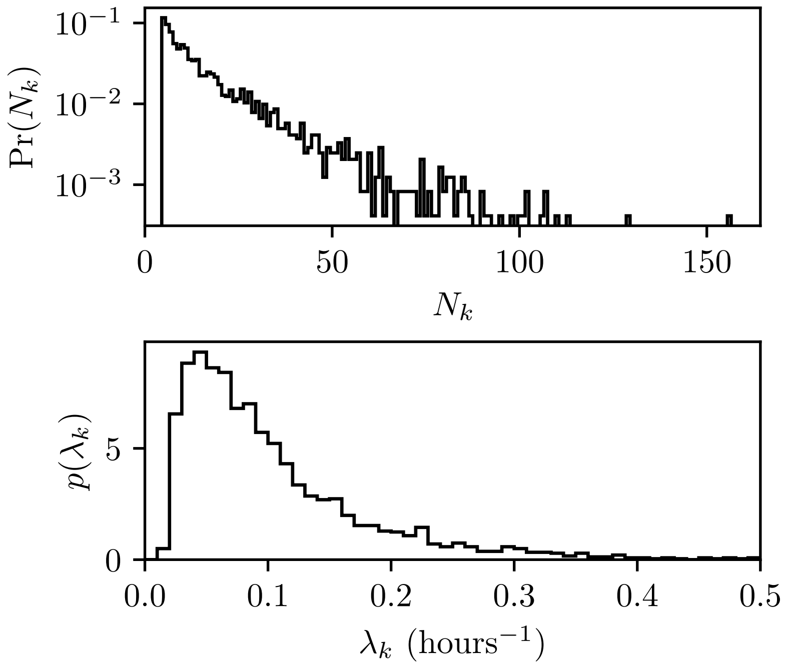

Figure 3.3: Top panel: Probability mass function of the number of flares per active region, N_k, for all active regions with $N_k \geq 5$. Regions with $0 \leq N_k \leq 4$ are excluded, as the number of samples per region is too small for the statistical tests in this paper. Bottom panel: PDF of the flare rate, λ_k, for all active regions with $N_k \geq 5$, binned into 50 uniformly spaced bins between 0 hours^{-1} and 0.5 hours^{-1}.

peak epochs, t^{p}, and end epochs, t^{e}. The peak flux (irradiance) of each flare, f^{p}, is calculated with reference to the recorded flare class, in units of W m^{-2}. The longitude and latitude of the flare are also often available, if the flare is associated with an active region. For clarity, we henceforth denote as $x_{i,k}$ an arbitrary measurement of the variable x in the i-th flare from the k-th active region.

We define the waiting time between two flare epochs as $\Delta t_{i,k} = t^{\mathrm{s}}_{i+1,k} - t^{\mathrm{s}}_{i,k}$. One could equally use the flare peak or end epochs to define the waiting time. We define the flare size as $\Delta s_{i,k} = f^{\mathrm{p}}_{i,k}\left(t^{\mathrm{e}}_{i,k} - t^{\mathrm{s}}_{i,k}\right)$; that is, we multiply the irradiance by the duration of the flare to obtain a flare size with dimensions of energy per unit area. The duration of an active region is $\Delta T_k = t^{\mathrm{e}}_{N_k,k} - t^{\mathrm{s}}_{1,k}$, where there are N_k flares in the region. The average flare rate in an active region is $\lambda_k = N_k/\Delta T_k$. The average λ_k overestimates systematically the true flare rate, as the duration ΔT_k is between two flare epochs, both of which are counted in N_k. An unbiased estimate would take ΔT_k as the difference between the epochs when the active region appears and disappears, but neither epoch is recorded in the *GOES* flare summary data[3]. A concern we touch on further in Section 3.4.3 is that $\lambda_k = N_k/\Delta T_k$ assumes that the flare catalog is complete, i.e. all flares from a given region are detected and correctly attributed to that region.

As of September 1 2022, there are 83283 flares in the catalog, 49328 of which are associated with an active region. There are 2429 active regions with $N_k \geq 5$, accounting

[3]The epochs when the active region appears and disappears may be extracted from other records in some instances. Such an analysis lies outside the scope of this paper.

for 42982 flares. The median number of flares in an active region (when considering only regions with $N_k \geq 5$) is 12, but the average is 17.7, as the distribution is peaked at $N_k = 5$ and monotonically decreases with N_k. We show the probability mass function of the number of flares in an active region, $\Pr(N_k)$, in the top panel of Figure 3.3 for regions with $N_k \geq 5$. The PDF of observed flare rates, $p(\lambda_k)$, across all active regions with $N_k \geq 5$, is displayed in the bottom panel of the same figure. The distribution of λ_k is well-described by a log-normal, with mean $0.08\,\text{hours}^{-1}$, and standard deviation $0.7\,\text{hours}^{-1}$. Henceforth, we typically only include regions with $N_k \geq 5$ in our analysis unless stated otherwise, as many of the subsequent statistical tests, such as the cross-correlation(s), have low statistical power with smaller sample sizes.

3.4. *Obscuration of subsequent flares after a large flare*

As described in section 2.2 of Wheatland [136], the *GOES* flare detection algorithm involves a selection effect that obscures the detection of flares following a large flare, due to the enhanced background soft X-ray flux. To detect a flare, the flux must monotonically increase for four consecutive minutes, with the last value 1.4 times the value three minutes earlier. Hence a flare must produce a 40% increase above the background flux. However, while flares typically rise rapidly to peak flux, the soft X-ray emission is observed to decay on the timescales of hours [107]. Thus, even large flares may be obscured by the enhanced background flux following, say, an X1 ($f^{\text{p}} = 10^{-4}\,\text{W}\,\text{m}^{-2}$) class flare.

A comprehensive re-analysis of the soft X-ray flux time-series may reveal flares that were not detected with the original flare detection algorithm. Such a re-analysis lies outside the scope of this paper. Acknowledging that the *GOES* catalog is incomplete, we mitigate the impact on our analysis by creating a secondary masked catalog that only includes flares with $f^{\text{p}} \geq 10^{-6}\,\text{W}\,\text{m}^{-2}$ (i.e. class C1 and higher), where we know the fraction of missed flares is smaller. This masked catalog is used in Sections 3.4.3 and 3.5.1 when we perform comparative studies and parametric fits for the waiting time and size PDFs.

3.4. *Aggregate size and waiting time statistics*

When we aggregate flare waiting times and sizes across all active regions with $N_k \geq 5$, we obtain the PDFs shown in the top and bottom panels of Figure 3.4 respectively. The data are shown as the black histograms. The grey region in the bottom panel shows the flare sizes that are not included in the masked catalog, as described in Section 3.4.2. The difference between the masked and full catalog is not visible in the top panel as the effect on $p(\Delta t)$ is minimal.

Three empirical trial distributions with common analytic forms are overlaid on each PDF for the masked catalog. The overlaid distributions have parameters fixed to their maximum likelihood values, given the data. By eye, it is clear that the log-normal distribution best describes both the aggregated waiting time PDF, $p(\Delta t)$, and the aggregated size PDF, $p(\Delta s)$. We formalize this comparison using the corrected Akaike Information Criterion (AICc) [36, 137]. The AICc calculates the model, among a set of possible models, which minimizes the information loss, while accounting for potential bias due to the number of model parameters and the sample size. When calculated for $p(\Delta t)$, the

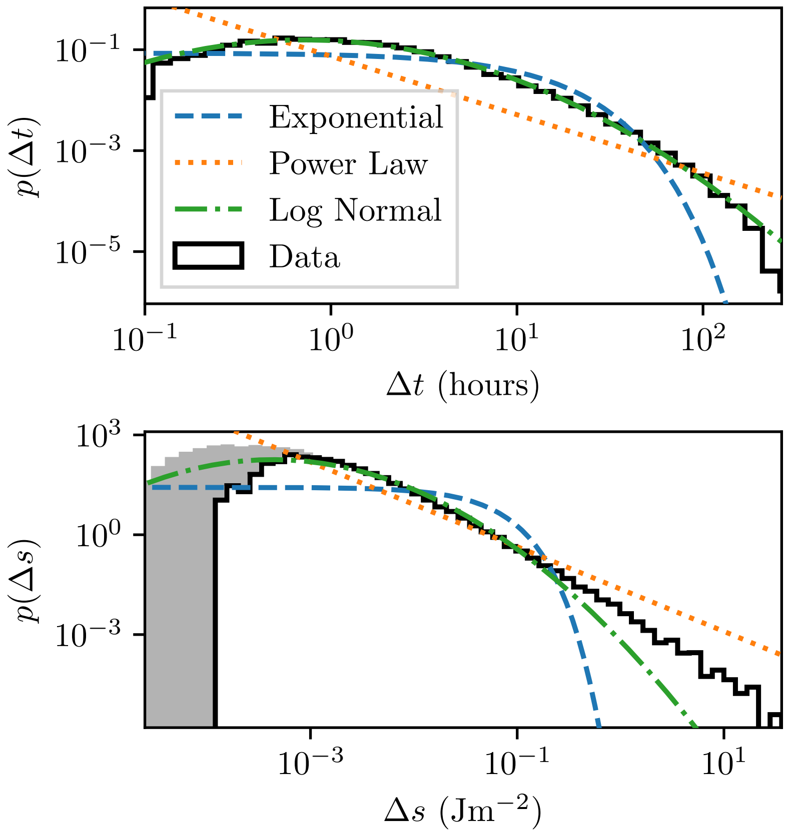

Figure 3.4: Top panel: PDF $p(\Delta t)$ of waiting times (thick black stepped curve), Δt, aggregated over all active regions with $N_k \geq 5$, binned into 50 logarithmically spaced bins between the minimum and maximum Δt in the full, unmasked catalog. Overlaid are the best fit estimates of an exponential (blue dashed curve), power law (orange dotted curve), and log-normal (green dot-dashed curve) PDF. Bottom panel: As for top panel, but for sizes Δs. The grey region in the bottom panel shows the difference between the size PDFs from the masked and full catalogs (see Section 3.4.2).

relative probability for a log-normal describing the data over an exponential or a power law is $e^{4\times10^3}$ and $e^{3\times10^4}$ respectively. When calculated for $p(\Delta s)$, the relative probability for a log-normal describing the data over an exponential or a power law is $e^{4\times10^4}$ and $e^{1\times10^4}$ respectively. The preference the data show for a log-normal over a power law is also noted in Verbeeck et al. [124]. The preference arises because of the small number of flares in the masked catalog with $10^{-4} < \Delta s/\mathrm{J\,m^{-2}} \lesssim 10^{-3}$. If we fit the full, unmasked catalog (i.e. include the flares shaded in grey in the bottom panel of Figure 3.4) we find that $p(\Delta s)$ is again fitted best with a log-normal. If instead we only include flares with $\Delta s \geq 10^{-3}\,\mathrm{J\,m^{-2}}$ we find that $p(\Delta s)$ is fitted best with a power law.

If we assume that the same α and $\eta\left[\Delta X_i|X(t_i^-)\right]$ apply to all regions, Figure 3.4 is consistent with the SDP framework for $\alpha \lesssim 10$ and if $\eta\left[\Delta X_i|X(t_i^-)\right]$ is a log-normal. However, as we discuss in Section 3.2.3, there is good reason to believe that α (and perhaps even $\eta\left[\Delta X_i|X(t_i^-)\right]$) may vary region-to-region.

3.5. Disaggregated data in individual active regions

The goal of this section is to search for signatures of a threshold-driven SDP process in individual active regions, rather than considering all flares in aggregate. In Section 3.5.1 we consider only waiting time and size PDFs, without regard to their potential cross-correlation. In Section 3.5.2 we calculate these cross-correlations, and in Section 3.5.3 we apply the test outlined in Section 3.3.3 by searching for an association between matching waiting time and size PDFs and the cross-correlation, in individual active regions. In Section 3.5.4 we perform a preliminary investigation of the longer-term memory in the system by calculating the autocorrelation between subsequent waiting times and subsequent sizes. The analysis in Section 3.5.1 involves parametric fitting of the size PDFs, so we use the masked catalog described in Section 3.4.2. However in Sections 3.5.2–3.5.4 we use the full, unmasked catalog, as the tests performed in these sections are non-parametric.

3.5. Waiting time and size PDFs versus flare rate

For regions with $N_k \geq 5$ we disaggregate the data, and ask what PDF shape best characterizes each region's waiting time and size PDFs, rather than considering only the aggregated dataset as in Section 3.4.3. Using the AICc, we find that for waiting time PDFs, 60% of regions are fitted best with an exponential distribution, 23% with a log-normal, and the remainder with a power law. For size PDFs, 41% of regions are fitted best with a power law distribution, 34% with an exponential, and the remainder with a log-normal. This is broadly consistent with the aggregate results above, i.e. that the aggregated $p(\Delta t)$ is fitted best with a log-normal, while the aggregated $p(\Delta s)$ is fitted best with either a log-normal or a power law, depending on how you attempt to mitigate the selection effect described in Section 3.4.2. However individual regions can occasionally be better represented with power law or exponential distributions, especially in regions with lower N_k.

One may reasonably ask whether there are clear trends, or predictors, for the waiting time and size PDFs in any given region. An exhaustive search for predictors, e.g. with a multiple regression analysis, lies outside the scope of this paper, but one sensible first step is to see if the shape that fits best evolves with λ_k. This test is performed for the waiting time and size PDFs in the top and bottom panels of Figure 3.5 respectively. This figure is constructed by binning all active regions with $N_k \geq 5$ into 20 uniformly spaced bins between $\lambda_k = 0.025\,\mathrm{hours}^{-1}$ and $\lambda_k = 0.3\,\mathrm{hours}^{-1}$, then calculating which distribution fits best the waiting times and sizes using the AICc. For the waiting time PDFs, the proportion of regions fitted best with a power law stays roughly constant as λ_k increases, at around 15%, while the proportion of regions fitted best with a log-normal grows with λ_k, at the expense of the exponential. For the size PDFs we see a similar trend, with the proportion of regions fitted best with a power law staying roughly constant as λ_k increases, this time at around 40%, while the proportion of regions fitted best with a log-normal grows with λ_k, at the expense of the exponential. In both panels we plot the cumulative distribution function (CDF) of λ_k to remind the reader that each λ_k bin does not contain the same number of regions; 80% of regions with $N_k \geq 5$ have $0.033 < \lambda_k < 0.21$.

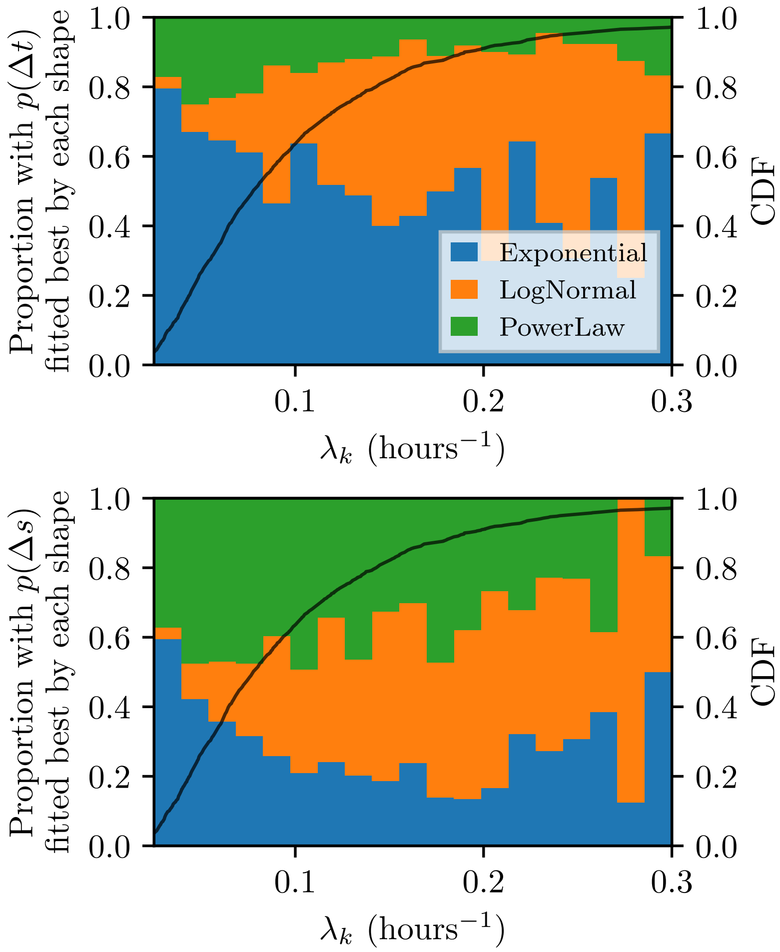

Figure 3.5: Top panel: Proportion of active regions with waiting time PDF fitted best by three possible shapes (a power law, an exponential, and a log-normal) as determined by the AICc, as a function of the region's flare rate, λ_k. The CDF of λ_k is overlaid in black. Bottom panel: As in the top panel, but for size PDFs.

Can the evolution of the proportion of each shape versus λ_k be explained with the SDP model? Under the assumption that λ_k is a tracer of the driving rate, i.e. $\lambda_k \propto \alpha^{-1}$, we expect to see a greater proportion of exponentially distributed waiting times at low λ_k (high α). This is the regime in which the stress does not approach the threshold at $X = X_c$ before each event, so waiting times are un-correlated with sizes and are (broadly) Poissonian, i.e. the waiting times are exponentially distributed. This expectation broadly conforms with what we see in the top panel of Figure 3.5.

The evolution versus λ_k in the bottom panel of Figure 3.5 is harder to explain with the SDP model, if each region has the same $\eta\left[\Delta X_i \,|\, X(t_i^-)\right]$. We expect $p(\Delta s) \propto \eta$, when α is low, but we see an almost even split between the three possible shapes at the highest values of λ_k. This implies at least one of the following: i) η truly varies from one region to the next, which implies different stress-release mechanisms are at play in different regions; or ii) $\lambda_k \gtrsim 0.2\,\text{hours}^{-1}$ does not correspond to $\alpha \ll 1$, and hence $p(\Delta s) \propto \eta$; or iii) the small sample size of events in each region results in the AICc not favoring the "true" size distribution; or iv) the obscuration effect described in Section 3.4.2 is stronger with higher λ_k, due to the enhanced background flux in regions that have many flares in a short period of time. To test iii), we generate Figure 3.5 again for regions with $N_k \geq 10$, instead of $N_k \geq 5$. For both the waiting times and sizes, the proportion fitted best by an exponential drops by $\sim 10\%$ in each λ_k bin, while the proportion fitted best by a log-normal increases. Qualitatively, however, the evolution with λ_k remains consistent with what is seen in Figure 3.5.

3.5. *Size–waiting-time cross-correlations*

The correlation between flare sizes and subsequent waiting times, i.e. the "forward" cross-correlation, is denoted as $\rho_{+,k}$, while the correlation between flare sizes and the preceding waiting times, i.e. the "backward" cross-correlation, is denoted as $\rho_{-,k}$. We calculate these correlations using the Spearman correlation coefficient [138].

The PDFs of forward and backward cross-correlations measured in all active regions with $N_k \geq 5$ are displayed in the top panel of Figure 3.6. The PDFs are broad, mostly because the median N_k is 12 (i.e. small). However, $p(\rho_{+,k})$ and $p(\rho_{-,k})$ are different; the latter has a median of $\rho_{-,k} = -0.02$, while the former has a median of $\rho_{+,k} = 0.10$. A Kolmogorov-Smirnov (KS) two-sample test provides quantitative evidence of the difference, returning a p-value of 10^{-28}.

The SDP process predicts a high forward cross-correlation for $\alpha \ll 1$, as discussed in Section 3.3.2. The data neither show evidence in favor of nor against such a correlation. In the bottom panel of Figure 3.6 we do not see a clear visual trend between $\rho_{+,k}$ and λ_k (for regions with $N_k \geq 10$), although a Spearman correlation test returns a small but non-zero correlation of 8×10^{-2} (p-value of 2×10^{-3}). We remind the reader that both $\rho_{+,k}$ and λ_k are empirical estimates for each active region, and the number of events per region is small. We do not plot uncertainties in the bottom panel of Figure 3.6, but they are typically comparable to the central value. These results imply that either i) all active regions have $\alpha \gtrsim 1$, where no forward cross-correlation is expected, i.e. $\lambda_k \gtrsim 0.2\,\text{hours}^{-1}$ does not correspond to the threshold-limited regime; or ii) some active regions have $\alpha \ll 1$, but either the trigger threshold or the driving rate is not constant with time, i.e. the random process triggering flares does not conform to the assumptions made in

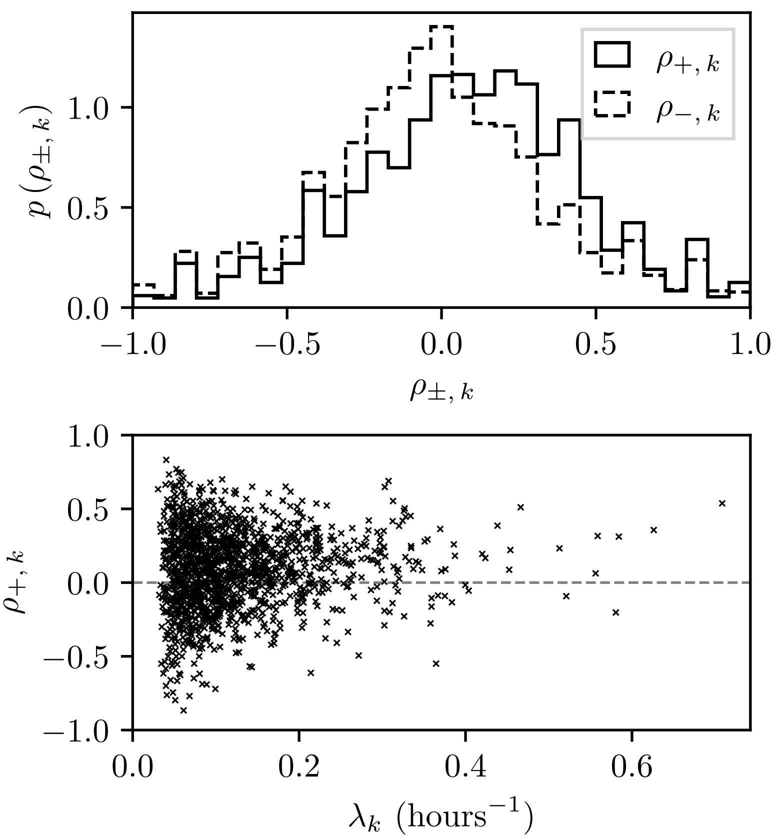

Figure 3.6: Top panel: PDF of forward cross-correlation, $\rho_{+,k}$ (black stepped curve), and backward cross-correlation, $\rho_{-,k}$ (black dashed curve), for all active regions with $N_k \geq 5$. Data binned into 30 uniformly spaced bins between $\rho_{\pm,k} = -1$ and $\rho_{\pm,k} = 1$. Bottom panel: Scatter plot of the forward cross-correlation, $\rho_{+,k}$, and flare rate, λ_k, for all regions with $N_k \geq 10$. The dashed grey line corresponds to $\rho_{+,k} = 0$.

the SDP framework.

As described in Section 3.4.2 the *GOES* catalog is not complete, i.e. while a given active region is visible, not all flares that occur are recorded. Wheatland [110] noted that the obscuration in Section 3.4.2 creates an artificial forward cross-correlation, which explains why the median $\rho_{+,k}$ is positive.

3.5. *Matching the shapes of the waiting time and size PDFs*

Another way to probe these data is to ask whether regions with relatively high $\rho_{+,k}$ exhibit "matching" functional forms for $p(\Delta t)$ and $p(\Delta s)$, as the SDP model predicts for $\alpha \lesssim 1$. We quantify the degree to which the PDFs match via the p-value $\mathcal{M}_k$ of the KS two-sample test applied to the sampled PDFs, $\{\Delta t_{i,k}\}$ and $\{\Delta s_{i,k}\}$. To calibrate, we perform a Monte Carlo simulation using sequences of events drawn from the SDP model. For each value of α we simulate 10^5 "regions". For each region we generate M events, where M is a random number drawn from $p(N_k)$, restricted to values $N_k \geq 10$, as empirically measured for the *GOES* regions (the distribution for $N_k \geq 5$ shown in Figure 3.3). From these M events we calculate summary statistics, e.g. $\mathcal{M}$ and ρ_+. This results in 10^5 pairs of $(\mathcal{M}, \rho_+)$, from which we construct a two-dimensional kernel density estimate (KDE) [139]. The KDE estimates the true joint PDF $p(\mathcal{M}, \rho_+)$, and is qualitatively equivalent to a smoothed, two-dimensional histogram.

The result of this procedure for four values of α is shown in the top panel of Figure 3.7. For $\alpha = 0.01$ (dark orange lines) the 10% and 50% credible interval contours are invisible in the top-right corner of the panel, as the vast majority of simulated regions have $\rho_+ \approx 1$ and $\mathcal{M} \approx 1$. For $\alpha = 0.1$ the KDE spreads out slightly, with the 50% credible interval reaching $\rho_+ \approx 0.8$ and $\mathcal{M} \approx 0.9$. For $\alpha = 1$, the PDF shifts such that the 50% credible interval contour stretches from $\mathcal{M} = 1$ to $\mathcal{M} \approx 0.8$, while we have $0 \lesssim \rho_+ \lesssim 0.8$. For $\alpha = 10$ we find ρ_+ centered around zero, while the 50% credible interval of $\mathcal{M}$ extends to $\mathcal{M} \approx 0.3$. The bottom panel of Figure 3.7 repeats the exercise for the backward cross-correlation. It confirms that ρ_- and $\mathcal{M}$ are uncorrelated, as predicted elsewhere [1, 18, 19]. Integrating over $\rho_\pm$ the reader would find that the marginal distribution of $\mathcal{M}$ is broad in both panels, for $\alpha \gtrsim 1$, as it is difficult to confidently reject the null hypothesis that two sets of samples are from the same distribution, when dealing with small sample sizes.

Monte Carlo calibration in hand, we present the equivalent data for all regions in the *GOES* catalog with $N_k \geq 10$ in Figure 3.8. To compute $\mathcal{M}_k$ for each region we first normalize both the waiting times and the sizes by their respective means for that region, before applying the KS two-sample test. In the top (bottom) panel we see no clear relationship between $\rho_{+,k}$ ($\rho_{-,k}$) and $\mathcal{M}_k$. Marginalizing over $\mathcal{M}_k$ we recover the PDFs of $\rho_{+,k}$ and $\rho_{-,k}$, shown in the top panel of Figure 3.6. If, for the sake of argument, we assume that all regions have the same value of α, we can compare the KDEs in Figure 3.8 to those in Figure 3.7. Under this assumption we are pushed into the regime $1 \lesssim \alpha \lesssim 10$, as the $p(\rho_{+,k}, \mathcal{M}_k)$ KDE is slightly off-set from the horizontal axis (i.e. median $\rho_{+,k} > 0$), but the 50% credible interval for $\mathcal{M}_k$ only extends to $\mathcal{M}_k \lesssim 0.4$. Even if α is not exactly the same in each region, we can interpret the above result as ruling out that a large proportion of regions have $\alpha \lesssim 1$, as if that were the case we would see higher values of $\mathcal{M}_k$ associated with higher $\rho_{+,k}$ more often than in Figure 3.8.

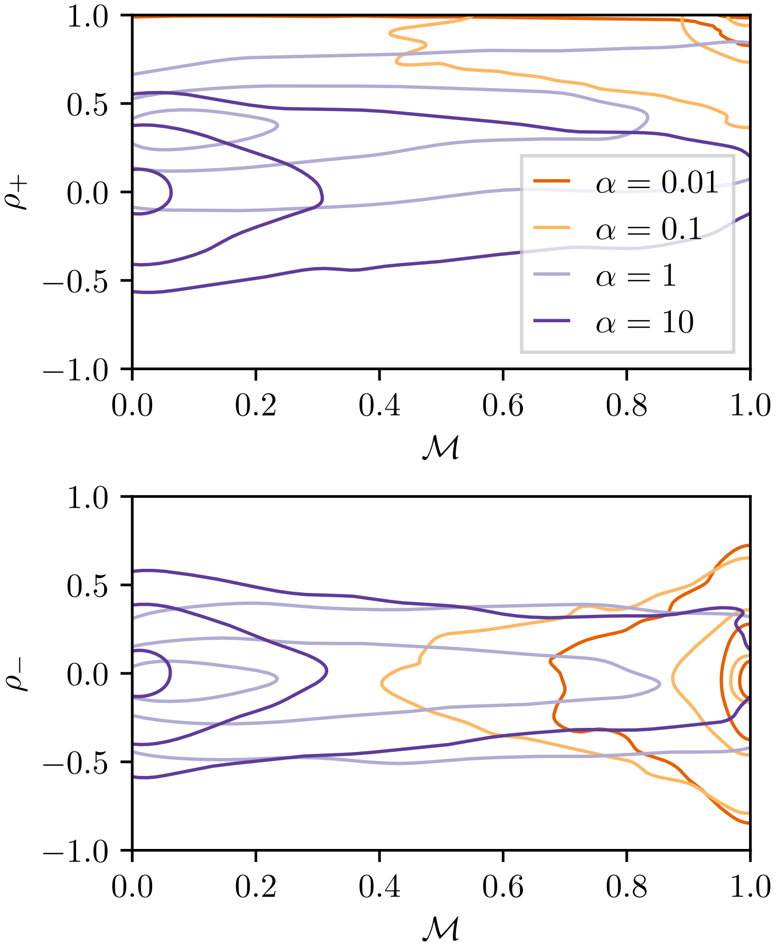

Figure 3.7: Calibrating the cross-correlation test in Section 3.5.3: two-dimensional KDEs of the relationship between ρ_+ and $\mathcal{M}$ (top panel), and ρ_- and $\mathcal{M}$ (bottom panel), for events simulated from the SDP model with four values of α (see legend for color code). The text in Section 3.5.3 reports details about the Monte Carlo procedure. Contours correspond to the 10%, 50%, and 90% credible intervals.

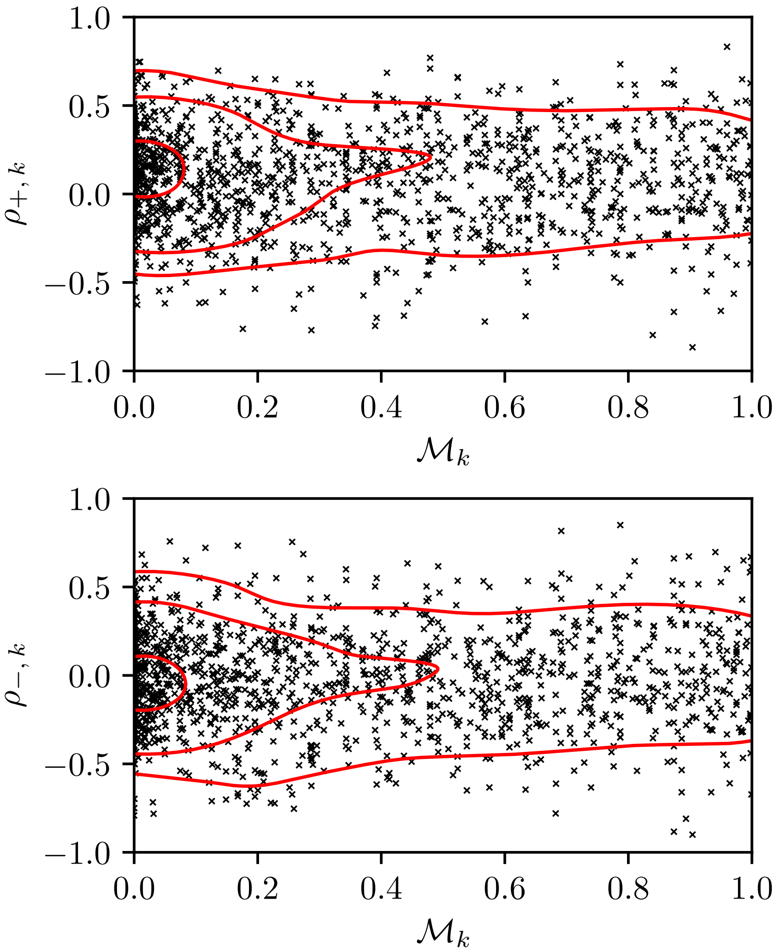

Figure 3.8: As for Figure 3.7 but for *GOES* data with black crosses marking all regions in the full, unmasked *GOES* catalog with $N_k \geq 10$. Red contours correspond to the 10%, 50%, and 90% credible intervals inferred from the black crosses.

3.5. *Autocorrelations and longer term memory*

While there is a wealth of information available in flare waiting time and size PDFs, as in Section 3.5.1, and cross-correlations, as in Sections 3.5.2 and 3.5.3, one may also consider statistics that quantify the longer term memory of the stress in the system. For example, as in the context of neutron star glitches [19], studying the autocorrelation between consecutive waiting times, $\rho_{\Delta t}$, or between consecutive sizes, $\rho_{\Delta s}$, allows one to place constraints on applicable SDP model parameters. In the fast-driven regime, $\alpha \ll 1$, we predict $\rho_{\Delta t} = 0$ and $\rho_{\Delta s} = 0$, as we have $X(t) \to X_{\rm c}$ before every stress-release event resulting in the system resetting at every event. If we have $\eta\left[\Delta X_i \,|\, X(t_i^-)\right] \propto \delta[X(t_i^-)]$, i.e. all stress in the system is released at each event, the same prediction of no autocorrelations holds — again the system is reset at every event. Observations of non-zero autocorrelations therefore rule out certain regimes in the SDP framework.

When we calculate $\rho_{\Delta t,k}$ and $\rho_{\Delta s,k}$ for all regions in the *GOES* catalog with $N_k \geq 10$, we find that the PDFs $p(\rho_{\Delta t,k})$ and $p(\rho_{\Delta s,k})$ are broad, akin to $p(\rho_{+,k})$ shown in Figure 3.6. The medians are 0.11 and 0.10 respectively. This result is incongruent with the assumption $\alpha \ll 1$ in all regions, as $\alpha \ll 1$ implies both PDFs should have a median of zero. These results likely stem from the obscuration effect described in Section 3.4.2. One tentative physical interpretation of a positive $\rho_{\Delta t}$ and $\rho_{\Delta s}$ is via analogy to terrestrial earthquakes which exhibit aftershocks, i.e. large events are often followed by larger-than-average events, with smaller-than-average waiting times [93]. In the context of solar flares, aftershock-like features are noted in the extreme ultraviolet in so-called "late-phase" flares [140].

3.6. Conclusion

In this paper, we revisit the long-standing question of whether solar flares in different active regions are triggered by a stress-relax process with a trigger threshold which is constant in time. We do so by mapping the flaring process to a SDP process, which operates independently in each active region. The SDP framework has been applied in related contexts to forest fires [135] and solar flares [111], before being extended in the context of neutron star glitches [1, 17–19]. If one assumes a constant driving rate, and a constant "stress" threshold at which relaxation events are guaranteed to occur, the model makes precise, falsifiable predictions regarding the statistics of sequences of waiting times and sizes, such as their PDFs, and cross-correlations. It is agnostic about the underlying microphysical mechanism.

Analyzing the historical *GOES* soft X-ray flare catalog, using data from 1975 until 2022, we systematically search all active regions for signatures that flares are consistent with the SDP model with $\alpha \ll 1$ (rapidly driven). We find no evidence that this is the case. Specifically, when considering just the waiting time and size PDFs of each active region we find that either i) the conditional PDF of stress-release sizes, $\eta\left[\Delta X_i \,|\, X(t_i^-)\right]$, varies from one region to another, or ii) a flare rate of $\lambda_k \gtrsim 0.2\,\text{hours}^{-1}$ does not correspond to $\alpha \ll 1$ (assuming that λ_k traces α). The analysis takes into account the selection effect that obscures the detection of flares following a large flare due to enhancement of the soft X-ray background.

On the other hand, if many active regions house a SDP process driven rapidly towards a static-in-time threshold before each event, i.e. have $\alpha \ll 1$, then those regions that have large cross-correlations between event sizes and subsequent waiting times should also have waiting time and size PDFs of the same shape. This prediction is not supported by the data, as proved clearly by Figure 3.8. The match between $p(\Delta t)$ and $p(\Delta s)$, quantified by $\mathcal{M}_k$ (the p-value from a KS two-sample test) for the k-th active region, does not correlate with the forward cross-correlation, $\rho_{+,k}$. If we assume each region has the same α, this test implies $1 \lesssim \alpha \lesssim 10$.

We emphasize that the prediction that $\mathcal{M}_k$ should correlate with $\rho_{+,k}$ for a process driven to a threshold does not rely on the specific details of the SDP framework, such as the relationship between flare rate and stress in Equation (3.2), nor the functional form of $\eta\left[\Delta X_i \,|\, X(t_i^-)\right]$. Any stochastic process that drives the stress towards a static threshold before each event would predict an equivalent observable, for example the Brownian stress-accumulation model [57].

There are many ways to interpret the results in Sections 3.4.3 and 3.5: i) solar flares may not be triggered by stress (e.g. magnetic energy density) breaching a threshold; a completely different process may trigger a flare. ii) The *GOES* flare catalog is incomplete; flares that occur in the aftermath of large flares are not recorded, creating an artificial cross-correlation. iii) The threshold at which a glitch is triggered and/or iv) the driving rate at which stress accumulates may vary with time; either of options iii) and iv) could wash out the observable signature. Untangling these explanations entails exploiting the entire wealth of data available in the flare catalog(s), rather than focussing on individual special flares or regions.

In closing, we touch on the following question: if option iii) above is true, is a threshold that varies with time compatible with any plausible microphysical flare triggers? The question falls outside the scope of this paper, which focuses on the microphysics-agnostic analysis in Sections 3.4 and 3.5, so we limit ourselves to the following brief remark. Magnetohydrodynamic instabilities relevant to solar flare activity are triggered above a threshold, which typically depends on the detailed geometry of a flaring magnetic loop, not just its bulk properties (e.g. magnetic energy density). The geometry of a flaring loop does vary with time in general. For example, the ideal kink instability occurs, when the total twist $\Phi = lB_\phi(r)/[rB_z(r)]$ satisfies $\Phi > \Phi_{\rm cr}(a) \sim 10$, where l and r are the length and minor radius of the current-carrying loop, $B_\phi(r)$ and $B_z(r)$ are the toroidal and axial magnetic field components, and a is the loop aspect ratio [141]. As sub-photospheric turbulence perturbs randomly the footpoints of a magnetic flux tube, the variables a and hence $\Phi_{\rm cr}(a)$ fluctuate stochastically. Quantifying the amplitude (drift and diffusion) of the fluctuations is a task for detailed magnetohydrodynamic simulations and lies well outside the scope of this paper, but it is conceivable that the amplitude is sufficiently large to render option iii) above viable.

Acknowledgements

We acknowledge helpful discussions with Kai Yang in the early stages of this paper. JBC, AM, and MSW are supported by the Australian Research Council (ARC) Centre of Excellence for Gravitational Wave Discovery (OzGrav) (project number CE170100004) and

ARC Discovery Project DP220102201. JBC is supported by an Australian Postgraduate Award.

Software: `Numpy` [142], `Scipy` [143], `Matplotlib` [144], and `Stan` [145] through the `cmdstanpy` interface.

3.A1. Magnetic energy density as a stress variable in an active region

The SDP framework described in Sections 3.2 and 3.3 is agnostic about the microphysics of solar flares, beyond the general assumption that the flaring rate increases with the stress in the system and diverges at a stress threshold. In this appendix, we sketch briefly one possible mapping between the SDP model and a specific microphysical flare model, in which the stress variable is the spatially-averaged magnetic energy density in an active region. We emphasize that the model is phenomenological and highly idealized. We do not favor it over the many alternatives; it is merely one possible illustration of how such a mapping may work, as a guide to the interested reader.

Let $X(t)$ correspond to the spatially-averaged magnetic energy density in an active region. The spatial average is taken in order to package the stress into a single variable, noting that the magnetic energy density is nonuniform in reality. Let the active region have characteristic linear dimension L. Let S be the magnetohydrodynamic Poynting flux through the photosphere. We assume that the Poynting flux deposits magnetic energy into the active region without losses and at a constant rate, so that one has $X(t) = X(t_i^+) + St/L$ between flares ($t_i^+ \leq t \leq t_{i+1}^-$). Recent vector magnetogram measurements allow direct observation of the Poynting flux, and the magnetic energy density of an active region, which are at-odds with our assumption that S is steady in time [146–149]. Putting aside the latter consideration for the moment, we can write the control parameter α as

$$\alpha = \frac{\lambda_0 S}{X_c L} \, , \tag{3.6}$$

where X_{cr} is the magnetic energy density threshold for a magnetohydrodynamic instability, for example, and λ_0 is the instability's trigger reference rate.

Several plausible magnetohydrodynamic instabilities have been suggested as solar flare triggers in the literature [150]. Some of them do not involve a magnetic energy density threshold at all. For example, the kink instability discussed at the end of Section 3.6 is triggered when the field-line twist Φ exceeds a threshold $\Phi_{cr}(a)$, whose value depends on the aspect ratio a of the flaring loop [141]. However, instabilities triggered by a magnetic energy density threshold do exist. One example is plasmoid-induced magnetic reconnection via tearing modes in a fractal current sheet [151], whose threshold depends on fractional powers of the Alfvén speed (or equivalently the Lundquist number) and hence on the magnetic energy density; see Ji and Daughton [150] or section 5 in Shibata and Tanuma [151] for example. In the latter reference, the threshold condition also depends on the aspect ratio a (width divided by length) of the current sheet, which can vary with time, as a flaring loop responds to sub-photospheric turbulence.

What are the time-scales on which S and X_c vary? In the SDP picture, both variables are steady, but the *GOES* analysis in Section 3.5 implies that one or both may vary in reality (although other scenarios are possible too, as discussed in Section 3.6). As far as S is concerned, one expects to find statistical fluctuations on the eddy turnover time-scale of sub-photospheric turbulence and flux emergence, τ_{flux}, as observed with vector magnetograms and Doppler measurements [146]. Magnetohydrodynamic simulations and G-band radiative signatures suggest $\tau_{\text{flux}} \sim$ minutes for magnetic features associated with solar granulation, with peak-to-peak fluctuation amplitude $\lesssim 30\%$ [152–154]. As far as X_{c} is concerned, in the plasmoid-induced reconnection picture as one illustrative example, the magnetic energy density threshold for a Sweet-Parker current sheet to undergo secondary tearing depends not only on the magnetic diffusivity, which fluctuates on the same time-scale as the local temperature, but also on a and L, which fluctuate on the turnover time-scale τ_{flux}, e.g. equation (15) in [151]. Flare waiting times are typically comparable to or longer than τ_{flux}, so it is conceivable that the constant-X_{c} approximation in the SDP theory does not apply to every active region.

We emphasize again that the mapping in this appendix is idealized and illustrative. None of the statistical analysis in Sections 3.4.3 and 3.5 is predicated on the microphysics in this appendix.

3.A2. Hierarchical Bayesian framework

This appendix lays out a complementary approach to the heuristic tests with which we analyze individual active regions in Section 3.5. We first write down the likelihood for a set of observed waiting times and sizes in an individual region, given a set of model parameters, in Appendix 3.A2.1. We introduce the hierarchical Bayesian framework which combines inference in different regions to estimate population-level parameters, in Appendix 3.A2.2. In Appendix 3.A2.3 we test the efficacy of this approach with synthetic data, and explain why it is not appropriate in this paper to apply this framework to the real *GOES* catalog despite its efficacy. Finally, in Appendix 3.A2.4 we propose an alternative approach using only the average waiting time in each region, as a motivation for future studies. The recipes in this appendix are included for completeness and as a starting point for readers, who wish to develop hierarchical methods of solar flare analysis further.

3.A2. Likelihood and Bayes' theorem

Solving Equations (3.1)–(3.3) for the long-term observable PDFs, $p(\Delta t)$ and $p(\Delta X)$, is intractable analytically for most choices of $\eta\left[\Delta X_i \,|\, X(t_i^-)\right]$. However, for the special case

$$\eta\left[\Delta X_i \,|\, X(t_i^-)\right] \propto \left[X(t_i^-) - \Delta X_i\right]^{\delta}, \tag{3.7}$$

we obtain the analytic result

$$p(z) = (\alpha + \delta + 1)(1 - z)^{\alpha+\delta}, \tag{3.8}$$

where the variable z is either Δt or ΔX, i.e. the waiting time and size PDFs are identical [1]. In Equation (3.7) we have $\delta > 0$ and the constant of proportionality is set by the condition that η must integrate to unity between $\Delta X_i = 0$ and $\Delta X_i = X(t_i^-)$; see section

6 and appendix D of Fulgenzi et al. [1] for a full derivation. Equation (3.7) is a monotonically decreasing function of ΔX_i, i.e. small stress-release events are preferred over large events. Its specific functional form is reasonable but arbitrary; it is not inferred from solar flare data. We adopt it here as a pedagogical device to illustrate the advantages and disadvantages of a hierarchical Bayesian approach to analyzing flare data.

When we restore the dimensions to Equation (3.8), and consider the set of observations in the k-th active region, $D_k = \{\Delta t_{i,k}, \Delta s_{i,k}\}$, with $1 \leq i \leq N_k$, we can write the likelihood

$$\mathcal{L}(D_k|\boldsymbol{\theta}_k) = \prod_{i=1}^{N_k-1} p(\Delta t_{i,k}|\boldsymbol{\theta}_k) \prod_{i=1}^{N_k} p(\Delta s_{i,k}|\boldsymbol{\theta}_k) \tag{3.9}$$

$$= \tau_k^{1-N_k}\, \xi_k^{-N_k}\, (\beta_k+1)^{2N_k-1} \prod_{i=1}^{N_k-1}\left(1-\frac{\Delta t_{i,k}}{\tau_k}\right)^{\beta_k} \prod_{i=1}^{N_k}\left(1-\frac{\Delta s_{i,k}}{\xi_k}\right)^{\beta_k} \tag{3.10}$$

where ξ_k is the constant of proportionality in Equation (3.5) which translates the drop in magnetic energy density ΔX to the observed flare size, Δs, and one has $\beta_k = \lambda_{0,k}\,\tau_k + \delta_k$. While there are N_k flare sizes in the region, there are only $N_k - 1$ waiting times. The three model parameters $\boldsymbol{\theta}_k = \{\tau_k, \xi_k, \beta_k\}$ are assumed constant in time for the lifetime of the active region. Bayes' theorem calculates the posterior probability distribution (henceforth "posterior"), $p(\boldsymbol{\theta}_k|D_k)$, i.e. the probability density of parameter vector $\boldsymbol{\theta}_k$ given the data D_k, using the prior probability distribution (henceforth "prior"), $\pi(\boldsymbol{\theta}_k)$, viz.

$$p(\boldsymbol{\theta}_k|D_k) \propto \mathcal{L}(D_k|\boldsymbol{\theta}_k)\pi(\boldsymbol{\theta}_k)\,. \tag{3.11}$$

The normalizing constant of proportionality is often called the evidence and, while essential for model comparison, is not relevant for the parameter estimation exercise below [155].

3.A2. *Population-level parameter estimation*

Suppose, for the sake of illustration, that X_c, λ_0, and every component of $\boldsymbol{\theta}_k$ are approximately the same in all active regions. In the language of hierarchical Bayesian inference, this corresponds to assuming that the value of $\boldsymbol{\theta}_k$ for each region is a random number drawn from a population-level distribution known as a "hyper-prior", with narrow extent. For concreteness, we assume the hyper-prior for each model parameter is a Gaussian with mean and standard deviation μ_a and σ_a respectively, with $a \in \{\tau, \xi, \beta\}$. While β_k does depend on τ_k, the inference remains accurate so long as the covariance between τ_k, $\lambda_{0,k}$, and δ_k is minimal. The marginal posterior distribution for the parameters describing the hyper-priors is calculated as

$$p(\boldsymbol{\Lambda}|\mathcal{D}) \propto \pi(\boldsymbol{\Lambda}) \prod_{k}^{M} \int \mathrm{d}\boldsymbol{\theta}_k\, \mathcal{L}(D_k|\boldsymbol{\theta}_k)\pi(\boldsymbol{\theta}_k|\boldsymbol{\Lambda}), \tag{3.12}$$

with $\boldsymbol{\Lambda} = \{\mu_a, \sigma_a\}$. In Equation (3.12), $\pi(\boldsymbol{\Lambda})$ is the prior on $\boldsymbol{\Lambda}$, and $\mathcal{D} = \{D_1, ..., D_k, ...D_M\}$ is the set of all data, D_k, from M different active regions.

In practice, we can use a Monte Carlo sampler to estimate Equation (3.12), and thus infer the posterior predictive distributions, $p(\boldsymbol{\theta})$, where we drop the subscript k to signify

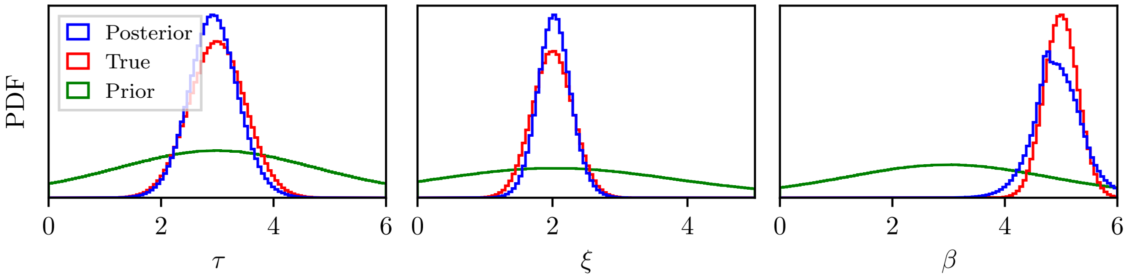

Figure 3.9: Posterior predictive check demonstrating the recovery of injected population-level parameters. The weakly informative priors set on the hyper-parameters τ, ξ, and β are shown in green, histograms of samples from the injected population parameters are shown in red, while histograms of samples from the posterior distributions are shown in blue. See text in Appendix 3.A2.3 for details on the procedure.

that these distributions bring together information from all active regions to inform the inference. We opt to sample using a Hamiltonian Monte Carlo No U-Turn Sampler [156], as implemented in the `Stan` programming language [145].

3.A2. Validation with synthetic data

To estimate the efficacy of the scheme in Appendix 3.A2.2 to infer population-level parameters, we first apply it to a set of synthetic data generated directly from the model. That is, we generate $M = 50$ fake "active regions", each with $N_k = 100$ events, with flare sizes and waiting times generated from the SDP framework with $\eta\left[\Delta X_i | X(t_i^-)\right]$ as in Equation (3.7). In what follows we use the compact notation $x \sim \mathcal{N}(\mu, \sigma)$ to denote that the random variable x is drawn from a Gaussian distribution with mean μ and standard deviation σ. To generate the data for each region we select a value $\tau_k \sim \mathcal{N}(\mu_\tau = 3\,\text{day}, \sigma_\tau = 0.5\,\text{day})$, a value $\xi_k \sim \mathcal{N}(\mu_\xi = 2\,\text{arb. units}, \sigma_\xi = 0.3\,\text{arb. units})$, and a value $\beta_k \sim \mathcal{N}(\mu_\beta = 5, \sigma_\beta = 0.3)$. Each Gaussian is truncated such that all variates are positive.

After running the sampler with the synthetic data we perform a posterior predictive check, i.e. compare the samples from our posterior distributions $p(\tau)$, $p(\xi)$, and $p(\beta)$ with the injected distributions and the priors on the hyper-parameters. We show the results in Figure 3.9. We see that the posterior samples (blue) appropriately overlap with the injected ground truth (red) for τ, ξ, and β.

Despite the encouraging results in Figure 3.9, we do not apply this hierarchical Bayesian scheme to the *GOES* catalog in this paper. This is because in most regions neither the waiting time nor the size PDFs follow the functional form in Equation (3.8). When we include Equation (3.8) in the set of options available for the AICc to select between, as in Section 3.5.1, fewer than 0.1% of active regions are fitted best with Equation (3.8). Therefore Equation (3.10) is not an appropriate likelihood for the data. Other choices of the jump distribution in Equation (3.7) may alleviate this problem but they lie outside the scope of this paper.

3.A2. *Likelihood based on the average waiting time*

An alternative approach is to build the likelihood out of a summary statistic, such as the average waiting time in a given region, $\langle \Delta t \rangle_k$, rather than each observed waiting time and/or size. In the SDP framework, we find [1, 157]

$$\langle \Delta t \rangle^{\mathrm{SDP}} = \frac{1}{\alpha + \alpha_0} \, , \tag{3.13}$$

where $\alpha_0 \sim 1$ is a dimensionless constant, whose exact value depends on the particular form of $\eta\left[\Delta X_i \,|\, X(t_i^-)\right]$. Restoring the dimensions to Equation (3.13) we can write the likelihood as

$$\mathcal{L}(\langle \Delta t \rangle_k \,|\, \boldsymbol{\theta}_k) = \frac{1}{\sqrt{2\pi\sigma_k}} \exp\left[\frac{-\left(\langle \Delta t \rangle_k - \frac{\tau_k}{\lambda_{0,k}\tau_k + \alpha_{0,k}}\right)^2}{2\sigma_k^2}\right] , \tag{3.14}$$

with $\boldsymbol{\theta}_k = \{\tau_k, \lambda_{0,k}, \alpha_{0,k}, \sigma_k\}$, where we assume the residual of $\langle \Delta t \rangle_k$ with the model subtracted is normally distributed, with zero mean and standard deviation σ_k. With the likelihood in Equation (3.14) one could perform population-level parameter estimation, as described in Section 3.A2.2. We leave this, and an exploration of how $\boldsymbol{\theta}_k$ depends on parameters intrinsic to each active region, to future work.

3.A3. Cleaning *GOES* flare summary data

The SWPC and NGDC File Transfer Protocol servers that host the *GOES* flare summary data, as well as other data portals such as the Heliophysics Event Knowledgebase[4], contain numerous typographical anomalies found when collating the data into a homogeneous catalog. These anomalies are found in the recorded active region number by checking whether one has $\Delta t_{i,k} < 14$ days for $1 \le i \le N_k - 1$ for each active region. The limit of 14 days applies because active regions are typically only visible for two weeks due to the rotation period of the Sun. The one exception in the *GOES* flare summary data is eight flares that occurred on 2002-11-02, and are assigned to active region number 10198. Two weeks later the active region appears on the eastern limb of the Sun, and 33 additional flares are assigned to active region number 10198, from 2002-11-17 until 2002-11-28. We opt not to consider the former eight flares as part of active region number 10198, and do not include them in the catalog.

The anomalies, and hand-corrected values, are tabulated in Table 3.1. The corrected values are determined manually by referring to the context of surrounding flares in the database. For example, the flare starting at 1981-07-18 11:46 is recorded with active region number 3121. Yet the other 11 flares associated with the latter region occurred between 1981-05-24 and 1981-06-01, while active region number 3221 has 32 flares recorded between 1981-07-17 and 1981-07-29, indicating that the anomalous flare should be associated with the latter active region. The latitude of the anomalous flare is also within $\pm 5^\circ$ of other flares from active region number 3221, while flares in active region number 3121 are $\gtrsim 10^\circ$ higher in latitude.

[4] Accessible through http://hec.helio-vo.eu/hec/hec_gui.php.

Table 3.1: Anomalous active region numbers found in the *GOES* flare summary data by checking whether one has $\Delta t_{i,k} < 14\,\text{days}$ for $1 \le i \le N_k - 1$ for each active region. Corrected values are determined manually, by considering the context of what active regions are present at the time of the anomalous flare at a similar latitude. Corrected values of "—" indicate that we cannot identify a reasonable active region to associate with the anomalous flare.

Flare start time	Anomalous active region number	Corrected active region number
1978-05-30 06:19	1000	1134
1981-07-18 11:46	3121	3221
1981-08-22 06:58	366	3266
1983-03-01 18:24	2102	4102
1983-03-01 18:54	2102	4102
1983-07-04 06:09	4135	4235
1983-07-29 03:53	4236	4263
1993-09-27 01:35	7500	7590
2000-11-09 21:13	9125	—
2002-06-14 20:18	1	10001
2003-07-31 07:59	422	10422
2003-12-21 04:10	10000	—
2011-12-22 13:04	11281	11381
2017-07-11 01:09	12655	12665
2017-07-16 10:25	12655	12665
2021-05-10 23:46	12282	12822
2021-09-01 03:03	12680	12860
2021-09-01 04:27	12680	12860
2021-11-06 22:01	12984	12894
2021-12-18 11:17	12807	12907
2021-12-18 17:27	12807	12907

CHAPTER 4

Search for continuous gravitational waves from 20 accreting millisecond x-ray pulsars in O3 LIGO data

4.1. Introduction

Second generation, ground-based gravitational wave detectors, specifically the Advanced Laser Interferometer Gravitational wave Observatory (Advanced LIGO) [158] and Advanced Virgo [159], have detected more than 50 compact binary coalescence events in recent years [160–162]. Continuous gravitational waves from rapidly-rotating neutron stars are also potential sources, e.g. a non-axisymmetry due to mountains on the surface, or stellar oscillation modes in the interior [163–165]. There are no reported detections of continuous gravitational waves to date, despite a number of searches in Advanced LIGO and Advanced Virgo data [166–187].

Low-mass X-ray binaries (LMXBs) are a high-priority target for continuous gravitational wave searches. LMXBs are composed of a compact object, such as a neutron star[1], which accretes matter from a stellar-mass ($\lesssim 1 M_{\odot}$) companion [188]. The accretion exerts a torque that may spin up the compact object. Electromagnetic (EM) observations show that even the pulsar with the highest known frequency, PSR J1748−2446ad at 716 Hz [189], rotates well below the centrifugal break-up frequency, estimated at ~ 1400 Hz [190]. Gravitational wave emission may provide the balancing torque in binary systems such as these, stopping the neutron star from spinning up to the break-up frequency [191, 192]. If so, there should thus be a correlation between accretion rate (which is inferred via X-ray flux) and the strength of the continuous gravitational wave emission [191–194]. The LMXB Scorpius X-1 is the brightest extra-Solar X-ray source in the sky, making it a prime target for searches for continuous gravitational waves [167, 181, 195, 196].

Some LMXBs have EM observations of pulsations during "outburst" events lasting days to months, which allow for measurement of their rotational frequency, $f_{\star}$, to an ac-

[1]LMXBs in which the compact object is a stellar-mass black hole are not expected to function as continuous gravitational wave sources and are not discussed in this paper.

curacy of $\sim 10^{-8}$ Hz, and measurement of their binary ephemerides [188, 197]. LMXBs that are observed to go into outburst and have measurable pulsations with millisecond periods are sometimes called accreting millisecond X-ray pulsars (AMXPs). If the rotational frequency is known, computationally cheap narrowband searches are possible. Six AMXPs were previously searched for continuous gravitational waves, one in Science Run 6 (S6) using the TwoSpect algorithm [198, 199], and five in Observing Run 2 (O2) using the same Hidden Markov Model (HMM) algorithm we use in this work [182, 200]. No significant candidates were found in either search. Searches for continuous gravitational waves from LMXBs are difficult as the rotation frequency may wander stochastically on timescales of $\lesssim 1$ yr [201], limiting the duration of coherent integration. A HMM tracks a wandering signal, and is the search algorithm we use here, following Refs. [181, 182, 200, 202].

Advanced LIGO and Advanced Virgo began the third Observing Run (O3) on April 1 2019, 15:00 UTC. There was a month-long commissioning break between October 1 2019, 15:00 UTC, and November 1 2019, 15:00 UTC, after which observations resumed until March 27, 2020, 17:00 UTC. This month-long break divides O3 into two segments: O3a and O3b. In this work we search the full O3 data set for continuous gravitational wave signals from AMXPs with known rotational frequencies. The search is a more sensitive version of an analogous search in O2 data [182], with an expanded target list. We briefly review the algorithm and O2 search in Sec. 4.2. In Secs. 4.3 and 4.4 we describe the targets and the parameter space respectively. We discuss the data used in Sec. 4.5. In Sec. 4.6 we describe the vetoes applied to discriminate between terrestrial and astrophysical candidates. In Sec. 4.7 we present the results of the search. In Sec. 4.8 we describe an additional target-of-opportunity search performed for one of the targets that was in outburst during O3a. We provide upper limits for the detectable wave-strain, and astrophysical implications thereof, in Sec. 4.9. We conclude in Sec. 4.10.

4.2. Search algorithm

The search in this paper follows the same prescription as the O2 searches for Scorpius X-1 [181] and LMXBs with known rotational frequency [182]. It is composed of two parts: a HMM which uses the Viterbi algorithm to efficiently track the most likely spin history, and the $\mathcal{J}$-statistic, which calculates the likelihood a gravitational wave is present given the detector data, and the orbital parameters of both the Earth and the LMXB. The HMM formalism is identical to that used in Refs. [181, 182, 195, 200, 202], and the $\mathcal{J}$-statistic was first introduced in Ref. [200]. Below, we provide a brief review of both the HMM and the $\mathcal{J}$-statistic.

4.2. HMM

In a Markov process, the probability of finding the system in the current state depends only on the previous state. In a hidden Markov process the states are not directly observable and must be inferred from noisy data. In this paper, the hidden state of interest is the gravitational wave frequency $f(t)$. Although the rotation frequency $f_\star(t)$ of every target in this search is measured accurately from EM pulsations, we allow $f(t) \neq f_\star(t)$ in general for three reasons: i) different emission mechanisms emit at different multiples of $f_\star$ [203]; ii) a small, fluctuating drift may arise between $f(t)$ and $f_\star(t)$, if the star's core (where the gravitational-wave-emitting mass or current quadrupole may reside) decouples partially from the crust (to which EM pulsations are locked) [202, 204]; and, iii) the rotational frequency of the crust may also drift stochastically due to a fluctuating accretion torque [188, 201]. The gravitational-wave frequency is therefore hidden even though the EM measurement of $f_\star$ helps restrict the searched frequency space, as described in Sec. 4.4.

Following the notation of Refs. [181, 182] we label the hidden state variable as $q(t)$. In our model, it transitions between a discrete set of allowed values $\{q_1, ..., q_{N_Q}\}$ at discrete times $\{t_0, ..., t_{N_T}\}$. The probability of the state transitioning from q_i at time t_n to q_j at time t_{n+1} is determined by the transition matrix $A_{q_j q_i}$. In this search, as in previous searches of LMXBs [181, 182, 195], the transition matrix is

$$A_{q_j q_i} = \frac{1}{3}\left(\delta_{q_j q_{i+1}} + \delta_{q_j q_i} + \delta_{q_j q_{i-1}}\right), \tag{4.1}$$

where δ_{ij} is the Kronecker delta. Eq. (4.1) corresponds to allowing $f(t)$ to move 0, or ± 1 frequency bins, with equal probability, at each discrete transition. It implicitly defines the signal model for $f(t)$ to be a piece-wise constant function, with jumps in frequency allowed at the discrete times $\{t_0, ..., t_{N_T}\}$. This is a well-tested approximation for an unbiased random walk [200, 202].

The total duration of the search is $T_{\rm obs}$, which we split into N_T coherent equal chunks of length $T_{\rm drift}$, where $N_T = \lfloor T_{\rm obs}/T_{\rm drift} \rfloor$, and $\lfloor ... \rfloor$ indicates rounding down to the nearest integer. We justify our choice of $T_{\rm drift}$ in Sec. 4.4. In essence, it needs to be short enough to ensure that $f_\star(t)$ does not wander by more than one frequency bin during each time segment, but ideally no shorter in order to maximize the signal-to-noise ratio in each segment. For each time segment the likelihood that the observation o_j is related to the hidden state q_i is given by the emission matrix $L_{o_j q_i}$. We calculate $L_{o_j q_i}$ from the data via a frequency domain estimator, e.g. the $\mathcal{J}$-statistic, as discussed in Sec. 4.2.2.

The probability that the hidden path is $Q = \{q(t_0), ..., q(t_{N_T})\}$ given a set of observations $O = \{o(t_0), ..., o(t_{N_T})\}$ is

$$\begin{aligned} P(Q|O) = {} & \Pi_{q(t_0)} A_{q(t_1)q(t_0)} L_{o(t_1)q(t_1)} \cdots \\ & \times A_{q(t_{N_T})q(t_{N_T-1})} L_{o(t_{N_T})q(t_{N_T})}, \end{aligned} \tag{4.2}$$

where $\Pi_{q(t_0)}$ is the prior probability of starting in the state $q(t_0)$, and is taken to be uniform within a certain range guided by EM measurements of $f_\star$. The Viterbi algorithm is a computationally efficient way to find the path Q^* that maximizes Eq. (4.2) [205].

The detection statistic we use in this work is $\mathcal{L} = \ln P(Q^*|O)$, i.e. the log-likelihood of the most likely path given the data. The search outputs one $P(Q^*|O)$ value per frequency bin, corresponding to the optimal path Q^* terminating in that frequency bin.

4.2. $\mathcal{J}$-statistic

Any long-lived gravitational wave signal from an LMXB observed by the detectors is Doppler modulated by the orbital motion of the detectors around the Solar System barycenter, and by the orbital motion of the compact object in its binary. The $\mathcal{F}$-statistic is a frequency domain estimator originally designed for isolated neutron stars, and accounts for the Earth's annual orbital motion (as well as the amplitude modulation caused by the Earth's diurnal rotation) [206]. Algorithms that implement the $\mathcal{F}$-statistic, such as `lalapps_ComputeFstatistic_v2` [207], have subsequently added functionality to account for modulation of the signal due to binary motion.

The $\mathcal{J}$-statistic accounts for the binary modulation via a Jacobi-Anger expansion of the orbit [200]. It ingests $\mathcal{F}$-statistic "atoms" as calculated for an isolated source as an input, assumes the binary is in a circular orbit[2], and requires three binary orbital parameters: the period P, the projected semi-major axis a_0, and the time of passage of the ascending node $T_{\rm asc}$. We use the $\mathcal{J}$-statistic as the frequency domain estimator $L_{o_j q_i}$ in this paper, as in Refs. [181, 182]. The $\mathcal{J}$-statistic is a computationally efficient algorithm, as it re-uses $\mathcal{F}$-statistic atoms when searching over a template bank of binary orbital parameters.

4.3. Targets

The AMXPs chosen as targets for this search, along with their positions, orbital elements, and pulsation frequencies are listed in Table 4.1. These 20 targets constitute all known AMXPs with observed coherent pulsations and precisely measured orbital elements as of April 2021[3]. For details on the relevant EM observations, principally in the X-ray band, see Refs. [188, 197, 210, 211].

Most AMXPs are transient, with "active" (outburst) and "quiescent" phases. Pulsations, and therefore $f_\star$, are only observed during the active phase. Active phases are typically associated with accretion onto the neutron star, however accretion can also happen during quiescence [212]. The frequency derivatives, $\dot{f}_\star$, in the active phase and in the quiescent phase are set by the accretion torque and magnetic dipole braking respectively [212, 213]. The value of $\dot{f}_\star$ has implications for the continuous gravitational wave signal strength (see Sec. 4.9.3), as well as the choice of $T_{\rm drift}$ (see Sec. 4.4.1).

One target, SAX J1808.4−3658, went into outburst during O3a [214–216]. It may be the case that continuous gravitational waves are only emitted when an AMXP is in outburst [217]. If so, we increase our signal-to-noise ratio by searching only data from the times that it was in outburst, compared to searching the entirety of O3 data. To investigate this possibility, we perform in Sec. 4.8 an additional target-of-opportunity search for continuous gravitational waves from SAX J1808.4−3658 while it is in outburst.

[2]This assumption is justified as none of the targets described in Sec. 4.3 have measurable eccentricity with sufficient precision [188, 197].

[3]We do not include the AMXP Aquila X-1 [208, 209] in our target list as there is a large uncertainty on all three binary orbital elements, compared to the other 20 AMXPs. One would need to search $> 10^{10}$ binary orbital templates, an order of magnitude more than the rest of the targets combined. The number of binary orbital templates is calculated as a function of the uncertainty in orbital elements in Sec. 4.4.2.

Table 4.1: Target list: position (RA and Dec), orbital period (P), projected semi-major axis in light-seconds (a_0), time of passage through the ascending node as measured near the time of the most recent outburst (T_{asc}), the time of passage through the ascending node as propagated to the start of O3 ($T_{\mathrm{asc,\,O3}}$), as described in Sec. 4.4.2, and frequency of observed pulsations ($f_\star$). Numbers in parentheses indicate reported 1σ errors (68% confidence level), unless otherwise noted. All objects have positional uncertainty ≤ 1 s in RA and $\leq 0.5''$ in Dec.

Target	RA	Dec	P/s	a_0/lt-s	T_{asc}/GPS time	$T_{\mathrm{asc,\,O3}}$/GPS time	$f_\star$/Hz	Re
IGR J00291+5934	00h29m03.05s	$+59°34'18.93''$	8844.07673(9)	0.064993(2)	1122149932.93(5)	1238157687(1)	598.89213099(6)	[21
MAXI J0911−655	09h12m02.46s	$-64°52'06.37''$	2659.93312(47)	0.017595(9)	1145507148.0(9)	1238165918(16)	339.9750123(3)	[22
XTE J0929−314	09h29m20.19s	$-31°23'03.2''$	2614.746(3)	0.006290(9)	705152406.1(9)	1238165763(612)	185.105254297(9)	[22
IGR J16597−3704	16h59m32.902s	$-37°07'14.3''$	2758.2(3)	0.00480(3)	1193053416(9)	1238163777(4907)	105.1758271(3)	[22
IGR J17062−6143	17h06m16.29s	$-61°42'40.6''$	2278.21124(2)	0.003963(6)	1239389342(4)	1238165942(4)	163.656110049(9)	[22
IGR J17379−3747	17h37m58.836s	$-37°46'18.35''$	6765.8388(17)	0.076979(14)	1206573046.6(3)	1238162748(8)	468.083266605(7)	[22
SAX J1748.9−2021	17h48m52.161s	$-20°21'32.406''$	31555.300(3)	0.38757(2)	1109500772.5(8)	1238151731(12)	442.3610957(2)	[19
NGC 6440 X−2	17h48m52.76s	$-20°21'24.0''$	3457.8929(7)	0.00614(1)	956797704(2)	1238166449(57)	205.89221(2)	[23
IGR J17494−3030	17h49m23.62s	$-30°29'58.999''$	4496.67(3)	0.015186(12)	1287797911(1)	1238163668(331)	376.05017022(4)	[23
Swift J1749.4−2807	17h49m31.728s	$-28°08'05.064''$	31740.8417(27)	1.899568(11)	1298634645.85(12)	1238136602(5)	517.92001385(6)	[23
IGR J17498−2921	17h49m56.02s	$-29°19'20.7''$	13835.619(1)	0.365165(5)	997147537.43(7)	1238164020(6)	400.99018734(9)	[23
IGR J17511−3057	17h51m08.66s	$-30°57'41.0''$	12487.5121(4)	0.2751952(18)	936924316.03(3)	1238160570(10)	244.83395145(9)	[23
XTE J1751−305	17h51m13.49s	$-30°37'23.4''$	2545.3414(38)	0.010125(5)	701914663.57(3)	1238164644(487)	435.31799357(3)	[24
Swift J1756.9−2508	17h56m57.43s	$-25°06'27.4''$	3282.40(4)	0.00596(2)	1207196675(9)	1238166119(378)	182.06580377(11)	[24
IGR J17591−2342	17h59m02.86s	$-23°43'08.3''$	31684.7503(5)	1.227714(4)	1218341207.72(8)	1238144176.7(3)	527.425700578(9)	[24
XTE J1807−294	18h06m59.8s	$-29°24'30''$	2404.4163(3)	0.004830(3)	732384720.7(3)	1238165711(63)	190.62350702(4)	[24
SAX J1808.4−3658	18h08m27.647s	$-36°58'43.90''$	7249.155(3)	0.062809(7)	1250296258.5(2)	1238161173(5)	400.97521037(1)	[21
XTE J1814−338	18h13m39.02s	$-33°46'22.3''$	15388.7229(2)	0.390633(9)	739049147.41(8)	1238151597(4)	314.35610879(1)	[24
IGR J18245−2452	18h24m32.51s	$-24°52'07.9''$	39692.812(7)	0.76591(1)	1049865088.37(9)	1238128096(33)	254.3330310(1)	[24
HETE J1900.1−2455	19h00m08.65s	$-24°55'13.7''$	4995.2630(5)	0.01844(2)	803963262.3(8)	1238161513(43)	377.296171971(5)	[25

90% confidence level

3σ error

4.4. Search parameters

The $\mathcal{J}$-statistic matched filter requires specification of the source sky position [right ascension (RA) and declination (Dec)], the orbital period P, the projected semi-major axis a_0, and the orbital phase ϕ_a at the start of the search. The orbital phase can be equivalently specified via a time of passage through the ascending node, $T_{\rm asc}$. EM observations constrain all of these parameters, as well as the spin frequency $f_\star$. These measurements, along with their associated uncertainties, are listed in Table 4.1.

There are several mechanisms that could lead to continuous gravitational wave emission from an AMXP, in its active or quiescent phase. "Mountains" on the neutron star surface, be they magnetically or elastically supported, emit at $2f_\star$ and potentially $f_\star$ [254]. The dominant continuous gravitational wave emission from r-mode oscillations (Rossby waves excited by radiation-reaction instabilities) is predicted to be at $\sim 4f_\star/3$ [255–258]. Thus, we search frequency sub-bands centered on $\{1, 4/3, 2\} f_\star$ for each target. As in Refs. [181, 182] we choose a sub-band width of $\sim 0.61\,\mathrm{Hz}$[4].

Recent work indicates that the continuous gravitational wave signal from r-modes could emit at a frequency far from $4f_\star/3$ due to equation-of-state-dependent relativistic corrections, and so comprehensive searches for r-modes may need to cover hundreds of Hz for the targets listed in Table 4.1 [260, 261]. The exact range of frequencies to search is a non-linear function of $f_\star$, and does not necessarily include $4f_\star/3$ (see equation (17) of Ref. [261]). However, these estimates are still uncertain. We deliberately search $\sim 0.61\,\mathrm{Hz}$ sub-bands centered on $4f_\star/3$, as an exhaustive broadband search lies outside the scope of this paper, which aims to conduct fast, narrowband searches at astrophysically motivated harmonics of $f_\star$ while accommodating frequency wandering within those sub-bands, a challenge in its own right.

4.4. *Coherence time and frequency binning*

Another key parameter for the search algorithm described in Sec. 4.2 is the coherence time $T_{\rm drift}$. As in Refs. [181, 182] we fix $T_{\rm drift} = 10\,\mathrm{d}$ for each target[5]. This choice of $T_{\rm drift}$ is guided by observations of Scorpius X-1 [201]. Quantitative studies of how X-ray flux variability in AMXPs impacts searches for continuous gravitational waves are absent from the literature. The choice to use $T_{\rm drift} = 10\,\mathrm{d}$ balances the increased sensitivity achieved via longer coherence times with the knowledge that the gravitational wave frequency may wander stochastically, e.g. due to fluctuations in the mass accretion rate. The particular value $T_{\rm drift} = 10\,\mathrm{d}$ has been adopted in all previous Viterbi LMXB searches [181, 182, 195] and is justified approximately with reference to a simple random-walk interpretation of fluctuations in the X-ray flux of Scorpius X-1 [201, 262, 263], but other values are reasonable too.

We remind the reader that the choice of $T_{\rm drift}$ implicitly fixes the proposed signal model as one in which the frequency may wander step-wise zero, plus or minus one

[4]Other narrowband searches, such as Refs. [177, 259], search sub-bands whose width, $\sim 10^{-3} f$, scales with frequency. We note that $0.61\,\mathrm{Hz}$ is comparable to $10^{-3} f$ for the harmonics of $f_\star$ that we search in this paper, but is $2^{20}\Delta f$, where Δf is the frequency bin size defined in Sec. 4.4.1. Having the number of frequency bins in the sub-band equal a power of two speeds up the Fourier transform [181].

[5]We consider additional $T_{\rm drift}$ durations for the target-of-opportunity search for continuous gravitational waves from SAX J1808.4–3658 during its O3a outburst in Sec. 4.8.

frequency bin every $T_{\rm drift} = 10\,{\rm d}$. The size of the frequency bins, Δf, is fixed by the resolution implied by the coherence time, i.e. $\Delta f = 1/(2\,T_{\rm drift}) = 5.787037 \times 10^{-7}\,{\rm Hz}$, for $T_{\rm drift} = 10\,{\rm d}$. As Δf depends on $T_{\rm drift}$, changing the coherence time explicitly changes the signal model, e.g. if $T_{\rm drift}$ is halved and $T_{\rm obs}$ is kept constant, then both N_T and Δf double; thus the signal can move up to a factor of four more in frequency in the same $T_{\rm obs}$. The connection between the coherence time and signal model features in all semi-coherent search methods. However, for a HMM-based search such as this, the choice of coherence time is not limited by computational cost, as it is in all-sky searches or searches based on the $\mathcal{F}$-statistic [187, 264].

This analysis does not search over any frequency derivatives. The maximum absolute frequency derivative, $|\dot{f}_{\rm max}|$, that does not change the frequency more than one frequency bin over the course of one coherent chunk is

$$\left|\dot{f}_{\rm max}\right| = \frac{\Delta f}{T_{\rm drift}} \approx 6.7 \times 10^{-13}\,{\rm Hz\,s^{-1}}\ . \tag{4.3}$$

When measured, the long-term secular frequency derivative is well below this value for all of our targets, see Sec. 4.9.3 for details.

4.4. *Number of orbital templates*

The orbital elements are known to high precision, with the uncertainty in P satisfying $\sigma_P \lesssim 10^{-3}\,{\rm s}$, the uncertainty in a_0 satisfying $\sigma_{a_0} \lesssim 10^{-4}$ light-seconds (lt-s), and the uncertainty in $T_{\rm asc}$ satisfying $\sigma_{T_{\rm asc}} \lesssim 1\,{\rm s}$. However, $T_{\rm asc}$ is measured relative to the target's most recent outburst, which is often years before the start of O3 ($T_{\rm O3,\,start} =$ 1238166483 GPS time). We need to propagate it forward in time. This propagation compounds the uncertainty in $T_{\rm asc}$, viz. [181, 182, 196]

$$\sigma_{T_{\rm asc,O3}} = \left[\sigma^2_{T_{\rm asc}} + (N_{\rm orb}\sigma_P)^2\right]^{1/2}\ , \tag{4.4}$$

where $N_{\rm orb}$ is the number of orbits between the observed $T_{\rm asc}$ and $T_{\rm asc,O3}$. Henceforth $T_{\rm asc}$ and $\sigma_{T_{\rm asc}}$ symbolize their values when propagated to $T_{\rm O3,\,start}$.

To conduct the search over the orbital elements for each target and sub-band we construct a rectangular grid in the parameter space defined by ($P \pm 3\sigma_P, a_0 \pm 3\sigma_{a_0}, T_{\rm asc} \pm 3\sigma_{T_{\rm asc}}$). For three targets, XTE J0929–314, IGR J16597–3704, and IGR J17494–3030, the range ($T_{\rm asc} \pm P/2$) is smaller than ($T_{\rm asc} \pm 3\sigma_{T_{\rm asc}}$) and we use the former. We assume that P and a_0 remain within the same bin for the entire search. While some targets have a non-zero measurement of $\dot{P}\,T_{\rm obs}$ ($\dot{a}_0\,T_{\rm obs}$), in all cases it is much smaller than the template spacing in P (a_0) [219, 226, 265].

It is unlikely that the true source parameters lie exactly on a grid point in the parameter space. Thus the grid is spaced such that the maximum mismatch, $\mu_{\rm max}$, is never more than an acceptable level. The mismatch is defined as the fractional loss in signal-to-noise ratio between the search executed at the true parameters and at the nearest grid point [266]. We calculate the number of grid points required for P, a_0 and $T_{\rm asc}$ using Eq. (71)

of Ref. [266], i.e.

$$N_P = \pi^2 \sqrt{6}\, \mu_{\max}^{-1/2} f\, a_0 \frac{\gamma T_{\text{drift}}}{P^2} \sigma_P \,, \tag{4.5}$$

$$N_{a_0} = 3\pi \sqrt{2}\, \mu_{\max}^{-1/2} f\, \sigma_{a_0} \,, \tag{4.6}$$

$$N_{T_{\text{asc}}} = 6\pi^2 \sqrt{2}\, \mu_{\max}^{-1/2} f\, a_0 \frac{1}{P} \sigma_{T_{\text{asc}}} \,, \tag{4.7}$$

where γ is a refinement factor defined in general in Eq. (67) of Ref. [266]. In the case of O3, the semi-coherent segments are contiguous so we have $\gamma = N_T = 36$. We fix $\mu_{\max} = 0.1$. A set of software injections into O3 data verifies that a template grid constructed with $\mu_{\max} = 0.1$ results in a maximum fractional loss in signal-to-noise ratio of 10%. We make the conservative choice of rounding N_P, N_{a_0}, and $N_{T_{\text{asc}}}$ up to the nearest integer, after setting f to the highest frequency in each 0.61 Hz sub-band. As in Ref. [182] we find $N_{a_0} = 1$ for each target and sub-band, and so hold a_0 constant at its central value while searching over P and T_{asc}. Table 4.2 shows N_P, $N_{T_{\text{asc}}}$, and $N_{\text{tot}} = N_P N_{T_{\text{asc}}}$ for each target and sub-band. When Eq. (4.5) or (4.7) predicts only two templates for a given sub-band we round up to three, ensuring that the central value of P or T_{asc} from EM observations is included in the template bank. Note that the EM observations are sufficiently precise that $< 5 \times 10^4$ templates are required across all targets and sub-bands. This is in contrast to the O2 search for continuous gravitational waves from Scorpius X-1, for which $\sim 10^9$ templates were needed, mainly due to the large uncertainty in a_0, and the unknown rotation frequency [181].

4.4. Thresholds

The output of the search algorithm outlined in Sec. 4.2 is a $\mathcal{L}$ value corresponding to the most likely path through each sub-band for each orbital template (P, a_0, T_{asc}). We flag a template for further follow-up if $\mathcal{L}$ exceeds a threshold, $\mathcal{L}_{\text{th}}$, given an acceptable probability of false alarm. To determine $\mathcal{L}_{\text{th}}$ we need to know how often pure noise yields $\mathcal{L} > \mathcal{L}_{\text{th}}$. The distribution of $\mathcal{L}$ in noise-only data is unknown analytically, but depends on P, a_0, and the frequency, so Monte-Carlo simulations are used to determine $\mathcal{L}_{\text{th}}$ in each sub-band for each target.

We estimate the distribution of $\mathcal{L}$ in noise via two methods: i) using realizations of synthetic Gaussian noise generated using the `lalapps_Makefakedata_v5` program in the LIGO Scientific Collaboration Algorithm Library (LALSuite) [207], and ii) searching O3 data in off-target locations to simulate different realizations of true detector noise. As in Refs. [181, 182] we generate realizations for each target and sub-band, and apply the search algorithm described in Sec. 4.2 to each realization to recover samples from the noise-only distribution of $\mathcal{L}$. Details on how we use these samples to find $\mathcal{L}_{\text{th}}$ for each sub-band are given in Appendix 4.A1. Unless otherwise noted, $\mathcal{L}_{\text{th}}$ refers to the lower of the two thresholds derived from the methods listed above to minimize false dismissals.

To define $\mathcal{L}_{\text{th}}$ we must also account for a "trials factor" due to the number of templates searched in each sub-band. We assume that in noise-only data the spacing between templates is sufficiently large such that each template returns a statistically independent $\mathcal{L}$. We can therefore relate the false alarm probability for a search of a sub-band with

Table 4.2: Starting frequencies, f_s, for each ~ 0.61 Hz-wide sub-band, number of templates needed to cover the P and T_{asc} domains in that sub-band, N_P and $N_{T_{asc}}$ respectively, and the total number of templates for each sub-band, $N_{tot} = N_P N_{T_{asc}}$. The projected semi-major axis a_0 is known precisely enough that we have $N_{a_0} = 1$ for each sub-band.

Target	f_s (Hz)	N_P	$N_{T_{asc}}$	N_{tot}
IGR J00291+5934	598.6	1	3	3
	798.5	1	3	3
	1197.8	1	3	3
MAXI J0911−655	339.7	1	10	10
	453.3	3	14	42
	679.9	3	20	60
XTE J0929−314	184.8	3	52	156
	246.8	3	69	207
	370.2	3	104	312
IGR J16597−3704	104.9	49	23	1127
	140.2	65	31	2015
	210.4	97	46	4462
IGR J17062−6143	163.4	1	1	1
	218.2	1	1	1
	327.3	1	1	1
IGR J17379−3747	467.8	4	12	48
	624.1	5	15	75
	936.2	7	23	161
SAX J1748.9−2021	442.1	3	18	54
	589.8	3	24	72
	884.7	3	36	108
NGC 6440 X−2	205.6	1	6	6
	274.5	1	8	8
	411.8	1	12	12
IGR J17494−3030	375.7	21	112	2352
	501.4	27	150	4050
	752.1	41	224	9184
Swift J1749.4−2807	517.6	7	43	301
	690.6	9	57	513
	1035.8	13	85	1105

Target	f_s (Hz)
IGR J17498−2921	400.7
	534.7
	802.0
IGR J17511−3057	244.5
	326.4
	489.7
XTE J1751−305	435.0
	580.4
	870.6
Swift J1756.9−2508	181.8
	242.8
	364.1
IGR J17591−2342	527.1
	703.2
	1054.9
XTE J1807−294	190.3
	254.2
	381.2
SAX J1808.4−3658	400.7
	534.6
	802.0
XTE J1814−338	314.1
	419.1
	628.7
IGR J18245−2452	254.0
	339.1
	508.7
HETE J1900.1−2455	377.0
	503.1
	754.6

N_{tot} templates, $\alpha_{N_{\text{tot}}}$, to the probability of a false alarm for a single template, α, viz.

$$\alpha_{N_{\text{tot}}} = 1 - (1-\alpha)^{N_{\text{tot}}}. \tag{4.8}$$

Previous comparable searches have set $\alpha_{N_{\text{tot}}}$ between 0.01 and 0.3 [181, 182, 195, 196]. In this search, we fix $\alpha_{N_{\text{tot}}} = 0.3$, i.e. set the acceptable probability of false alarm at 30% per sub-band. As we search a total of $20 \times 3 = 60$ sub-bands, we expect ~ 18 candidates above $\mathcal{L}_{\text{th}}$ due to noise alone (i.e. false alarms), a reasonable number on which to perform more exhaustive follow-up. Looking ahead to the results in Sec. 4.7 we recover 4611 candidates above $\mathcal{L}_{\text{th}}$. While this number is much higher than the ~ 18 false alarms expected, almost all of these candidates are non-Gaussian noise artifacts in one (or both) of the detectors. All but 16 of the 4611 candidates are eliminated by the vetoes outlined in Sec. 4.6. We reiterate that $\mathcal{L}_{\text{th}}$ in each sub-band is the lower of the two thresholds described in Appendix 4.A1, lowering conservatively the probability of false dismissal.

4.4. *Computing resources*

A mix of central processing unit (CPU) and graphical processing unit (GPU) resources are used. The GPU implementation of the $\mathcal{J}$-statistic is identical to that used in Refs. [181, 182]. The entire search across all targets and sub-bands takes ~ 30 CPU-hours and ~ 40 GPU-hours when using compute nodes equipped with Xeon Gold 6140 CPUs and NVIDIA P100 12GB PCIe GPUs. Producing $\mathcal{L}_{\text{th}}$ for each sub-band, as described in Sec. 4.4.3, takes an additional $\sim 5\times10^2$ CPU-hours and $\sim 4\times10^3$ GPU-hours to perform the search on different noise realizations. The additional follow-up in Appendix 4.A2.1 requires an additional $\sim 10^3$ CPU-hours and $\sim 10^2$ GPU-hours.

4.5. O3 DATA

We use the full dataset from O3, spanning from April 1, 2019, 15:00 UTC to March 27, 2020, 17:00 UTC, from the LIGO Livingston and Hanford observatories. We do not use any data from the Virgo interferometer in this analysis, due to its lower sensitivity compared to the two LIGO observatories in the frequency sub-bands over which we search [267]. The data products ingested by the search algorithm described in Sec. 4.2 are short Fourier transforms (SFTs) lasting 1800 s. Times when the detectors were offline, poorly calibrated, or were impacted by egregious noise, are excluded from analysis by using "Category 1" vetoes as defined in section 5.2 of Ref. [267]. The SFTs are generated from the "C01 calibrated self-gated" dataset, which is the calibrated strain data with loud transient glitches removed [268]. Transient glitches otherwise impact the noise floor, as described in section 6.1 of Ref. [267]. The median systematic error of the strain magnitude across O3 is < 2% [269, 270].

The coherence time $T_{\text{drift}} = 10\,\text{d}$ splits the data into $N_T = 36$ segments. However, due to the month-long commissioning break between O3a and O3b there are two segments without any SFTs. These two segments, starting at October 8, 2019, 15:00 UTC and October 15, 2019, 15:00 UTC, are replaced with a uniform log-likelihood for all frequency bins, which allows the HMM to effectively skip over them while still allowing spin wandering. When generating synthetic data in Secs. 4.4.3 and 4.9 the same two data segments are also replaced with uniform log-likelihoods to emulate the real search.

4.6. Vetoes

When a candidate is returned with $\mathcal{L} > \mathcal{L}_{\text{th}}$ we must decide whether there are reasonable grounds to veto the candidate as non-astrophysical. We use three of the vetoes from Ref. [182]: the known line veto, detailed in Sec. 4.6.1, the single interferometer veto, detailed in Sec. 4.6.2, and the off-target veto, detailed in Sec. 4.6.3. The false dismissal rate of these vetoes is less than 5% (see detailed safety investigations in section IVB of Ref. [195] and section IVB of Ref. [181]).

4.6. Known line veto

As part of the detector characterization process many harmonic features are identified as instrumental "known lines" [267, 271]. However, the exact source of these harmonic features is sometimes unidentified, and their impact cannot always be mitigated through isolating hardware components or post-processing the data [267, 271]. We use the vetted known lines list in Ref. [272].

Any candidate close to a known line at frequency f_{line} is vetoed. Precisely, if for any time $0 \leq t \leq T_{\text{obs}}$ the candidate's frequency path $f(t)$ satisfies

$$|f(t) - f_{\text{line}}| < 2\pi a_0 f_{\text{line}}/P\,, \tag{4.9}$$

then the candidate is vetoed[6].

4.6. Single interferometer veto

An instrumental artifact is unlikely to be coincident in both detectors, so the candidate's $\mathcal{L}$ should be dominated by only one of the detectors if the signal is non-astrophysical. On the other hand, an astrophysical signal may need data from both detectors to be detected, or if it is particularly strong may be seen in both detectors individually.

We label the original log-likelihood as $\mathcal{L}_{\cup}$, and we also calculate the two single interferometer log-likelihoods $\mathcal{L}_a$ and $\mathcal{L}_b$ (where the higher $\mathcal{L}$ is labeled with b for definiteness). There are four possible outcomes for this veto:

i) If the $\mathcal{L}$ value in one detector is sub-threshold, while the other is above the two-detector $\mathcal{L}$ value, i.e. one has $\mathcal{L}_a < \mathcal{L}_{\text{th}}$ and $\mathcal{L}_b > \mathcal{L}_{\cup}$ and $f_b(t)$, the frequency path associated with $\mathcal{L}_b$, is close to the frequency path of the candidate when using data from both detectors, $f_{\cup}(t)$, i.e.

$$|f_{\cup}(t) - f_b(t)| < 2\pi a_0 f_{\cup}/P\,, \tag{4.10}$$

then the candidate is likely to be a noise artifact in detector b, and is vetoed.

[6]One might consider an additional Doppler broadening factor of $2\pi a_{\oplus}/1\,\text{yr}$, where $a_{\oplus}$ is the mean Earth-Sun distance, as stationary lines in the detector frame get Doppler shifted when transforming the data to the frame of reference of the source. We opt not to apply this factor for simplicity in this search, as the exact pattern of Doppler modulation depends strongly on the sky location of the target. Looking ahead to the results in Sec. 4.7, we note that none of the 16 surviving candidates is within $2\pi f a_{\oplus}/1\,\text{yr}$ of any known line.

ii) If one has $\mathcal{L}_a < \mathcal{L}_{\mathrm{th}}$ and $\mathcal{L}_b > \mathcal{L}_{\cup}$, but Eq. (4.10) does not hold then the candidate signal cannot be vetoed, as the single-interferometer searches did not find the same candidate. This could indicate that the candidate is a weak astrophysical signal that needs data from both detectors to be detectable.

iii) If one has $\mathcal{L}_a > \mathcal{L}_{\mathrm{th}}$ and $\mathcal{L}_b > \mathcal{L}_{\mathrm{th}}$, the candidate could represent a strong astrophysical signal that is visible in data from both detectors independently, or it could represent a common noise source. Candidates in this category cannot be vetoed.

iv) If one has $\mathcal{L}_a < \mathcal{L}_{\mathrm{th}}$ and $\mathcal{L}_b < \mathcal{L}_{\cup}$, data from both detectors is needed for the candidate to be above threshold, possible indicating a weak astrophysical signal. Candidates in this category cannot be vetoed.

4.6. Off-target veto

The third veto we apply to a candidate is to search an off-target sky position with the same orbital template. If the off-target search returns $\mathcal{L} > \mathcal{L}_{\mathrm{th}}$ then the candidate is likely instrumental rather than astrophysical. For this veto, off-target corresponds to shifting the target sky position $+40\,\mathrm{m}$ in RA and $+10^\circ$ in Dec.

4.7. O3 search results

The results of the search of all 20 targets are summarized in Fig. 4.1, with $\alpha_{N_{\mathrm{tot}}} = 0.3$, i.e. a nominal probability of false alarm per sub-band of 30%. Each symbol indicates, for all templates with $\mathcal{L} > \mathcal{L}_{\mathrm{th}}$, the terminating frequency bin and p_{noise}, the probability that a search of that candidate's sub-band in pure noise would return at least one candidate at least as loud as the one seen. Equation (4.21) in Appendix 4.A1.5 defines p_{noise} explicitly. Each candidate is colored according to $\mathcal{L}$. We note that high $\mathcal{L}$ does not always correspond to low p_{noise} due to the differing "trials factors" in each sub-band, as accounted for when calculating $\mathcal{L}_{\mathrm{th}}$ via Eq. (4.8). A low value of p_{noise} corresponds to a higher probability that the candidate is a true astrophysical signal. Targets not listed in the legend return zero candidates above threshold. We do not display in Fig. 4.1 candidates that are eliminated by any of the vetoes described in Sec. 4.6 for clarity.

In total, across all targets and sub-bands, there are 4611 candidates with $\mathcal{L} > \mathcal{L}_{\mathrm{th}}$, before the vetoes are applied. All but 100 are eliminated by veto A (known line veto). A further 84 candidates are eliminated by veto B (single interferometer veto). None of the remaining candidates are eliminated by veto C (off-target veto), leaving 16 candidates passing all of the vetoes outlined in Sec. 4.6. None of the surviving candidates from the O3 search coincide in their orbital template and terminating frequency bin with the seven above- or sub-threshold candidates from the O2 search (c.f. Table VI of Ref. [182]). If we set $\alpha_{N_{\mathrm{tot}}} = 0.01$, i.e. set the probability of false alarm per sub-band to 1%, the search does not return any candidates with $\mathcal{L} > \mathcal{L}_{\mathrm{th}}$ for any target or sub-band, after vetoes are applied.

In Secs. 4.7.1–4.7.20 we summarize the search results for each of the 20 targets. To guide the reader, and not clutter the main body of the paper, the full search results for one target, IGR J18245−2452, are shown in Fig. 4.2, while the full search results for the

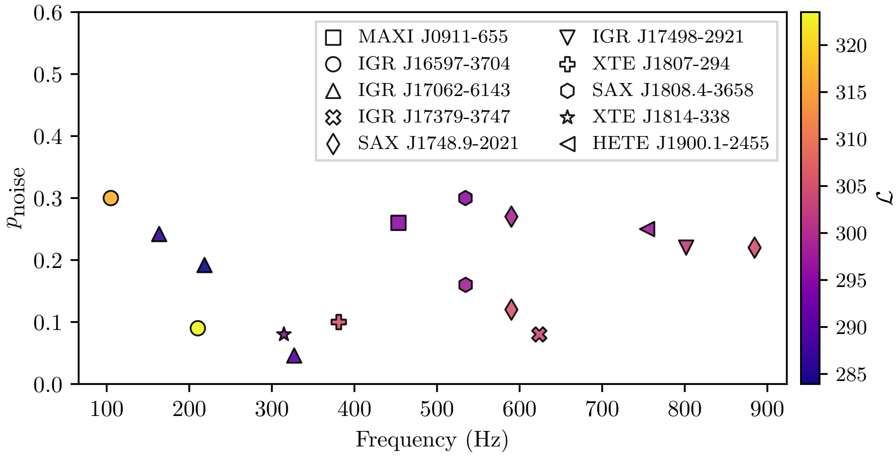

Figure 4.1: Summary of search results across all targets and sub-bands with $\mathcal{L} > \mathcal{L}_{\rm th}$. The different symbols correspond to candidates from different targets. The ordinate shows $p_{\rm noise}$ for each candidate, the probability that a search of that candidate's sub-band in pure noise would return at least one candidate at least as loud as the one seen. The color of each candidate indicates $\mathcal{L}$ (see color bar at right). Candidates that are eliminated by the vetoes outlined in Sec. 4.6 are not shown for clarity. Details on the search results are in Sec. 4.7 and Appendix 4.A2.

other 19 targets are shown in Figs. 4.4a–4.4s in Appendix 4.A2. The orbital template, terminating frequency bin, $\mathcal{L}$, and $p_{\rm noise}$ for all 16 candidates with $\mathcal{L} > \mathcal{L}_{\rm th}$ are collated in Table 4.6 in Appendix 4.A2. We present further follow-up of the 16 candidates in Appendix 4.A2.1. We find no convincing evidence that any are a true astrophysical signal.

4.7. *IGR J18245−2452*

The search results for IGR J18245−2452 are presented in Fig. 4.2. Each marker in Fig. 4.2 shows the terminating frequency and associated $\mathcal{L}$ of the most likely path through the sub-band for a given template, i.e. choice of P and $T_{\rm asc}$. The vertical blue dashed (green dot-dashed) lines correspond to the threshold set via Gaussian (off-target) noise realizations, $\mathcal{L}_{\rm th,G}$ ($\mathcal{L}_{\rm th,OT}$), in each sub-band, with $\alpha_{N_{\rm tot}} = 0.3$. See Appendix 4.A1 for details on how we set thresholds in each sub-band. The horizontal red lines indicate known instrumental lines in the detector with bandwidth indicated by the shading. There are zero above-threshold candidates in the $f_\star$ and $4f_\star/3$ sub-bands. There are 435 above-threshold candidates in the $2f_\star$ sub-band, which are all coincident with known noise lines in both the Livingston and Hanford detectors, and are therefore eliminated by veto A. The sub-band around 508 Hz is especially noisy due to violin mode resonances [267].

4.7. *IGR J00291+5934*

The search results for IGR J00291+5934 are shown in Fig. 4.4a, which is laid out identically to Fig. 4.2. There are zero above-threshold candidates in the $4f_\star/3$ and $2f_\star$ sub-bands. There are three above-threshold candidates in the $f_\star$ sub-band, however all three of these candidates are coincident with known noise lines in the Hanford detector, and

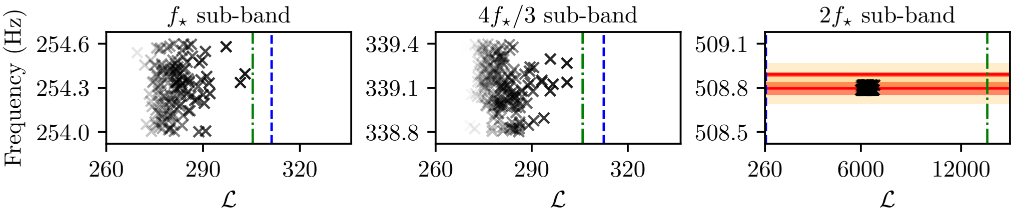

Figure 4.2: Search results for IGR J18245−2452. Black crosses indicate the terminating frequency and $\mathcal{L}$ for the most likely path through the sub-band for each binary template. The vertical blue dashed (green dot-dashed) lines correspond to the threshold set via Gaussian (off-target) noise realizations, $\mathcal{L}_{\rm th,G}$ ($\mathcal{L}_{\rm th,OT}$), in each sub-band. Solid red lines in the right panel indicate the peak frequency of known instrumental lines in the Hanford detector; the orange band indicates the width of the line in the detector frame and the yellow band indicates the increased effective width due to Doppler broadening, as described in Sec. 4.6.1. Multiple overlapping orange bands creates the red bands. The sub-band around 508.8 Hz is especially noisy due to test mass suspension violin mode resonances [267]. The transparency of crosses in sub-bands with many templates, is adjusted relative to the maximum $\mathcal{L}$ in that sub-band for clarity.

are therefore eliminated with veto A.

4.7. MAXI J0911−655

The search results for MAXI J0911−655 are shown in Fig. 4.4b, which is laid out identically to Fig. 4.2. There are zero above-threshold candidates in the $f_\star$ and $2f_\star$ sub-bands. There is one above-threshold candidate in the $4f_\star/3$ sub-band which survives all of the vetoes and has $p_{\rm noise} = 0.26$. Additional follow-up, presented in Appendix 4.A2.1, does not provide any evidence that this candidate is a true astrophysical signal.

4.7. XTE J0929−314

The search results for XTE J0929−314 are shown in Fig. 4.4c, which is laid out identically to Fig. 4.2. There are zero above-threshold candidates across all three sub-bands.

4.7. IGR J16597−3704

The search results for IGR J16597−3704 are shown in Fig. 4.4d, which is laid out identically to Fig. 4.2. Each sub-band for this target is contaminated with known noise lines. There are 84 above-threshold candidates in the $4f_\star/3$ sub-band, however they are all eliminated by veto B. One above-threshold candidate is returned in each of the $f_\star$ and $2f_\star$ sub-bands. Both of these candidates survive all of the vetoes, and have $p_{\rm noise} = 0.30$ and $p_{\rm noise} = 0.09$ respectively. Further follow-up, including the frequency path and cumulative log-likelihood for the latter candidate, is presented in Appendix 4.A2.1. This follow-up does not provide any evidence that either candidate is a true astrophysical signal.

4.7. IGR J17062–6143

The search results for IGR J17062–6143 are shown in Fig. 4.4e, which is laid out identically to Fig. 4.2. Given the long-term timing presented in Ref. [226] there is only one template needed in each of the three sub-bands for this target. The template returns $\mathcal{L} > \mathcal{L}_{\text{th}}$ in all three of the $f_\star$, $4f_\star/3$, and $2f_\star$ sub-bands. All of these candidates survive all of the vetoes, and have $p_{\text{noise}} = 0.24$, $p_{\text{noise}} = 0.19$, and $p_{\text{noise}} = 0.05$ respectively. Further follow-up, including the frequency path and cumulative log-likelihood for the candidate with $p_{\text{noise}} = 0.05$, is presented in Appendix 4.A2.1. This follow-up does not provide any evidence that any of the three candidates are a true astrophysical signal.

4.7. IGR J17379–3747

The search results for IGR J17379–3747 are shown in Fig. 4.4f, which is laid out identically to Fig. 4.2. There are zero above-threshold candidates in the $f_\star$ and $2f_\star$ sub-bands. There is one above-threshold candidate in the $4f_\star/3$ sub-band which survives all of the vetoes and has $p_{\text{noise}} = 0.08$. Further follow-up, including the frequency path and cumulative log-likelihood, for this candidate is presented in Appendix 4.A2.1. This follow-up does not provide any evidence that the candidate is a true astrophysical signal.

4.7. SAX J1748.9–2021

The search results for SAX J1748.9–2021 are shown in Fig. 4.4g, which is laid out identically to Fig. 4.2. There are zero above-threshold candidates in the $f_\star$ sub-band. There are two above-threshold candidates in the $4f_\star/3$ sub-band which survive all of the vetoes and have $p_{\text{noise}} = 0.12$ and $p_{\text{noise}} = 0.27$. There is one above-threshold candidate in the $2f_\star$ sub-band which survives all of the vetoes and has $p_{\text{noise}} = 0.22$. Additional follow-up, presented in Appendix 4.A2.1, does not provide any evidence that any of the three candidates are a true astrophysical signal.

4.7. NGC 6440 X–2

The search results for NGC 6440 X–2 are shown in Fig. 4.4h, which is laid out identically to Fig. 4.2. There are zero above-threshold candidates across all three sub-bands.

4.7. IGR J17494–3030

The search results for IGR J17494–3030 are shown in Fig. 4.4i, which is laid out identically to Fig. 4.2. There are zero above-threshold candidates in the $f_\star$ and $2f_\star$ sub-bands. All 4050 candidates in the $4f_\star/3$ sub-band are above threshold, however all of them are coincident with a known noise line in the Hanford detector, and are therefore eliminated with veto A. The sub-band around 501.7 Hz is especially noisy due to violin mode resonances [267].

4.7. Swift J1749.4−2807

The search results for Swift J1749.4−2807 are shown in Fig. 4.4j, which is laid out identically to Fig. 4.2. There are zero above-threshold candidates in the $f_\star$ and $4f_\star/3$ sub-bands. There is one above threshold candidate in the $2f_\star$ sub-band. However it is coincident with a known noise line in the Hanford detector, and is therefore eliminated by veto A.

4.7. IGR J17498−2921

The search results for IGR J17498−2921 are shown in Fig. 4.4k, which is laid out identically to Fig. 4.2. There are zero above-threshold candidates in the $f_\star$, and $4f_\star/3$ sub-bands. There is one above-threshold candidate in the $2f_\star$ sub-band which survives all of the vetoes and has $p_{\rm noise} = 0.22$. Additional follow-up, presented in Appendix 4.A2.1, does not provide any evidence that this candidate is a true astrophysical signal.

4.7. IGR J17511−3057

The search results for IGR J17511−3057 are shown in Fig. 4.4l, which is laid out identically to Fig. 4.2. There are zero above-threshold candidates across all three sub-bands.

4.7. XTE J1751−305

The search results for XTE J1751−305 are shown in Fig. 4.4m, which is laid out identically to Fig. 4.2. There are zero above-threshold candidates across all three sub-bands.

4.7. Swift J1756.9−2508

The search results for Swift J1756.9−2508 are shown in Fig. 4.4n, which is laid out identically to Fig. 4.2. There are zero above-threshold candidates across all three sub-bands.

4.7. IGR J17591−2342

The search results for IGR J17591−2342 are shown in Fig. 4.4o, which is laid out identically to Fig. 4.2. There are zero above-threshold candidates across all three sub-bands.

4.7. XTE J1807−294

The search results for XTE J1807−294 are shown in Fig. 4.4p, which is laid out identically to Fig. 4.2. There are zero above-threshold candidates in the $f_\star$ and $4f_\star/3$ sub-bands. There is one above-threshold candidate in the $2f_\star$ sub-band which survives all of the vetoes and has $p_{\rm noise} = 0.10$. Further follow-up, including the frequency path and cumulative log-likelihood, for this candidate is presented in Appendix 4.A2.1. This follow-up does not provide any evidence that the candidate is a true astrophysical signal.

4.7. SAX J1808.4−3658

The search results for SAX J1808.4−3658 are shown in Fig. 4.4q, which is laid out identically to Fig. 4.2. There are zero above-threshold candidates in the $f_\star$ and $2f_\star$ sub-bands. There are two above-threshold candidates in the $4f_\star/3$ sub-band which survive all of the vetoes and have $p_{\text{noise}} = 0.16$ and $p_{\text{noise}} = 0.30$. Additional follow-up, presented in Appendix 4.A2.1, does not provide any evidence that either candidate is a true astrophysical signal.

SAX J1808.4−3658 was observed in outburst in August 2019, during O3a [215, 216]. This allows us to perform an additional target-of-opportunity search during only its active phase. If the target only emits continuous gravitational waves during outburst, searching a shorter duration of data increases the probability of detection by increasing the signal-to-noise ratio. The details and results of this target-of-opportunity search are in Sec. 4.8. In summary, after searching with three separate coherence times of $T_{\text{drift}} = 1\,\text{d}$, $T_{\text{drift}} = 8\,\text{d}$, and $T_{\text{drift}} = 24\,\text{d}$, only one candidate is above threshold and survives all of the vetoes. The candidate is found using $T_{\text{drift}} = 24\,\text{d}$ in the $f_\star$ sub-band, and has $p_{\text{noise}} = 0.02$. Additional follow-up does not reveal any informative features that would distinguish between an astrophysical signal and noise. It does not coincide with either of the two candidates in the $4f_\star/3$ sub-band found in the semi-coherent search using the full O3 data set.

4.7. XTE J1814−338

The search results for XTE J1814−338 are shown in Fig. 4.4r, which is laid out identically to Fig. 4.2. There are zero above-threshold candidates in the $4f_\star/3$ and $2f_\star$ sub-bands. There is one above-threshold candidate in the $f_\star$ sub-band which survives all of the vetoes and has $p_{\text{noise}} = 0.08$. Further follow-up, including the frequency path and cumulative log-likelihood, for this candidate is presented in Appendix 4.A2.1. This follow-up does not provide any evidence that the candidate is a true astrophysical signal.

4.7. HETE J1900.1−2455

The search results for HETE J1900.1−2455 are shown in Fig. 4.4s, which is laid out identically to Fig. 4.2. There are zero above-threshold candidates in the $f_\star$ sub-band. All 22 templates in the $4f_\star/3$ sub-band return candidates above $\mathcal{L}_{\text{th}}$, however these candidates are all coincident with known noise lines in the Hanford detector, and are summarily eliminated with veto A. The sub-band around $503\,\text{Hz}$ is especially noisy due to violin mode resonances [267]. There is one above-threshold candidate in the $2f_\star$ sub-band which survives all of the vetoes and has $p_{\text{noise}} = 0.25$. Additional follow-up, presented in Appendix 4.A2.1, does not provide any evidence that this candidate is a true astrophysical signal.

4.8. Target-of-opportunity search: SAX J1808.4−3658 in outburst

On August 7 2019 SAX J1808.4−3658 went into outburst [214]. The Neutron star Interior Composition Explorer (NICER) team undertook a high-cadence monitoring campaign, and performed a timing analysis of the pulsations [215]. The outburst lasted for roughly 24 days, with enhanced X-ray flux observed between August 7 2019 and August 31 2019 (see Fig. 1 of Ref. [215]). We note that the *Swift* X-ray Telescope observed increased X-ray activity from August 6 2019, and observations in the optical i'-band with the Las Cumbres Observatory network detected an increased flux from July 25 2019 [216].

Outburst events are attributed to in-falling plasma that is channeled by the magnetosphere onto a localized region on the neutron star surface, creating a hot spot that rotates with the star [273]. As the observed X-ray flux is assumed to be linearly proportional to the mass accretion rate, an outburst could result in a larger mountain on the neutron star surface (or excite r-modes in the interior), compared to when the AMXP is in quiescence [217, 274].

If continuous gravitational waves are only emitted from SAX J1808.4−3658 when it is in outburst, searching all of the O3 data decreases the signal-to-noise ratio, as compared to only searching data from the outburst. To protect against this possibility, we do an additional search for continuous gravitational waves from SAX J1808.4−3658 using data from both LIGO observatories between 1249171218 GPS time (August 7 2019) and 1251244818 GPS time (August 31 2019), rather than data from the entirety of O3, as in Sec. 4.7.18.

4.8. *Search parameters*

The search algorithm is laid out in Sec. 4.2. We run the search using three different coherence times, setting $T_{\text{drift}} = 1$ d, $T_{\text{drift}} = 8$ d, and $T_{\text{drift}} = 24$ d. We search three sub-bands centered on $\{1, 4/3, 2\}f_\star$, for each T_{drift}. The width of the sub-band depends on T_{drift}. It is ~ 0.76 Hz for the searches with $T_{\text{drift}} = 1$ d and 8 d, and is ~ 1.01 Hz for the search with $T_{\text{drift}} = 24$ d. Given the precise timing achieved during the outburst in 2019 [215], and the shorter search duration, only one $\{P,\ T_{\text{asc}},\ a_0\}$ template is required for each sub-band, according to Eqs. (4.5)–(4.7). Due to the different values of T_{drift}, shorter total duration, and different number of templates, we re-calculate $\mathcal{L}_{\text{th}}$ for each sub-band and value of T_{drift}, using the procedure outlined in Sec. 4.4.3 and Appendix 4.A1. As in the full O3 search, we set the probability of false alarm in each sub-band at $\alpha_{N_{\text{tot}}} = 0.3$. For all candidates that have $\mathcal{L} > \mathcal{L}_{\text{th}}$ we apply the three vetoes described in 4.6.

4.8. *Search results*

For $T_{\text{drift}} = 1$ d, the search in the $f_\star$ sub-band returns one candidate above $\mathcal{L}_{\text{th}}$. The candidate survives both veto A (known line) and veto B (single interferometer), but fails veto C (off-target). The searches in the $4/3f_\star$ and $2f_\star$ sub-bands do not return any candidates above $\mathcal{L}_{\text{th}}$.

For $T_{\text{drift}} = 8$ d, there are no candidates above $\mathcal{L}_{\text{th}}$ in any of the three sub-bands.

For $T_{\text{drift}} = 24\,\text{d}$, the searches in the $4f_\star/3$ and $2f_\star$ sub-bands do not return any candidates above $\mathcal{L}_{\text{th}}$. The search in the $f_\star$ sub-band does return one candidate above $\mathcal{L}_{\text{th}}$. This candidate survives all of the vetoes outlined in Sec. 4.6. We remind the reader that with $\alpha_{N_{\text{tot}}} = 0.3$ and nine sub-bands searched (three for each of the three choices of T_{drift}), we should expect ~ 3 candidates above threshold purely due to noise. The probability that we would see a value of $\mathcal{L}$ at least this large if this sub-band is pure noise, p_{noise}, is 0.02. The template and frequency of the candidate are not coincident with any candidate from the full O3 search (see Table 4.6) or the sub-threshold candidate found in the search of this sub-band in O2 data [182]. By setting $T_{\text{drift}} = T_{\text{obs}} = 24\,\text{d}$ we perform a fully coherent search across this time period, with a frequency bin size of $\Delta f = 2.4 \times 10^{-7}\,\text{Hz}$. We describe in Appendix 4.A3 further follow-up of this candidate. In summary, we find no significant evidence that it is an astrophysical signal rather than a noise fluctuation.

4.9. Frequentist upper limits

If we assume that the remaining candidates reported in Sec. 4.7 and Appendix 4.A2 are false alarms, we can place an upper limit on the wave strain that is detectable at a confidence level of 95%, $h_0^{95\%}$, in a sub-band. The value of $h_0^{95\%}$ is a function of our algorithm, the detector configuration during O3, and our assumptions about the signal model. We describe the method used to estimate $h_0^{95\%}$ in Sec. 4.9.1, present the upper limits in each sub-band in Sec. 4.9.2, and compare the results to indirect methods that calculate the expected strain in the $2f_\star$ sub-band in Sec. 4.9.3. The astrophysical implications are discussed in Sec. 4.9.4.

4.9. Upper limit procedure in a sub-band

We set empirical frequentist upper limits in each sub-band using a sequence of injections into O3 SFTs. For each sub-band we inject $N_{\text{trials}} = 100$ simulated binary signals at 12–15 fixed values of h_0 using `lalapps_Makefakedata_v5` [207]. For each of the N_{trials} injections at a fixed h_0 we select a constant injection frequency, f_{inj}, uniformly from the sub-band. While the injected signal has zero spin-wandering, we still use $T_{\text{drift}} = 10\,\text{d}$ in the search algorithm outlined in Sec. 4.2 to mimic the real search. The injected period, P_{inj}, and time of ascension, $T_{\text{asc,inj}}$ are chosen uniformly from the ranges $[P - 3\sigma_P, P + 3\sigma_P]$ and $[T_{\text{asc}} - 3\sigma_{T_{\text{asc}}}, T_{\text{asc}} + 3\sigma_{T_{\text{asc}}}]$ respectively. We keep a_0 fixed at the precisely known value for each target. The polarization, ψ, is chosen uniformly from the range $[0, 2\pi]$. The cosine of the projected inclination angle of the neutron star spin axis with our line of sight, $\cos\iota$, is chosen uniformly from the range $[-1, 1]$[7]. We then search for the injected signal with the template in this sub-band's template grid that is nearest to $\{P_{\text{inj}}, T_{\text{asc,inj}}\}$. We re-calculate $\mathcal{L}_{\text{th}}$ such that the probability of false alarm in each sub-band is $\alpha_{N_{\text{tot}}} = 0.01$. This allows us to set conservative upper limits, even in sub-bands where we have marginal candidates above a threshold corresponding to a probability of false alarm of

[7] While the inclination angle of the binary with respect to our line of sight is restricted via EM observations for some of our targets, we opt to marginalize over $\cos\iota$ as the neutron star spin axis may not necessarily align with the orbital axis of the binary. It is possible to scale our results via equation (19) of Ref. [263], if one wishes to fix $\cos\iota$.

30% per sub-band. By recording the fraction of injected signals we recover at each h_0 with $\mathcal{L} > \mathcal{L}_{\rm th}$ we estimate the efficiency, ε, as a function of h_0. We then perform a logistic regression [155] to obtain a sigmoid fit to $\varepsilon(h_0)$, and solve

$$\varepsilon(h_0^{95\%}) = 0.95\,, \tag{4.11}$$

to find an estimate of $h_0^{95\%}$ in the given sub-band.

One might reasonably ask, how precise is this estimate of $h_0^{95\%}$? The main factors impacting the precision are: i) the precision of the most likely parameters of the sigmoid, as estimated via logistic regression, when solving Eq. (4.11) for $h_0^{95\%}$, given the $N_{\rm trials}$ injections done at 12–15 values of h_0; and ii) the assumption that the strain data (and hence the SFTs) are perfectly calibrated. We investigate the impact of (i) by drawing alternative sigmoid fits of $\varepsilon(h_0)$ using the covariance matrix of the parameters returned by the logistic regression. We find that inverting these alternative fits through Eq. (4.11) results in a value of $h_0^{95\%}$ that varies by less than 5% from the value calculated via the most likely parameters (at the 95% confidence level). The impact of (ii) is trickier to quantify. As described in Refs. [269, 270] the median systematic error in the magnitude of the strain is less than 2% in the 20–2000 Hz frequency band across O3a. The statistical uncertainty around the measurement of calibration bias means that in the worst case the true magnitude of the calibration bias may be as large as 7%. However, the calibration bias at a given frequency is not correlated between the detectors (see Figures 16 and 17 in Ref. [269]), and so the impact on a continuous gravitational wave search that combines data from both detectors is likely to be less than 7%.

In light of the above considerations we quote $h_0^{95\%}$ to a precision of two significant figures, but we emphasize that estimating $h_0^{95\%}$ involves many (potentially compounding) uncertainties. Subsequent conclusions about the physical system that are drawn from estimates of $h_0^{95\%}$ cannot be more precise than the estimate of $h_0^{95\%}$ itself.

4.9. *Upper limits*

The estimates of $h_0^{95\%}$ for each target and sub-band are listed in Table 4.3. Dashes correspond to sub-bands that are highly contaminated with noise lines, which preclude the procedure described in Sec. 4.9.1, as one always finds $\mathcal{L} > \mathcal{L}_{\rm th}$, regardless of h_0. The most sensitive sub-bands are for IGR J17062–6143 with $h_0^{95\%} = 4.7 \times 10^{-26}$ in both the $4f_\star/3$ and $2f_\star$ sub-bands (centered around 218.2 Hz and 327.6 Hz respectively). These sub-bands lie in the most sensitive band of the detector, and the binary elements are known to high precision [226], so only one template is needed in each sub-band, corresponding to a relatively lower $\mathcal{L}_{\rm th}$ at fixed probability of false alarm.

No estimates of $h_0^{95\%}$ were established in Ref. [182] for the five targets therein. The search of XTE J1751–305 in S6 data estimated $h_0^{95\%} \approx 3.3 \times 10^{-24}$, 4.7×10^{-24}, and 7.8×10^{-24} in three sub-bands corresponding to $f_\star$, an r-mode frequency, and $2f_\star$ respectively [199]. Our estimates of $h_0^{95\%}$ for XTE J1751–305 improve these results by two orders of magnitude, because the detector is more sensitive, and $T_{\rm drift}$ is longer.

Table 4.3: Upper limits on the detectable gravitational wave strain at a 95% confidence level, $h_0^{95\%}$, in each of the sub-bands for each target. See Sec. 4.9.1 for details on how they are estimated, and the precision to which they are known. Upper limits are not estimated in sub-bands marked with a "–" as these sub-bands are highly contaminated with known noise lines.

	$h_0^{95\%}$ in each sub-band ($\times 10^{-26}$)		
Target	$f_\star$	$4f_\star/3$	$2f_\star$
IGR J00291+5934	–	7.6	11
MAXI J0911−655	7.7	6.4	7.3
XTE J0929−314	5.1	5.3	6.4
IGR J16597−3704	7.5	–	5.6
IGR J17062−6143	8.1	4.7	4.7
IGR J17379−3747	8.5	7.4	10
SAX J1748.9−2021	9.2	7.7	10
NGC 6440 X−2	6.2	7.2	5.8
IGR J17494−3030	8.3	–	9.0
Swift J1749.4−2807	11	17	24
IGR J17498−2921	7.0	6.6	8.4
IGR J17511−3057	7.5	5.5	6.6
XTE J1751−305	10	8.3	9.7
Swift J1756.9−2508	8.1	8.8	6.3
IGR J17591−2342	9.5	11	14
XTE J1807−294	6.1	5.0	5.6
SAX J1808.4−3658	6.4	6.9	8.8
XTE J1814−338	9.4	6.0	6.9
IGR J18245−2452	9.0	6.3	–
HETE J1900.1−2455	5.6	–	8.4

4.9. *Comparison to expected strain from AMXPs*

It is valuable to consider how strong the signal from our targets could be, given EM observations. If we assume that all rotational energy losses, as observed in the frequency derivative $\dot{f}_\star$, are converted into gravitational radiation, the indirect spin-down limit on the maximum strain, $h_{0,\mathrm{sd}}$, is [203]

$$h_{0,\mathrm{sd}} = 4.0 \times 10^{-28} \left(\frac{8\,\mathrm{kpc}}{D} \right) \times \left(\frac{600\,\mathrm{Hz}}{f_{\mathrm{GW}}} \right)^{1/2} \left(\frac{-\dot{f}_{\mathrm{GW}}}{10^{-14}\,\mathrm{Hz\,s^{-1}}} \right)^{1/2}, \tag{4.12}$$

where D is the distance to the target, f_{GW} is the gravitational wave frequency, and $\dot{f}_{\mathrm{GW}}$ is its derivative. In Eq. (4.12) we assume $I_{zz}/I_0 \approx 1$, i.e. the zz component of the moment-of-inertia tensor (I_{zz}) is very close to the moment-of-inertia of an undeformed star (I_0). We assume $f_{\mathrm{GW}} \approx 2f_\star$ when computing Eq. (4.12) for each of our targets. We list the best estimates for the distance to each target in the second column of Table 4.4.

These estimates are typically poorly known, especially if there is no known counterpart observed in wavelengths other than X-ray for the target. We use the central estimate of the distance in Eq. (4.12).

For AMXPs, $\dot{f}_\star$ is estimated by constructing a phase-connected timing solution when the target is in outburst, but estimates for $\dot{f}_\star$ in quiescence are also possible for targets that have gone into outburst multiple times. The $\dot{f}_\star$ observed during outburst can be either positive (corresponding to spin-up) or negative (corresponding to spin-down), while in quiescence $\dot{f}_\star$ is typically (but not always) negative [212, 213]. The third column of Table 4.4 records $\dot{f}_\star$ for each of our targets. When $\dot{f}_\star$ has been measured in multiple outburst events, only the $\dot{f}_\star$ from the most recent outburst is listed. For $\dot{f}_\star < 0$ we assume $\dot{f}_{\rm GW} \approx 2\dot{f}_\star$ in Eq. (4.12). For targets with $\dot{f}_\star < 0$ (in either quiescent or active phases) we find $10^{-28} \lesssim h_{0,\rm sd} \lesssim 10^{-27}$ (fourth column of Table 4.4), an order of magnitude lower than the estimated value of $h_0^{95\%}$.

As argued in Ref. [182], for $\dot{f}_\star > 0$ the torque due to gravitational radiation reaction may be masked by the accretion torque, allowing larger values of $\dot{f}_{\rm GW}$, as long as one has $\dot{f}_\star = \dot{f}_{\rm acc} + \dot{f}_{\rm GW}$, where $\dot{f}_{\rm acc}$ is the spin-up rate due to accretion. A reasonable choice, without excessive fine-tuning, is to set $\dot{f}_{\rm GW} \approx -\dot{f}_\star$, for an order-of-magnitude estimate in Eq. (4.12), i.e. assuming $|\dot{f}_{\rm acc}| \approx 2|\dot{f}_{\rm GW}|$. The resultant values for $h_{0,\rm sd}$ for targets with $\dot{f}_\star > 0$ are all well below the estimates of $h_0^{95\%}$ set in Sec. 4.9.2, and fall in the range $10^{-28} \lesssim h_{0,\rm sd} \lesssim 10^{-27}$.

Another avenue through which EM observations can constrain h_0 is by assuming that the X-ray flux is proportional to the mass accretion rate, and that the torque due to accretion balances the gravitational radiation reaction. The torque-balance limit is [167, 203]

$$\begin{aligned} h_{0,\rm torque} = 5 \times 10^{-27} \left(\frac{600\,\rm Hz}{f_{\rm GW}} \right)^{1/2} \\ \times \left(\frac{F_X}{10^{-8}\,\rm erg\,s^{-1}\,cm^{-2}} \right)^{1/2} , \end{aligned} \tag{4.13}$$

where F_X is the observed bolometric X-ray flux. Eq. (4.13) has a few hidden assumptions, namely: i) that the mass of the neutron star is $1.4M_\odot$, ii) that all of the accretion luminosity is radiated as an X-ray flux, and iii) that the accretion torque is applied at the radius of the neutron star, which is set to 10 km. The exact dependence of the torque-balance limit on these assumptions is discussed in Ref. [167]. We take $f_{\rm GW} \approx 2f_\star$ for each of our targets, as for Eq. (4.12). We take $F_X = F_{X,\rm max}$, the maximum recorded X-ray flux from each target when it was in outburst (fifth column of Table 4.4), providing an upper limit on $h_{0,\rm torque}$ (sixth column of Table 4.4). We find $5 \times 10^{-28} \lesssim h_{0,\rm torque} \lesssim 1 \times 10^{-27}$ across all targets.

4.9. Astrophysical implications

The estimates of $h_0^{95\%}$ given in Sec. 4.9.2 can be converted into constraints on the physical parameters that govern the mechanism putatively generating continuous gravitational waves in each sub-band.

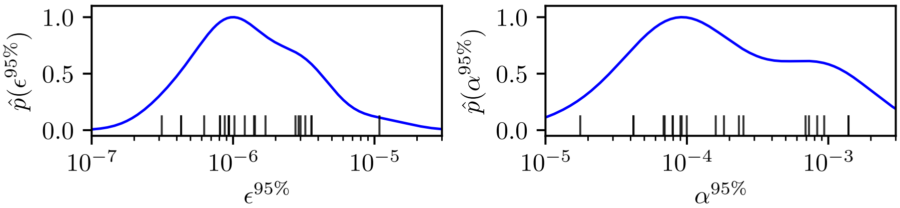

Figure 4.3: Kernel density estimate of the PDF of the constraints on ellipticity $\epsilon^{95\%}$ (left panel) and dimensionless r-mode amplitude $\alpha^{95\%}$ (right panel) via Eqs. (4.14) and (4.15) respectively. Both PDFs are normalized to a height of one. The black dashes in both panels correspond to the individual estimates of $\epsilon^{95\%}$ or $\alpha^{95\%}$ from each target.

In the $2f_\star$ sub-band the simplest emission mechanism is that of a perpendicular biaxial rotator (using the language from Ref. [297]), for which we calculate the upper limit of the ellipticity of the neutron star as [206]

$$\epsilon^{95\%} = 2.1 \times 10^{-6} \left(\frac{h_0^{95\%}}{10^{-25}} \right) \left(\frac{D}{8\,\mathrm{kpc}} \right) \left(\frac{600\,\mathrm{Hz}}{f_{\mathrm{GW}}} \right)^2 , \tag{4.14}$$

assuming $I_{zz} = 10^{38}\,\mathrm{kg\,m}^2$. Using the central estimate for D (second column of Table 4.4), we find the strictest constraint, from all of our targets, $\epsilon^{95\%} = 3.1 \times 10^{-7}$ for IGR J00291+5934. A kernel density estimate of the probability density function (PDF) of the constraints $\epsilon^{95\%}$, $\hat{p}(\epsilon^{95\%})$, for all our targets, is shown in the left panel of Fig. 4.3. It is peaked around $\epsilon^{95\%} \sim 10^{-6}$.

In the $4f_\star/3$ sub-band the emission mechanism is via r-modes, the strength of which is parametrized as [298]

$$\alpha^{95\%} = 1.0 \times 10^{-4} \left(\frac{h_0^{95\%}}{10^{-25}} \right) \left(\frac{D}{8\,\mathrm{kpc}} \right) \left(\frac{600\,\mathrm{Hz}}{f_{\mathrm{GW}}} \right)^3 . \tag{4.15}$$

Eq. (4.15) assumes $f_{\mathrm{GW}} \approx 4f_\star/3$, which may not be true, as discussed in Sec. 4.4 [260, 261]. The strictest constraint, from all of our targets, is $\alpha^{95\%} = 1.8 \times 10^{-5}$, again for IGR J00291+5934. A kernel density estimate of the PDF of the constraints $\alpha^{95\%}$, $\hat{p}(\alpha^{95\%})$, for all our targets, is shown in the right panel of Fig. 4.3. It is peaked around $\alpha^{95\%} \sim 10^{-4}$.

The kernel density estimates of the PDFs $\hat{p}(\epsilon^{95\%})$ and $\hat{p}(\alpha^{95\%})$ in Fig. 4.3 are not constraints on ϵ and α respectively, nor are they expressing the uncertainty in each individual estimate of $\epsilon^{95\%}$ or $\alpha^{95\%}$ (which are dominated by the uncertainty in $h_0^{95\%}$, and the distance, see column two of Table 4.4). They are instead presented to indicate where the constraints on $\epsilon^{95\%}$ and $\alpha^{95\%}$ lie, given the strain upper limits calculated for the targets in this search. That is, they are estimates of the true probability distribution of the constraints one would obtain for ϵ and α, given a large population of AMXPs (assuming the targets studied here are representative of this larger population). The kernel density estimates are calculated by summing Gaussian kernels centered on each data point, with bandwidth chosen to minimize the asymptotic mean integrated square error [139].

The physical mechanism for emission in the $f_\star$ sub-band is less well-defined. A biaxial non-perpendicular rotator emits gravitational radiation at both $f_\star$ and $2f_\star$ [206, 254, 299]. The emission at $f_\star$ dominates the $2f_\star$ emission for both $\theta \lesssim 20^\circ$ and $|\cos\iota| \lesssim 0.8$, where θ is the wobble angle (see figure 5 of Ref. [297] for details). The value of θ is low for certain models involving pinned superfluid interiors [47, 254]. Other possibilities exist, including a triaxial rotator [300–302]. We recommend future searches to also consider searching the $f_\star$ sub-band, due to the wealth of information that a continuous gravitational wave detection at this frequency would provide regarding neutron star structure.

4.10. Conclusions

We present the results of a search for continuous gravitational waves from 20 accreting low-mass X-ray binaries in the Advanced LIGO O3 dataset. Five of these targets were searched before in O2 [182], and one was searched in S6 [199]. The search pipeline we use allows for spin-wandering and tracks the orbital phase of the binary via a hidden Markov model and the $\mathcal{J}$-statistic respectively. The targets have well-constrained rotational frequencies, $f_\star$, and orbital elements from electromagnetic observations of outburst events, restricting the parameter space. For each target we search three ~ 0.61 Hz-wide sub-bands centered on $\{1, 4/3, 2\}f_\star$. We also perform a target-of-opportunity search for emission from SAX J1808.4–3658, which went into outburst during O3a.

We find no candidates that survive our veto procedure and are above a threshold corresponding to a 1% false alarm probability per sub-band. We find 16 candidates that survive our astrophysical vetoes when we set the threshold to 30% false alarm probability per sub-band. As we search a total of 60 sub-bands, this number of surviving candidates is consistent with the expected number of false alarms. These candidates are systematically investigated with further follow-up. In all cases, the follow-up does not provide convincing evidence that any are real astrophysical signals. However, they could not be convincingly ruled out, which is not surprising given their borderline significance. We record the orbital template and frequencies recovered for these candidates, and recommend that they are followed up in future gravitational wave data sets, and with different pipelines.

The target-of-opportunity search returns one candidate above threshold that survives our veto procedure. Additional, detailed follow-up of this candidate does not produce convincing evidence that it is a true astrophysical signal rather than a noise fluctuation.

Assuming all of the candidates are not astrophysical, we set upper limits on the strain at 95% confidence in each sub-band. Using these estimates, the strictest constraint on neutron star ellipticity is $\epsilon^{95\%} = 3.1 \times 10^{-7}$. The strictest constraint we place on the r-mode amplitude is $\alpha^{95\%} = 1.8 \times 10^{-5}$. Both of these constraints come from IGR J00291+5934.

Acknowledgments

This material is based upon work supported by NSF's LIGO Laboratory which is a major facility fully funded by the National Science Foundation. The authors also gratefully acknowledge the support of the Science and Technology Facilities Council (STFC) of the United Kingdom, the Max-Planck-Society (MPS), and the State of Niedersachsen/Germany for support of the construction of Advanced LIGO and construction and operation of the GEO600 detector. Additional support for Advanced LIGO was provided by the Australian Research Council. The authors gratefully acknowledge the Italian Istituto Nazionale di Fisica Nucleare (INFN), the French Centre National de la Recherche Scientifique (CNRS) and the Netherlands Organization for Scientific Research, for the construction and operation of the Virgo detector and the creation and support of the EGO consortium. The authors also gratefully acknowledge research support from these agencies as well as by the Council of Scientific and Industrial Research of India, the Department of Science and Technology, India, the Science & Engineering Research Board (SERB), India, the Ministry of Human Resource Development, India, the Spanish Agencia Estatal de Investigación, the Vicepresidència i Conselleria d'Innovació, Recerca i Turisme and the Conselleria d'Educació i Universitat del Govern de les Illes Balears, the Conselleria d'Innovació, Universitats, Ciència i Societat Digital de la Generalitat Valenciana and the CERCA Programme Generalitat de Catalunya, Spain, the National Science Centre of Poland and the Foundation for Polish Science (FNP), the Swiss National Science Foundation (SNSF), the Russian Foundation for Basic Research, the Russian Science Foundation, the European Commission, the European Regional Development Funds (ERDF), the Royal Society, the Scottish Funding Council, the Scottish Universities Physics Alliance, the Hungarian Scientific Research Fund (OTKA), the French Lyon Institute of Origins (LIO), the Belgian Fonds de la Recherche Scientifique (FRS-FNRS), Actions de Recherche Concertées (ARC) and Fonds Wetenschappelijk Onderzoek – Vlaanderen (FWO), Belgium, the Paris Île-de-France Region, the National Research, Development and Innovation Office Hungary (NKFIH), the National Research Foundation of Korea, the Natural Science and Engineering Research Council Canada, Canadian Foundation for Innovation (CFI), the Brazilian Ministry of Science, Technology, and Innovations, the International Center for Theoretical Physics South American Institute for Fundamental Research (ICTP-SAIFR), the Research Grants Council of Hong Kong, the National Natural Science Foundation of China (NSFC), the Leverhulme Trust, the Research Corporation, the Ministry of Science and Technology (MOST), Taiwan, the United States Department of Energy, and the Kavli Foundation. The authors gratefully acknowledge the support of the NSF, STFC, INFN and CNRS for provision of computational resources. This work was supported by MEXT, JSPS Leading-edge Research Infrastructure Program, JSPS Grant-in-Aid for Specially Promoted Research 26000005, JSPS Grant-in-Aid for Scientific Research on Innovative Areas 2905: JP17H06358, JP17H06361 and JP17H06364, JSPS Core-to-Core Program A. Advanced Research Networks, JSPS Grant-in-Aid for Scientific Research (S) 17H06133, the joint research program of the Institute for Cosmic Ray Research, University of Tokyo, National Research Foundation (NRF) and Computing Infrastructure Project of KISTI-GSDC in Korea, Academia Sinica (AS), AS Grid Center (ASGC) and the Ministry of Science and Technology (MoST) in Taiwan under grants including AS-CDA-105-M06, Advanced Technology Center (ATC) of NAOJ, and Mechanical Engineering Center of KEK.

This work is supported by NASA through the NICER mission and the Astrophysics Explorers Program and uses data and software provided by the High Energy Astrophysics Science Archive Research Center (HEASARC), which is a service of the Astrophysics Science Division at NASA/GSFC and High Energy Astrophysics Division of the

Smithsonian Astrophysical Observatory.

4.A1. Threshold setting

In this Appendix we outline two alternative methods to set thresholds for the search. In Appendix 4.A1.1 we detail the method in Ref. [181] to set thresholds by modeling the tail of the log-likelihood distribution in noise as an exponential. In Appendix 4.A1.2 we review the non-parametric method in Refs. [168, 169, 182, 195, 303], which takes a certain percentile detection statistic from noise-only realizations as the threshold. We compare the methods in Appendix 4.A1.3. In Appendix 4.A1.4 we discuss generating noise realizations using off-target searches, and justify the approach taken in this paper. In Appendix 4.A1.5 we specify how to calculate p_{noise}, the probability that we see a value of $\mathcal{L}$ at least as high as a certain candidate in a given sub-band.

Whatever the method, the threshold depends on both the target's projected semi-major axis, a_0, and the sub-band frequency, f, as log-likelihoods depend non-linearly on $a_0 f$ as an increased number orbital sidebands are included in the $\mathcal{J}$-statistic at higher $a_0 f$ [see equation (6) in Ref. [181] and Ref. [200] for details]. For this reason we set thresholds independently for each target and sub-band.

4.A1. Exponential tail method

The PDF of the log-likelihood, $p(\mathcal{L})$, for the most likely path for a given template is observed to have an exponentially distributed tail in noise,

$$p(\mathcal{L}) = A\lambda \exp\left[-\lambda\left(\mathcal{L} - \mathcal{L}_{\text{tail}}\right)\right] \quad \text{for} \quad \mathcal{L} > \mathcal{L}_{\text{tail}} \,, \tag{4.16}$$

where A is a normalization constant, λ is a parameter to be found empirically, and $\mathcal{L}_{\text{tail}}$ is a cut-off that must also be determined empirically.

For each target and sub-band we estimate λ and $\mathcal{L}_{\text{tail}}$ using a set of M sample log-likelihoods, a subset of which have $\mathcal{L} > \mathcal{L}_{\text{tail}}$. This subset is denoted $S_{N_{\text{tail}}} \equiv \{\mathcal{L}_i\}$, $i \in \{1, ..., N_{\text{tail}}\}$. The entire set of M samples is generated by running the search on $N_{\text{G}} = 100$ realizations of Gaussian noise. To keep N_{G} small enough to be computationally feasible we include log-likelihoods from all possible Viterbi paths through the sub-band for each template, instead of just the log-likelihood from the most likely path. Thus, we have $M = N_{\text{G}} N_f N_B$, where $N_f = 2^{20}$ is the number of frequency bins in each sub-band, and N_B is the number of binary orbital templates needed for each individual sub-band, as listed in Table 4.2. Separate tests, not shown here, indicate that including the log-likelihoods from non-maximal paths does not change the shape of $p(\mathcal{L})$, and therefore does not change the thresholds $\mathcal{L}_{\text{th}}$, if the appropriate trials factor is taken into account.

Assuming each $\mathcal{L}_i$ is independent, the maximum likelihood estimator, $\hat{\lambda}$, for λ is

$$\hat{\lambda} = \frac{N_{\text{tail}}}{\sum_{i=1}^{N_{\text{tail}}} \left(\mathcal{L}_i - \mathcal{L}_{\text{tail}}\right)} \,. \tag{4.17}$$

The normalization $A = N_{\text{tail}}/M$ is fixed via the fraction of total samples used to construct $p(\mathcal{L})$. The cut-off $\mathcal{L}_{\text{tail}}$ is estimated in each sub-band as the smallest value $\mathcal{L}^*$ where a histogram of the samples $\mathcal{L}_i > \mathcal{L}^*$ has approximately constant slope when viewed on log-linear axes. Each $\mathcal{L}_i$ is independent for the long coherence times ($T_{\text{drift}} = 10\,\text{d}$) used in this search, as $N_T \ll N_f$ implies most optimal paths through the sub-band are not correlated.

The probability, α, that $\mathcal{L}$ is above some threshold $\mathcal{L}_{\text{th}} > \mathcal{L}_{\text{tail}}$ if no signal is present (i.e. in pure noise) is

$$\int_{\mathcal{L}_{\text{th}}}^{\infty} \mathrm{d}\mathcal{L}\, p(\mathcal{L}) = \alpha \ . \tag{4.18}$$

Combining Eqs. (4.8), (4.16), and (4.18) we solve for $\mathcal{L}_{\text{th}}$ in a given sub-band, viz.

$$\mathcal{L}_{\text{th}} = -\frac{1}{\hat{\lambda}} \log\left(\frac{N_{\text{G}}\alpha_{N_{\text{tot}}}}{N_{\text{tail}}}\right) + \mathcal{L}_{\text{tail}} \ , \tag{4.19}$$

where Eq. (4.8) is simplified via the binomial approximation ($N_{\text{tot}} = N_f N_B \gg 1$), and $\alpha_{N_{\text{tot}}}$ is the desired false alarm probability for the search over the sub-band. Note Eq. (4.19) depends implicitly on the sub-band frequency and N_B, through $\hat{\lambda}$ and N_{tail}.

Across all targets and sub-bands we find $0.195 < \hat{\lambda} < 0.248$, with larger values corresponding to higher frequency sub-bands, and those with larger N_B. A simple rule-of-thumb is that, for a median value of $\hat{\lambda} = 0.218$, an increment of ≈ 3 in $\mathcal{L}$ is $\approx 50\%$ less likely to occur in pure noise.

4.A1. Percentile method

Given a sorted set of most likely log-likelihoods $\{\mathcal{L}_i\}$, $i \in \{1, \ldots, M\}$ with $M = N_{\text{G}} N_B$, generated via running the search algorithm over N_{G} realizations of noise for a single target and sub-band, one can pick as the threshold the $\mathcal{L}_i$ corresponding to the percentile equal to the desired false alarm probability, i.e.

$$\mathcal{L}_{\text{th}} = \mathcal{L}_j \ , \tag{4.20}$$

with $j = \lfloor \alpha_{N_{\text{tot}}} M \rfloor$. As with the method described in Appendix 4.A1.1 we may opt to use the log-likelihoods from all possible Viterbi paths through the sub-band for a given orbital template, to reduce the number of realizations of noise we need to generate. With this set of log-likelihoods, we have $M = N_{\text{G}} N_f N_B$.

4.A1. Comparison of methods

The two methods described in Appendices 4.A1.1 and 4.A1.2 give broadly similar results for $\mathcal{L}_{\text{th}}$ for a given probability of false alarm. Ref. [181] opts for the method in Appendix 4.A1.1. When Viterbi scores are used as the detection statistic, as in Ref. [181], the PDF of the score in noise does not vary with frequency, and thus the thresholds in each sub-band can be extrapolated from a small set of Gaussian noise realizations. If the PDF of the detection statistic varies with target search parameters, then the method in Appendix 4.A1.2 is used, as in Refs. [168, 169, 182, 303]. The percentile method has inherently fewer assumptions, as it does not fit a parametric model to $p(\mathcal{L})$. However it is not possible to extrapolate thresholds calculated in one sub-band to other sub-bands.

For our targets and sub-bands, we find $\mathcal{L}_{\text{th}}^{e} - \mathcal{L}_{\text{th}}^{p} \approx 2$, where the superscripts e and p correspond to the exponential tail and percentile methods respectively. However the exact difference depends on the realizations of Gaussian noise; Monte Carlo simulations indicate that with $N_{\mathrm{G}} = 100$ the calculated threshold is usually within 2% of the true value, so thresholds should only be considered precise to 2%.

4.A1. Off-target thresholds

Both methods derive $\mathcal{L}_{\mathrm{th}}$ based on realizations of Gaussian noise. However, the noise in real detector data is non-Gaussian in general [267]. To account for this we search O3 data at N_{OT} randomly chosen, but well-separated, off-target positions, to generate N_{OT} realizations of real detector noise, as originally done in Ref. [182]. We set N_{OT} such that $N_B N_{\mathrm{OT}} > 500$, with a minimum value of $N_{\mathrm{OT}} = 100$, to ensure enough samples are generated.

If there are no known noise lines in the sub-band, we find $4 < \mathcal{L}^e_{\mathrm{th,G}} - \mathcal{L}^p_{\mathrm{th,OT}} < 12$, where the subscripts G and OT correspond to thresholds calculated using Gaussian and off-target noise realizations respectively. That is, the thresholds calculated from Gaussian noise, using the exponential tail method are considerably more conservative than those calculated from off-target noise and the percentile method. If there are loud noise lines in the sub-band, $\mathcal{L}_{\mathrm{th,OT}}$ is often much higher, as these lines appear in the off-target noise realizations. Because off-target noise realizations are impacted by noise lines, $p(\mathcal{L})$ is not necessarily exponential in its tail. We thus opt to use the percentile method when calculating thresholds with off-target noise realizations. Table 4.5 contains the calculated $\mathcal{L}^e_{\mathrm{th,G}}$ and $\mathcal{L}^p_{\mathrm{th,OT}}$ for each target and sub-band.

As in Ref. [182] we consider $\mathcal{L}_{\mathrm{th}}$ for each sub-band to be the minimum of $\mathcal{L}^e_{\mathrm{th,G}}$ and $\mathcal{L}^p_{\mathrm{th,OT}}$, with $\alpha_{N_{\mathrm{tot}}} = 0.3$. This choice minimizes the probability that we will miss a potential candidate due to inadvertently setting our threshold too high.

4.A1. Probability that a candidate arises due to noise

As discussed in Sec. 4.4.3, when we set $\alpha_{N_{\mathrm{tot}}} = 0.3$ we expect ~ 18 candidates above $\mathcal{L}_{\mathrm{th}}$, across all targets and sub-bands. Let us quantify empirically the probability, p_{noise}, that, if the data in a given sub-band are pure noise, we see at least one template with log-likelihood higher than that of the candidate, $\mathcal{L}_{\mathrm{cand}}$. We have

$$p_{\mathrm{noise}} = \frac{\sum_{i=1}^{M} \mathbb{1}\left(\mathcal{L}_i > \mathcal{L}_{\mathrm{cand}}\right)}{M} , \qquad (4.21)$$

where $\mathbb{1}(\ldots)$ is the indicator function which returns 1 when the argument is true, otherwise 0. In this paper we calculate Eq. (4.21) for each candidate with $\mathcal{L} > \mathcal{L}_{\mathrm{th}}$ using the set of log-likelihoods, $\{\mathcal{L}_i\}$, generated via off-target realizations as discussed in Appendix 4.A1.4. As in Appendix 4.A1.2, we set $M = N_{\mathrm{G}} N_B$ to account for the extra "trials factor" needed for sub-bands with multiple templates.

4.A2. Full search results and survivor follow-up

This Appendix collates the full search results for reference and reproducibility for all targets in Figs. 4.4a–4.4s (except for IGR J18245−2452 which is shown in Fig. 4.2). Each of Figs. 4.4a–4.4s is laid out identically to Fig. 4.2.

The orbital parameters (P, a_0, and $T_{\rm asc}$), terminating frequency bin [$f(N_T)$], log-likelihood ($\mathcal{L}$), and $p_{\rm noise}$, the probability that a search of that candidate's sub-band in pure noise would return at least one candidate at least as loud as the one seen are shown in Table 4.6, for each of the candidates that survive all vetoes and have $\mathcal{L} > \mathcal{L}_{\rm th}$.

4.A2. *Additional follow-up for survivors*

The full frequency paths, $f(t) - f(N_T)$, for all candidates with $p_{\rm noise} \leq 0.1$ are shown in the top panels of Figs. 4.5a–4.5e. The bottom panels of Figs. 4.5a–4.5e display the cumulative log-likelihood along the frequency path relative to the average sum log-likelihood needed to reach $\mathcal{L}_{\rm th}$, namely $C\mathcal{L} \equiv \sum_{i=0}^{i=t}\left[\mathcal{L}(i) - \mathcal{L}_{\rm th}/N_T\right]$, where $\sum_{i=0}^{i=t}\mathcal{L}(i)$ is $\ln P(Q^*|O)$ from Eq. (4.2) truncated after the t-th segment. Over-plotted (blue dashed line) is the average cumulative log-likelihood needed at each data segment in order to reach $\mathcal{L}_{\rm th}$. This diagnostic indicates whether a handful of segments dominate in making the candidate's frequency path the optimal one for that template. If the candidate is a true signal, we would expect the signal strength to be approximately constant, and thus the cumulative log-likelihood should grow linearly as more data are considered. However, Monte Carlo tests with injections show that the cumulative log-likelihood only becomes linear for $\mathcal{L} \gtrsim \mathcal{L}_{\rm th} + 200$. This is not the case for any of the 16 survivor candidates, and thus their cumulative log-likelihood cannot help us distinguish whether they are truly astrophysical signals.

The sky resolution of the algorithm described in Sec. 4.2 is roughly 2 arcmin in RA and Dec., for an injection with $\mathcal{L}_{\rm th} \lesssim \mathcal{L} \lesssim \mathcal{L}_{\rm th} + 50$. The point-spread-function of an injection is an ellipse, which has a varying orientation and eccentricity dependent on the sky position. For each of our candidates we calculate $\mathcal{L}$ at 440 regularly spaced sky positions in a 100 arcmin^2 grid around the target's true location, using the template recovered from the search and listed in Table 4.6. For almost all survivor candidates, the distribution of $\mathcal{L}$ values in the patch of sky around the candidate does not match the elliptical point-spread-function we see in injections for their respective sky locations. The sole exception is Candidate 2 from IGR J16597−3704. Figure 4.6 shows $\mathcal{L}$ at 3721 regularly spaced sky positions in a 100 arcmin^2 grid around the target's true location, again using the template as listed in Table 4.6. The roughly elliptical shape is consistent with the point-spread-function of injections at this sky location. However, the region of sky with $\mathcal{L} \gtrsim \mathcal{L}_{\rm th}$ is centered ~ 1 arcmin lower in Dec. than the true declination of the source, which is known to a precision of 0.01 arcmin [224].

One final follow-up we perform for these candidates is to calculate $\mathcal{L}$ in a small, densely sampled patch of the $\{P,\ T_{\rm asc}\}$ parameter space around each candidate's template. Moderately loud injections ($\mathcal{L} \gtrsim \mathcal{L}_{\rm th} + 100$) are seen to "spread out" in the $\{P,\ T_{\rm asc}\}$ plane, and are detectable with $\mathcal{L} > \mathcal{L}_{\rm th}$ even when searching a template that has a slightly incorrect value of P and $T_{\rm asc}$. However, none of our candidates are this loud, so this diagnostic does not help us distinguish whether they are truly astrophysical signals or merely noise fluctuations.

We do not use any data from LIGO's Observing Runs 1 or 2 (O1 and O2 respectively) to aid in following up these candidates, as the detector is considerably more sensitive in O3. The duration of O3 was also longer than the durations of O1 and O2. If a candidate is only marginally above threshold in O3 data, it may be hidden in the noise in O1 and O2 data, so including data from those observing runs is not likely to increase the candidate's signal-to-noise ratio.

4.A3. Survivor follow-up for target-of-opportunity search candidate

For posterity, and to aid future follow-up with different pipelines, we record in Table 4.7 the template, the frequency f, the log-likelihood $\mathcal{L}$, and $p_{\rm noise}$, of the candidate from the target-of-opportunity search in Sec. 4.8 that survives all vetoes.

As in Appendix 4.A2.1, we perform additional follow-up for this remaining candidate. With $T_{\rm obs} = 24\,{\rm d}$ the point-spread-function of a moderately loud injection ($\mathcal{L} \gtrsim \mathcal{L}_{\rm th}+20$), at the sky location of the target, is a narrow ellipse $\sim 2\,$arcmin wide in RA, but over $\sim 30\,$arcmin tall in Dec. When we search a $100\,{\rm arcmin}^2$ patch of sky around the location of SAX J1808.4−3658 we do not see any evidence of this point-spread-function at the source location. There is an ellipse with $\mathcal{L} > \mathcal{L}_{\rm th}$ roughly $-2\,$arcmin away in RA from SAX J1808.4−3658, but as the location of the target is known to sub-arcsec precision [215], this ellipse is likely a noise fluctuation, rather than an astrophysical signal.

We also calculate $\mathcal{L}$ in a small, densely sampled patch of the $\{P,\ T_{\rm asc}\}$ parameter space around the candidate's template. As discussed in Appendix 4.A2.1, moderately loud injections ($\mathcal{L} \gtrsim \mathcal{L}_{\rm th}+20$) "spread out" in the $\{P,\ T_{\rm asc}\}$ plane. However, the candidate is not loud enough for this diagnostic to provide evidence for or against the hypothesis that the candidate is a noise fluctuation.

If we assume that the remaining candidate is a false alarm, we calculate $h_0^{95\%}$ for the 24 d coherent search, using the procedure outlined in Sec. 4.9.1. We find $h_0^{95\%} = 1.3 \times 10^{-25}$ for the sub-bands centered on $f_\star$ and $4f_\star/3$, and $h_0^{95\%} = 1.7 \times 10^{-25}$ for the sub-band centered on $2f_\star$. These upper limits are higher than the ones listed in Sec. 4.9.2 because the longer coherence time does not completely compensate for the shorter observation time.

Finally, we perform a complementary follow-up search using a deterministic signal template on the candidate of interest using `PyFstat` [304, 305]. The use of the `PyFstat` algorithm as a follow-up technique was applied to the last surviving outlier of Ref. [178] and previously in Refs. [173, 306]. The follow-up procedure, thoroughly described in Ref. [307], uses a Markov chain Monte Carlo (MCMC) sampler [308, 309] to explore a parameter-space region using the $\mathcal{F}$-statistic as log-likelihood [206]. Two coherence times are used here, namely $T_{\rm coh} = 12\,{\rm d}$ and $T_{\rm coh} = 24\,{\rm d}$. Prior distributions are Gaussian distributions centered at the outlier parameters (Table 4.7) using a standard deviation of one parameter-space bin with maximum mismatch $\mu_{\rm max} = 1$ [266]. The results of the follow-up are evaluated using a Bayes factor, $\mathcal{B}_{\rm S/N}$, that compares the evidence for a model that the data contain a coherent signal to the evidence for a model that the data contain only noise. The value of $\mathcal{B}_{\rm S/N}$ is computed by comparing the change in the $\mathcal{F}$-statistic of the loudest candidate between the two follow-up stages with different coherence times: if a signal is present in the data, the $\mathcal{F}$-statistic should provide a consistent estimate of the signal-to-noise ratio; otherwise, the loudest candidate is a result of noise, the distribution of which follows a Gumbel distribution. This noise distribution is estimated using a similar method to the one described in Appendix 4.A1.4, with 600

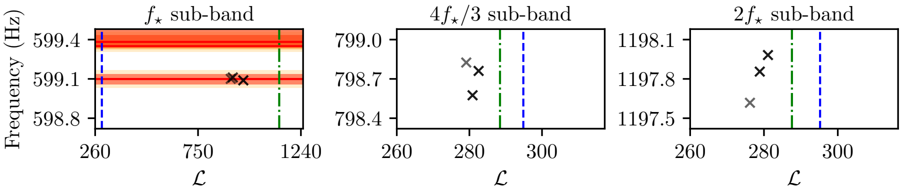

(a) Search results for IGR J00291+5934.

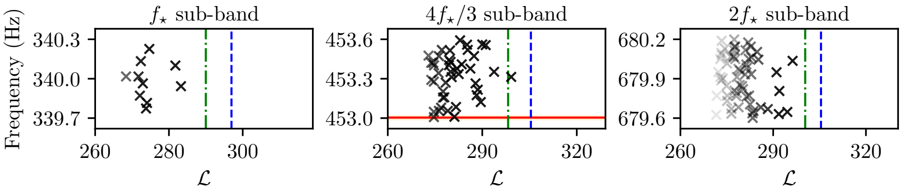

(b) Search results for MAXI J0911−655.

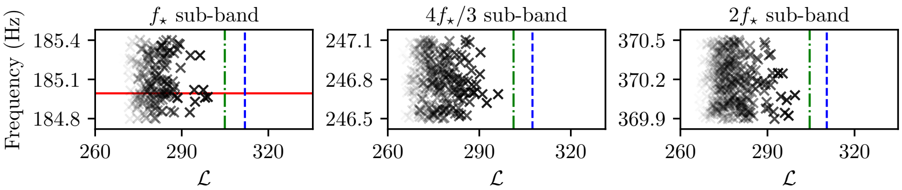

(c) Search results for XTE J0929−314.

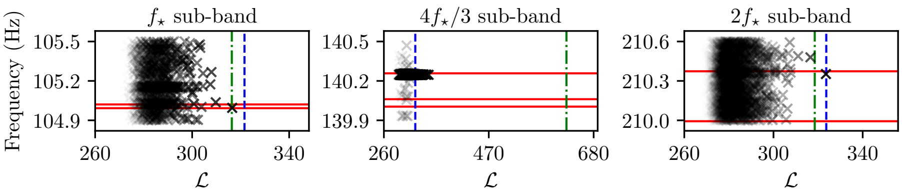

(d) Search results for IGR J16597−3704.

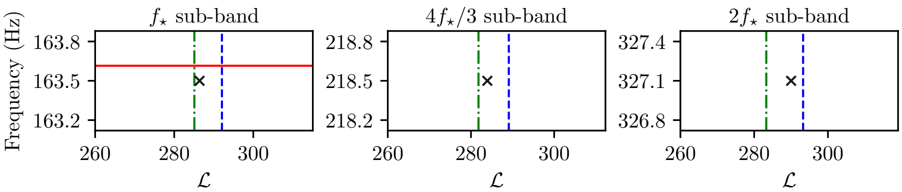

(e) Search results for IGR J17062−6143.

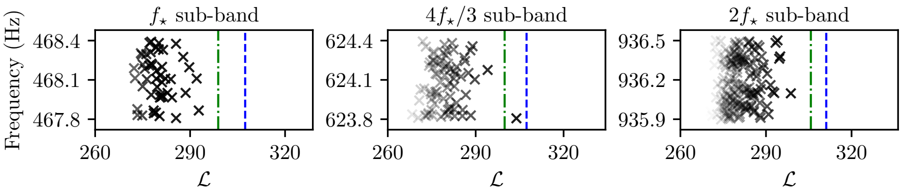

(f) Search results for IGR J17379−3747.

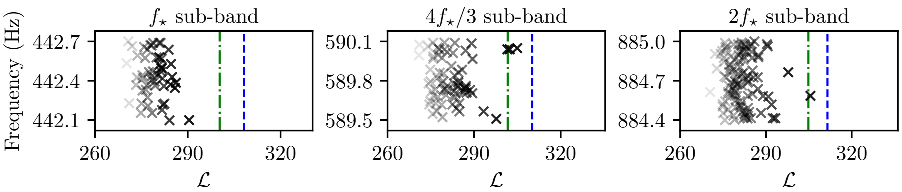

(g) Search results for SAX J1748.9−2021.

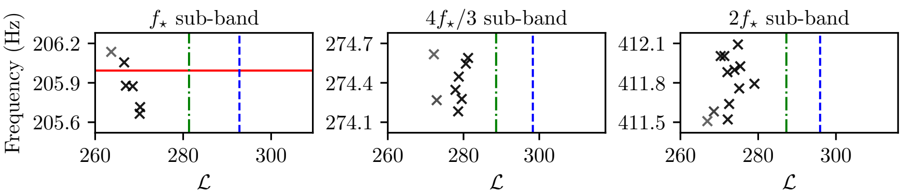

(h) Search results for NGC 6440 X−2.

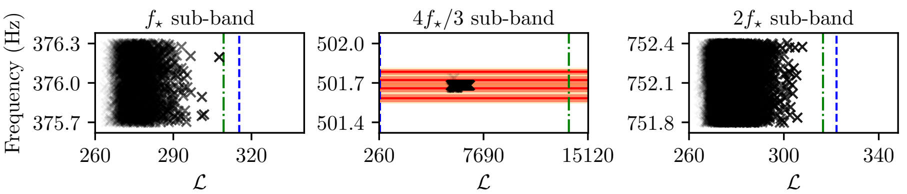

(i) Search results for IGR J17494−3030.

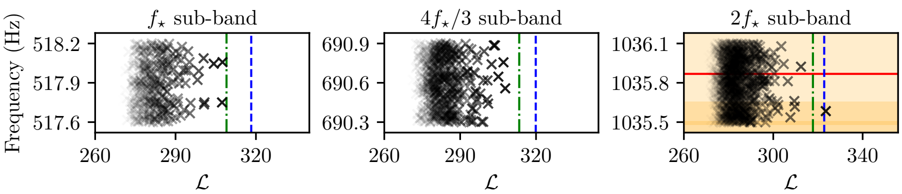

(j) Search results for Swift J1749.4−2807.

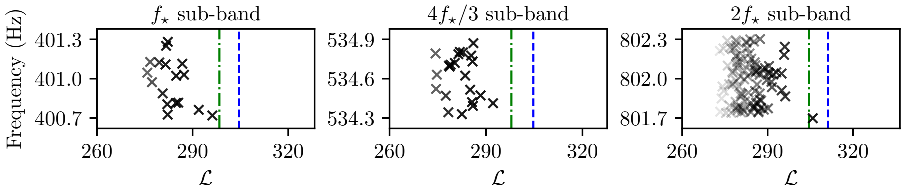

(k) Search results for IGR J17498−2921.

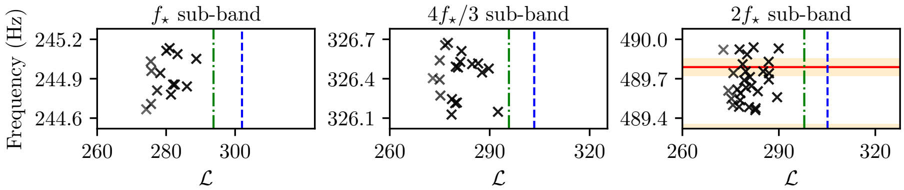

(l) Search results for IGR J17511−3057.

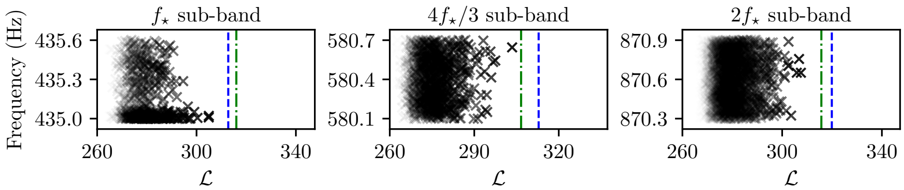

(m) Search results for XTE J1751−305.

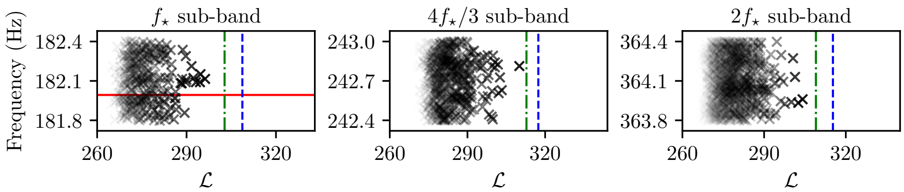

(n) Search results for Swift J1756.9−2508.

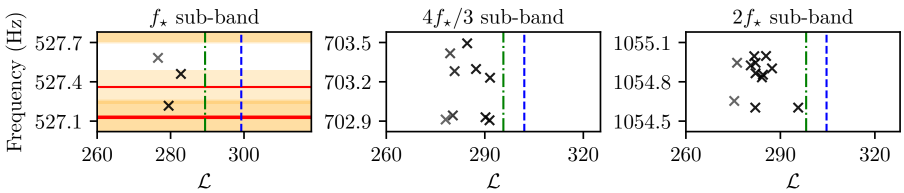

(o) Search results for IGR J17591−2342.

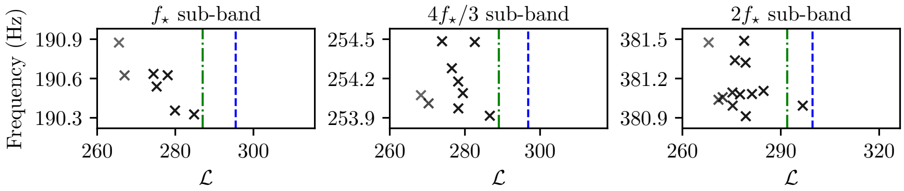

(p) Search results for XTE J1807−294.

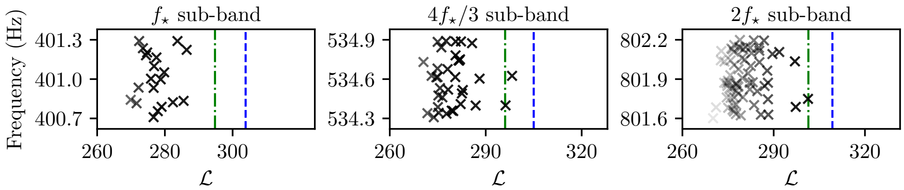

(q) Search results for SAX J1808.4−3658.

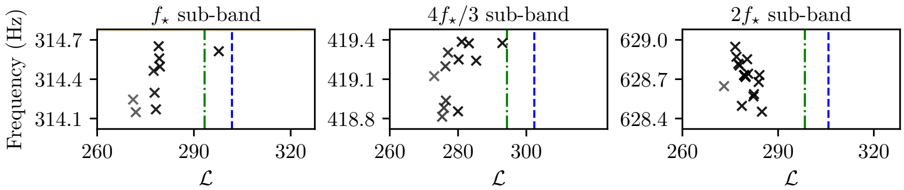

(r) Search results for XTE J1814−338.

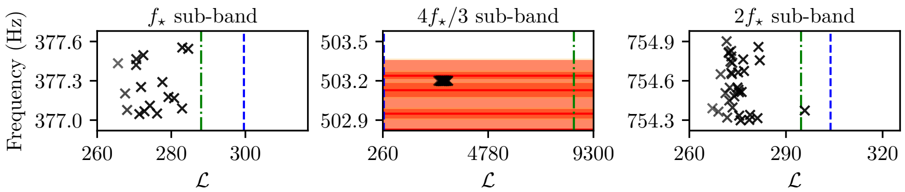

(s) Search results for HETE J1900.1−2455.

Figure 4.4: Search results for each target and sub-band, laid out as in Fig 4.2. Black crosses indicate the frequency and $\mathcal{L}$ for the most likely path through the sub-band for each binary template. The vertical blue dashed (green dot-dashed) lines correspond to the threshold set via Gaussian (off-target) noise realizations, $\mathcal{L}_{\mathrm{th,G}}$ ($\mathcal{L}_{\mathrm{th,OT}}$), in each sub-band. Solid red lines indicate the peak frequency of known instrumental lines in the Hanford or Livingston detectors; the red band indicates the width of the line and the yellow band indicates the increased effective width due to Doppler broadening, as described in Sec. 4.6.1. Multiple overlapping orange bands creates the red bands. The transparency of crosses in sub-bands with many templates, e.g. the sub-bands of IGR J16597−3704, is adjusted relative to the maximum $\mathcal{L}$ in that sub-band for clarity.

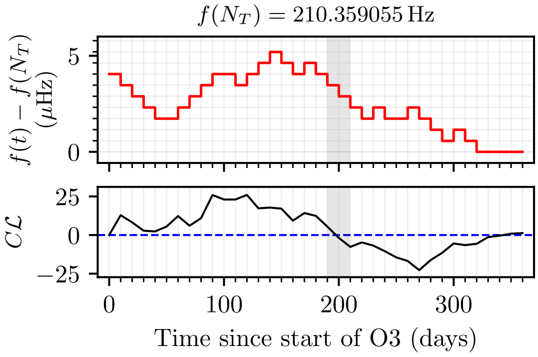

(a) Surviving candidate 2 from IGR J16597−3704.

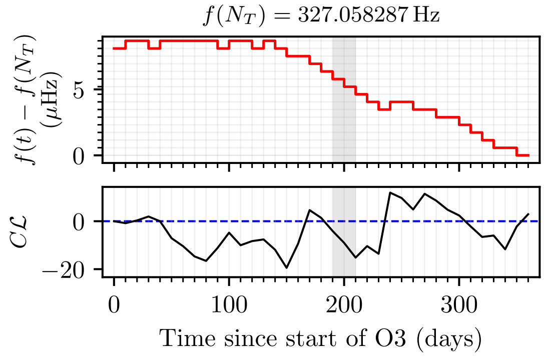

(b) Surviving candidate 3 from IGR J17062−6143.

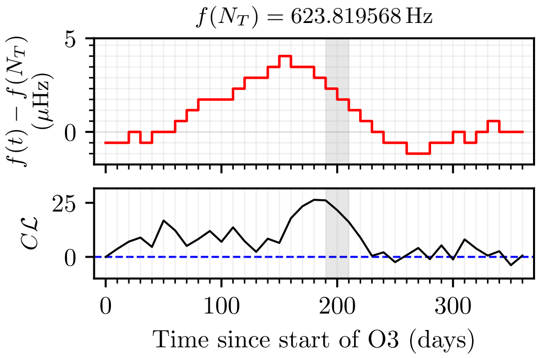

(c) Surviving candidate 1 from IGR J17379−3747.

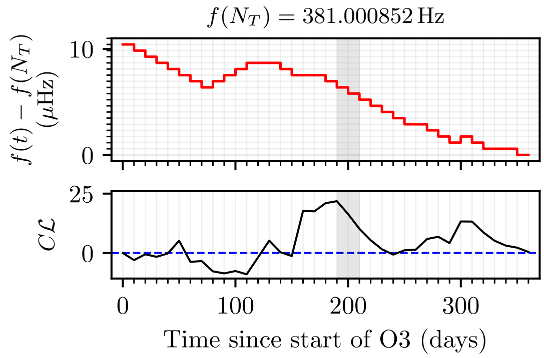

(d) Surviving candidate 1 from XTE J1807−294.

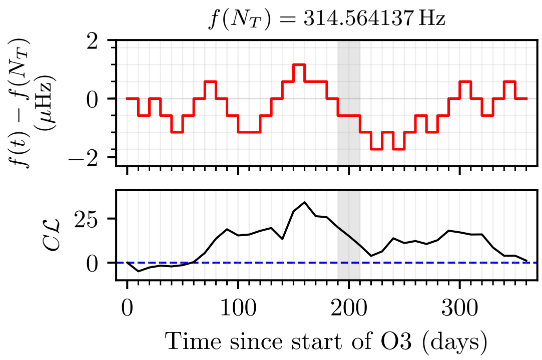

(e) Surviving candidate 1 from XTE J1814−338.

Figure 4.5: Top panels: frequency paths, $f(t)$, for candidates with $p_{\rm noise} \leq 0.1$. The terminating frequency bin, $f(N_T)$, is subtracted and displayed in the title of each figure for clarity. Faint horizontal grey lines demarcate frequency bins of size $\Delta f = 5.787037 \times 10^{-7}$ Hz, while faint vertical grey lines demarcate chunks of length $T_{\rm drift} = 10$ d. Bottom panels: the cumulative log-likelihood along the frequency path relative to the average sum log-likelihood needed to reach $\mathcal{L}_{\rm th}$, $C\mathcal{L} \equiv \sum_{i=0}^{i=t} \left[\mathcal{L}(i) - \mathcal{L}_{\rm th}/N_T\right]$, where $\sum_{i=0}^{i=t} \mathcal{L}(i)$ is $\ln P(Q^*|O)$ from Eq. (4.2) truncated after the t-th segment. The horizontal blue dashed line corresponds to $\sum_{i=0}^{i=t} \mathcal{L}(i) = t\mathcal{L}_{\rm th}/N_T$. The grey shaded regions in both top and bottom panels correspond to the segments which have no SFTs and are therefore filled with a uniform log-likelihood, as described in Sec. 4.5.

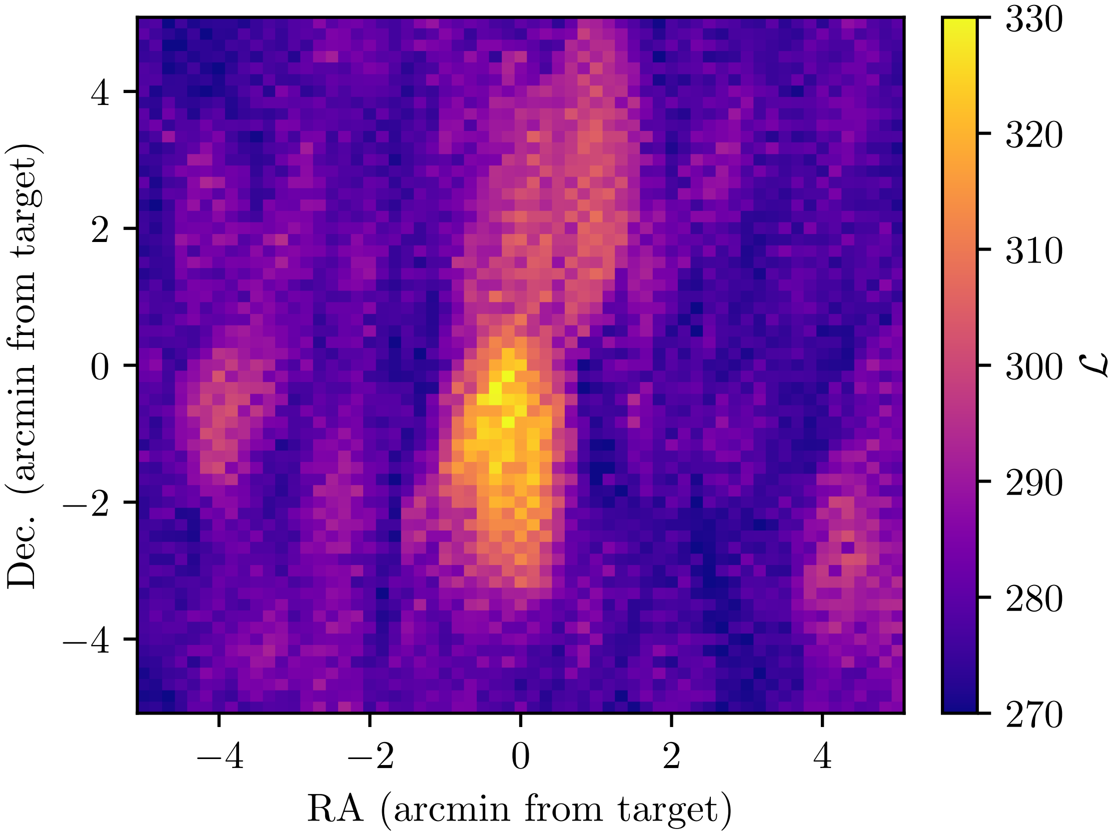

Figure 4.6: $\mathcal{L}$, as represented by the color of each pixel, calculated at 3721 regularly spaced sky locations in a 100 arcmin^2 patch of sky, centered on IGR J16597−3704. See text in Appendix 4.A2.1 for details.

off-source calculations performed.

The loudest candidate of the follow-up returns a log-Bayes factor of $\log_{10} \mathcal{B}_{\mathrm{S/N}} = 1.45$. We characterize the $\log_{10} \mathcal{B}_{\mathrm{S/N}}$ distribution using 400 isotropically distributed sources injected into the real data with an amplitude of $h_0^{95\%}$. We obtain a 1% false dismissal threshold of 8.75, which is significantly larger than the candidate's log-Bayes factor of 1.45. That is, if this were a true signal, with $h_0 = h_0^{95\%}$, we would expect the log-Bayes factor to be higher than what we see in the real data by about 7. We conclude that there is no significant evidence of continuous gravitational wave emission from this target.

Table 4.4: Maximum expected strain from each target, as inferred from EM observations. The second estimate for the distance to the target. Targets with "-" listed as the frequency derivative (third column), value during outburst, and also do not have a long-term (quiescent) $\dot{f}_\star$ measured either. The labels (A) measured in outburst and quiescence respectively. The scaling equations used to estimate the maximum column), $h_{0,\mathrm{sd}}$, and the maximum strain assuming torque-balance (sixth column), $h_{0\,\mathrm{torque}}$, are Eqs. (4.12) $h_{0,\mathrm{sd}}$ value is calculated using the central distance and $\dot{f}_\star$ estimates. The $h_{0\,\mathrm{torque}}$ value is calculated using X-ray flux measured during outburst (fifth column), $F_{X,\mathrm{max}}$, which is typically measured to a precision of each target in quiescence is not shown, as it is only measured for half of the targets, and is usually $\sim 1-2$ than $F_{X,\mathrm{max}}$. The seventh column contains $h_0^{95\%}$ in the $2f_\star$ sub-band (fourth column of Table 4.3) to facil $h_0^{95\%}$ and $h_{0\,\mathrm{torque}}$ or $h_{0,\mathrm{sd}}$.

Target	Distance (kpc)	$\dot{f}_\star$ (Hz s^{-1})	$h_{0,\mathrm{sd}}$ ($\times10^{-26}$)	$F_{X,\mathrm{max}}$ ($\times10^{-8}$ erg s^{-1} cm^{-2})	$h_{0,\mathrm{torque}}$ ($\times10^{-26}$)	h ($\times10$
IGR J00291+5934	4.2(5)	$-4.0(1.4)\times10^{-15}$ (Q)	0.05	0.35	0.2	
MAXI J0911−655	9.45(15)	-	-	0.047	0.1	
XTE J0929−314	7.4[a]	$-9.2(4)\times10^{-14}$ (A)	0.2	0.1	0.2	
IGR J16597−3704	9.1[b]	-	-	0.065	0.2	
IGR J17062−6143	7.3(5)	$+3.77(9)\times10^{-15}$ (A)	0.04[f]	0.006	0.05	
IGR J17379−3747	8[c]	$-1.2(1.9)\times10^{-14}$[e] (A)	0.05	0.04	0.08	
SAX J1748.9−2021	8.5[b]	-	-	0.077	0.1	
NGC 6440 X−2	8.5[b]	-	-	0.02	0.09	
IGR J17494−3030	8[c]	$-2.1(7)\times10^{-14}$ (Q)	0.07	0.0143	0.05	
Swift J1749.4−2807	6.7(1.3)	-	-	0.0352	0.07	
IGR J17498−2921	7.6(1.1)	$-6.3(1.9)\times10^{-14}$[e] (A)	0.1	0.2	0.2	
IGR J17511−3057	3.6(5)	$+4.8(1.4)\times10^{-14}$ (A)	0.2[f]	0.2	0.2	
XTE J1751−305	6.7[d]	$-5.5(1.2)\times10^{-15}$ (Q)	0.04	0.29	0.2	
		$+3.7(1.0)\times10^{-13}$ (A)	0.2[f]			
Swift J1756.9−2508	8[c]	$-4.8(6)\times10^{-16}$ (Q)	0.02	0.288	0.3	
		$-4.3(2.1)\times10^{-11}$[e] (A)	5			
IGR J17591−2342	7.6(7)	$-7.1(4)\times10^{-14}$ (A)	0.1	0.0535	0.09	
XTE J1807−294	8[c]	$+2.7(1.0)\times10^{-14}$ (A)	0.08[f]	0.2	0.3	
SAX J1808.4−3658	$3.3^{+0.3}_{-0.2}$	$-1.01(7)\times10^{-15}$ (Q)	0.04	0.103	0.1	
		$-3.02(13)\times10^{-13}$ (A)	0.7			
XTE J1814−338	10.25(1)	$-6.7(7)\times10^{-14}$ (A)	0.1	0.069	0.1	
IGR J18245−2452	5.5[b]	-	-	0.0466	0.1	
HETE J1900.1−2455	4.5(2)	$+4.2(1)\times10^{-13}$ (A)	0.4[f]	0.09	0.1	

[a] Estimate assumes conservative mass transfer during accretion. An alternative estimate gives less than
[b] Uncertainty not quoted as target located in a globular cluster.
[c] Unknown, but as the target is in the direction of the galactic centre a fiducial value of 8 kpc is assume
[d] Lower limit.
[e] Estimate of $\dot{f}_\star$ consistent with zero at a 3σ level.
[f] Assumes $\dot{f}_{\mathrm{GW}} \approx -\dot{f}_\star$, see text for details.

Table 4.5: Target, starting frequency, f_s, for each $\sim 0.61\,\mathrm{Hz}$-wide sub-band, threshold calculated using Gaussian noise realizations and the exponential tail method, $\mathcal{L}^{e}_{\mathrm{th,G}}$, and threshold calculated using off-target noise realizations and the percentile method, $\mathcal{L}^{p}_{\mathrm{th,OT}}$. All thresholds are calculated with $\alpha_{N_{\mathrm{tot}}} = 0.3$.

Target	f_s (Hz)	$\mathcal{L}^{e}_{\mathrm{th,G}}$	$\mathcal{L}^{p}_{\mathrm{th,OT}}$	Target	f_s (Hz)	$\mathcal{L}^{e}_{\mathrm{th,G}}$
IGR J00291+5934	598.6	291.9	1136.7	IGR J17498−2921	400.7	304.
	798.2	294.9	288.4		534.4	304.
	1197.5	295.2	287.6		801.7	311.
MAXI J0911−655	339.7	297.0	290.0	IGR J17511−3057	244.5	302.
	453.0	305.4	298.2		326.1	303.
	679.6	305.5	300.4		489.4	305.
XTE J0929−314	184.8	311.9	304.9	XTE J1751−305	435.0	312.
	246.5	307.4	301.2		580.1	312.
	369.9	310.4	304.5		870.3	319.
IGR J16597−3704	104.9	321.6	316.4	Swift J1756.9−2508	181.8	308.
	139.9	322.9	625.5		242.5	317.
	210.0	323.7	318.5		363.8	315.
IGR J17062−6143	163.4	292.1	285.1	IGR J17591−2342	527.1	299.
	217.9	289.1	281.8		702.9	302.
	327.0	293.3	283.3		1054.5	304.
IGR J17379−3747	467.8	307.4	298.9	SAX J1808.4−3658	400.7	303.
	623.8	307.4	299.9		534.3	305.
	935.9	311.1	305.7		801.6	309.
SAX J1748.9−2021	442.1	308.2	300.3	XTE J1807−294	190.3	295.
	589.5	310.1	301.6		253.9	296.
	884.4	311.5	304.9		380.9	299.
NGC 6440 X−2	205.6	292.8	281.3	XTE J1814−338	314.1	301.
	274.2	298.3	288.6		418.8	302.
	411.5	295.9	287.2		628.4	305.
IGR J17494−3030	375.7	315.3	309.3	IGR J18245−2452	254.0	311.
	501.1	317.5	13763.8		338.8	312.
	751.8	322.2	316.5		508.4	317.
Swift J1749.4−2807	517.6	316.4	308.8	HETE J1900.1−2455	377.0	299.
	690.3	318.4	311.9		502.8	303.
	1035.5	321.0	316.3		754.3	303.

Table 4.6: Orbital template, (P, a_0, $T_{\rm asc}$), terminating frequency bin, $f(N_T)$, log-likelihood, $\mathcal{L}$, and the probability that a search of the candidate's sub-band in pure noise would return a candidate just as loud, $p_{\rm noise}$, for the 16 candidates with $\mathcal{L} > \mathcal{L}_{\rm th}$ that cannot be eliminated by any of the vetoes detailed in Sec. 4.6.

Target	Candidate	P (s)	a_0 (lt-s)	$T_{\rm asc}$ (GPS time)	$f(N_T)$ (Hz)	$\mathcal{L}$	$p_{\rm noise}$
MAXI J0911−655	1	2659.933	0.0176	1238165869.0437	453.309532	299.2	0.26
IGR J16597−3704	1	2758.61	0.0048	1238163275.6122	105.002195	316.5	0.30
	2	2757.90	0.0048	1238163010.7583	210.359055	323.5	0.09
IGR J17062−6143	1	2278.2112	0.0040	1238165942.2745	163.531805	286.4	0.24
	2	2278.2112	0.0040	1238165942.2745	218.452091	283.9	0.19
	3	2278.2112	0.0040	1238165942.2745	327.058287	290.0	0.05
IGR J17379−3747	1	6765.84	0.0770	1238162768.3832	623.819568	303.9	0.08
SAX J1748.9−2021	1	31555.29	0.3876	1238151700.2214	590.048237	304.9	0.12
	2	31555.30	0.3876	1238151760.9764	590.040010	302.3	0.27
	3	31555.31	0.3876	1238151710.6406	884.592276	305.6	0.22
IGR J17498−2921	1	13835.619	0.36517	1238164013.8774	801.703605	305.8	0.22
XTE J1807−294	1	2404.416	0.00483	1238165585.2721	381.000852	296.7	0.10
SAX J1808.4−3658	1	7249.15	0.0628	1238161168.0040	534.633578	298.2	0.16
	2	7249.16	0.0628	1238161183.0831	534.407934	296.2	0.30
XTE J1814−338	1	15388.723	0.3906	1238151585.3941	314.564137	297.7	0.08
HETE J1900.1−2455	1	4995.26	0.0184	1238161529.0866	754.378543	295.8	0.25

Table 4.7: Orbital template, (P, a_0, $T_{\rm asc}$), frequency, f, log-likelihood, $\mathcal{L}$, and the probability of seeing a candidate at least this loud in pure noise, $p_{\rm noise}$, for the remaining candidate from the target-of-opportunity, 24 d coherent search when SAX J1808.4−3658 was in outburst. The candidate cannot be eliminated by any of the vetoes detailed in Sec. 4.6.

P (s)	a_0 (lt-s)	$T_{\rm asc}$ (GPS time)	f (Hz)	$\mathcal{L}$	$p_{\rm noise}$
7249.155	0.062809	1249163578.03125	400.59656098	42.5	0.02

References

[1]W. Fulgenzi, A. Melatos, and B. D. Hughes, “Radio pulsar glitches as a state-dependent Poisson process”, Monthly Notices of the Royal Astronomical Society **470**, 4307–4329 (2017).

[2]A. Melatos, C. Peralta, and J. S. B. Wyithe, “Avalanche dynamics of radio pulsar glitches”, The Astrophysical Journal **672**, 1103–1118 (2008).

[3]G. Howitt, A. Melatos, and A. Delaigle, “Nonparametric Estimation of the Size and Waiting Time Distributions of Pulsar Glitches”, The Astrophysical Journal **867**, 60 (2018).

[4]J. R. Fuentes, C. M. Espinoza, and A. Reisenegger, “Glitch time series and size distributions in eight prolific pulsars”, Astronomy and Astrophysics **630**, A115 (2019).

[5]J. M. Cordes and D. J. Helfand, “Pulsar timing. III - Timing noise of 50 pulsars”, The Astrophysical Journal **239**, 640–650 (1980).

[6]S. Price, B. Link, S. N. Shore, and D. J. Nice, “Time-correlated structure in spin fluctuations in pulsars: Time-correlated structure in pulsars”, Monthly Notices of the Royal Astronomical Society **426**, 2507–2521 (2012).

[7]A. Parthasarathy et al., “Timing of young radio pulsars $\rm {I}$: Timing noise, periodic modulation and proper motion.”, Monthly Notices of the Royal Astronomical Society **489**, 3810 (2019).

[8]C. M. Espinoza, A. G. Lyne, B. W. Stappers, and M. Kramer, “A study of 315 glitches in the rotation of 102 pulsars”, Monthly Notices of the Royal Astronomical Society **414**, 1679–1704 (2011).

[9]P. W. Anderson and N. Itoh, “Pulsar glitches and restlessness as a hard superfluidity phenomenon”, Nature **256**, 25–27 (1975).

[10]L. Warszawski and A. Melatos, “Gross-Pitaevskii model of pulsar glitches”, Monthly Notices of the Royal Astronomical Society **415**, 1611–1630 (2011).

[11]M. B. Larson and B. Link, “Simulations of glitches in isolated pulsars”, Monthly Notices of the Royal Astronomical Society **333**, 613–622 (2002).

[12]J. Middleditch, F. E. Marshall, Q. D. Wang, E. V. Gotthelf, and W. Zhang, "Predicting the Starquakes in PSR J0537-6910", The Astrophysical Journal **652**, 1531–1546 (2006).

[13]N. Andersson, G. L. Comer, and R. Prix, "Are Pulsar Glitches Triggered by a Superfluid Two-Stream Instability?", Physical Review Letters **90**, 091101 (2003).

[14]A. Mastrano and A. Melatos, "Kelvin-Helmholtz instability and circulation transfer at an isotropic-anisotropic superfluid interface in a neutron star", Monthly Notices of the Royal Astronomical Society **361**, 927–941 (2005).

[15]K. Glampedakis and N. Andersson, "Hydrodynamical Trigger Mechanism for Pulsar Glitches", Physical Review Letters **102**, 141101 (2009).

[16]B. Haskell and A. Melatos, "Models of Pulsar Glitches", International Journal of Modern Physics D **24**, 1530008 (2015).

[17]A. Melatos, G. Howitt, and W. Fulgenzi, "Size-waiting-time Correlations in Pulsar Glitches", The Astrophysical Journal **863**, 196 (2018).

[18]J. B. Carlin and A. Melatos, "Generating quasi-periodic pulsar glitches using a state-dependent Poisson process", Monthly Notices of the Royal Astronomical Society **483**, 4742–4750 (2019).

[19]J. B. Carlin and A. Melatos, "Autocorrelations in pulsar glitch waiting times and sizes", Monthly Notices of the Royal Astronomical Society **488**, 4890–4896 (2019).

[20]J. Palfreyman, J. M. Dickey, A. Hotan, S. Ellingsen, and W. van Straten, "Alteration of the magnetosphere of the Vela pulsar during a glitch", Nature **556**, 219–222 (2018).

[21]G. Ashton, P. D. Lasky, V. Graber, and J. Palfreyman, "Rotational evolution of the Vela pulsar during the 2016 glitch", Nature Astronomy **3**, 1143–1148 (2019).

[22]A. Melatos and C. Peralta, "Superfluid Turbulence and Pulsar Glitch Statistics", The Astrophysical Journal **662**, L99–L102 (2007).

[23]A. Melatos and B. Link, "Pulsar timing noise from superfluid turbulence", Monthly Notices of the Royal Astronomical Society **437**, 21–31 (2014).

[24]V. Khomenko, M. Antonelli, and B. Haskell, "Hydrodynamical instabilities in the superfluid interior of neutron stars with background flows between the components", Physical Review D **100**, 123002 (2019).

[25]D. R. Cox and H. D. Miller, *The Theory of Stochastic Processes*, 1st (Chapman and Hall, London, 1965).

[26]C. Gardiner, *Stochastic Methods: A Handbook for the Natural and Social Sciences*, Fourth (Springer-Verlag, Berlin Heidelberg, 2009).

[27]A. L. Sweet and J. C. Hardin, "Solutions for Some Diffusion Processes with Two Barriers", Journal of Applied Probability **7**, 423–431 (1970).

[28]M. A. Alpar and A. Baykal, "Pulsar braking indices, glitches and energy dissipation in neutron stars", Monthly Notices of the Royal Astronomical Society **372**, 489–496 (2006).

[29]O. Akbal, M. A. Alpar, S. Buchner, and D. Pines, "Nonlinear interglitch dynamics, the braking index of the Vela pulsar and the time to the next glitch", Monthly Notices of the Royal Astronomical Society **469**, 4183–4192 (2017).

[30] A. I. Chugunov and C. J. Horowitz, "Breaking stress of neutron star crust", Monthly Notices of the Royal Astronomical Society: Letters **407**, 54–58 (2010).

[31] M. J. Aschwanden et al., "Order out of Randomness: Self-Organization Processes in Astrophysics", Space Science Reviews **214**, 55 (2018).

[32] H. J. Jensen, *Self-Organized Criticality. Emergent Complex Behavior in Physical and Biological Systems*, Cambridge Lecture Notes in Physics (Cambridge University Press, Cambridge, 1998).

[33] M. E. Lower et al., "The UTMOST pulsar timing programme – II. Timing noise across the pulsar population", Monthly Notices of the Royal Astronomical Society **494**, 228–245 (2020).

[34] T. Celora, V. Khomenko, M. Antonelli, and B. Haskell, "The effect of non-linear mutual friction on pulsar glitch sizes and rise times", Monthly Notices of the Royal Astronomical Society **496**, 5564–5574 (2020).

[35] R. N. Manchester, G. B. Hobbs, A. Teoh, and M. Hobbs, "The Australia Telescope National Facility pulsar catalogue", The Astronomical Journal **129**, 1993–2006 (2005).

[36] H. Akaike, "A New Look at the Statistical Model Identification", IEEE Transactions on Automatic Control **19**, 716 (1974).

[37] D. Antonopoulou, C. M. Espinoza, L. Kuiper, and N. Andersson, "Pulsar spin-down: the glitch-dominated rotation of PSR J0537-6910", Monthly Notices of the Royal Astronomical Society **473**, 1644–1655 (2018).

[38] R. D. Ferdman, R. F. Archibald, K. N. Gourgouliatos, and V. M. Kaspi, "The Glitches and Rotational History of the Highly Energetic Young Pulsar PSR J0537-6910", The Astrophysical Journal **852**, 123 (2018).

[39] A. G. Lyne, C. A. Jordan, F. Graham-Smith, C. M. Espinoza, B. W. Stappers, and P. Weltevrede, "45 Years of Rotation of the Crab Pulsar", Monthly Notices of the Royal Astronomical Society **446**, 857–864 (2015).

[40] C. M. Espinoza, D. Antonopoulou, B. W. Stappers, A. Watts, and A. G. Lyne, "Neutron star glitches have a substantial minimum size", Monthly Notices of the Royal Astronomical Society **440**, 2755–2762 (2014).

[41] M. Yu and Q.-J. Liu, "On the detection probability of neutron star glitches", Monthly Notices of the Royal Astronomical Society **468**, 3031–3041 (2017).

[42] M. Yu et al., "Detection of 107 glitches in 36 southern pulsars", Monthly Notices of the Royal Astronomical Society **429**, 688–724 (2013).

[43] G. H. Janssen and B. W. Stappers, "30 glitches in slow pulsars", Astronomy and Astrophysics **457**, 611–618 (2006).

[44] M. A. Alpar, S. A. Langer, and J. A. Sauls, "Rapid postglitch spin-up of the superfluid core in pulsars", The Astrophysical Journal **282**, 533 (1984).

[45] C. A. van Eysden and A. Melatos, "Pulsar glitch recovery and the superfluidity coefficients of bulk nuclear matter", Monthly Notices of the Royal Astronomical Society **409**, 1253 (2010).

[46] R. M. Shannon, L. T. Lentati, M. Kerr, S. Johnston, G. Hobbs, and R. N. Manchester, "Characterizing the rotational irregularities of the Vela pulsar from 21 yr of phase-coherent timing", Monthly Notices of the Royal Astronomical Society **459**, 3104–3111 (2016).

[47] A. Melatos, J. A. Douglass, and T. P. Simula, "Persistent Gravitational Radiation from Glitching Pulsars", The Astrophysical Journal **807**, 132 (2015).

[48] N. Andersson, K. Glampedakis, W. C. G. Ho, and C. M. Espinoza, "Pulsar Glitches: The Crust is not Enough", Physical Review Letters **109**, 241103 (2012).

[49] J. Hooker, W. G. Newton, and B.-A. Li, "Efficacy of crustal superfluid neutrons in pulsar glitch models", Monthly Notices of the Royal Astronomical Society **449**, 3559–3567 (2015).

[50] B. Link, R. I. Epstein, and J. M. Lattimer, "Pulsar Constraints on Neutron Star Structure and Equation of State", Physical Review Letters **83**, 3362–3365 (1999).

[51] A. G. Lyne, S. L. Shemar, and F. G. Smith, "Statistical studies of pulsar glitches", Monthly Notices of the Royal Astronomical Society **315**, 534–542 (2000).

[52] R. M. Shannon and J. M. Cordes, "Assessing the Role of Spin Noise in the Precision Timing of Millisecond Pulsars", The Astrophysical Journal **725**, 1607–1619 (2010).

[53] B. K. Link and R. I. Epstein, "Mechanics and energetics of vortex unpinning in neutron stars", The Astrophysical Journal **373**, 592–603 (1991).

[54] A. Melatos and C. Peralta, "Gravitational Radiation from Hydrodynamic Turbulence in a Differentially Rotating Neutron Star", The Astrophysical Journal **709**, 77–87 (2010).

[55] C. J. Horowitz and K. Kadau, "Breaking Strain of Neutron Star Crust and Gravitational Waves", Physical Review Letters **102**, `10.1103/PhysRevLett.102.191102` (2009).

[56] P. M. Morse and H. Feshbach, *Methods of Theoretical Physics* (McGraw-Hill, New York, 1953).

[57] J. B. Carlin and A. Melatos, "Long-term statistics of pulsar glitches triggered by a Brownian stress accumulation process", Monthly Notices of the Royal Astronomical Society **494**, 3383–3391 (2020).

[58] L. Warszawski and A. Melatos, "Knock-on processes in superfluid vortex avalanches and pulsar glitch statistics", Monthly Notices of the Royal Astronomical Society **428**, 1911–1926 (2013).

[59] L. Warszawski, A. Melatos, and N. G. Berloff, "Unpinning triggers for superfluid vortex avalanches", Physical Review B **85**, `10.1103/PhysRevB.85.104503` (2012).

[60] J. R. Lönnborn, A. Melatos, and B. Haskell, "Collective, glitch-like vortex motion in a neutron star with an annular pinning barrier", Monthly Notices of the Royal Astronomical Society **487**, 702–710 (2019).

[61] V. Khomenko and B. Haskell, "Modelling Pulsar Glitches: The Hydrodynamics of Superfluid Vortex Avalanches in Neutron Stars", Publications of the Astronomical Society of Australia **35**, e020 (2018).

[62] G. Howitt, A. Melatos, and B. Haskell, "Simulating pulsar glitches: an N-body solver for superfluid vortex motion in two dimensions", Monthly Notices of the Royal Astronomical Society **498**, 320–331 (2020).

[63] S. Field, J. Witt, F. Nori, and X. Ling, “Superconducting Vortex Avalanches”, Physical Review Letters **74**, 1206–1209 (1995).

[64] K. Sneppen and M. Newman, “Coherent noise, scale invariance and intermittency in large systems”, Physica D: Nonlinear Phenomena **110**, 209–222 (1997).

[65] M. E. J. Newman and K. Sneppen, “Avalanches, scaling, and coherent noise”, Physical Review E **54**, 6226–6231 (1996).

[66] M. E. J. Newman, “Self-Organized Criticality, Evolution and the Fossil Extinction Record”, Proceedings of the Royal Society of London, B **263**, 1605–1610 (1996).

[67] A. Melatos and L. Warszawski, “Superfluid Vortex Unpinning as a Coherent Noise Process, and the Scale Invariance of Pulsar Glitches”, The Astrophysical Journal **700**, 1524 (2009).

[68] B. Haskell, “The effect of superfluid hydrodynamics on pulsar glitch sizes and waiting times”, Monthly Notices of the Royal Astronomical Society: Letters **461**, L77–L81 (2016).

[69] P. M. Pizzochero, “Angular momentum transfer in Vela-like pulsar glitches”, The Astrophysical Journal **743**, L20 (2011).

[70] B. Haskell and D. Antonopoulou, “Glitch recoveries in radio-pulsars and magnetars”, Monthly Notices of the Royal Astronomical Society **438**, L16–L20 (2014).

[71] P. B. Jones, “The origin of pulsar glitches”, Monthly Notices of the Royal Astronomical Society **296**, 217–224 (1998).

[72] P. Donati and P. M. Pizzochero, “Realistic energies for vortex pinning in intermediate-density neutron star matter”, Physics Letters B **640**, 74–81 (2006).

[73] P. Avogadro, F. Barranco, R. A. Broglia, and E. Vigezzi, “Quantum calculation of vortices in the inner crust of neutron stars”, Physical Review C **75**, 012805 (2007).

[74] M. Ruderman, T. Zhu, and K. Chen, “Neutron Star Magnetic Field Evolution, Crust Movement, and Glitches”, The Astrophysical Journal **492**, 267–280 (1998).

[75] M. A. Alpar, H. F. Chau, K. S. Cheng, and D. Pines, “Postglitch Relaxation of the Crab Pulsar after Its First Four Major Glitches: The Combined Effects of Crust Cracking, Formation of Vortex Depletion Region and Vortex Creep”, The Astrophysical Journal **459**, 706 (1996).

[76] N. Chamel and P. Haensel, “Physics of Neutron Star Crusts”, Living Reviews in Relativity **11**, 10 (2008).

[77] A. Melatos and L. V. Drummond, “Pulsar Glitch Activity as a State-dependent Poisson Process: Parameter Estimation and Epoch Prediction”, The Astrophysical Journal **885**, 37 (2019).

[78] P. M. McCulloch, P. A. Hamilton, D. McConnell, and E. A. King, “The Vela Glitch of Christmas 1988”, Nature **346**, 822 (1990).

[79] R. G. Dodson, P. M. McCulloch, and D. R. Lewis, “High Time Resolution Observations of the January 2000 Glitch in the Vela Pulsar”, The Astrophysical Journal Letters **564**, L85–L88 (2002).

[80] G. Srinivasan, D. Bhattacharya, A. G. Muslimov, and A. J. Tsygan, “A novel mechanism for the decay of neutron star magnetic fields”, Current Science **59**, 31–38 (1990).

[81] P. M. Pizzochero, A. Montoli, and M. Antonelli, “Core and crust contributions in overshooting glitches: the Vela pulsar 2016 glitch”, Astronomy and Astrophysics **636**, A101 (2020).

[82] B. Haskell and A. Melatos, “Pinned vortex hopping in a neutron star crust”, Monthly Notices of the Royal Astronomical Society **461**, 2200–2211 (2016).

[83] D. R. Cox, “Some Statistical Methods Connected with Series of Events”, Journal of the Royal Statistical Society, B **17**, 129–164 (1955).

[84] W. H. Press, S. A. Teukolsky, W. T. Vetterling, and B. P. Flannery, *Numerical Recipes 3rd Edition: The Art of Scientific Computing* (Cambridge University Press, Sept. 2007).

[85] H. E. Hall and W. F. Vinen, “The Rotation of Liquid Helium II. II. The Theory of Mutual Friction in Uniformly Rotating Helium II”, Proceedings of the Royal Society of London, A **238**, 215–234 (1956).

[86] C. F. Barenghi, R. J. Donnelly, and W. F. Vinen, “Friction on quantized vortices in helium II. A review”, Journal of Low Temperature Physics **52**, 189–247 (1983).

[87] N. Andersson, T. Sidery, and G. L. Comer, “Mutual friction in superfluid neutron stars”, Monthly Notices of the Royal Astronomical Society **368**, 162–170 (2006).

[88] V. Graber, A. Cumming, and N. Andersson, “Glitch Rises as a Test for Rapid Superfluid Coupling in Neutron Stars”, The Astrophysical Journal **865**, 23 (2018).

[89] C. Peralta, A. Melatos, M. Giacobello, and A. Ooi, “Transitions between Turbulent and Laminar Superfluid Vorticity States in the Outer Core of a Neutron Star”, The Astrophysical Journal **651**, 1079–1091 (2006).

[90] M. S. Mongiovì, F. G. Russo, and M. Sciacca, “A mathematical description of glitches in neutron stars”, Monthly Notices of the Royal Astronomical Society **469**, 2141–2150 (2017).

[91] B. Haskell, D. Antonopoulou, and C. Barenghi, “Turbulent, pinned superfluids in neutron stars and pulsar glitch recoveries”, Monthly Notices of the Royal Astronomical Society **499**, 161–170 (2020).

[92] Y. Y. Kagan and D. D. Jackson, “Long-Term Earthquake Clustering”, Geophysical Journal International **104**, 117–134 (1991).

[93] T. Utsu, Y. Ogata, R. S, and Matsu’ura, “The Centenary of the Omori Formula for a Decay Law of Aftershock Activity.”, Journal of Physics of the Earth **43**, 1–33 (1995).

[94] E. Gügercinoğlu and M. A. Alpar, “The largest Crab glitch and the vortex creep model”, Monthly Notices of the Royal Astronomical Society **488**, 2275–2282 (2019).

[95] C. M. Espinoza, D. Antonopoulou, R. Dodson, M. Stepanova, and A. Scherer, “Small glitches and other rotational irregularities of the Vela pulsar”, Astronomy and Astrophysics **647**, A25 (2021).

[96] A. Melatos, L. M. Dunn, S. Suvorova, W. Moran, and R. J. Evans, “Pulsar Glitch Detection with a Hidden Markov Model”, The Astrophysical Journal **896**, 78 (2020).

[97] F. Jankowski et al., “The UTMOST pulsar timing programme I: Overview and first results”, Monthly Notices of the Royal Astronomical Society **484**, 3691–3712 (2019).

[98] B. W. Stappers et al., “Observing pulsars and fast transients with LOFAR”, Astronomy and Astrophysics **530**, A80 (2011).

[99] E. Daly and A. Porporato, “Intertime jump statistics of state-dependent Poisson processes”, Physical Review E **75**, 11119 (2007).

[100] D. R. Cox and P. A. W. Lewis, *The Statistical Analysis of Series of Events* (Chapman and Hall, 1966).

[101] E. Çinlar, *Introduction to stochastic processes* (Englewood Cliffs, N.J. : Prentice-Hall, 1975).

[102] J. F. C. Kingman, *Poisson processes* (Oxford: Clarendon Press; New York: Oxford University Press, 1993., 1993).

[103] G. E. P. Box, G. M. Jenkins, G. C. Reinsel, and G. M. Ljung, *Time Series Analysis: Forecasting and Control* (John Wiley and Sons Inc., Hoboken, New Jersey, June 2015).

[104] E. D. Feigelson, G. J. Babu, and G. A. Caceres, “Autoregressive Times Series Methods for Time Domain Astronomy”, Frontiers in Physics **6**, 80 (2018).

[105] J. van der Hoek and R. J. Elliott, *Introduction to Hidden Semi-Markov Models*, London Mathematical Society Lecture Note Series (Cambridge University Press, Cambridge, 2018).

[106] E. Priest and T. Forbes, “The magnetic nature of solar flares”, The Astronomy and Astrophysics Review **10**, 313–377 (2002).

[107] A. O. Benz, “Flare Observations”, Living Reviews in Solar Physics **14**, 2 (2016).

[108] R. Rosner and G. S. Vaiana, “Cosmic flare transients - Constraints upon models for energy storage and release derived from the event frequency distribution”, The Astrophysical Journal **222**, 1104 (1978).

[109] M. S. Wheatland and S. Glukhov, “Flare Frequency Distributions Based on a Master Equation”, The Astrophysical Journal **494**, 858–863 (1998).

[110] M. S. Wheatland, “Do solar flares exhibit an interval-size relationship?”, Solar Physics **191**, 381–389 (2000).

[111] M. S. Wheatland, “The Energetics of a Flaring Solar Active Region and Observed Flare Statistics”, The Astrophysical Journal **679**, 1621–1628 (2008).

[112] M. Kanazir and M. S. Wheatland, “Time-Dependent Stochastic Modeling of Solar Active Region Energy”, Solar Physics **266**, 301–321 (2010).

[113] H. S. Hudson, “A Correlation in the Waiting-time Distributions of Solar Flares”, Monthly Notices of the Royal Astronomical Society, stz3121 (2019).

[114] E. T. Lu and R. J. Hamilton, “Avalanches and the Distribution of Solar Flares”, The Astrophysical Journal Letters **380**, L89 (1991).

[115] E. T. Lu, R. J. Hamilton, J. M. McTiernan, and K. R. Bromund, “Solar Flares and Avalanches in Driven Dissipative Systems”, The Astrophysical Journal **412**, 841 (1993).

[116]E. T. Lu, “The Statistical Physics of Solar Active Regions and the Fundamental Nature of Solar Flares”, The Astrophysical Journal **446**, L109–L112 (1995).

[117]P. Bak, C. Tang, and K. Wiesenfeld, “Self-organized criticality: An explanation of the 1/f noise”, Physical Review Letters **59**, 381–384 (1987).

[118]P. Bak, C. Tang, and K. Wiesenfeld, “Self-organized criticality”, Physical Review A **38**, 364–374 (1988).

[119]E. T. Lu, “Constraints on Energy Storage and Release Models for Astrophysical Transients and Solar Flares”, The Astrophysical Journal **447**, 416 (1995).

[120]G. Boffetta, V. Carbone, P. Giuliani, P. Veltri, and A. Vulpiani, “Power Laws in Solar Flares: Self-Organized Criticality or Turbulence?”, Physical Review Letters **83**, 4662–4665 (1999).

[121]E. Lippiello, L. de Arcangelis, and C. Godano, “Time-energy correlations in solar flare occurrence”, Astronomy and Astrophysics **511**, L2 (2010).

[122]N. Farhang, M. S. Wheatland, and H. Safari, “Energy Balance in Avalanche Models for Solar Flares”, The Astrophysical Journal **883**, L20 (2019).

[123]M. J. Aschwanden and J. R. Johnson, “The Solar Memory from Hours to Decades”, The Astrophysical Journal **921**, 82 (2021).

[124]C. Verbeeck, E. Kraaikamp, D. F. Ryan, and O. Podladchikova, “Solar Flare Distributions: Lognormal Instead of Power Law?”, The Astrophysical Journal **884**, 50 (2019).

[125]M. S. Wheatland, “The Origin of the Solar Flare Waiting-Time Distribution”, The Astrophysical Journal **536**, L109 (2000).

[126]M. J. Aschwanden, J. R. Johnson, and Y. I. Nurhan, “The Poissonian Origin of Power Laws in Solar Flare Waiting Time Distributions”, The Astrophysical Journal **921**, 166 (2021).

[127]F. Lepreti, V. Carbone, and P. Veltri, “Solar Flare Waiting Time Distribution: Varying-Rate Poisson or Lévy Function?”, The Astrophysical Journal **555**, L133 (2001).

[128]A. Gorobets and M. Messerotti, “Solar Flare Occurrence Rate and Waiting Time Statistics”, Solar Physics **281**, 651–667 (2012).

[129]D. A. Biesecker, “On the Occurrence of Solar Flares Observed with the Burst and Transient Source Experiment”, PhD thesis (University of New Hampshire, Jan. 1994).

[130]H. S. Hudson, B. J. Labonte, A. C. Sterling, and T. Watanabe, “NOAA 7978: The Last Best Old-Cycle Region?”, in *Observational Plasma Astrophysics: Five Years of Yohkoh and Beyond*, Vol. 229, Space Science Library (Springer Dordrecht, 1998), p. 237.

[131]N. Crosby, N. Vilmer, N. Lund, and R. Sunyaev, “Deka-keV X-ray observations of solar bursts with WATCH/GRANAT: frequency distributions of burst parameters”, Astronomy and Astrophysics **334**, 299–313 (1998).

[132]A. Lyne and F. Graham-Smith, *Pulsar Astronomy* (Cambridge University Press, Cambridge, UK, Mar. 2012).

[133]J. B. Carlin and A. Melatos, “Long-term Statistics of Pulsar Glitches Due to History-dependent Avalanches”, The Astrophysical Journal **917**, 1 (2021).

[134]L. Fletcher et al., "An Observational Overview of Solar Flares", Space Science Reviews **159**, 19 (2011).

[135]E. Daly and A. Porporato, "State-dependent fire models and related renewal processes", Physical Review E **74**, 1–9 (2006).

[136]M. Wheatland, "Rates of Flaring in Individual Active Regions", Solar Physics **203**, 87–106 (2001).

[137]C. M. Hurvich and C.-L. Tsai, "Regression and time series model selection in small samples", Biometrika **76**, 297–307 (1989).

[138]E. L. Lehmann and H. J. M. D'Abrera, *Nonparametrics: Statistical Methods Based on Ranks* (Springer-Verlag, New York, 2006).

[139]M. P. Wand and M. C. Jones, *Kernel Smoothing* (Chapman & Hall, London; New York, 1995).

[140]T. N. Woods et al., "New Solar extreme-ultraviolet irradiance observations during flares", The Astrophysical Journal **739**, 59 (2011).

[141]T. Török, B. Kliem, and V. S. Titov, "Ideal kink instability of a magnetic loop equilibrium", Astronomy and Astrophysics **413**, L27–L30 (2004).

[142]C. R. Harris et al., "Array programming with NumPy", Nature **585**, 357–362 (2020).

[143]P. Virtanen et al., "SciPy 1.0: fundamental algorithms for scientific computing in Python", Nature Methods **17**, 261–272 (2020).

[144]J. D. Hunter, "Matplotlib: A 2D Graphics Environment", Computing in Science and Engineering **9**, 90–95 (2007).

[145]Stan Development Team, *Stan Modeling Language Users Guide and Reference Manual, 2.30*, 2022.

[146]G. H. Fisher, B. T. Welsch, and W. P. Abbett, "Can We Determine Electric Fields and Poynting Fluxes from Vector Magnetograms and Doppler Measurements?", Solar Physics **277**, 153–163 (2012).

[147]X. Sun, J. T. Hoeksema, Y. Liu, T. Wiegelmann, K. Hayashi, Q. Chen, and J. Thalmann, "Evolution of Magnetic Field and Energy in a Major Eruptive Active Region Based on SDO/HMI Observation", The Astrophysical Journal **748**, 77 (2012).

[148]X. Sun, J. T. Hoeksema, Y. Liu, M. Kazachenko, and R. Chen, "Investigating the Magnetic Imprints of Major Solar Eruptions with SDO/HMI High-cadence Vector Magnetograms", The Astrophysical Journal **839**, 67 (2017).

[149]S. Sahu, B. Joshi, A. Prasad, and K.-S. Cho, *Evolution of magnetic fields and energy release processes during homologous eruptive flares*, Dec. 2022.

[150]H. Ji and W. Daughton, "Phase diagram for magnetic reconnection in heliophysical, astrophysical, and laboratory plasmas", Physics of Plasmas **18**, 111207 (2011).

[151]K. Shibata and S. Tanuma, "Plasmoid-induced-reconnection and fractal reconnection", Earth, Planets and Space **53**, 473–482 (2001).

[152]P. H. Keys, M. Mathioudakis, D. B. Jess, S. Shelyag, P. J. Crockett, D. J. Christian, and F. P. Keenan, "The Velocity Distribution of Solar Photospheric Magnetic Bright Points", The Astrophysical Journal Letters **740**, L40 (2011).

[153] S. Shelyag, P. Keys, M. Mathioudakis, and F. P. Keenan, “Vorticity in the solar photosphere”, Astronomy and Astrophysics **526**, A5 (2011).

[154] S. Shelyag, V. Fedun, F. P. Keenan, R. Erdélyi, and M. Mathioudakis, “Photospheric magnetic vortex structures”, Annales Geophysicae **29**, 883–887 (2011).

[155] A. Gelman, J. B. Carlin, H. S. Stern, D. Dunson, A. Vehtari, and D. B. Rubin, *Bayesian data analysis*, 3rd Editio (Chapman and Hall/CRC, New York, 2013).

[156] M. Betancourt, “A Conceptual Introduction to Hamiltonian Monte Carlo”, arXiv e-prints (2018).

[157] M. Millhouse, A. Melatos, G. Howitt, J. B. Carlin, L. Dunn, and G. Ashton, “An updated glitch rate law inferred from radio pulsars”, Monthly Notices of the Royal Astronomical Society **511**, 3304–3319 (2022).

[158] J. Aasi et al., “Advanced LIGO”, Classical and Quantum Gravity **32**, 074001 (2015).

[159] F. Acernese et al., “Advanced Virgo: a second-generation interferometric gravitational wave detector”, Classical and Quantum Gravity **32**, 024001 (2014).

[160] LIGO Scientific Collaboration and Virgo Collaboration et al., “GWTC-1: A Gravitational-Wave Transient Catalog of Compact Binary Mergers Observed by LIGO and Virgo during the First and Second Observing Runs”, Physical Review X **9**, 031040 (2019).

[161] LIGO Scientific Collaboration and Virgo Collaboration et al., “GWTC-2: Compact Binary Coalescences Observed by LIGO and Virgo during the First Half of the Third Observing Run”, Physical Review X **11**, 021053 (2021).

[162] The LIGO Scientific Collaboration et al., “GWTC-2.1: Deep Extended Catalog of Compact Binary Coalescences Observed by LIGO and Virgo During the First Half of the Third Observing Run”, arXiv e-prints, arXiv:2108.01045 (2021).

[163] K. Glampedakis and L. Gualtieri, “Gravitational Waves from Single Neutron Stars: An Advanced Detector Era Survey”, in *The Physics and Astrophysics of Neutron Stars*, edited by L. Rezzolla, P. Pizzochero, D. I. Jones, N. Rea, and I. Vidaña, Astrophysics and Space Science Library (Springer International Publishing, Cham, 2018), pp. 673–736.

[164] M. Sieniawska and M. Bejger, “Continuous Gravitational Waves from Neutron Stars: Current Status and Prospects”, Universe **5**, 217 (2019).

[165] B. Haskell and K. Schwenzer, “Isolated Neutron Stars”, in *Handbook of Gravitational Wave Astronomy*, edited by C. Bambi, S. Katsanevas, and K. D. Kokkotas (Springer, Singapore, 2021), pp. 1–28.

[166] B. P. Abbott et al., “Search for Gravitational Waves from a Long-lived Remnant of the Binary Neutron Star Merger GW170817”, The Astrophysical Journal **875**, 160 (2019).

[167] Y. Zhang, M. A. Papa, B. Krishnan, and A. L. Watts, “Search for Continuous Gravitational Waves from Scorpius X-1 in LIGO O2 Data”, The Astrophysical Journal **906**, L14 (2021).

[168] D. Beniwal, P. Clearwater, L. Dunn, A. Melatos, and D. Ottaway, “Search for continuous gravitational waves from ten H.E.S.S. sources using a hidden Markov model”, Physical Review D **103**, 083009 (2021).

[169]D. Jones and L. Sun, “Search for continuous gravitational waves from Fomalhaut b in the second Advanced LIGO observing run with a hidden Markov model”, Physical Review D **103**, 023020 (2021).

[170]R. Abbott et al., “Gravitational-wave Constraints on the Equatorial Ellipticity of Millisecond Pulsars”, The Astrophysical Journal Letters **902**, L21 (2020).

[171]V. Dergachev and M. A. Papa, “Search for continuous gravitational waves from small-ellipticity sources at low frequencies”, Physical Review D **104**, 043003 (2021).

[172]B. Rajbhandari, B. J. Owen, S. Caride, and R. Inta, “First searches for gravitational waves from \$r\$-modes of the Crab pulsar”, Physical Review D **104**, 122008 (2021).

[173]The LIGO Scientific Collaboration and the Virgo Collaboration et al., “All-sky search in early O3 LIGO data for continuous gravitational-wave signals from unknown neutron stars in binary systems”, Physical Review D **103**, 064017 (2021).

[174]K. Wette, L. Dunn, P. Clearwater, and A. Melatos, “Deep exploration for continuous gravitational waves at 171–172 Hz in LIGO second observing run data”, Physical Review D **103**, 083020 (2021).

[175]R. Abbott et al., “Diving below the Spin-down Limit: Constraints on Gravitational Waves from the Energetic Young Pulsar PSR J0537-6910”, The Astrophysical Journal Letters **913**, L27 (2021).

[176]R. Abbott et al., “Constraints from LIGO O3 Data on Gravitational-wave Emission Due to R-modes in the Glitching Pulsar PSR J0537−6910”, The Astrophysical Journal **922**, 71 (2021).

[177]LIGO Scientific Collaboration and Virgo Collaboration et al., “Narrow-band search for gravitational waves from known pulsars using the second LIGO observing run”, Physical Review D **99**, 122002 (2019).

[178]V. C. LIGO Scientific Collaboration and KAGRA Collaboration et al., “All-sky search for continuous gravitational waves from isolated neutron stars in the early O3 LIGO data”, Physical Review D **104**, 082004 (2021).

[179]R. Abbott et al., “Searches for Continuous Gravitational Waves from Young Supernova Remnants in the Early Third Observing Run of Advanced LIGO and Virgo”, The Astrophysical Journal **921**, 80 (2021).

[180]A. Ashok, B. Beheshtipour, M. A. Papa, P. C. C. Freire, B. Steltner, B. Machenschalk, O. Behnke, B. Allen, and R. Prix, “New Searches for Continuous Gravitational Waves from Seven Fast Pulsars”, The Astrophysical Journal **923**, 85 (2021).

[181]LIGO Scientific Collaboration and Virgo Collaboration et al., “Search for gravitational waves from Scorpius X-1 in the second Advanced LIGO observing run with an improved hidden Markov model”, Physical Review D **100**, 122002 (2019).

[182]H. Middleton, P. Clearwater, A. Melatos, and L. Dunn, “Search for gravitational waves from five low mass x-ray binaries in the second Advanced LIGO observing run with an improved hidden Markov model”, Physical Review D **102**, 023006 (2020).

[183] M. A. Papa, J. Ming, E. V. Gotthelf, B. Allen, R. Prix, V. Dergachev, H.-B. Eggenstein, A. Singh, and S. J. Zhu, "Search for Continuous Gravitational Waves from the Central Compact Objects in Supernova Remnants Cassiopeia A, Vela Jr., and G347.3−0.5", The Astrophysical Journal **897**, 22 (2020).

[184] L. Fesik and M. A. Papa, "First Search for r-mode Gravitational Waves from PSR J0537−6910", The Astrophysical Journal **895**, 11 (2020).

[185] L. Fesik and M. A. Papa, "Erratum: "First Search for r-mode Gravitational Waves from PSR J0537−6910" (2020, ApJ, 895, 11)", The Astrophysical Journal **897**, 185 (2020).

[186] O. J. Piccinni, P. Astone, S. D'Antonio, S. Frasca, G. Intini, I. La Rosa, P. Leaci, S. Mastrogiovanni, A. Miller, and C. Palomba, "Directed search for continuous gravitational-wave signals from the Galactic Center in the Advanced LIGO second observing run", Physical Review D **101**, 082004 (2020).

[187] B. Steltner et al., "Einstein@Home All-sky Search for Continuous Gravitational Waves in LIGO O2 Public Data", The Astrophysical Journal **909**, 79 (2021).

[188] A. Patruno and A. L. Watts, "Accreting Millisecond X-ray Pulsars", in *Timing Neutron Stars: Pulsations, Oscillations and Explosions*, edited by T. M. Belloni, M. Méndez, and C. Zhang, Astrophysics and Space Science Library (Springer, Berlin, Heidelberg, 2021), pp. 143–208.

[189] J. W. T. Hessels, S. M. Ransom, I. H. Stairs, P. C. C. Freire, V. M. Kaspi, and F. Camilo, "A Radio Pulsar Spinning at 716 Hz", Science **311**, 1901–1904 (2006).

[190] G. B. Cook, S. L. Shapiro, and S. A. Teukolsky, "Rapidly rotating neutron stars in general relativity: Realistic equations of state", The Astrophysical Journal **424**, 823–845 (1994).

[191] L. Bildsten, "Gravitational Radiation and Rotation of Accreting Neutron Stars", The Astrophysical Journal Letters **501**, L89 (1998).

[192] N. Andersson, K. D. Kokkotas, and N. Stergioulas, "On the Relevance of the R-Mode Instability for Accreting Neutron Stars and White Dwarfs", The Astrophysical Journal **516**, 307–314 (1999).

[193] J. Papaloizou and J. E. Pringle, "Gravitational radiation and the stability of rotating stars", Monthly Notices of the Royal Astronomical Society **184**, 501–508 (1978).

[194] R. V. Wagoner, "Gravitational radiation from accreting neutron stars", The Astrophysical Journal **278**, 345–348 (1984).

[195] B. P. Abbott et al., "Search for gravitational waves from Scorpius X-1 in the first Advanced LIGO observing run with a hidden Markov model", Physical Review D **95**, 122003 (2017).

[196] B. P. Abbott et al., "Upper Limits on Gravitational Waves from Scorpius X-1 from a Model-based Cross-correlation Search in Advanced LIGO Data", The Astrophysical Journal **847**, 47 (2017).

[197] T. Di Salvo and A. Sanna, "Accretion Powered X-ray Millisecond Pulsars", in *Millisecond Pulsars*, edited by S. Bhattacharyya, A. Papitto, and D. Bhattacharya, Astrophysics and Space Science Library (Springer International Publishing, Cham, 2022), pp. 87–124.

[198] E. Goetz and K. Riles, “An all-sky search algorithm for continuous gravitational waves from spinning neutron stars in binary systems”, Classical and Quantum Gravity **28**, 215006 (2011).

[199] G. D. Meadors, E. Goetz, K. Riles, T. Creighton, and F. Robinet, “Searches for continuous gravitational waves from Scorpius X-1 and XTE J1751-305 in LIGO’s sixth science run”, Physical Review D **95**, 042005 (2017).

[200] S. Suvorova, P. Clearwater, A. Melatos, L. Sun, W. Moran, and R. J. Evans, “Hidden Markov model tracking of continuous gravitational waves from a binary neutron star with wandering spin. II. Binary orbital phase tracking”, Physical Review D **96**, 102006 (2017).

[201] A. Mukherjee, C. Messenger, and K. Riles, “Accretion-induced spin-wandering effects on the neutron star in Scorpius X-1: Implications for continuous gravitational wave searches”, Physical Review D **97**, 043016 (2018).

[202] S. Suvorova, L. Sun, A. Melatos, W. Moran, and R. J. Evans, “Hidden Markov model tracking of continuous gravitational waves from a neutron star with wandering spin”, Physical Review D **93**, 123009 (2016).

[203] K. Riles, “Gravitational waves: Sources, detectors and searches”, Progress in Particle and Nuclear Physics **68**, 1–54 (2013).

[204] B. Abbott et al., “Beating the Spin-Down Limit on Gravitational Wave Emission from the Crab Pulsar”, The Astrophysical Journal Letters **683**, L45 (2008).

[205] A. Viterbi, “Error bounds for convolutional codes and an asymptotically optimum decoding algorithm”, IEEE Transactions on Information Theory **13**, 260–269 (1967).

[206] P. Jaranowski, A. Królak, and B. F. Schutz, “Data analysis of gravitational-wave signals from spinning neutron stars: The signal and its detection”, Physical Review D **58**, 063001 (1998).

[207] LIGO Scientific Collaboration, “LIGO Algorithm Library - LALSuite”, 10.7935/GT1W-FZ16 (2018).

[208] P. Casella, D. Altamirano, A. Patruno, R. Wijnands, and M. van der Klis, “Discovery of Coherent Millisecond X-Ray Pulsations in Aquila X-1”, The Astrophysical Journal Letters **674**, L41 (2008).

[209] D. Mata Sánchez, T. Muñoz-Darias, J. Casares, and F. Jiménez-Ibarra, “The donor of Aquila X-1 revealed by high-angular resolution near-infrared spectroscopy”, Monthly Notices of the Royal Astronomical Society **464**, L41–L45 (2017).

[210] A. L. Watts, B. Krishnan, L. Bildsten, and B. F. Schutz, “Detecting gravitational wave emission from the known accreting neutron stars”, Monthly Notices of the Royal Astronomical Society **389**, 839–868 (2008).

[211] A. Marino, T. Di Salvo, L. Burderi, A. Sanna, A. Riggio, A. Papitto, M. Del Santo, A. F. Gambino, R. Iaria, and S. M. Mazzola, “Indications of non-conservative mass transfer in AMXPs”, Astronomy and Astrophysics **627**, 11 (2019).

[212] A. Melatos and A. Mastrano, “Electromagnetic Spindown of a Transient Accreting Millisecond Pulsar During Quiescence”, The Astrophysical Journal **818**, 49 (2016).

[213] P. Ghosh, F. K. Lamb, and C. J. Pethick, "Accretion by rotating magnetic neutron stars. I - Flow of matter inside the magnetosphere and its implications for spin-up and spin-down of the star", The Astrophysical Journal **217**, 578–596 (1977).

[214] P. M. Bult, K. C. Gendreau, Z. Arzoumanian, D. Chakrabarty, P. S. Ray, S. Guillot, M. T. Wolff, S. Bogdanov, and R. M. Ludlam, "NICER detects X-ray pulsations from the rapidly brightening SAX J1808.4-3658", The Astronomer's Telegram **3001** (2019).

[215] P. Bult, D. Chakrabarty, Z. Arzoumanian, K. C. Gendreau, S. Guillot, C. Malacaria, P. S. Ray, and T. E. Strohmayer, "Timing the Pulsations of the Accreting Millisecond Pulsar SAX J1808.4−3658 during Its 2019 Outburst", The Astrophysical Journal **898**, 38 (2020).

[216] A. J. Goodwin et al., "Enhanced optical activity 12 d before X-ray activity, and a 4 d X-ray delay during outburst rise, in a low-mass X-ray binary", Monthly Notices of the Royal Astronomical Society **498**, 3429–3439 (2020).

[217] B. Haskell and A. Patruno, "Are Gravitational Waves Spinning Down PSR J1023+0038?", Physical Review Letters **119**, 161103 (2017).

[218] M. A. P. Torres et al., "Observations of the 599 Hz Accreting X-Ray Pulsar IGR J00291+5934 during the 2004 Outburst and in Quiescence", The Astrophysical Journal **672**, 1079–1090 (2008).

[219] A. Patruno, "The Slow Orbital Evolution of the Accreting Millisecond Pulsar IGR J0029+5934", The Astrophysical Journal **839**, 51 (2017).

[220] J. Homan, G. Sivakoff, D. Pooley, C. Heinke, J. Strader, V. Tudor, and J. Miller-Jones, "Chandra identification of the X-ray transient MAXI J0911-635/Swift J0911.9-6452 in NGC 2808", The Astronomer's Telegram **8971** (2016).

[221] A. Sanna, A. Papitto, L. Burderi, E. Bozzo, A. Riggio, T. Di Salvo, C. Ferrigno, N. Rea, and R. Iaria, "Discovery of a new accreting millisecond X-ray pulsar in the globular cluster NGC 2808", Astronomy and Astrophysics **598**, A34 (2017).

[222] D. K. Galloway, D. Chakrabarty, E. H. Morgan, and R. A. Remillard, "Discovery of a High-Latitude Accreting Millisecond Pulsar in an Ultracompact Binary", The Astrophysical Journal Letters **576**, L137–L140 (2002).

[223] A. B. Giles, J. G. Greenhill, K. M. Hill, and E. Sanders, "The optical counterpart of XTE J0929-314: the third transient millisecond X-ray pulsar", Monthly Notices of the Royal Astronomical Society **361**, 1180–1186 (2005).

[224] A. J. Tetarenko et al., "A Radio Frequency Study of the Accreting Millisecond X-ray Pulsar, IGR J16597-3704, in the Globular Cluster NGC 6256", The Astrophysical Journal **854**, 125 (2018).

[225] A. Sanna et al., "Discovery of 105 Hz coherent pulsations in the ultracompact binary IGR J16597-3704", Astronomy and Astrophysics **610**, L2 (2018).

[226] P. Bult, T. E. Strohmayer, C. Malacaria, M. Ng, and Z. Wadiasingh, "Long-term Coherent Timing of the Accreting Millisecond Pulsar IGR J17062−6143", The Astrophysical Journal **912**, 120 (2021).

[227] A. Sanna, E. Bozzo, A. Papitto, A. Riggio, C. Ferrigno, T. Di Salvo, R. Iaria, S. M. Mazzola, N. D'Amico, and L. Burderi, "XMM-Newton detection of the 2.1 ms coherent pulsations from IGR J17379-3747", Astronomy and Astrophysics **616**, L17 (2018).

[228] P. Bult, C. B. Markwardt, D. Altamirano, Z. Arzoumanian, D. Chakrabarty, K. C. Gendreau, S. Guillot, G. K. Jaisawal, P. S. Ray, and T. E. Strohmayer, "On the Curious Pulsation Properties of the Accreting Millisecond Pulsar IGR J17379-3747", The Astrophysical Journal **877**, 70 (2019).

[229] A. Sanna, L. Burderi, A. Riggio, F. Pintore, T. Di Salvo, A. F. Gambino, R. Iaria, M. Matranga, and F. Scarano, "Timing of the accreting millisecond pulsar SAX J1748.9-2021 during its 2015 outburst", Monthly Notices of the Royal Astronomical Society **459**, 1340–1349 (2016).

[230] C. O. Heinke et al., "Discovery of a Second Transient Low-Mass X-ray Binary in the Globular Cluster Ngc 6440", The Astrophysical Journal **714**, 894–903 (2010).

[231] P. Bult, A. Patruno, and M. van der Klis, "Coherent Timing of the Accreting Millisecond Pulsar NGC 6440 X-2", The Astrophysical Journal **814**, 138 (2015).

[232] M. Ng et al., "NICER Discovery of Millisecond X-Ray Pulsations and an Ultracompact Orbit in IGR J17494-3030", The Astrophysical Journal Letters **908**, L15 (2021).

[233] P. G. Jonker, M. A. P. Torres, D. Steeghs, and D. Chakrabarty, "Chandra X-ray and Gemini near-infrared observations of the eclipsing millisecond pulsar SWIFT J1749.4-2807 in quiescence", Monthly Notices of the Royal Astronomical Society **429**, 523–528 (2013).

[234] P. M. Bult, D. Altamirano, A. C. Albayati, T. E. Strohmayer, P. S. Ray, D. Chakrabarty, M. Ng, K. C. Gendreau, Z. Arzoumanian, and A. Sanna, "NICER detects pulsations from Swift J1749.4-2807", The Astronomer's Telegram **4428** (2021).

[235] A. Sanna et al., "On the peculiar long-term orbital evolution of the eclipsing accreting millisecond X-ray pulsar SWIFT J1749.4 - 2807", Monthly Notices of the Royal Astronomical Society **514**, 4385–4397 (2022).

[236] A. Papitto, E. Bozzo, C. Ferrigno, T. Belloni, L. Burderi, T. di Salvo, A. Riggio, A. D'Aì, and R. Iaria, "The discovery of the 401 Hz accreting millisecond pulsar IGR J17498-2921 in a 3.8 h orbit", Astronomy and Astrophysics **535**, L4 (2011).

[237] M. Falanga, L. Kuiper, J. Poutanen, D. K. Galloway, E. Bozzo, A. Goldwurm, W. Hermsen, and L. Stella, "Spectral and timing properties of the accreting X-ray millisecond pulsar IGR J17498-2921", Astronomy and Astrophysics **545**, A26 (2012).

[238] A. Paizis, M. A. Nowak, J. Rodriguez, J. Wilms, S. Chaty, M. Del Santo, and P. Ubertini, "A Chandra Observation of the Bursting Millisecond X-Ray Pulsar IGR J17511-3057", The Astrophysical Journal **755**, 52 (2012).

[239] A. Riggio, A. Papitto, L. Burderi, T. di Salvo, M. Bachetti, R. Iaria, A. D'Aì, and M. T. Menna, "Timing of the accreting millisecond pulsar IGR J17511-3057", Astronomy and Astrophysics **526**, A95 (2011).

[240] C. B. Markwardt, J. H. Swank, T. E. Strohmayer, J. J. M. in 't Zand, and F. E. Marshall, "Discovery of a Second Millisecond Accreting Pulsar: XTE J1751-305", The Astrophysical Journal Letters **575**, L21–L24 (2002).

[241] A. Papitto, M. T. Menna, L. Burderi, T. di Salvo, and A. Riggio, “Measuring the spin up of the accreting millisecond pulsar XTEJ1751-305”, Monthly Notices of the Royal Astronomical Society **383**, 411–416 (2008).

[242] A. Sanna et al., “SWIFT J1756.9-2508: spectral and timing properties of its 2018 outburst”, Monthly Notices of the Royal Astronomical Society **481**, 1658–1666 (2018).

[243] T. D. Russell, N. Degenaar, R. Wijnands, J. van den Eijnden, N. V. Gusinskaia, J. W. T. Hessels, and J. C. A. Miller-Jones, “The Radio-bright Accreting Millisecond X-Ray Pulsar IGR J17591-2342”, The Astrophysical Journal Letters **869**, L16 (2018).

[244] A. Sanna et al., “Timing of the accreting millisecond pulsar IGR J17591−2342: evidence of spin-down during accretion”, Monthly Notices of the Royal Astronomical Society **495**, 1641–1649 (2020).

[245] C. B. Markwardt, M. Juda, and J. H. Swank, “XTE J1807-294”, International Astronomical Union Circular **8095**, 2 (2003).

[246] A. Patruno, J. M. Hartman, R. Wijnands, D. Chakrabarty, and M. van der Klis, “Accretion Torques and Motion of the Hot Spot on the Accreting Millisecond Pulsar XTE J1807-294”, The Astrophysical Journal **717**, 1253–1261 (2010).

[247] M. I. Krauss, Z. Wang, A. Dullighan, A. M. Juett, D. L. Kaplan, D. Chakrabarty, M. H. van Kerkwijk, D. Steeghs, P. G. Jonker, and C. B. Markwardt, “The X-Ray Position and Optical Counterpart of the Accretion-powered Millisecond Pulsar XTE J1814-338”, The Astrophysical Journal **627**, 910–914 (2005).

[248] A. Papitto, T. di Salvo, L. Burderi, M. T. Menna, G. Lavagetto, and A. Riggio, “Timing of the accreting millisecond pulsar XTE J1814-338”, Monthly Notices of the Royal Astronomical Society **375**, 971–976 (2007).

[249] C. Pallanca, E. Dalessandro, F. R. Ferraro, B. Lanzoni, and G. Beccari, “The Optical Counterpart to the X-Ray Transient IGR J1824-24525 in the Globular Cluster M28”, The Astrophysical Journal **773**, 122 (2013).

[250] A. Papitto et al., “Swings between rotation and accretion power in a binary millisecond pulsar”, Nature **501**, 517–520 (2013).

[251] D. B. Fox, “HETE J1900.1-2455 Optical Counterpart”, The Astronomer’s Telegram **526** (2005).

[252] P. Kaaret, E. H. Morgan, R. Vanderspek, and J. A. Tomsick, “Discovery of the Millisecond X-Ray Pulsar HETE J1900.1-2455”, The Astrophysical Journal **638**, 963–967 (2006).

[253] A. Patruno, “Evidence of Fast Magnetic Field Evolution in an Accreting Millisecond Pulsar”, The Astrophysical Journal Letters **753**, L12 (2012).

[254] D. I. Jones, “Gravitational wave emission from rotating superfluid neutron stars”, Monthly Notices of the Royal Astronomical Society **402**, 2503–2519 (2010).

[255] N. Andersson, “A New Class of Unstable Modes of Rotating Relativistic Stars”, The Astrophysical Journal **502**, 708 (1998).

[256] J. L. Friedman and S. M. Morsink, “Axial Instability of Rotating Relativistic Stars”, The Astrophysical Journal **502**, 714 (1998).

[257] S. Yoshida and U. Lee, "R-Modes of Neutron Stars with a Solid Crust", The Astrophysical Journal **546**, 1121–1125 (2001).

[258] M. G. Alford, S. Mahmoodifar, and K. Schwenzer, "Viscous damping of r-modes: Small amplitude instability", Physical Review D **85**, 024007 (2012).

[259] LIGO Scientific Collaboration and Virgo Collaboration et al., "First narrow-band search for continuous gravitational waves from known pulsars in advanced detector data", Physical Review D **96**, 122006 (2017).

[260] A. Idrisy, B. J. Owen, and D. I. Jones, "R-mode frequencies of slowly rotating relativistic neutron stars with realistic equations of state", Physical Review D **91**, 024001 (2015).

[261] S. Caride, R. Inta, B. J. Owen, and B. Rajbhandari, "How to search for gravitational waves from r-modes of known pulsars", Physical Review D **100**, 064013 (2019).

[262] L. Sammut, C. Messenger, A. Melatos, and B. J. Owen, "Implementation of the frequency-modulated sideband search method for gravitational waves from low mass x-ray binaries", Physical Review D **89**, 043001 (2014).

[263] C. Messenger et al., "Gravitational waves from Scorpius X-1: A comparison of search methods and prospects for detection with advanced detectors", Physical Review D **92**, 023006 (2015).

[264] LIGO Scientific Collaboration and Virgo Collaboration et al., "All-sky search for continuous gravitational waves from isolated neutron stars using Advanced LIGO O2 data", Physical Review D **100**, 024004 (2019).

[265] A. Patruno, P. Bult, A. Gopakumar, J. M. Hartman, R. Wijnands, M. van der Klis, and D. Chakrabarty, "Accelerated Orbital Expansion and Secular Spin-down of the Accreting Millisecond Pulsar SAX J1808.4-3658", The Astrophysical Journal Letters **746**, L27 (2012).

[266] P. Leaci and R. Prix, "Directed searches for continuous gravitational waves from binary systems: Parameter-space metrics and optimal Scorpius X-1 sensitivity", Physical Review D **91**, 102003 (2015).

[267] D. Davis et al., "LIGO detector characterization in the second and third observing runs", Classical and Quantum Gravity **38**, 135014 (2021).

[268] J. Zweizig and K. Riles, *LIGO-T2000384-v4: Information on self-gating of h(t) used in O3 continuous-wave and stochastic searches.*

[269] L. Sun et al., "Characterization of systematic error in Advanced LIGO calibration", Classical and Quantum Gravity **37**, 225008 (2020).

[270] L. Sun et al., "Characterization of systematic error in Advanced LIGO calibration in the second half of O3", arXiv e-prints, arXiv:2107.00129 (2021).

[271] LSC Instrument Authors et al., "Identification and mitigation of narrow spectral artifacts that degrade searches for persistent gravitational waves in the first two observing runs of Advanced LIGO", Physical Review D **97**, 082002 (2018).

[272] E. Goetz et al., *LIGO-T2100200-v1: O3 lines and combs in found in self-gated C01 data.*

[273] M. M. Romanova, G. V. Ustyugova, A. V. Koldoba, and R. V. E. Lovelace, "Three-dimensional Simulations of Disk Accretion to an Inclined Dipole. II. Hot Spots and Variability", The Astrophysical Journal **610**, 920 (2004).

[274]B. Haskell, M. Priymak, A. Patruno, M. Oppenoorth, A. Melatos, and P. D. Lasky, "Detecting gravitational waves from mountains on neutron stars in the advanced detector era", Monthly Notices of the Royal Astronomical Society **450**, 2393–2403 (2015).

[275]A. Papitto, A. Riggio, L. Burderi, T. di Salvo, A. D'Aí, and R. Iaria, "Spin down during quiescence of the fastest known accretion-powered pulsar", Astronomy and Astrophysics **528**, A55 (2011).

[276]A. Sanna et al., "Spectral and timing properties of IGR J00291+5934 during its 2015 outburst", Monthly Notices of the Royal Astronomical Society **466**, 2910–2917 (2017).

[277]V. De Falco, L. Kuiper, E. Bozzo, D. K. Galloway, J. Poutanen, C. Ferrigno, L. Stella, and M. Falanga, "The 2015 outburst of the accretion-powered pulsar IGR J00291+5934: INTEGRAL and Swift observations", Astronomy and Astrophysics **599**, A88 (2017).

[278]L. L. Watkins, R. P. van der Marel, A. Bellini, and J. Anderson, "Hubble Space Telescope Proper Motion (HSTPROMO) Catalogs of Galactic Globular Clusters. III. Dynamical Distances and Mass-to-Light Ratios", The Astrophysical Journal **812**, 149 (2015).

[279]A. Marino, T. Di Salvo, A. F. Gambino, R. Iaria, L. Burderi, M. Matranga, A. Sanna, and A. Riggio, "Evidence of a non-conservative mass transfer for XTE J0929-314", Astronomy and Astrophysics **603**, A137 (2017).

[280]L. Keek, W. Iwakiri, M. Serino, D. R. Ballantyne, J. J. M. in't Zand, and T. E. Strohmayer, "X-Ray Reflection and an Exceptionally Long Thermonuclear Helium Burst from IGR J17062-6143", The Astrophysical Journal **836**, 111 (2017).

[281]J. van den Eijnden et al., "VLA radio detection of the very-faint X-ray transient IGR J17379-3747", The Astronomer's Telegram **1487** (2018).

[282]H. Negoro et al., "MAXI/GSC detection of renewed activity from the gamma-ray source IGR J17379-3747", The Astronomer's Telegram **1447** (2018).

[283]W. E. Harris, "A New Catalog of Globular Clusters in the Milky Way", arXiv e-prints, arXiv:1012.3224 (2010).

[284]R. Sharma, A. Beri, A. Sanna, and A. Dutta, "A broad-band look of the accreting millisecond X-ray pulsar SAX J1748.9-2021 using AstroSat and XMM-Newton", Monthly Notices of the Royal Astronomical Society **492**, 4361–4368 (2020).

[285]R. Wijnands, E. Rol, E. Cackett, R. L. C. Starling, and R. A. Remillard, "GRB060602B = Swift J1749.4-2807: an unusual transiently accreting neutron-star X-ray binary", Monthly Notices of the Royal Astronomical Society **393**, 126–132 (2009).

[286]M. Linares et al., "RXTE detection of a thermonuclear burst from IGR J17498-2921: distance estimate and burst oscillations", The Astronomer's Telegram **3568** (2011).

[287]A. Riggio, L. Burderi, T. di Salvo, A. Papitto, A. D'Aì, R. Iaria, and M. T. Menna, "Secular spin-down of the AMP XTE J1751-305", Astronomy and Astrophysics **531**, A140 (2011).

[288]N. V. Gusinskaia, T. D. Russell, J. W. T. Hessels, S. Bogdanov, N. Degenaar, A. T. Deller, J. van den Eijnden, A. D. Jaodand, J. C. A. Miller-Jones, and R. Wijnands, "Radio and X-ray monitoring of the accreting millisecond X-ray pulsar IGR J17591-2342 in outburst", Monthly Notices of the Royal Astronomical Society **492**, 1091–1101 (2020).

[289] L. Kuiper, S. S. Tsygankov, M. Falanga, I. A. Mereminskiy, D. K. Galloway, J. Poutanen, and Z. Li, “High-energy characteristics of the accretion-powered millisecond pulsar IGR J17591-2342 during its 2018 outburst. XMM-Newton, NICER, NuSTAR, and INTEGRAL view of the 0.3-300 keV X-ray band”, Astronomy and Astrophysics **641**, A37 (2020).

[290] A. Riggio, T. Di Salvo, L. Burderi, M. T. Menna, A. Papitto, R. Iaria, and G. Lavagetto, “Spin-up and Phase Fluctuations in the Timing of the Accreting Millisecond Pulsar XTE J1807-294”, The Astrophysical Journal **678**, 1273–1278 (2008).

[291] D. K. Galloway and A. Cumming, “Helium-rich Thermonuclear Bursts and the Distance to the Accretion-powered Millisecond Pulsar SAX J1808.4-3658”, The Astrophysical Journal **652**, 559–568 (2006).

[292] A. J. Goodwin, D. K. Galloway, A. Heger, A. Cumming, and Z. Johnston, “A Bayesian approach to matching thermonuclear X-ray burst observations with models”, Monthly Notices of the Royal Astronomical Society **490**, 2228–2240 (2019).

[293] P. D’Avanzo, S. Campana, J. Casares, S. Covino, G. L. Israel, and L. Stella, “The optical counterparts of accreting millisecond X-ray pulsars during quiescence”, Astronomy and Astrophysics **508**, 297–308 (2009).

[294] S. Campana and T. Di Salvo, “Accreting Pulsars: Mixing-up Accretion Phases in Transitional Systems”, in *The Physics and Astrophysics of Neutron Stars*, edited by L. Rezzolla, P. Pizzochero, D. I. Jones, N. Rea, and I. Vidaña, Astrophysics and Space Science Library (Springer International Publishing, Cham, 2018), pp. 149–184.

[295] M. Suzuki et al., “Discovery of a New X-Ray Burst/Millisecond Accreting Pulsar, HETE J1900.1-2455”, Publications of the Astronomical Society of Japan **59**, 263–268 (2007).

[296] D. K. Galloway, M. P. Muno, J. M. Hartman, D. Psaltis, and D. Chakrabarty, “Thermonuclear (Type I) X-Ray Bursts Observed by the Rossi X-Ray Timing Explorer”, The Astrophysical Journal Supplement Series **179**, 360 (2008).

[297] L. Sun, A. Melatos, and P. D. Lasky, “Tracking continuous gravitational waves from a neutron star at once and twice the spin frequency with a hidden Markov model”, Physical Review D **99**, 123010 (2019).

[298] B. J. Owen, “How to adapt broad-band gravitational-wave searches for r-modes”, Physical Review D **82**, 104002 (2010).

[299] D. I. Jones, “Parameter choices and ranges for continuous gravitational wave searches for steadily spinning neutron stars”, Monthly Notices of the Royal Astronomical Society **453**, 53–66 (2015).

[300] M. Zimmermann, “Gravitational waves from rotating and precessing rigid bodies. II. General solutions and computationally useful formulas”, Physical Review D **21**, 891–898 (1980).

[301] C. V. D. Broeck, “The gravitational wave spectrum of non-axisymmetric, freely precessing neutron stars”, Classical and Quantum Gravity **22**, 1825–1839 (2005).

[302] P. D. Lasky and A. Melatos, “Tilted torus magnetic fields in neutron stars and their gravitational wave signatures”, Physical Review D **88**, 103005 (2013).

[303] M. Millhouse, L. Strang, and A. Melatos, "Search for gravitational waves from 12 young supernova remnants with a hidden Markov model in Advanced LIGO's second observing run", Physical Review D **102**, 083025 (2020).

[304] G. Ashton and R. Prix, "Hierarchical multistage MCMC follow-up of continuous gravitational wave candidates", Physical Review D **97**, 103020 (2018).

[305] D. Keitel, R. Tenorio, G. Ashton, and R. Prix, "PyFstat: a Python package for continuous gravitational-wave data analysis", Journal of Open Source Software **6**, 3000 (2021).

[306] P. B. Covas and A. M. Sintes, "First All-Sky Search for Continuous Gravitational-Wave Signals from Unknown Neutron Stars in Binary Systems Using Advanced LIGO Data", Physical Review Letters **124**, 191102 (2020).

[307] R. Tenorio, D. Keitel, and A. M. Sintes, "Application of a hierarchical MCMC follow-up to Advanced LIGO continuous gravitational-wave candidates", Physical Review D **104**, 084012 (2021).

[308] D. Foreman-Mackey, D. W. Hogg, D. Lang, and J. Goodman, "Emcee: The MCMC Hammer", Publications of the Astronomical Society of the Pacific **125**, 306 (2013).

[309] W. D. Vousden, W. M. Farr, and I. Mandel, "Dynamic temperature selection for parallel tempering in Markov chain Monte Carlo simulations", Monthly Notices of the Royal Astronomical Society **455**, 1919–1937 (2016).